CARDIFF UNIVERSITY

SCHOOL OF ENGINEERING

Thesis Titled:

Exact Strip Analysis and Experiments on Buckling and Post-buckling of Plates and Stiffened Panels with Mode Jumping

By

Muthana Shaker Mahdi Al-Saymaree

A thesis submitted in fulfilment of the requirements for the degree of Doctor of Philosophy in Structural Engineering, 2019

Declaration

This work has not been submitted in substance for any other degree or award at this or any other university or place of learning, nor is being submitted concurrently in candidature for any degree or other award.

Signed ..Muthana Al-Saymaree..... (Candidate) Date ....19/09/2019.....

STATEMENT 1

This thesis is being submitted in partial fulfilment of the requirements for the degree of Doctor of Philosophy (PhD).

Signed ..Muthana Al-Saymaree..... (Candidate) Date ....19/09/2019.....

STATEMENT 2

This thesis is the result of my own independent work/investigation, except where otherwise stated, and the thesis has not been edited by a third party beyond what is permitted by Cardiff University's Policy on the Use of Third Party Editors by Research Degree Students. Other sources are acknowledged by explicit references. The views expressed are my own.

Signed ..Muthana Al-Saymaree..... (Candidate) Date ....19/09/2019.....

STATEMENT 3

I hereby give consent for my thesis, if accepted, to be available online in the University's Open Access repository and for inter-library loan, and for the title and summary to be made available to outside organisations.

Signed ..Muthana Al-Saymaree..... (Candidate) Date ....19/09/2019.....

Abstract

Engineering components consisting of plated structures subjected to in plane loading can potentially fail due to buckling. This work focuses on presenting novel approaches to enhance the buckling and post-buckling behaviour of flat plates and stiffened panels made with metal and composite materials under in-plane loading conditions. A better understanding of post-buckling behaviour, including the phenomenon of mode jumping, will lead to improvements in both design criteria and manufacturing processes.

The first part of this thesis describes an extensive study using the exact finite strip computer program VICONOPT and the finite element method to investigate the buckling of simply supported composite plates under different in plane loads. This approach utilises the lamination parameters to enhance the buckling capacity through the anisotropic properties of the laminate. Numerical relationships are presented as an optimisation procedure to maximise the buckling load under in plane uniaxial compression, shear or a combination of both. The procedure is applied to a series of anisotropic symmetric and balanced laminates with varying thickness and aspect ratios.

The second part presents a numerical and experimental study to explore the post-buckling phenomenon of mode jumping phenomenon in plates and stiffened panels. The VICONOPT post-buckling analysis is extended to predict mode jumping, and the resulting numerical investigations are validated by finite element analysis. Furthermore, a series of experimental tests have been devised to investigate the buckling, post-buckling and mode jumping behaviour of curved stiffened panels with different radii of curvature. The experimental results are compared with finite element results in order to examine the similarities and differences between simulations and real behaviour of panels under compressive load.

Acknowledgement

I would like to take this opportunity to express my great debt of gratitude to my academic supervisors Professor David Kennedy and Professor Carol Featherston for their unlimited continuous guidance, patience, encouragement and immense support, through the four years of my PhD study. Their valuable proofreading, feedbacks and comments help me in all my steps of research and writing of this thesis.

I would like to thank Dr John McCrory for his advice and help and would also like to thank the technical staff at Cardiff School of Engineering especially Ian King, Richard Rogers and Harry Lane.

Further gratitude and appreciation is expressed to my sponsor (The Higher Committee for Education Development in Iraq) for funding my study and giving me this unique opportunity. I would also like to thank all my friends and colleagues for their support and company especially my research group members.

I dedicate this work to my father spirit who spent his life in raising me with compassion and I really miss his support, to my mother who encourages and supports me through her tenderness and praying.

I would like to dedicate this work to my faithful wife for her great patience, encouragement and understanding during the years of living away from home and to my lovely son Ali for giving me the hope and help me to pass through my hard time during the study. I would also like to thank my brother and sisters and the rest of my family for their support and encouragement.

Finally I wish to dedicate this work to Professor Fred Williams's memory who inspired us through his valuable contributions in the structural engineering field.

Contents

List of Figures

List of Tables

Nomenclature

a	Length of plate
b	Width of plate
b_e	Effective width
h , t	Plate thickness
u , v	In plane displacement
w	Out of plane displacement
θ	Rotation
E_1	Modulus of elasticity in the fibre direction
E_2	Modulus of elasticity in the transvers direction
G_{12}	Shear modules
$\mathscr{v}$	Poisson ratio
ρ	Density
N_{xx}, N_{yy}, N_{xy}	Stress resultant
M_{xx}, M_{yy}, M_{xy}	Moment resultant
K_{xx}, K_{yy}, K_{xy}	Curvature
$\sigma_{xx}, \sigma_{yy}, \sigma_{zz}$	Stress components
A	Membrane stiffness matrix
B	Bending-membrane stiffness matrix
D	Flexural stiffness matrix
$\varepsilon_{xx}, \varepsilon_{yy}, \varepsilon_{zz}$	Strain components
$\tau_{xy}, \tau_{yz}, \tau_{xz}$	Shear stress components
ε_{cr}	Critical buckling strain
σ_{cr}	Critical buckling stress
m	Number of half wavelength in x direction
P	Axial force
ε_t	Modified strain values
ε_j	Jumping strain
Enr_{acc}	Cumulative energy
i	Number of post buckling cycle
$\xi_1^A, \xi_2^A, \xi_3^A, \xi_4^A$	In plane lamination parameters
$\xi_1^B, \xi_2^B, \xi_3^B, \xi_4^B$	Coupling lamination parameters
$\xi_1^D, \xi_2^D, \xi_3^D, \xi_4^D$	Out of plane lamination parameters

Chapter 1: Introduction

1.1 General overview

Thin-walled structures are utilised for different purposes in many engineering sectors ranging from aerospace applications to the marine industry and wind turbines. According to structural engineering, high-performance aerospace structures can be inherently categorised as thin-walled because of their relatively low thickness in comparison with other dimensions of the structure [1]. Research related to aircraft design and manufacturing has focused on improving the performance under various usage conditions to reduce their impact on our planet in two ways. The first is decreasing harmful emissions such as CO_2 to reduce environmental pollutants and global warming while the second is reducing the consumption of natural resources by decreasing the weight of structural components and increasing engine efficiency.

The UK aerospace sector is not just a world leader in a highly competitive global market, it also makes a significant contribution to the nation's economy. And over the past six years productivity growth in the industry has been six times more than in the economy as a whole. UK aerospace is the powerhouse of United Kingdom manufacturing sector, as it is Europe's leading aerospace manufacturing nation and second only to the United States. In numbers language, the productivity has grown by 39% since 2010 with exports earning £27 billion a year and the industry directly employs over 128,000 people. Greener, quieter and more economical aircraft worth over $5.5 trillion will be required over the next 20 years [2].

The long-term government commitment to research and technology (R&T) funding through the Aerospace Technology Institute (ATI) has been instrumental. Matched by industry to total £3.9 billion between 2013 and 2026,

this instils business confidence and crowds in higher private investment. It also leads to social returns that far exceed the commercial returns of the companies undertaking the research. The ATI analysis shows that sustaining current level of support to aerospace industrial strategy could return around £114 billion to the UK economy over the next 20 years and create and secure an additional 95,000 jobs by 2035 [3].

The resulting increasing demands on commercial aircraft require their components to have the minimal thickness, reducing weight and cost. Moreover, improving the structural performance of these components allows their usage to be extended to a wider set of flight conditions because they can carry more load. The basic parts of an aircraft wing or fuselage consist of thin plates and shells in the form of stiffened panels forming these huge structures. More recently, composite materials (comprising mainly carbon and glass fibre composites) have been increasingly applied in a variety of aerospace industries due to their attractive characteristics, providing mass reductions whilst maintaining high levels of strength and stiffness. For example the Airbus A380 uses 30 metric tonnes of composite material amounting to 16% of the total airframe weight [4] and the Boeing 787 which utilises up to 50% of carbon fibre reinforced plastic and other composites that offers weight saving on average of 20% compared to conventional material [5].

Consequently, the components of these structures have been major research topics with studies examining structural behaviour, materials, damage tolerance and optimum design to provide a reliable understanding that leads to better designs and manufacturing techniques providing significantly lighter and more efficient future aircraft.

1.2 Aims and objectives

The work described in this thesis aims to:

• Recommend an optimisation process to maximise the buckling load of composite flat plates based on anisotropy.

• Improve the exact strip software VICONOPT by including mode jumping in the post-buckling analysis.

The following objectives are set for this work:

• To explore the buckling and post-buckling behaviour of flat plates and stiffened panels through analysis using the VICONOPT software for both isotropic and composite materials under in-plane loading.

• To develop an optimisation process to improve the buckling capacity of composite plates under different in-plane loading conditions.

• To improve VICONOPT post-buckling analysis by including the mode-jumping phenomenon in the geometrical nonlinear buckling capability provided by the software.

• To apply the suggested approaches to predict the jumping strain in a range of plates and panels to verify these methods.

• To develop a finite element model to provide reliable validation of the suggested mathematical approach for mode jumping point detection.

• To investigate the effect of buckling mode change on the post-buckling behaviour of stiffened panels experimentally in order to examine the real response of similar structures.

• To compare the experimental behaviour of these stiffened panels with the results of the numerical analysis using finite element models created for this purpose.

1.3 Contributions and novelty statements

This thesis investigates in two parts the buckling and post-buckling behaviour of thin-walled structures including mode jumping. The work focuses on enhancing the performance of these structures under different in-plane loading conditions. The main contributions and novelty in this work are:

i. Buckling analysis (part 1)

• A study of the initial buckling behaviour of anisotropic composite plates using the exact strip software VICONOPT and finite element software ABAQUS.

• A novel optimisation procedure introduced to improve the buckling capacity of composite plates using the anisotropy of the laminates.

ii. Post-buckling and mode jumping phenomenon (part 2)

• Improved post-buckling analysis in the VICONOPT software, including the buckling mode jumping effect in the post-buckling region.

• A new mathematical calculation procedure based on von Karman's effective width concepts to provide a fast prediction of mode jumping strain value.

• A modified mathematical method, which uses strain energy comparison in order to evaluate the point where the mode jumping might occur.

• Finite element models to validate the exact strip post-buckling analysis results including the mode jumping effect.

• An experimental investigation of stiffened panels to evaluate actual post-buckling and mode jumping behaviour, used to match the simulation results using finite element models.

1.4 Thesis organisation

The work which is described in this thesis can be divided into two parts. The first (chapters 4 and 5), is an extensive study of the buckling behaviour of composite flat plates with anisotropic characteristics which leads to the proposal of an optimisation procedure to maximise buckling capacity using anisotropic lay-ups. The second (chapters 6 and 7), is an investigation into the mode jumping phenomenon which occurs during the post-buckling of plates and stiffened panels. The aim of this part is to improve understanding of buckling and post-buckling behaviour by including the buckling mode change effect.

This chapter provides a general introduction to the application of thin-walled structures, the aims and objectives of the work presented in this thesis and the main contributions of that work.

Chapter 2 includes a brief overview of plate types and the theories that have been developed to predict their behaviour, starting with classical plate theory (CPT) and moving through to techniques which can incorporate increasing levels of complexity such as material and geometrical non-linearity including finite strip and finite element methods.

Chapter 3 reviews previous studies starting with a short description of the pioneering researches dealing with the buckling of plates and then moving on to more recent studies covering different sources of nonlinearity during the post-buckling stage. This is expanded to review the studies that explore mode jumping as an observable phenomenon through the post-buckling behaviour. A brief review of the exact strip software VICONOPT is presented at the end of this chapter.

Chapter 4 outlines the development of an optimisation process proposed to improve the buckling behaviour of composite plates by utilizing their

anisotropic properties. The process is based on the use of non-dimensional lamination parameters to control the laminate stiffness matrix in order to maximise buckling capacity.

Chapter 5 presents an examination of a range of laminates with different aspect ratios, stacking sequences and loading types to verify the proposed optimisation procedure described in the previous chapter. The investigation uses the exact strip method VICONOPT and finite element ABAQUS software for buckling analysis.

Chapter 6 begins the second part of this work, focusing on a theoretical investigation of mode jumping and including mode changes in the post-buckling analysis of the VICONOPT software. It then validates the approaches proposed by using finite element analysis.

Chapter 7 presents an experimental investigation to explore the buckling and post-buckling behaviour with mode jumping of stiffened panels with L-shape stiffeners which have different radii of curvature. The results obtained from these tests are compared with finite element models generate using the ABAQUS software. Matching the simulations with experiments results provides a better understanding of the behaviour of stiffened panels under similar load and boundary conditions.

Chapter 8 summarise the main conclusions obtained from the two parts of this thesis. It also discusses potential directions for future work.

1.5 Published output

- **M. S. Al-Saymaree**, D. Kennedy and C. A. Featherston. Effect of shear load direction in the critical buckling of composite laminates under combined in-plane loading. ACME-UK2016: 24th Conference on

Computational Mechanics, Cardiff, UK, 31 Mar-1 Apr 2016, Paper 88638.

- **M. S. Al-Saymaree**, C. A. Featherston and D. Kennedy. Mode jumping in the post-buckling analysis of plates using exact strip method. ICCS-20: 20th International Conference on Composite Structure, Paris, France, 4-7 September 2017, Paper 282.
- Al-Azzawi, **M. S. Al-Saymaree**, L. Kawashita and C. A. Featherston. Quasi-static damage in fibre metal laminate adhesive joints: experimental investigations. ICCS-20: 20th International Conference on Composite Structure, Paris, France, 4-7 September 2017, Paper 738.
- **M. S. Al-Saymaree**, C.A. Featherston and D. Kennedy. Mode jumping in post-buckling of simply supported thin plates using exact strip method. WCCM 2018: 13th World Congress on Computational Mechanics, New York City, USA, 22-27 July 2018, Minisymposium 1010.
- **M. S. Al-Saymaree**, C.A. Featherston and D. Kennedy. Mode jumping in post-buckling Analysis of curved stiffened panels. BSSM: 14th International Conference on Advances in Experimental Mechanics, Belfast, UK 10-12 September 2019 (Accepted).
- **M. S. Al-Saymaree**, X. Liu, D. Kennedy and C. A. Featherston. Buckling behaviour of optimized flat composite plates under in-plane loading using flexure/twisting anisotropy properties. Journal paper (to be submitted to Composite Structures in summer 2019).
- **M. S. Al-Saymaree**, D. Kennedy and C. A. Featherston. Mode jumping in Post-buckling region of plates and stiffened panels (theoretical and experimental investigations). Journal paper (to be submitted to Thin-Walled Structures in summer 2019).

Chapter 2: Theory and Background

2.1 Introduction

This chapter summarises the main theories developed to derive mathematical relationships and formulas that describe the behaviour of thin-walled structures (plates and shells). Plate structures are shells with zero curvature, and therefore plate theories can be derived from shell theories. Plate structures are commonly used in different engineering sectors because of their unique characteristics including high stiffness, efficiency and strength to weight ratios, which enable engineering designs with lower material requirements. Traditional plate theory is based on the work of Kirchhoff and Love [6] who established the classical linear plate theory (CPT). The main studies, which have been carried out in relation to plate behaviour, are summarised in Figure 2.1 below.

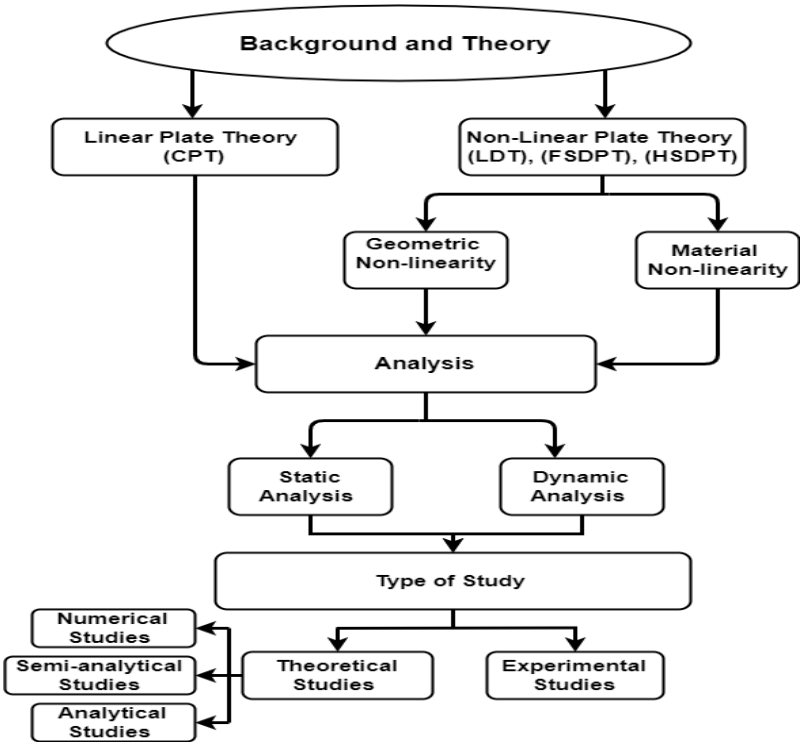

Figure 2.1: Plate studies

Many aspects of the theory and analysis of plate and shell structures are described in the textbooks such as Timoshenko [7], Novozhilof [8], Dym [9], Ugural [10], Ventsel and Krauthammer [11], Szilard [12], Sadd [13] and Reddy [14]. The majority of plate theories rely on the following relationships:

1. Displacement fields, usually determined by the kinematic equations for the entire structure experiencing deformation. For example plates and shells are often assumed to have a constant thickness under loading, meaning that the deflections along a normal to the mid-surface of the plate are constant.

2. Strain-displacement relationships, which reflect the proportion of deformations relative to characteristic dimensions of the structure. These relationships are influenced by the kinematic equations so that they can incorporate effects such as transverse shear deformability into the analysis. When the displacements of a plate or shell are relatively small, the strain can be assumed to be a linear function of displacement. However, in the case of large deformations, the strains are non-linear functions of displacements. In particular cases, it is possible to assume a linear strain-displacement relationship for more general non-linear formulations.

3. Constitutive relationships take into account the physical properties of the material that define the stress tensors in term of the strain tensors. Thus, elastic, elastic–plastic, viscoelastic, visco-plastic, shape memory, piezoelectric and other materials can be characterised by the appropriate theory.

A plate's structural behaviour depends greatly on its thickness, which has a noticeable effect on the governing equations, especially the deformation relationships.

2.2 Plate classification

A plate resists transverse loads in terms of bending, exclusively. The flexural properties of the plate depend significantly on its thickness in comparison with other dimensions. Plates can be divided into three groups according to the thickness ratio ($\frac{a}{h}$), where *a* is a typical dimension of plate in a plane and *h* is its thickness. These groups are:

- Thick plates: represent plates having $\frac{a}{h} \leq 8$ to 10. The analysis of such structures includes all the components of stress, strain and displacement as for solid bodies using the general equations of three-dimensional elasticity. Problems related to this type of plates are more complicated and need advanced plate theory to predict their engineering behaviours.
- Plates with $\frac{a}{h} \geq 80$ to 100. These plates are referred as membranes. They are devoid of flexural rigidity. Membranes carry the lateral loads by axial tensile forces and a shear force acting on the plate middle surface. These forces, called membrane forces, produce projections on the vertical axis and thus balance a lateral load applied to the plate membrane.
- The most extensive group represents an intermediate type of plate, which is called thin. A thin plate has a ratio $8 \text{ to } 10 \leq \frac{a}{h} \leq 80 \text{ to } 100$.

These three plate types are described in Figure 2.2. Depending on the value of the ratio $\frac{w}{h}$, the ratio of the maximum deflection *w* of the plate to its thickness, the flexural or membrane forces may be dominant. Therefore, thin plates can be divided into two different sub-groups; (a) Stiff plates which can be defined as the plates with $\frac{w}{h} \leq 0.2$. Stiff plates are flexurally rigid thin plates.

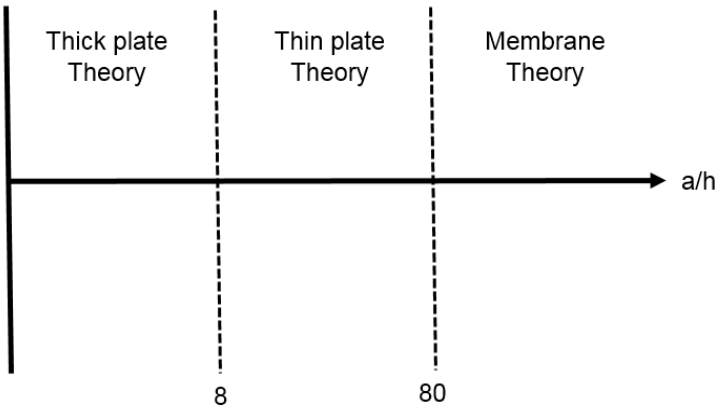

Figure 2.2: Plate classification depending on the (*a/h*) ratio

They carry load two-dimensionally, mostly by internal bending and twisting moments and by transverse shear. The middle surface deformations and membrane forces are negligible. (b) Flexible plates: if the plate deflections are beyond a certain level, $\frac{w}{h} \geq 0.3$, then the lateral deflections will be accompanied by stretching of the middle surface. Such plates are classified as flexible plates. These plates represent a combination of stiff plates and membranes and carry external loads by a combined action of internal moments, shear forces, and membrane (axial) forces. Such plates, because of their favourable weight-to-load ratio, are widely used by the aerospace industry. When the magnitude of the maximum deflection is considerably greater than the plate thickness, the membrane action predominates. Therefore if $\frac{w}{h} \geq 5.0$, the flexural stress can be neglected compared with the membrane stress. Consequently, the load carrying mechanism of such plates becomes of the membrane type, i.e., the stress is uniformly distributed over the plate thickness. The above classification is conditional because the assignment of a plate to one or another group depends on the accuracy of the analysis, type of loading, boundary conditions, etc. The behaviour of a plate structure is widely dependent on the stability of the equilibrium conditions under different types of loading.

2.3 Classical plate theory (CPT)

CPT states that the deformation of the mid-plane (MP) of a plate describes its whole deformation. The linear mechanics of deformable bodies assume that the displacements are proportional to loads. The main kinematic assumption of this theory is based on Kirchhoff's hypothesis:

- Straight lines normal to the mid-plane remain straight (and normal to the mid-plane) after deformation.
- The deflection of the mid-plane is small compared to the plate thickness.
- The thickness of the plate is constant during deformation.
- The transverse shear force is small compared to the bending force.
- The stress normal to mid-plane, σ_z, is small compared with other components and may be neglected, the mid-plane remains unrestrained after bending (because the displacements are small).

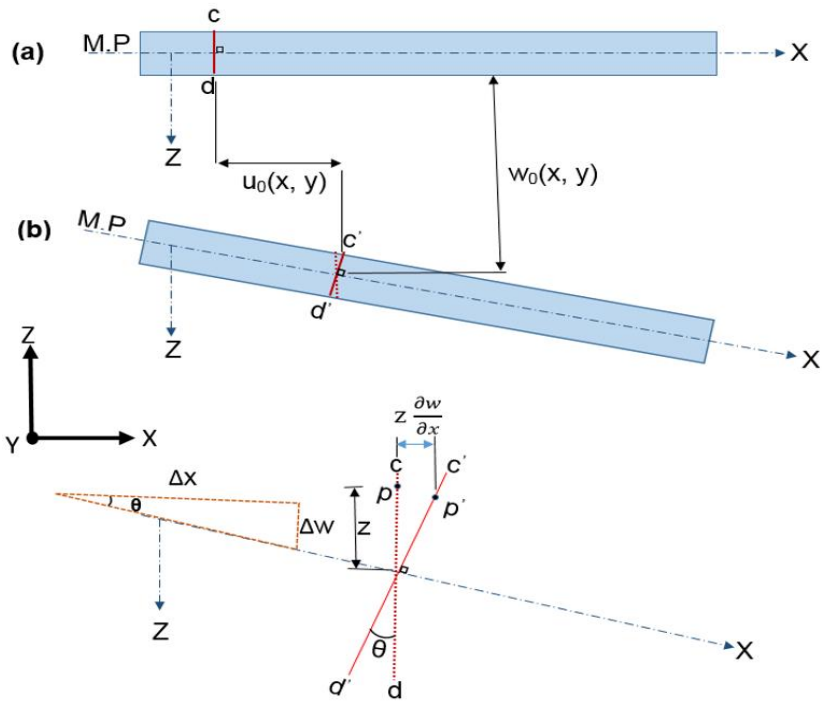

Figure 2.3: Deflection of a thin plate according to CPT (*y*-direction view)

2.3.1 Displacement field in CPT

For small deformation $\tan\theta \approx \theta$, then $\theta \approx \partial w/\partial x$, therefore the in-plane deformation due to the rigid rotation of the normal is $-z\,\partial w/\partial x$. Thus the deformation of a generic point on the normal due to stretching and bending is

$$u(x,y,z) = u_0(x,y) - z\left(\frac{\partial w}{\partial x}\right) \tag{2.1}$$

In the same way, the deformation in the y-direction is

$$v(x,y,z) = v_0(x,y) - z\left(\frac{\partial w}{\partial y}\right) \tag{2.2}$$

Moreover, the deformation in the z-direction is:

$$w(x,y,z) = w_0(x,y) \tag{2.3}$$

where u_0, v_0, w_0 are the mid-surface displacements. According to the Kirchhoff hypothesis, the transverse shear strains are zero $\gamma_{xz} = \gamma_{yz} = 0$. In addition, the normal transverse strain is zero $\varepsilon_{zz} = \frac{\partial w}{\partial z} = 0$.

2.3.2 Strain and stress field in CPT

The strain components are functions of the displacement field, which have the form:

$$\begin{Bmatrix}\varepsilon_{xx}\\ \varepsilon_{yy}\\ \varepsilon_{xy}\end{Bmatrix} = \begin{Bmatrix}\varepsilon^0_{xx}\\ \varepsilon^0_{yy}\\ \varepsilon^0_{xy}\end{Bmatrix} + z\begin{Bmatrix}K_{xx}\\ K_{yy}\\ K_{xy}\end{Bmatrix} \tag{2.4}$$

where equation (2.4) can be written in two parts, the first one represents the in-plane strain while the other is midplane curvature as shown below:

$$\begin{Bmatrix}\varepsilon^0_{xx}\\ \varepsilon^0_{yy}\\ \varepsilon^0_{xy}\end{Bmatrix} = \begin{Bmatrix}\dfrac{\partial u_0}{\partial x}\\ \dfrac{\partial v_0}{\partial y}\\ \dfrac{\partial u_0}{\partial y} + \dfrac{\partial v_0}{\partial x}\end{Bmatrix} \tag{2.5}$$

$$\begin{Bmatrix} K_{xx} \\ K_{yy} \\ K_{xy} \end{Bmatrix} = \begin{Bmatrix} -\dfrac{\partial^2 w}{\partial x^2} \\ -\dfrac{\partial^2 w}{\partial y^2} \\ -2\dfrac{\partial^2 w}{\partial x\,\partial y} \end{Bmatrix} \tag{2.6}$$

For isotropic materials, the stress-strain relations will be a function of Young's modulus and Poisson's ratio. Strains are given in terms of stresses as

$$\begin{Bmatrix} \mathcal{E}_{xx} \\ \mathcal{E}_{yy} \\ \mathcal{E}_{xy} \end{Bmatrix} = \frac{1}{E}\begin{bmatrix} 1 & -\nu & 0 \\ -\nu & 1 & 0 \\ 0 & 0 & 1+\nu \end{bmatrix} \begin{Bmatrix} \sigma_{xx} \\ \sigma_{yy} \\ \sigma_{xy} \end{Bmatrix} \tag{2.7}$$

while stresses are given in terms of strains as

$$\begin{Bmatrix} \sigma_{xx} \\ \sigma_{yy} \\ \sigma_{xy} \end{Bmatrix} = \frac{E}{1-\nu}\begin{bmatrix} 1 & \nu & 0 \\ \nu & 1 & 0 \\ 0 & 0 & 1-\nu \end{bmatrix} \begin{Bmatrix} \mathcal{E}_{xx} \\ \mathcal{E}_{yy} \\ \mathcal{E}_{xy} \end{Bmatrix} \tag{2.8}$$

Figure 2.4 shows the stresses in a plate element. The membrane stress resultants (load per unit length) which are applied in the plane of plates N_{xx}, N_{yy} are the resultants of an integration of the normal stresses while the shear force per unit length N_{xy} resultant of an integration of shear stress. The bending moments come from normal stresses and twisting moments produced by edge shear force. The mathematical expressions of these three force components are:

$$\begin{Bmatrix} N_{xx} \\ N_{yy} \\ N_{xy} \end{Bmatrix} = \int_{-\frac{h}{2}}^{\frac{h}{2}} \begin{bmatrix} \sigma_{xx} \\ \sigma_{yy} \\ \tau_{xy} \end{bmatrix} dz \quad , \quad \begin{Bmatrix} M_{xx} \\ M_{yy} \\ M_{xy} \end{Bmatrix} = \int_{-\frac{h}{2}}^{\frac{h}{2}} \begin{bmatrix} \sigma_{xx} \\ \sigma_{yy} \\ \tau_{xy} \end{bmatrix} z\, dz \tag{2.9}$$

Moreover, the stress resultants for isotropic material with Young's modulus E and Poisson's ratio ν can be written as:

$$\begin{Bmatrix} N_{xx} \\ N_{yy} \\ N_{xy} \end{Bmatrix} = A\begin{bmatrix} 1 & \nu & 0 \\ \nu & 1 & 0 \\ 0 & 0 & 1-\nu \end{bmatrix} \begin{Bmatrix} \mathcal{E}^0_{xx} \\ \mathcal{E}^0_{yy} \\ \mathcal{E}^0_{xy} \end{Bmatrix} \quad \text{where } A = \frac{E\,h}{1-\nu^2} \tag{2.10}$$

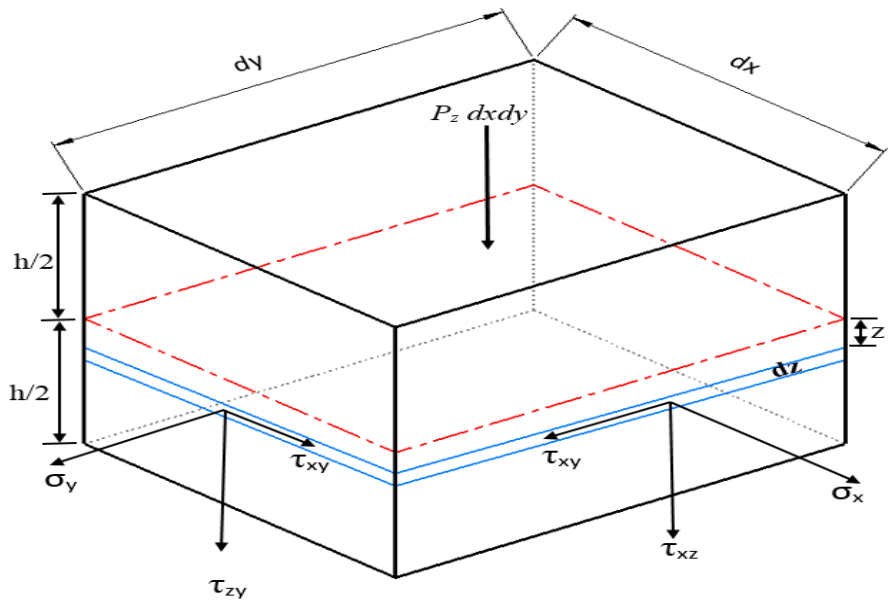

Figure 2.4: Stresses in the plate element

$$\begin{Bmatrix} M_{xx} \\ M_{yy} \\ M_{xy} \end{Bmatrix} = D \begin{bmatrix} 1 & \nu & 0 \\ \nu & 1 & 0 \\ 0 & 0 & \frac{1-\nu}{2} \end{bmatrix} \begin{Bmatrix} K_{xx} \\ K_{yy} \\ K_{xy} \end{Bmatrix} \quad \text{where } D = \frac{E\,h^3}{12(1-\nu^2)} \tag{2.11}$$

The equilibrium equations in the *x*-direction and *y*-direction respectively are:

$$\frac{\partial M_{xx}}{\partial x} + \frac{\partial M_{xy}}{\partial y} = Q_x \quad , \quad \frac{\partial M_{yy}}{\partial y} + \frac{\partial M_{xy}}{\partial x} = Q_y \tag{2.12}$$

where Q_x and Q_y are the transverse shear force per unit length.

Integrating the equilibrium equation in the z-direction over the plate thickness.

$$\frac{\partial Q_x}{\partial x} + \frac{\partial Q_y}{\partial y} = -P(x,y) \tag{2.13}$$

Combining equations (2.12) and (2.13) into a single equation and eliminating Q_x and Q_y:

$$\frac{\partial^2 M_{xx}}{\partial x^2} + 2\frac{\partial^2 M_{xy}}{\partial x\,\partial y} + \frac{\partial^2 M_{yy}}{\partial y^2} + P(x,y) = 0 \tag{2.14}$$

From elasticity theory:

$$M_{xx} = -D\left(\frac{\partial^2 w}{\partial x^2} + \nu\frac{\partial^2 w}{\partial y^2}\right) \tag{2.15}$$

$$M_{yy} = -D\left(\frac{\partial^2 w}{\partial y^2} + \nu\frac{\partial^2 w}{\partial x^2}\right) \tag{2.16}$$

Finally, equation (2.14) can be expressed in terms of out of plane displacement as:

$$\nabla^4 w \equiv \left(\frac{\partial^4}{\partial x^4} + \frac{\partial^4}{\partial x^2\,\partial y^2} + \frac{\partial^4}{\partial y^4}\right) w = \frac{P}{D} \tag{2.17}$$

where $D = (E\,h^3)/12(1-\nu^2)$ as mentioned previously in equation (2.11).

2.4 Nonlinear plate theory

When thin plates are subjected to external loading, they will bend. If a plate behaves elastically, the deflections are small i.e. $w < h/10$ where w is the transverse deflection (out of plate plane displacement), and h is the structure thickness, it is possible to ignore geometric non-linearity and the plate can be analysed using the classical plate theory. That means neglecting the parts of the equations which include the out of plane displacement terms. However, in most cases and due to the small thickness of plate structures, the mid-plane deflection w is usually higher than this. Thus, non-linear geometrical effects should be considered.

Initially, nonlinearities exist in the equation of motion when the products of variables, or their derivatives, exist. Moreover, they can exist when there are discontinuities or jumps in the system. This nonlinear behaviour may come from different sources. One of these sources is geometric nonlinearity, which is important in the case of structures with large deformations. Non-linear (large) deformation theory (LDT) considers the effects of both bending and stretching of the middle surface of the plate.

This requires linear plate theory to be extended by performing the non-linear strain term when the out of plane displacement is coupled to in-plane strain.

Von Karman [15] first derived the mathematical formulas for this theory in 1910 by connecting axial forces with transverse displacement. However, in the case of large deflections, a significant membrane force can be caused due to transverse deformations. As a result, an equation that relates to the amplitude of the transverse deflection due to the membrane forces is required. The basic assumptions of von Karman theory are:

- The plate is a thin plate. The thickness h is much smaller than the typical plate dimension, $\boldsymbol{h}<<\boldsymbol{a}$.
- The magnitude of the transverse deflection is of the same order as the thickness of the plate, |w| = O (h). In practice, the present theory is still a good engineering approximation for deflections up to ten plate thicknesses.
- Gradients of in-plane displacements are small so that their product or square can be neglected.
- The Love-Kirchhoff hypothesis is satisfied and in-plane displacements are linear functions of the z-coordinate.

The deflections of thin plates are large in comparison with the nominal plate thickness. However, they are still small when compared with the other dimensions. This deformation is governed by von Karman's equations:

$$\frac{1}{D}\left(N_x \frac{\partial^2 w}{\partial x^2} + 2N_{xy}\frac{\partial^2 w}{\partial x\,\partial y} + N_y \frac{\partial^2 w}{\partial y^2}\right) = \nabla^4 w \tag{2.18}$$

$$Et\left(\left(\frac{\partial^2 w}{\partial x\,\partial y}\right)^2 - \frac{\partial^2 w}{\partial x^2}\frac{\partial^2 w}{\partial y^2}\right) = \left(\frac{\partial^2 N_x}{\partial y^2} - \frac{\partial^2 N_{xy}}{\partial x\,\partial y} + \frac{\partial^2 N_y}{\partial x^2}\right) \tag{2.19}$$

Moreover, the equilibrium equations are still applicable:

$$\frac{\partial N_x}{\partial x} + \frac{\partial N_{xy}}{\partial y} = 0 \tag{2.20}$$

$$\frac{\partial N_{xy}}{\partial x} + \frac{\partial N_y}{\partial y} = 0 \tag{2.21}$$

According to plate and shell theories, this analysis will generate a number of differential equations, which can be solved by either applying equilibrium between the stress resultants and the applied loads or by energy considerations. Thin-walled structures are sensitive to in-plane loading and deform with different buckling configurations. During buckling, a disproportionate displacement occurs when the load is increased by a specific amount, thus buckling behaviour is considered as a nonlinear rather than linear behaviour. To address the buckling behaviour of structures, it is necessary to start with stability consideration.

2.5 The concept of stability

There are many ways a structure or structural element can become unstable depending on structural geometry and load characteristics. The spatial geometry, the material, along with its distribution and properties, the character of the connections (riveted joints, welded, etc.) and the support comprise the structural geometry. As external forces are applied quasi-statically, the elastic structure deforms, and static equilibrium is maintained. When 'small' external disturbances are applied, the structure reacts by simply performing oscillations about the deformed equilibrium state, and the equilibrium is said to be stable. The disturbance can be in the form of deformations or velocities. On the other hand, if an elastic structure either tends to or remains in the disturbing position or tends to and diverges from the deformed equilibrium state, the equilibrium is said to be unstable.

2.6 Buckling behaviour of structures

Buckling of structures is defined by many authors with different definitions. Several hypotheses have been presented over the years to predict the elastic stability and buckling of beams, columns, plates and shells, and the problem of buckling represents a particular class of bifurcation phenomena. One of the basic and general meanings of buckling corresponds to a “critical state of structural instability at a particular load level at which the structure exhibits a large displacement or collapse”.

Jones [16] describes the buckling phenomenon with a more accurate definition of instability, which is: “An equilibrium state or configuration of a structural element, structure, or mechanical system is unstable if any 'small' disturbance of the system results in a sudden change in deformation mode or displacement value after which the system does not return to its original equilibrium state”. Figure 2.5 illustrates structural response incorporating of linear and non-linear behaviour. Research into buckling and elasticity theory for structures has a long history, which started with a study by Leonard Euler [17] who presented an analytical approach for the theory of column flexural buckling subjected to axial load. He was followed by followed many pioneer researchers, who developed the Euler theory. Buckling may be classified into two categories (1) bifurcation buckling and (2) limit load buckling Chen and Lui [18]. In the first type of buckling the deformation under compressive load changes from one direction to a different direction, for example from axial shortening to lateral deflection. The load at which the bifurcation occurs in the load-deformation space is called the critical buckling load. The deflection path before the bifurcation point is known as the primary path while the path after that point is called the secondary path Figure 2.6. The secondary path may be symmetric or asymmetric and rise or fall below the critical buckling load depending on the structure and the type of loading.

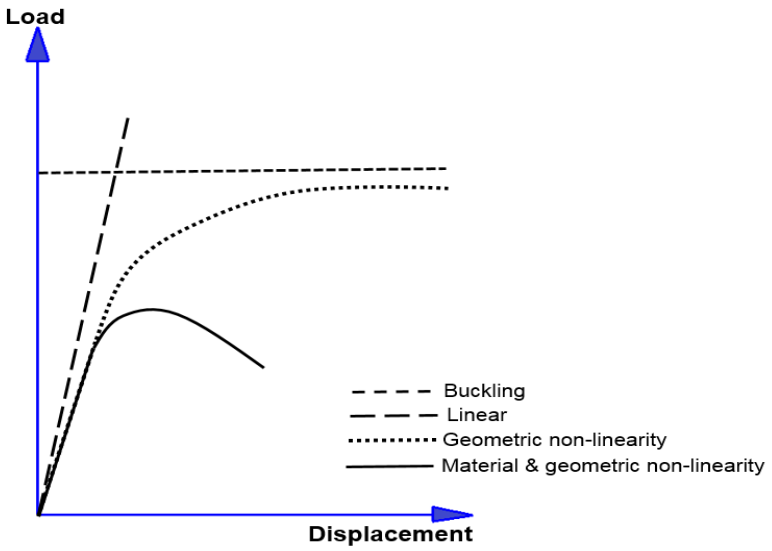

Figure 2.5: Structural behaviour

In limit load buckling, the structure reaches a maximum load without any bifurcation, i.e., with the only one mode of deflection. As the first buckling theory was derived for a column, it is important to provide a comparison between column and plate stability. In the case of a perfect column, the lateral displacement remains zero as the load increases until the attainment of buckling load (Euler load).

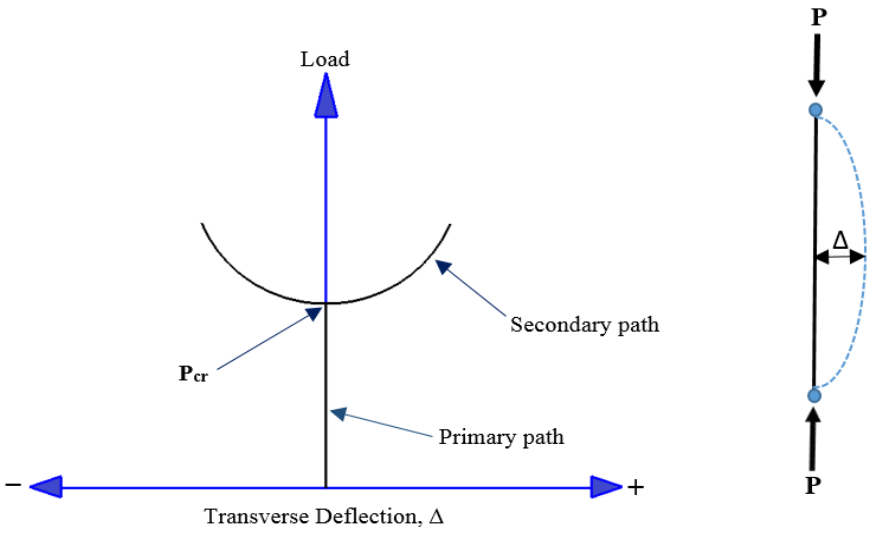

Figure 2.6: Bifurcation buckling, symmetric and stable post-buckling curve

The lateral deformation increases indefinitely at constant load as shown in Figure 2.7a, and the secondary path of the column represents a neutral equilibrium. The fundamental path (primary path) for a perfect flat plate is similar to that of an ideal column. At the point of critical buckling, the path will bifurcate into the secondary path as shown in Figure 2.7b. The equilibrium path in Figure 2.7b shows the ability of the plate to carry loads beyond the initial buckling load. Moreover, the plate secondary path is stable unlike that for the column. Thus, the initial buckling of the plate cannot be considered a collapse load. The theoretical buckling problems of plates and shell structures are traditionally solved by one of the following techniques: analytical, numerical or the semi-analytical solutions. The analytical solution is sometimes called the exact solution of the problem and solves the governing equations using the boundary and initial conditions of the problem. The solution in this method satisfies the governing equations of the boundary and initial conditions of the problem.

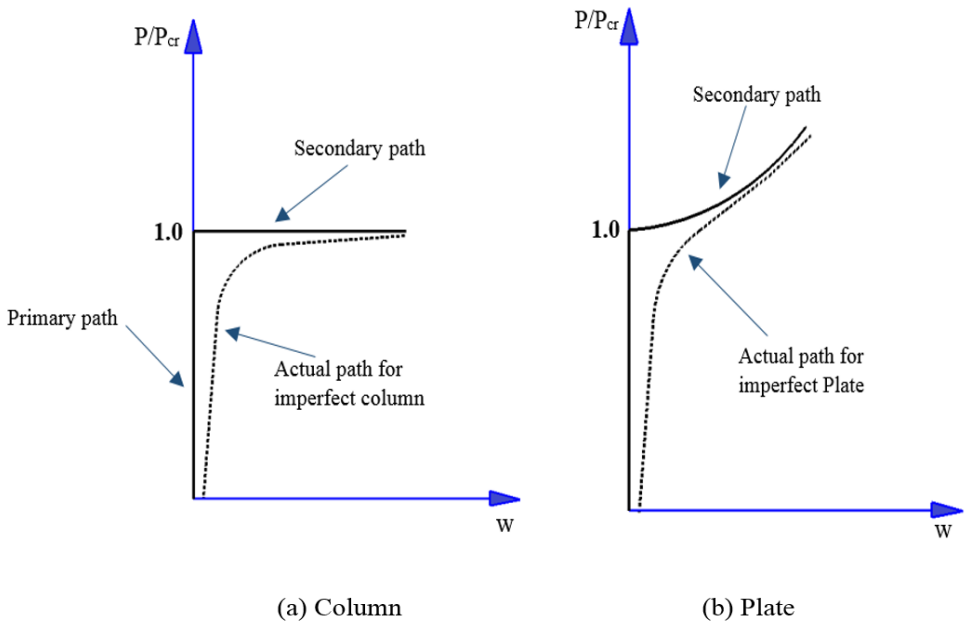

(a) Column (b) Plate

Figure 2.7: Load versus out of plane displacement relationship differences between column and plate

The analytical solutions can be either closed-form or an infinite series, such as Navier, Levy and Ritz methods [19]. While numerical solutions are obtained by satisfying the governing equations and the boundary conditions of problems approximately, real-life problems are normally defined based on domains which are geometrically complicated and have many different parts with various boundary conditions. Such structures will generate problematic functions, which require complex solutions in order to apply the traditional analytical methods mentioned. Numerical solutions using any numerical techniques such as the finite difference method and finite element method need to solve a system of linear algebraic equations. These solutions require long calculations, which are usually performed by computers, employing matrix methods. The results from the finite difference method have acceptable accuracy for most technical purposes if a relatively fine mesh is used. While finite element methods have proved to be extremely powerful and versatile tools for static and dynamic analysis of a wide variety of beam, plate, and shell problems; they, however, require the use of a computer with considerable speed and storage capacity. A semi-numerical, or semi-analytical, solution of a problem is one that satisfies the governing equations analytically, in one or two directions, and numerically, in the remaining directions. A typical semi-numerical solution is achieved by the finite strip method. In comparison with numerical methods, the main advantage is that the effort and expense of data preparation and input are minimised.

2.7 Finite strip method

The finite element method (FEM) is a powerful and efficient tool for the solution of plate and shell problems for structural analysis and is well known and established. The cost and time of solutions can be very expensive even for super-computers, and even today some computational problems require many

hours, days, and even weeks to solve. The finite strip method (FSM) is an alternative method, which can reduce the computational cost and time especially for structures having regular geometry and relatively simple boundary conditions. Cheung [20] in 1976 introduced the philosophy of finite strip analysis as an alternative approach to finite element analysis for particular cases. It is mostly used for structures with two opposite simply supported edges and with or without intermediate elastic supports in the case of static analysis such as bridges. He summarised the main differences between finite element (FE) and classical finite strip methods as below:

- FE is applicable for any geometry and boundary conditions and material variations, which makes it extremely versatile and powerful. FSM is more often used for structures with two opposite simply supported ends, with or without intermediate elastic supports.
- FE analyses have large quantities of input data making it easier to make mistakes. In addition, they require automatic mesh and load generation schemes. On the other hand, FSM models have very small amounts of input data because of the small number of mesh lines involved due to a reduction in dimensional analysis.
- Large quantities of output data, as a rule, all nodal displacements and element stresses are printed during FE analysis while it is easy for FSM to specify only those locations at which the displacements and stresses are required.

On top of this, FSM usually produces a much smaller number of equations and matrices with narrow bandwidth. Moreover, the amount of input data is relatively small when compared with FEM because of the smaller number of mesh lines. Unlike the finite element method, which uses polynomial displacement functions in all directions the finite strip method calls for the use

of simple polynomials in some directions and continuously differentiable series in other directions, with the stipulation that such series should satisfy the boundary conditions at the end of the strips. The general form of the displacement function is given as a product of polynomials and series:

$$w = \sum_{m=1}^{r} f_m(x)\ Y_m \tag{2.22}$$

In equation (2.22), the series has been truncated at the r^{th} term, $f_m(x)$ is a polynomial expression with undetermined constants for the m^{th}, while Y_m is a series, which satisfies the end conditions in the y-direction and also specifies the deflected shape in that direction. Early applications of FSM to the stability and analysis of prismatic plates, shells and thin-walled structures were to find their natural frequencies and buckling loads. These works include Cheung and Cheung [21] , Babu and Reddy [22], Turvey and Wittrick [23], Dawe [24] and Graves Smith and Sridharan [25].

2.8 Chapter Summary

This chapter includes a general description of plate and shell behaviour and response under loading. The classification of plates according to their thickness is highlighted briefly in the second section. In addition, the main theories used to investigate the plate structures including classical plate theory and nonlinear deformation theory are highlighted. The chapter also includes a short description related to stability concepts as an introduction to the buckling of a structure, which is illustrated in the following section. It then moves to the main solution techniques, which are used to solve the partial differential equations using analytical, numerical and semi-analytical methods. Finally, an introduction to the finite strip method was given since this will be the cornerstone of this study.

Chapter 3: Literature Review

3.1 Introduction

This chapter illustrates the theoretical and experimental research and studies, which have investigated the buckling, post-buckling behaviour and mode jumping phenomenon of thin plates and shells with different analysis variables such as material properties (isotropic and composite), loading types, boundary conditions etc. In the following, a literature review will be presented, which begins with studies focused on plate and shell linear buckling and moves on to the most recent studies, which deal with the post-buckling behaviour analysis and mode jumping phenomenon.

3.2 Linear (initial) buckling review

Over the past century, many studies have been conducted to determine the elastic buckling of plates. The stability equation for rectangular plates was derived by Navier (1823). Investigations were carried out using the Kirchhoff hypothesis [6] on the buckling behaviour of plates with many different shapes, material properties, loads and edge boundary conditions. Since then, a large number of theoretical and experimental researches have investigated the behaviour of plate and shell structures, particularly due to the significant demand for plated structures in the aeronautic, marine, automobiles and renewable energy industries during the second half of the last century. Studies of buckling may be divided into elastic buckling and plastic buckling; the former assumes that the plate reaches its critical buckling load below the elastic limit of the material while the latter is more relevant to the practical problem when the plate might be stressed beyond the elastic limit before initial buckling occurs. Therefore, plastic buckling theories are considered for

particular practical cases. Traditionally the initial form of buckling problem for the plates began with the assumption of simply supported edge condition under uniaxial compression load. In 1891, Bryan [26] presented the first solution to this problem by using the energy method to calculate the critical buckling load. This was followed by Timoshenko [27] who solved the same problem with a different proposal for the plate deflection equation. Levy [28] in 1942 submitted the earliest accurate solution for plate buckling with built-in (clamped) edge conditions.

Batdorf and Stein [29] in 1947 calculated the critical buckling load for simply supported plates under combined in-plane compression and shear stress; the two researchers adopted an infinite series as an out of plane displacement function. In the same year, Stein and Neff [30] published a technical report, which evaluated the buckling capacity of a simply supported plate under in-plane shear load with a general form for the plate deflection satisfying the boundary conditions by using a series of sinusoidal mode shapes in both x and y-directions. Experimental studies that investigated the buckling behaviour of the thin-walled structure include those by Rhodes [31], Bradfield [32] [33], Stonor [34] and Mofflin [35] [36].

Williams and Wittrick [37] presented their paper, describing the general-purpose of the computer program, VIPASA (Vibration and Instability of Plate Assemblies including Shear and Anisotropy) for determining the critical buckling stresses or natural frequencies of thin prismatic structures. They introduced a method to simplify the stiffness matrix method to ensure that the calculation includes all the critical buckling load factors, as well as natural frequencies, for vibration problems [38]. They emphasised that the method presented was not suitable for use with transfer matrix methods. Therefore, the use of such methods where natural frequencies or critical load factors could be missed seems most unwise. Anderson and Williams [39] discussed in their

study which was published in 1983, how they overcome an important limitation on the general applicability of VIPASA in the case of skewing modes when a shear load or anisotropy is present. They called the new program VICON (VIPASA with constraints). More recently, Kennedy and Williams [40] showed the main features of VIPASA and VICON analysis with a full explanation of buckling and vibration analysis using that software, including convergence techniques which ensure a reduction in the analysis time. Lam et al. [41] described the additional features introduced into VICON analysis to investigate the buckling of stiffened panels using point connections, e.g. to model the riveted connections between skin and stiffeners. More information about this software and its features will be explained at the end of this chapter. Nemeth [42] investigated the buckling behaviour of infinitely long composite plates subjected to combined loading. His parametric study focused on symmetric laminates which are affected by anisotropy. He introduced non-dimensional parameters ($\alpha = \frac{b}{\lambda}(\frac{D_{11}}{D_{22}})^{0.25}$, $\beta = \frac{D_{12}+2D_{66}}{\sqrt{D_{11}D_{22}}}$, $\gamma = \frac{D_{16}}{(D_{11}^3 D_{22})^{0.25}}$, $\delta = \frac{D_{26}}{(D_{11}D_{22}^3)^{0.25}}$) to represent the stiffness of the laminates, where λ is the half-wavelength of the buckling mode (D_{ij} are defined in Section 4.3, equation 4.14), while the plate was under different load conditions including tension, compression and shear. He also examined the effect of laminate fibre angle variation for different materials. His calculations showed that a 45 degree fibre angle produces the highest values of parameter β while a fibre angle of 30° - 40° maximises parameter γ whatever material properties are used. The effects of the fibre orientation on other parameters are summarised in Figure 3.1.

In 1995, Nemeth [43] published a technical report, which deals with long symmetric laminates, with the layup (±45) and with simply supported and clamped edge conditions. He concentrated on the effect of combined load interaction and the importance of anisotropy in relation to its effect on buckling behaviour.

He also studied the response of long symmetric laminated plates subject to shear and varying axial [44] or in-plane bending [45] load with the same edge conditions as in his previous study and his main conclusions were highlighted by the effect of these different loads on the buckling behaviour of these infinitely long plates.

A paper by Watson et al. [46] described an efficient method for determining the buckling and vibration behaviour of plates and stiffened panels with clamped edges by using Lagrangian multipliers to couple sinusoidal modes with appropriate half-wavelengths of response, thereby enforcing the end conditions at discrete point supports in the exact strip software VICONOPT (VICON with OPTimisation).

Featherston and Ruiz [47] conducted an experimental work to study the buckling behaviour of metal flat plates under shear load. Moreover, they utilised ABAQUS finite element software to validate their experimental results. Another experimental and numerical study by Featherston and Watson [48], which deals with buckling of the optimised composite flat plate under combined shear and in-plane bending tested optimised laminate samples that had a two opposite built-in edges with the other two simply supported, see Figure 3.2.

The laminates were first optimised by using VICONOPT software and finite element analysis and then the optimum layer orientations were used to manufacture specimens. The initial buckling loads were then examined for laminates with different aspect ratios. They compared their buckling and post-buckling experimental results with finite element analysis, which showed a good agreement in terms of load versus in plane and out of plane displacements by using a different numerical analysis method. Also, the researchers applied different imperfection amplitudes to examine the effect on the post-buckling numerical results.

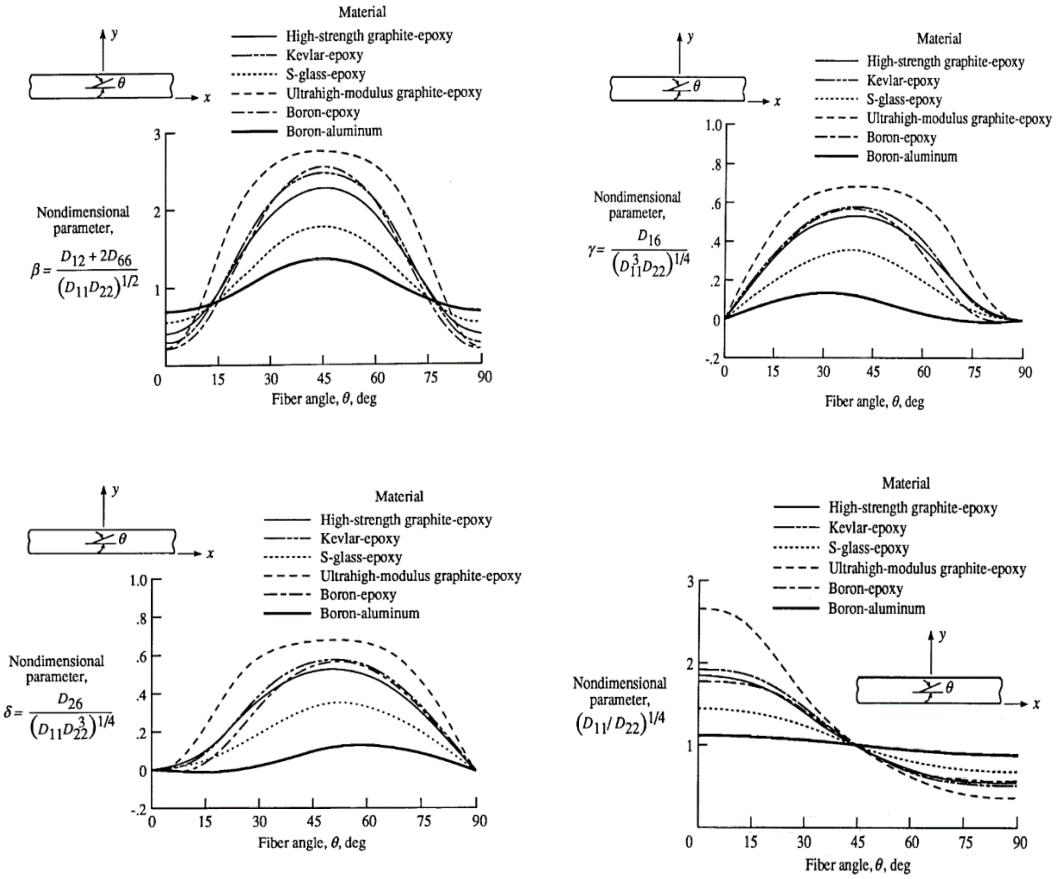

Figure 3.1: The effect of fibre angle on the non-dimensional stiffness parameter [42]

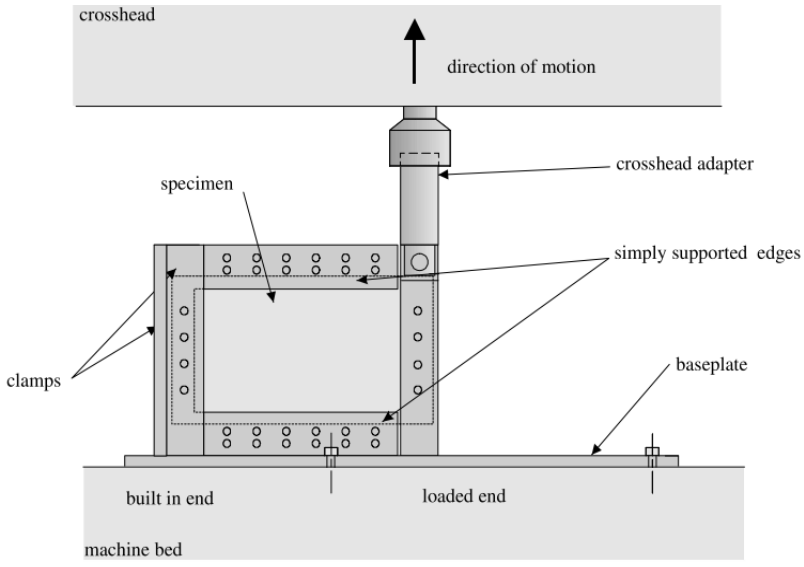

Figure 3.2: Test rig and set up used by Featherston and Watson [48]

They concluded that the initial buckling of optimised laminates decreases with increased aspect ratio and that the plates are sensitive to imperfections such as geometrical non-linearity, which had a noticeable effect especially in the post-buckling stage. Finally, they ensured that the eigenvalue analysis gave an accurate prediction for the critical buckling load.

Loughlan [49] [50] presented a theoretical investigation, which used the finite strip method to analyse the effect of bending-twisting coupling on the shear buckling behaviour of symmetric laminated composites of balanced and unbalanced lay-up ply configurations. In addition, he compared the coupled and orthotropic solutions.

In the same context, an approximate analysis including the effect of anisotropy based on non-dimensional parameters to predict the buckling behaviour of long rectangular plates loaded in compression and shear was performed by Weaver [51] [52]. The next chapter in this thesis will investigate the anisotropic properties of composite plates to optimise the buckling capacity under different in plane loading.

More recently, Abramovich et al. [53] examined the buckling behaviour of stiffened composite panels under combined in plane shear and compression. Vescovini and Bisagni [54] studied the buckling behaviour and optimisation techniques for flat and curved composite panels.

Many researchers and authors have studied the initial buckling of plates by adopting various solution techniques such as analytical methods by Liu and Pavlović [55], Jana and Bhaskar [56], a semi-analytical analysis method by Byklum and Amdahl [57], Eisenberger and Shufrin [58], Khedmati et al. [59] and finally numerical methods by Zhang et al. [60], Grondin and Cheng [61], Azhari et al. [62].

3.3 Post-buckling review

As mentioned previously, plates as opposed to columns have the ability to carry stresses beyond their initial buckling load. This behaviour is of significant interest to designers since it can be utilised to reduce the mass of some structures when the weight is a vital necessity, such as in the aerospace industry and marine structures, in order to save fuel and decrease emissions. The review of works concerning the post-buckling behaviour of thin-walled structures aims to obtain a better understanding of the region beyond initial buckling.

In 1910, von Karman [15] presented his significant contribution to this field in which he added the geometric non-linearity effect to the kinematic, strain and stress expressions derived in classical plate theory. After von Karman, many researchers discussed the post-buckling behaviour as a complex non-linear equilibrium case. Consequently, these studies suggested different hypotheses to explain the non-linear buckling behaviour of plates as well as shells. This significant interest was linked to rapid developments in the industry (e.g. aerospace and marine manufacture) which use many parts consisting of plates and shell components. Earlier investigations which focused on the elastic instability of buckled plates with large deformation were produced by Cox [63] [64], Friedrichs and Stoker [65] [66], Bodner [67], Levy [68] [69] and Van der Neut [70]. Koiter made substantial contributions to this field through his work between 1962 and 1967 in the post-buckling behaviour of plate structures [71] [72] [73].

Mayers and Budiansky [74] clarified in their technical report the behaviour of simply supported buckled plates and the response when the material passes the elastic limit and enters the plastic range. This was followed by Walker [75] who studied the a flat square plate in post-buckling equilibrium states for the simply supported edges conditions based on the von Karman equations. The

unloaded edges were considered to be either free or able to distort in the plane of the plate. The importance of the post-buckling phenomenon in thin-walled structure instabilities motivated the following researchers to perform more studies considering different aspects such as new materials (e.g. composite laminates) to actively entre the field, examining the effects of boundary conditions and loads.

Manuel Stein [76] delved into post-buckling behaviour through his technical report in which he studied the behaviour of buckled plates. The main features of his approach were:

- To convert the von Karman nonlinear large-deflection equations to a set of linear equations by expanding the deformation terms into a power series in the form of arbitrary parameters.
- Since the plates had simply supported edge conditions and were subjected to a longitudinal compressive load, both load and displacement functions were satisfied at the plate edges.
- The effect of change in uniform thermal stresses was investigated in his report. Moreover, a comparison with the experimental results from stiffened panels was presented.
- The analytical solution of the large deflection behaviour included two approximate solutions depending on the power of an arbitrary parameter; the two suggested solutions were compared with experimental results.
- The limitations in the solution suggested that the methods might not converge satisfactorily for certain problems and that linear equations cannot be used to solve post-buckling problems for plates with initial eccentricities.

A further subsequent study was carried out by Rhodes and Harvey [77] who investigated the case of flat plates loaded in compression with the specific boundary edges that the unloaded plate edges were elastically constrained against rotation. They explained the importance of these boundaries in the buckling and post-buckling of compressed plates. They summarised their conclusions as follows:

- Rotational restraints increase both the buckling load and post-buckling stiffness of a plate in compression.
- The wavelength at which the plate buckles has quite a large effect on the plate's post-buckling stiffness for all degrees of edge rotational restraint.
- The ultimate load carried by a compressed plate is relatively unaffected by the buckling wavelength but is quite dependent on the degree of rotational restraint at the plate edges.

Reddy and Chao [78] highlighted in their numerical study the large deflection behaviour of composite laminated plates including transverse shear, with many parameters such as plate aspect ratio, side to thickness ratio and the orientation of layers and anisotropy. Their model accounts for transverse shear strain and large rotations. They compared their results with exact closed form solutions in the linear case and with perturbation solutions in the non-linear case. The results showed good agreement with exact results and a fair agreement in case of a perturbation solution. In 1983, a paper by Stein [79] presented a study focused on the post-buckling of orthotropic composite plates subjected to in plane compression. He showed that only two parameters are needed beyond those required for buckling using von Karman's nonlinear equations. By assuming a trigonometric function in one direction, the plate equations are converted to ordinary nonlinear differential equations that are solved numerically. He also described his analytical results in a report [80] on

nonlinear buckling behaviour of flat plates subjected to in-plane compression or shear load. The author proposed trigonometric displacement functions to perform the post-buckling solution procedure. The same researcher investigated theoretically the post-buckling behaviour of long orthotropic composite plates under combined in plane shear and compression. He based this on von Karman's nonlinear equations and used Newton's numerical techniques to simplify and solve those partial differential equations[81] [82].

More recently, Sun and Williams [83] studied the post-buckling analysis of prismatic plate assemblies made of isotropic materials by using Koiter's theory to analyse the initial post-buckling of flat plates under uniaxial compression load. They assumed that the structure consisted of a series of long flat strips. These strips were rigidly connected together at their longitudinal edges. The post-buckling equations were solved exactly based on Wittrick and Williams' theory for eigenproblems and Koiter's general theory of elastic stability. The post-buckling coefficients were calculated by exact integration for all component plates. Examples of asymmetrically and symmetrically stiffened plates were included, which confirmed the idea that the post-buckling behaviour depends significantly on the geometry of the stiffeners considered.

A study by Wang and Dawe [84] highlighted the post-buckling response of rectangular composite laminated plates by using the spline finite strip method in the context of first-order deformation theory. The study included some examples to assess the suggested method. In all cases, the finite strip results were compared with those obtained from finite element analysis. The authors concluded that for a moderately thick plate geometry, the effect of shear deformation through the thickness is substantial.

Lillico et al. [85] described the post-buckling responses of a stiffened panel by using strut, strip and finite element methods. Two models were studied, namely single and multi-bay panels. The researchers used the exact strip

method software VICONOPT to design the panels and then compared the results using a finite element model which included the material non-linearity. However, they found that the skin buckling load for the panels used in the study was substantially lower than its yield load, which was directly proportional to the skin thickness. The paper also showed that a newly developed strut model could be used to represent the out-of-plane deflection of axially loaded, post-buckled panels. The model showed good agreement with finite element results in the case of a single bay panel.

The buckling and post bucking behaviour of curved CFRP stiffened panels with a T stiffeners was investigated by Degenhard et al. [86]. The authors focused on the responses of the panels under quasi-static and dynamic loads. The paper was divided into experimental and numerical parts. The experimental results for the curved stiffened panels were compared with the finite element model results and showed acceptable agreement. The work included a numerical study of the unstiffened composite cylindrical shell and the changes in its longitudinal mode shapes under axial loading.

Byklum et al. [87] carried out a further semi-analytical investigation of global buckling and post-buckling of stiffened panels subjected to different loading conditions such as biaxial compression, tension, shear and lateral pressure. They derived a computational model by using large deflection plate theory and energy principles. The energy formulations were derived analytically while the other calculations were performed numerically. A comparison was made between the semi-analytical results and the finite element model in terms of load-deflection curves to show the efficiency of the proposed method. The importance of stiffened panels as a component of fuselage, wings and other applications in various industries was highlighted. Lynch et al. [88] presented their finite element model for accurate production of the post-buckling behaviour of aircraft fuselage panels under combined compression

and shear loading. The study considered the different stiffener skin connections shown in Figure 3.3. Moreover, it produced a guide to modelling similar structures in terms of the elements mesh, idealisation, imperfection and solution procedure. The study included an experimental part, which tested two fuselage specimens to validate the numerical results.

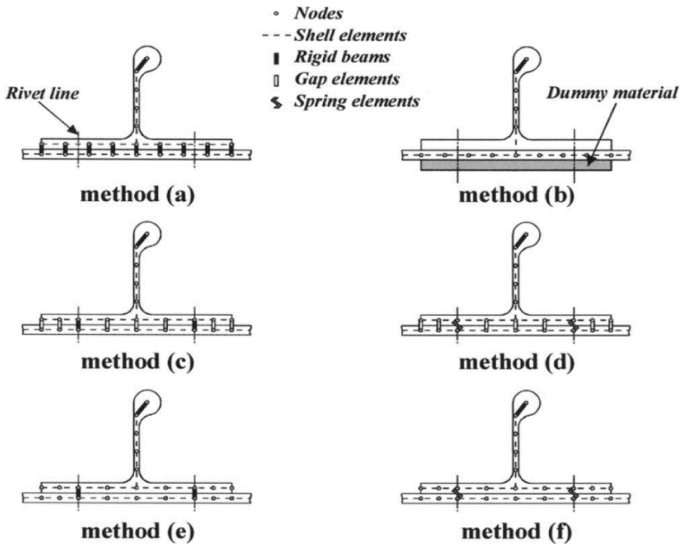

Figure 3.3: Skin –rivet –stiffener connection proposed by Lynch et al. [88]

Degenhardt and Delsemme [89] examined the post-buckling behaviour of curved stiffened panel experimentally and numerically. The two researchers tested a CFRP curved stringer stiffened panel under axial compression, then simulated a model using the finite element method to validate their results. The model they produced was included a skin-stringer delamination damage region. The numerical output data using shell elements predicted an axial stiffness higher than observed in the experimental results. The researchers explain that as a results of some hypothesis made in the model simulation were not coherent with the experimental results. Zimmermann et al. [90] investigated experimentally and theoretically the buckling and post-buckling behaviour of stringer stiffened fibre composite curved panels under axial

compression. A nonlinear finite element model was used to compare with the experimental results. The post-buckling responses of a flat fuselage stiffened panel subjected to in-plane shear loads were considered in a paper by Murphy et al. [91]. They used the finite element method to carry out a theoretical analysis; subsequently, an experimental test was preformed to validate the computational results. Material and geometrical non-linearity were taken into account; the numerical model included first and second order elements to obtain a better assessment of the buckling and post-buckling behaviour.

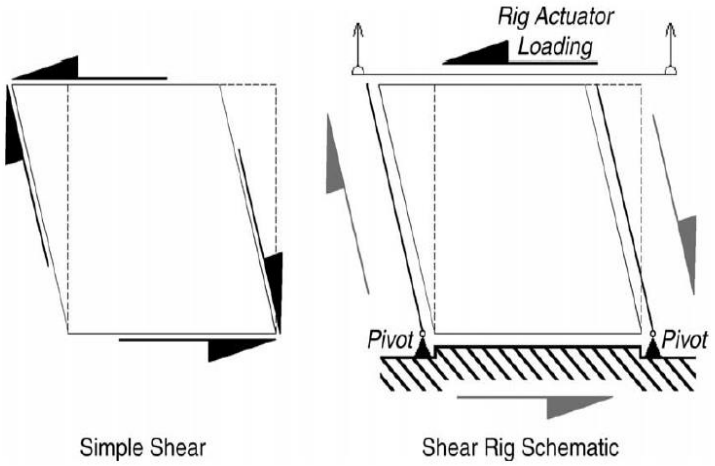

Figure 3.4 Schematic of shear rig used by Murphy [91]

Möcker and Reimerdes [92] preformed a post-buckling simulation of curved stiffened panels. They applied a solution procedure based on the discretisation of the structure into strip elements. This procedure enabled the determination of element stiffness matrices representing analytical solutions of the governing differential equations. The two researchers verified their approach by comparing it with experimental results. They used composite materials with [0, ±45] orientation angles. The main conclusions of their work were a significant reduction in the number of degrees of freedom; also, the fact that the proposed approach determined the element stiffness matrices that represented an analytical solution of the governing differential equations.

A semi-analytical model for the post-buckling analysis of stiffened cylindrical panels was presented by Buemann et al. [93]. Their panel consisted of a curved skin (shell) with longitudinal stringers and circumferential direction frames as shown in Figure 3.5. Local buckling modes were considered. The panel was modelled using the computer code 'IBUCK' developed at the Institute of Structural Mechanics at DLR Braunschweig. A comparison with finite element analysis to verify the results that was obtained from experiment.

Elaldi [94] focused on the buckling and post-buckling analysis and failure mechanisms of a hat stiffened composite panel under compression loading. Experimental test results were compared with a finite element model for validation. His panel consisted of three integrated hat stiffeners. Both experimental results and the numerical model showed local buckling mode failure with five buckles, prior to a jump to a configuration with seven buckles. The panel failed at a load of 3.3 times the initial buckling load.

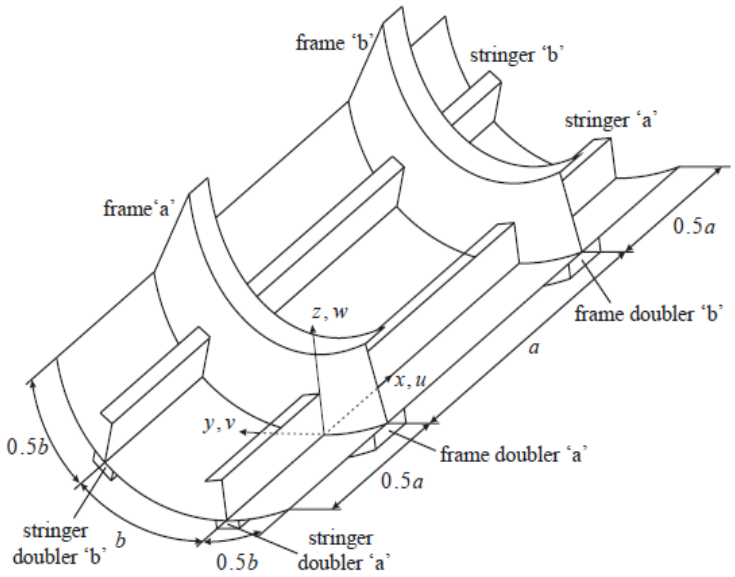

Figure 3.5 A typical stiffened structure proposed by Buemann et al. [93]

The complexity of the calculations required for instability problems using either theoretical or experimental analysis motivated Bakker et al. [95] to introduce their elastic post-buckling analysis of plates subjected to compressive load using a two-strip model to simplify the analysis steps. They based their method on the non-linear differential compatibility and equilibrium equations with a potential energy approach. They modelled a plate with simply supported edges. Relationships between the force and the maximum in and out of plane displacement were described.

Shufrin et al. [96] suggested a semi-analytical model to predict the nonlinear buckling of a rectangular plate in the elastic zone. They proposed a model with general boundary conditions and a plate subjected to combined in plane and out of plane loading components, their model was able to capture the mode change phenomenon for compressed plates, and the results were compared to experiments. Rhodes [97] described some of the previous research in post-buckling of plates and plate structures; comparing the load–shortening behaviour of plates with parameters such as initial imperfection, boundary conditions and buckling mode shapes. Ghannadpour et al. [98] published a paper which investigated the nonlinear buckling analysis of isotropic plates by using two finite strip methods; one semi-analytical and another fully analytical to predict the post-buckling behaviour of isotropic plates. Their work was based on solving von Karman's equations by a novel technique.

Bisagni and Vescovini [99] proposed an analytical formulation to study the local buckling and post-buckling of composite panels with T-shape stiffeners under compression. They used the Donnell-von Karman hypothesis and classical lamination theory to model the skin buckling mode. Their approach did not consider the overall buckling mode. The same researchers [100] suggested a single mode solution to study the post-buckling responses of flat

stiffened panels under uniaxial compression. They recommended their approach for the following cases:

- Calculating the buckling load for panels of finite and infinite length.
- Deflection and stress distributions for different values of the applied end shortening.
- To determine the post-buckling stiffness of perfect and imperfect panels.

Stamatelos et al. [101] investigated the buckling and post-buckling of stiffened panels analytically; their main interest was the behaviour of the skin between the stiffeners. Thus, the researchers concentrated on local mode buckling. They used a two-dimensional Ritz displacement function to examine the local buckling of isotropic and laminated symmetric composite panels with arbitrary edge boundary conditions. The solution was then extended to the local post-buckling of the skin. Brubak and Hellesland [102] used their semi-analytical method to study the post-buckling behaviour of stiffened panels including the effect of imperfections in their model. One edge was free or flexibly supported and the other three laterally supported and the structure was loaded in in-plane compression. The model was able to capture both local and overall modes with out-of-plane and in-plane displacements represented by trigonometric functions and linearly varying functions defined over the entire plate. The authors proposed their approach as an efficient tool to reduce the computational effort in terms of time and cost, comparing with other numerical solutions such as the finite element method. However, the solution was suitable only for the specific boundaries conditions in their study. Variable stiffness shells are defined as curved composite structures in which the fibre-reinforcement follows a curvilinear path in space. The main difference between variable stiffness shells and traditional composite shells is that they

occupy a wider design space than traditional composite shells and they have the potential to improve a wide variety of weight-critical structures.

White et al. [103] proposed a method for predicting the initial post-buckling behaviour of variable-stiffness cylindrical panels. They based this on the differential quadrature method with the implementation of Koiter's approach [73] for variable-stiffness shell structures. The authors compared their results with a non-linear finite element model and results from literature to validate the proposed method.

Shanmugam et al. [104] studied the practical response of flat stiffened plates under combined in-plane compression and lateral pressure experimentally in the laboratory and numerically by using the finite element analysis. Their model included elastic and inelastic behaviour.

The authors summarised some of their conclusion as follows:

- Both experimental and numerical results show that the lateral load carrying capacity of a stiffened plate drops with an increase in axial load and vice-versa.
- The reduction in the axial strength of stiffened panels was not significant due to smaller lateral pressure than for non-stiffened plates.
- The effects of lateral pressure on strength appear to be similar to those of initial imperfections with a pattern of small overall deformation of the stiffened plate.

Splichal et al. [105] tested a composite panel of an aircraft wing subjected to dynamic loading. The experimental specimens were simulated using the finite element method for comparison. In the same context, the buckling and post-buckling behaviour of curved cylindrical stringer- stiffened laminated composite and metal panels under axial compression were investigated both numerically and experimentally by Abramovich and Bisagni [106] to evaluate

the buckling and collapse loads. The wide applications of plates and panels with simply supported or free edges motivated Oguaghamba et al. [107] to undertake a theoretical investigation to determine the main load characteristics of buckling and post-buckling behaviour of rectangular plates with clamped edges on all boundaries of a plate subjected to a uniaxial compression load.

Seo et al. [108] examined the ultimate strength of stiffened curved plates under compressive load. They used a numerical approach to estimate the compressive strength of curved stiffened plates for marine applications, while Lyman et al. [109] conducted a study which used mathematical techniques to get more accurate, fast solutions for the static and dynamic nonlinear behaviour of buckled plates subjected to uniaxial loading by implementing continuation methods. The limitation of using this method was that it is restricted to simpler geometries and any changes to the boundary conditions require a new analytical solution. Their study included an experimental test on a flat plate with simply supported unloaded edges while the loaded edges were restricted against out of plane displacement but allowed to rotate as shown in Figure 3.6.

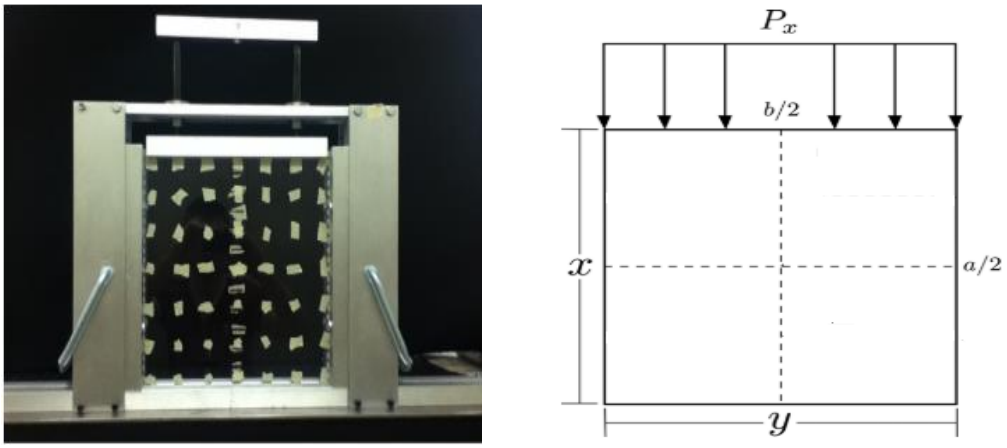

Figure 3.6 Test rigs for a plate under uniaxial compression [109]

3.4 Mode jumping phenomenon

The study of the post-buckling behaviour of plates and stiffened panels allows designers to work flexibly between the design limit and ultimate loads, potentially leading to significant reductions in the mass of aerospace and marine structures. Experiments on thin-walled structures in the post-buckling stages showed that there can be a sudden change in the initial buckling mode in terms of out of plane deformation patterns. This phenomenon is known as mode jumping and in some literature is called the secondary instability. Mode jumping may be the most noteworthy feature of the experimental post-buckling behaviour of thin plates, as the nature of these structures means they can exhibit a number of different buckle configurations. Investigations of this behaviour have demonstrated that the main factors that have a major effect on the phenomenon are the aspect ratio of the plates (length to width ratio), the boundary conditions at the plate edges and the load increments in the post-buckling region. There are other influential factors such as initial imperfections and load eccentricity, which may also have an important role in mode jumping. In this section, the studies, which dealt with the post-buckling behaviour of plates or panels including mode jumping will be reviewed.

The mode jumping phenomenon was first observed by Stein [76] during an experimental test of an isotropic stiffened panel with knife stiffeners when the local initial buckling mode changed suddenly from five buckles (five half wavelengths of sinusoidal buckling) to six, then to seven and then to eight buckles by the end of the test. He compared his experimental results with theoretical calculations. His experimental load-shortening curve showed abrupt changes corresponding to a sudden change in the buckling pattern, while the theoretical curve, which was based on continuing change to the buckling pattern, was smooth. Bauer and Reiss [110] studied the non-linear buckling of rectangular plates subjected to compressive thrust. They used a

numerical method to explain the mode-jumping phenomenon. They used an energy comparison to show the possibility of mode jumping occurring under the condition that the two modes should be close and the structure would jump to a preferred equilibrium state which has similar stresses.

In 1970, Supple [111] conducted an investigation related to the post-buckling of simply supported rectangular plate behaviour under a compressive load, which included changes in the buckling form during the post-buckling analysis. The main assumptions for his study were:

- There is no out of plane deformation at the boundaries.
- The loaded edges remain straight.
- The longitudinal edges stay straight in the plane of the plate.
- There is no restraint against the lateral expansion of the plate in its plane.
- A term for initial imperfection was included in his calculations.

His main conclusions were that the post-buckling behaviour, which considered the change in the buckling pattern, was dependent on the prevailing boundary conditions and the existing of initial geometric imperfections. Cheo and Reiss [112] referred to the possibility of mode jumping from one mode to another, which depended on the dynamic stability of the primary and secondary state of equilibrium and the amplitude of disturbance.

Nakamura and Uetani [113] presented their theoretical work in which they focused on the secondary buckling, and post-secondary buckling of rectangular flat plates with simply supported edge conditions under compressive loading. They worked particularly with rectangular plates having a buckling mode which contained more than one-half wavelength. They assumed two cases of longitudinal edges; the former was perfectly rigid while the latter was free. Their analytical investigation had three stages:

- The point of secondary buckling was searched along the primary buckling path by a linearized buckling analysis
- The secondary buckling point stability was based on the post-buckling theory.
- The equilibrium paths of post-secondary buckling were numerically traced at every incremental step analysis of the equilibrium.

Their main conclusions were that:

- The secondary buckling loads for free longitudinal edges were much higher than those for rigid edges.
- The secondary buckling loads become smaller as the aspect ratio increased for a plate with a fixed number of longitudinal half-wavelengths.
- The obtained secondary mode for both edge conditions corresponded to a change in the phase of the longitudinal waveform without a clear increase of wave amplitude. However, the types of the waveform changes were different between the two longitudinal boundary cases.
- The authors conducted that secondary buckling points are unstable branching points for plates with an initial buckling mode with more than two buckles, while they were more stable for plates with an initial mode with two buckles.
- The differences in the primary buckling mode between the two longitudinal edge conditions mentioned previously are related to the change in the secondary buckling mode shape, i.e. the mode changed from three to five half waves for plates with rigid edges while it changed from five to seven half waves for the free longitudinal edge condition. Schaeffer and Golubitsky [114] studied the mode jumping of rectangular plates. They started with Stein's experimental model [76]

and then applied the von-Karman equations to determine the effect on the mode jumping occurrence of different boundary conditions (simply supported and clamped edges). Matkowsky et al. [115] investigated the secondary buckling path for plates with different aspect ratios. Their work highlighted that if the primary buckling state loses stability then the plate will buckle a second time into the secondary state. The paper also described some previous experimental studies which dealt with secondary buckling. Their work was based on von Karman theory and studied the secondary equilibrium path of rectangular plates. Holder and Schaeffer [116] also linked the boundary conditions of the plate edges with the mode-jumping phenomenon in terms of the von Karman equations. They explored clamped and simply supported edge conditions for long plates in compression. The main conclusion of their work was that it was possible for mode jumping to occur if the boundary conditions were simply supported on the unloaded edges and clamped on the loaded ends.

Shen and Zhang [117] investigated mode shape change in the post-buckling analysis of rectangular plates subject to uniaxial compressive loading by applying the perturbation method to the von Karman large deflection equations. The authors proposed two in plane boundary conditions and considered the effect of initial imperfections. They compared their theoretical results with previous experimental studies for validation. One of the main conclusions was that the change in the buckling pattern would occur earlier in the presence of an initial imperfection. Their load-shortening curve showed a smooth transition when compared with Stein's experimental curve which had a sudden jump between the post-buckling pattern configurations.

In 1992, Maaskant and Roorda [118] published a paper which studied the effect of interactions between buckling modes leading to a mode jump in a simply

supported plate subjected to compression. They concluded based on the results of their investigation:

- The ideal plate post-buckling behaviour was particularly sensitive to the manner in which the loads were applied and the plate aspect ratio.
- As it is difficult to manufacture an ideal plate, it is more realistic to consider the effects of imperfection in such behaviour.
- They proposed that a combination of many buckling modes should be considered in order to have a complete picture of the mode-jumping phenomenon.

Riks et al. [119] [120] proposed a numerical study to explore the mode-jumping phenomenon in a thin-walled shell. They suggested a solution procedure which consisted of a combination of the classical path, which was used for the quasi-static (stable) parts and a transient integration for the simulation that belonged to the transient domain. The authors described their approach as a robust strategy to solve a similar problem, and they applied it to mode jumping of a plate strip and composite cylinder collapse under compression to verify their method.

The finite element method was used by Salerno and Casciaro [121] to develop a multi-mode model of thin-walled structure buckling in the elastic zone considering the imperfection effect. Their work focused on frames and thin-walled beams. Cheng and Shang [122] presented work which related to the mode jumping of a rectangular plate with simply supported edges on an elastic foundation. They based their study on bifurcation theory to predict the non-linear stability and the buckling mode change.

Bushnell et al. [123] published a report that investigated the optimisation of stiffened panels which considered the occurrence of mode jumping. They used the PANDA2 code in their study to explain the strategy, which was adopted by

that code to prevent serious mode jumping before the design load is reached for an optimised panel. In addition, the researchers defined two reference words to express the mode change, “mode interaction” and “mode jumping”. The former was defined as the interaction between buckling modes with a long wavelength and one or more modes of short wave, while the latter was the interaction between one short wave with another short wavelength to generate a local buckling mode.

A comparative study was published by Everall and Hunt [124] that dealt with mode jumping behaviour in the post-buckling analysis of struts and plates subjected to compressive loads. They highlighted the effect of edge boundary conditions in such unstable behaviour, on the changes in the buckling mode. Their main conclusion are summarised as:

- Simply supported edge conditions protect the plate against early mode jumps.
- Mode jumps occur at an earlier stage when the plate ends are restrained against in plane movement. The jump is delayed by restraining the same edges against rotation only.
- Restricting in plane movement from free to straight to clamped edges leads to a decrease in plate stability in the post-buckling region.
- Constraining long edges against bending could lead to a significant increase in secondary buckling load for both straight edged and clamped edged plates.

Hunt and Everall [125] carried out a systematic appraisal of the phenomena of mode locking and mode jumping in a structural buckling problem of finite length. The study also included a review of previous studies dealing with post-buckling and mode jumping of thin-walled structures.

Chien et al. [126] presented a numerical study to find approximate bifurcation solution curves for the von Karman equation for both simply supported and clamped plate edges. Their results were verified and showed considerable agreement when they were compared with the theoretical results in reference [114]. An experimental study was carried out to test rectangular plates to investigate the post-buckling and mode jumping phenomenon by Chai [127]. His work included a numerical model to elucidate the post-buckling response of unilaterally constrained plates under monotonically increasing edge thrust, in both tests and finite element analysis. He used displacement control and the samples had clamp boundary supports.

The main conclusions were:

- The interaction of the plate with the adjoining rigid substrate following buckling leads to some unique deformation sequences, and this behaviour includes both buckling and post-buckling stages.
- A rapid transition of the buckling waveform to a new equilibrium configuration occurs in which the specific details strongly depend on the plate aspect ratio and other system parameters.
- The plate deformation at buckling is quite random. However, it tends towards an extreme form of asymmetry with increasing load.
- The results provide an insight into the fracture behaviour of imperfectly bonded materials. Boundary contact suppresses mode I (with one buckle) in favour of mode II (with more than one buckle) fracture. However, As soon as a mode transition occurs, the opposite can occur, which can lead to a catastrophic detachment in brittle intermediate layers. Mode jumping configurations are shown Figure 3.7.

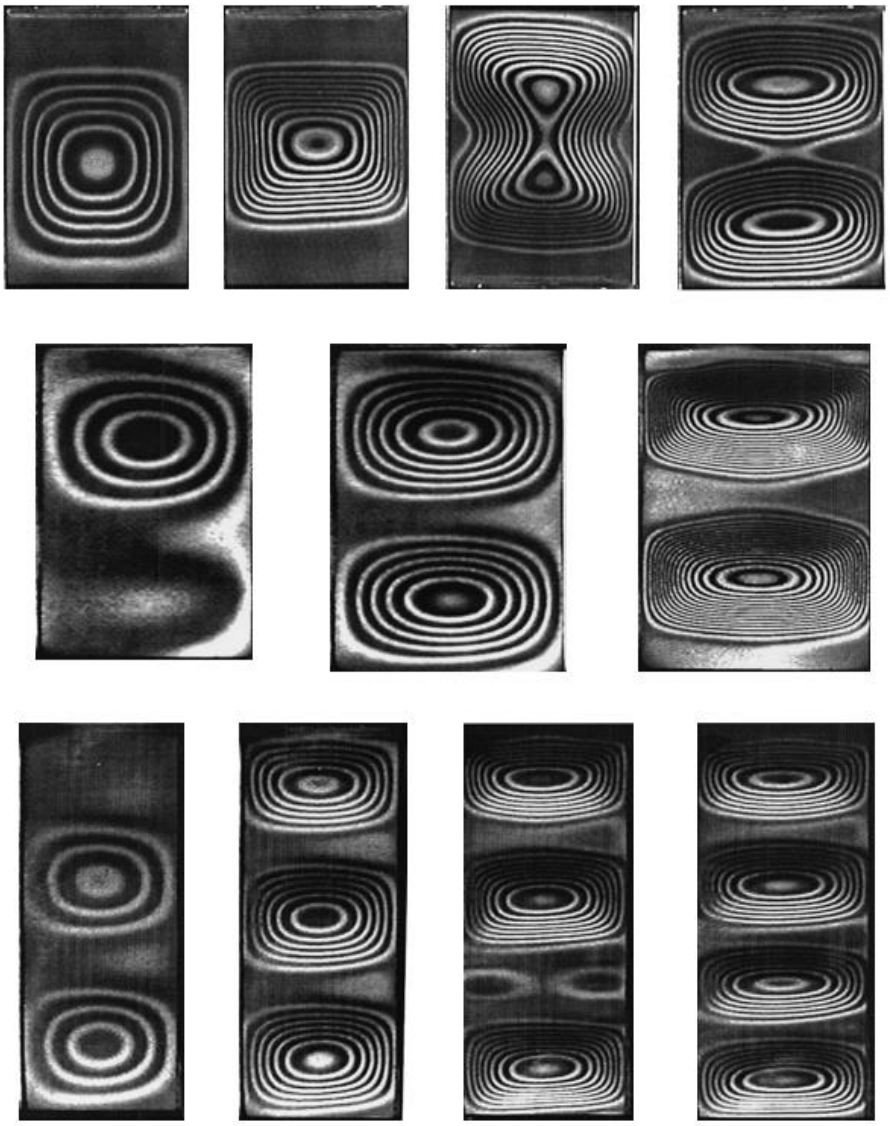

Figure 3.7 Mode changes of buckled rectangular plates with aspect ratio = 1.2, 1.7, 2.9 respectively [127]

More recently, Falzon [128] [129] investigated the post-buckling and damage behaviour of hat-stiffened panels under uniaxial compression. The study consisted of an experimental part and a numerical part, and was based on a panel made of a composite material with (0, ±45, 90) orientation angles. The experimental test included two types of panel with and without a circular cut out in the middle of the panel, see Figure 3.8.

The results of a finite element analysis to simulate the panels were compared with the results from the experiments. Both panels buckled and failed by local buckling. The non-linear finite element analysis was successful in predicting buckling and initial post-buckling behaviour. However, the model was less successful in capturing the mode jumping observed in the experimental results.

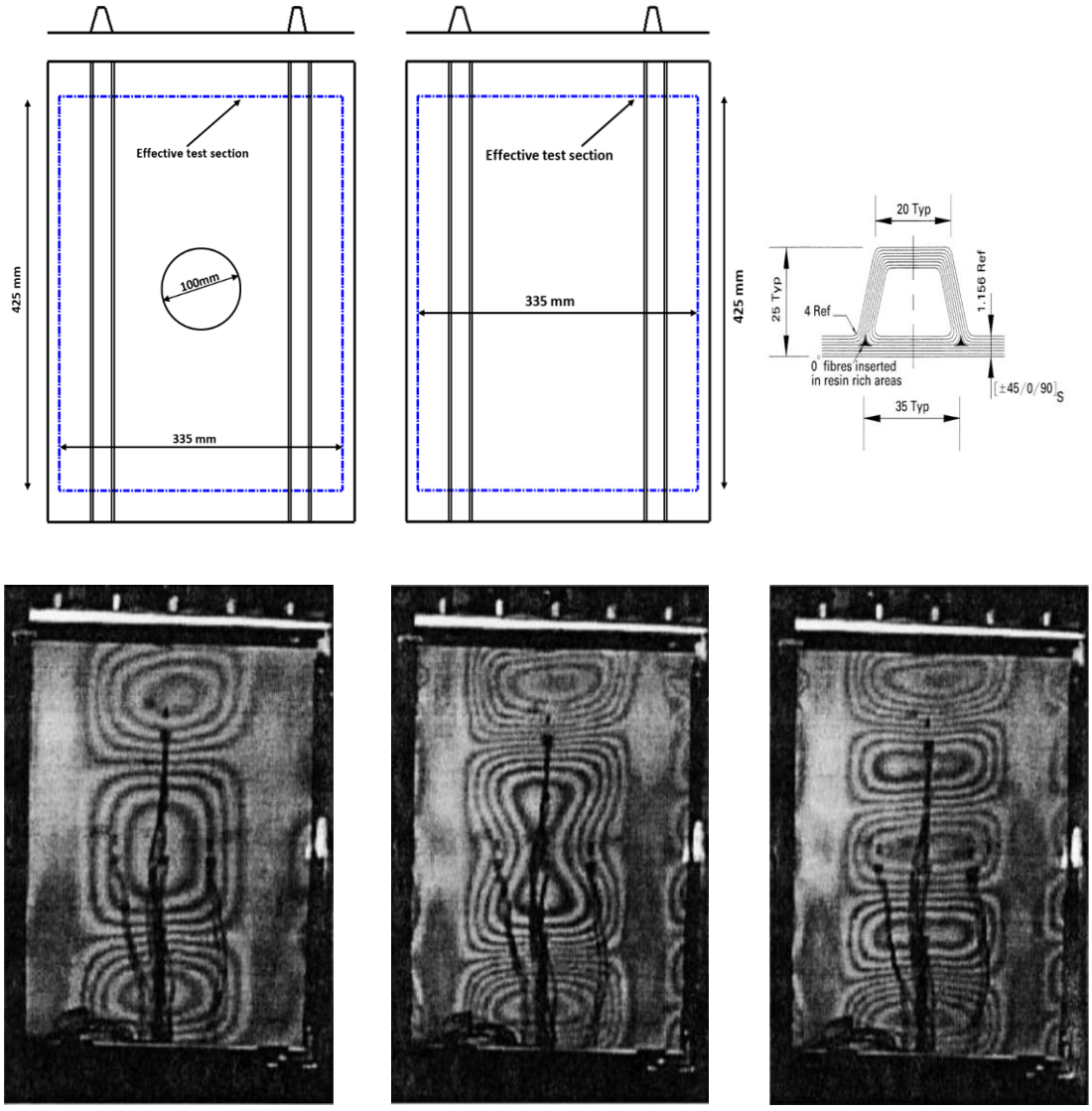

Figure 3.8 : Panel details and mode change tested by Falzon [128]

Falzon and Hitchings [130] introduced a study which focused on capturing mode jumping experimentally and numerically in the post-buckling of composite stiffened panels with four blade-stiffeners. They used a modified explicit dynamic method to capture local mode switching.

Chen and Virgin [131] investigated analytically and numerically the mode shifting of simply supported buckled plates loaded thermally. They proposed an analytical solution by reducing the Von Karman equations to a system of non-linear ordinary differential equations. They described mode shifting in the vibration mode shapes at particular points in the temperature versus natural frequency relations. The results were checked and compared with a static-dynamic finite element model.

The same researchers [132] [133] [134] published papers two years later, which dealt with the dynamic response of thin plate post-buckling behaviour that included the transition of the buckled pattern. They used an asymptotical and non-stationary finite element method. Their work highlighted the secondary dynamic instability and local post-buckling behaviour of rectangular plates subjected to mechanical and thermal loading. The solution method combined Koiter's nonlinear instability theory with finite element techniques for both isotropic and composite plates.

Falzon and Cerini [135] proposed a procedure to capture mode jumping based on finite element solution schemes. They applied an arc-length constraint to model the quasi-static responses of composite stiffened panels and explicit dynamic routines. The suggested procedure was computationally more efficient to capture mode jumps than full dynamic analysis.

Murphy et al. [136] focused their experimental work on the local post-buckling of metallic stiffened panels and on the mode shape changes. They summarised their test observations as follows:

- For all tests, the skin mode pattern changed, and the number of buckles (half waves) increased.
- The new half-waves developed within the skin; they initiated at either the top or bottom of the bay.
- The additional buckles started small and grew with increasing load. The new half waves appear to grow steadily from their initiation.
- Changes in local skin bay behaviour correspond to changes in global specimen behaviour with reductions in post-buckling stiffness.

A parametric study by Hofmeyer and Jaspart [137], which described a dynamic explicit solution procedure used to study the compressed plates with or without stiffeners, concluded that for a long plate without stiffeners, the mode jump occurred before the plasticity range if the imperfection was small, whereas for large imperfections the jump would occur later. Moreover, there was a significant difference in the ultimate strength due to different imperfection sizes and shapes.

An experimental and numerical study that used genetic algorithms to optimise stiffened composite panels by investigating the post-buckling behaviour were published by Falzon et al. [138] [139]. The algorithm used for layup optimisation aimed to delay the mode jumping. The numerical results showed that the increase in damage resistance of an optimised panel would delay the mode jumping compared to the original unoptimised panel. The results of clamped edge plates under uniaxial compressive load were compared with previous experimental results for validation. The theoretical results showed good agreement in terms of out of plane displacements and mode jumping in buckling mode configurations as shown in Figure 3.9.

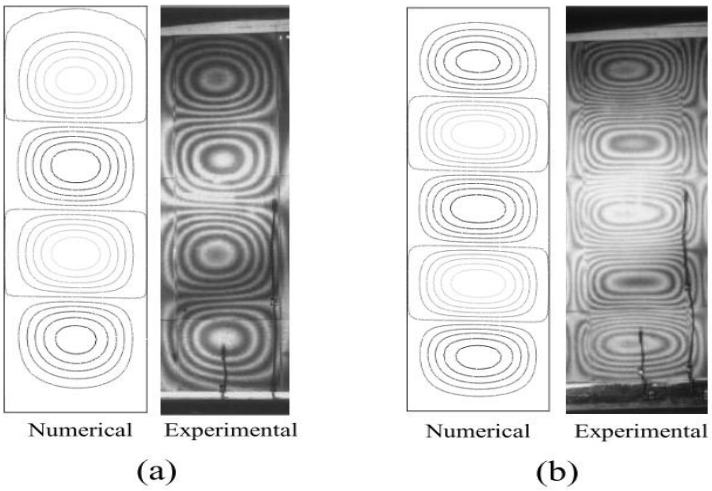

Figure 3.9: A comparison between the numerical and experimental out of plane displacement pattern after a- buckling, b- mode jump [138]

The second work focused on composite stiffened panels with four I stiffeners, the panel investigated experimentally and showed a local buckling mode started with five buckles (half wavelength), jumped to six and then finally with seven Figure 3.10. A finite element model was used to verify the experimental results using ABAQUS.

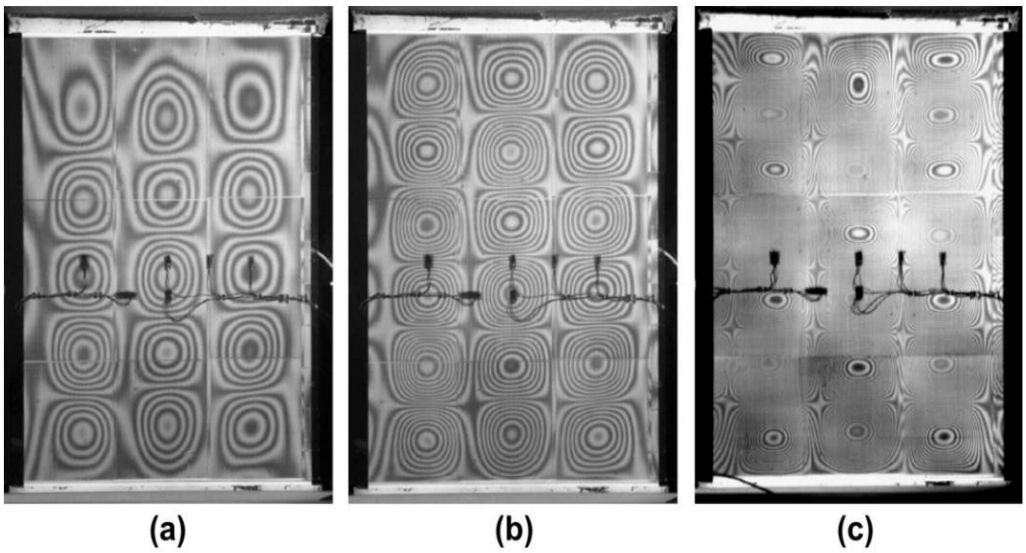

Figure 3.10: Experimental results that showed the mode jumping in skin buckling mode [139]

The researchers used both the overall and local buckling mode assumption to compare with experiments. They utilised conventional shell elements and an initial imperfection of 0.03 of the skin thickness for the first model, while solid and interface elements were used in the second finite element model to capture the mechanism of skin-stiffener interaction.

Hofmeyer and Courage [140] studied the mode-jumping phenomenon analytically and numerically in the post-buckling analysis of square and long plates. The analytical model was based on several displacement functions and using the principle of minimum potential energy. A dynamic implicit finite element model was employed to compare with analytical results.

Wang et al. [141] presented a mathematical expression to describe the mode jumping and equilibrium path configuration of thin film secondary wrinkling by applying the bifurcation theory.

Finally, the next section of this chapter will describe the main features of the VICONOPT software, which was mentioned previously in section (3.2), as the main motivation of this work is to improve the post-buckling analysis of that program by including the mode jumping.

The paper which represents a basis for the main objectives of this thesis, is a study by Watson and Kennedy [142]. The authors used VICONOPT software to investigate this phenomenon for a stiffened panel that buckled locally. The study included a comparison between the equilibrium paths with a different number of half wavelengths (buckles) in order to predict the jumping points under both strain control and stress control. The results were presented in terms of load-axial strain relations and compared with previous experimental work. This paper will be discussed in more detail in Chapter 6.

3.5 Exact strip analysis and VICONOPT

The finite strip method (FSM) was described in the previous chapter as an alternative technique which is used to solve stability problems efficiently. The FSM considered as a particular case of finite element analysis that can provide an efficient tool for numerical analysis in terms of computational time and cost. The use of this method in vibration, buckling and post-buckling problem expanded gradually after Cheung [20]. The simplicity provided by semi-analytical analysis using FSM motivate the researchers in stability problems to adopt it as an alternative method of finite element analysis when FSM was applicable for their case studies. For example, Li et al. [143], Bradford and Azhari [144], Dawe and Peshkam [145], Ovesy et al. [146].

The exact strip method was proposed in 1968 by Wittrick [147] who utilised it to determine the elastic stability of plate assemblies. This technique assumes a sinusoidal variation of the buckling mode in the longitudinal direction and the governing differential equations of strips are transformed to transcendental ordinary differential equations according to classical plate theory. Exact strip analysis assumes a continuous distribution of stiffness and mass over the entire structure and thus avoids the approximations resulting from discretisation in the classical finite element analysis method. Consequently, the partial differential equations that govern the deformations of the plate's components are solved exactly Kennedy et al. [148]. Consequently, the main differences between the exact stiffness method and the other traditional FSM that the strip properties are based on the direct solution of the governing differential equations of classical plate theory, rather than on the use of energy or work principles. Solving the governing differential equations for each strip explicitly will lead to a stiffness matrix containing transcendental coefficients. Since the eigenproblem is transcendental the standard linear eigenvalue solver routines cannot be used to extract the buckling load [149]. Also root search methods are

unreliable because of the highly nonlinear behaviour of the stiffness matrix determinant. Thus the Wittrick-Williams (W-W) algorithm was proposed to calculate the eigenvalues.

3.5.1 Wittrick-Williams algorithm

Wittrick and Williams [149] presented an algorithm to be used for determining the natural frequencies of vibration of any linearly elastic structure when using the exact method. The algorithm was able to calculate how many natural frequencies lie below any target frequency, without determining them directly and hence to converge on any natural frequency with the required accuracy. The Wittrick-Williams algorithm was first applied to vibration problems and later extended to include buckling problems [150]. The way in which this is achieved is outlined briefly as follows. The natural frequencies or load factors were calculated by solving the transcendental eigenvalue equation:

$$KD = 0 \tag{3.1}$$

where **K** is the overall global stiffness matrix of the structure and it is assembled from the member stiffness matrices. The elements of **K** are transcendental functions of the eigenvalue (critical load factor F or frequency ω^*). **D** is the displacement amplitude vector. Equation 3.1 is solved by Wittrick-Williams algorithm. The role of the algorithm is in calculating the number of eigenvalues $J(\omega^*)$ lying below a trial value ω^* (or F). The value of J can be evaluated by the equation below:

$$J(\omega^*) = J_0(\omega^*) + s\{K(\omega^*)\} \tag{3.2}$$

where $J(\omega^*)$ represents the number of natural frequencies of the system which are less than the chosen frequency ω^*. $J_0(\omega^*)$ denotes the number of natural frequencies which would still be exceeded by ω^* if the ends of every member were clamped, while $s\{K(\omega^*)\}$ is the sign count of the transcendental stiffness matrix $K(\omega^*)$, which is the number of the negative elements on the leading

diagonal of the upper triangular matrix $\mathbf{K}^{\Delta}$ when the standard form of Gauss elimination without row interchanges is performed on $\mathbf{K}$. J_0 can be obtained by summation over the whole structure.

$$J_0 = \sum_m J_m \tag{3.3}$$

where J_m can be calculated analytically for every member m.

3.5.2 VICONOPT software

VICONOPT is a FORTRAN 77 program which incorporates the exact strip method and the Wittrick-Williams algorithm. The software was developed at Cardiff University since 1970 with the collaboration of British Aerospace, Airbus and NASA. The story of VICONOPT began in 1974 when Wittrick and Williams presented the computer program (Vibration and Instability of Plates Assemblies including Shear and Anisotropy) known as VIPASA [37]. VIPASA analysis was used initially to calculate the natural frequencies and buckling load factor. Analysis using VIPASA assumes that the mode of vibration or buckling varies with a sinusoidal shape in the longitudinal direction x. Thus the displacement amplitudes and rotations in the x-direction that relate to the global axes x, y, z are sinusoidal too. Moreover, the length of the plate is divided into a range of half wavelengths, which can be defined by the user, see Figure 3.11.

VIPASA analysis requires the in plane stiffness matrix **A** and the out of plane bending stiffness matrix **D** to be uncoupled. i.e., the coupling stiffness matrix **B** must be null. In the case of isotropic or orthotropic plates in the absence of shear load, the nodal lines between the buckled regions (the lines of zero out of plane displacement) remain straight and perpendicular to the longitudinal edges, leading them to satisfy simply supported boundary conditions. The length of the plate ℓ can be divided into an integer number of half wavelengths λ in the x direction.

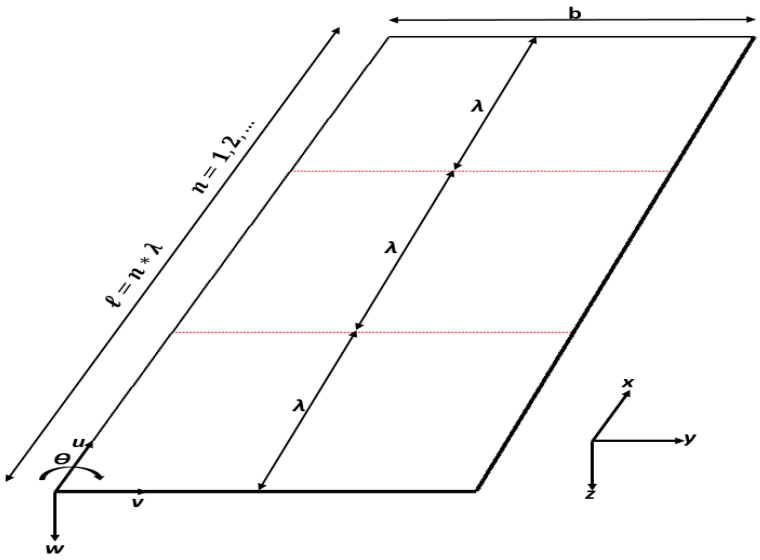

Figure 3.11: VIPASA analysis features

Conversely, if the plates have anisotropic properties or are in the presence of shear load, the nodal lines will skew and the simply supported end conditions will not be satisfied. This is considered the main limitation of VIPASA analysis. However, despite this, the analysis using VIPASA, which is based on the exact plate theory, avoids approximations and reduces the analysis time when it is compared with finite element analysis.

To tackle this problem VICON [151] analysis was developed. VICON analysis removes the main VIPASA limitation, and is able to deal with structures which have anisotropic properties or are subjected to a shear load. The essential feature of VICON, which can be considered as the main difference when it is compared with VIPASA analysis, is the inclusion of Lagrangian Multipliers. The function of these multipliers is to couple the responses of different half wavelengths λ. The modelling of plates using VICON analysis assumes that the plate has infinite length and is assembled with constraints that represent either rigid or elastic point supports repeating at an interval of ℓ as shown in Figure 3.12.

The buckling or vibration modes will repeat with n intervals over a length of $L = M\ell$, where M and n are integers. The different half wavelengths are coupled to calculate the buckling and vibration modes accurately. Although VICON analysis assumes that, the plate has infinite length, the vibration and buckling modes repeat over a length $L = 2\ell/\xi$ where $\xi = 2n/M$ and $0 \leq \xi \leq 1$. The values of half wavelength in VICON analysis are therefore calculated according to:

$$\lambda_m = \frac{\ell}{(\xi + 2m)} \quad where\ (m = 0, \pm1, \pm2, \pm3, \ldots. \ \pm q) \tag{3.4}$$

The values of ξ and q may be provided by the user to evaluate the buckling load.

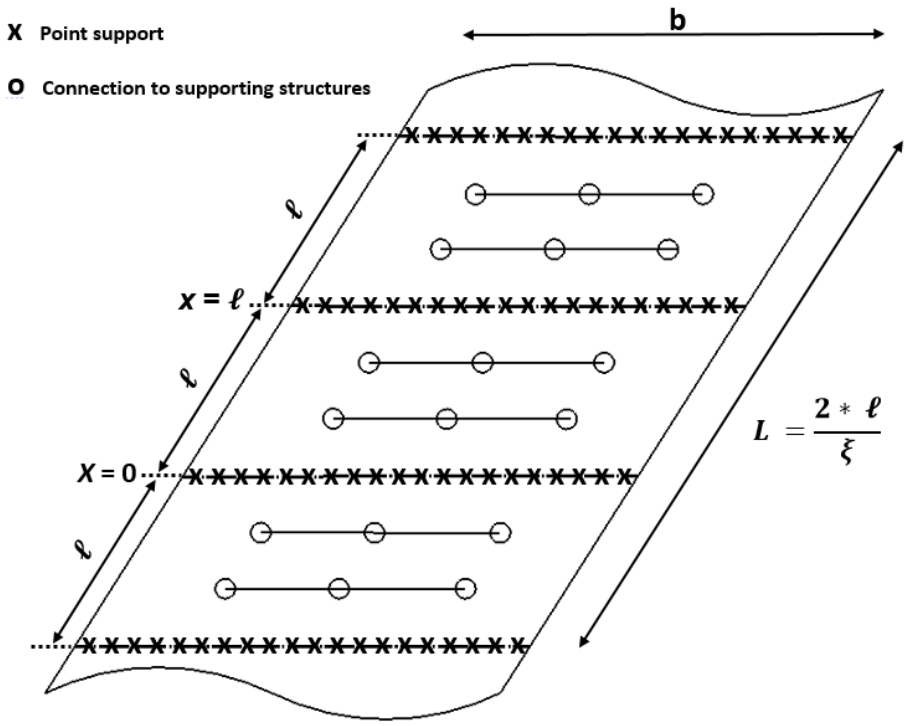

Figure 3.12: Infinite plate assembly in VICON analysis

3.5.3 VICONOPT software post-buckling analysis

The VIPASA analysis in VICONOPT (VICON with OPTimisation) is a Fortran 77 computer program which covers both prismatic plate assembly analysis and optimisation (evaluate the minimum mass). The VICONOPT analysis incorporates the features of both VIPASA and VICON which were described previously to calculate the critical buckling load factors and natural frequencies. In terms of design procedure, VICONOPT has an efficient optimisation tool which can specify the minimum mass of structural components that will lead to reducing the cost [152].

The VIPASA analysis in VICONOPT was extended to include the non-linear geometrical buckling analysis by Powell et al. [153]. The post-buckling analysis procedure calculates the exact stiffness by utilising the Wittrick-Williams algorithm. The output data includes the initial critical buckling load and strains. The buckling mode shape and the post-buckling applied load are founded initially by iteration depending on amplitude of the post-buckling mode. The total axial load, axial strain, mode shape and stress resultants at each strip are then computed. The post-buckling solution procedure assumes the same initial buckling mode through the rest of the analysis. Anderson and Kennedy [154] introduced an alternative procedure using Newton iterations to achieve more accurate convergence in terms of the post-buckling mode and stress distributions. An improved stress distribution method based on Stein's non-linear buckling hypothesis was developed to predict with higher accuracy the stress resultants at each post-buckling cycle [155].

3.6 Chapter summary

In this chapter, a review of previous investigations focusing on buckling, post-buckling and the mode jumping phenomenon was presented. It started with a short description of the main stability concepts because the buckling of

structures is a type of instability problem. Following a brief overview of the buckling behaviour and the different responses involved in the column and plate buckling, a review of previous initial buckling investigations, which represent the base of instability problems of thin-walled structures, was given, beginning with the pioneering researchers in the field. These studies illustrate the effect of anisotropy on the buckling capacity of composite plates. The first objective in the current study will extend these previous studies by utilising the anisotropic characteristics of the laminate to optimise the buckling load.

A summary of theoretical and experimental post-buckling studies was then presented, followed by reviews related to the mode-jumping phenomenon which is the main focus of this thesis. The second objective in this thesis will extend the post buckling analysis in VICONOPT software to include the mode jumping effect, which will lead to improved results compared to finite element analysis and experimental results. The chosen techniques have not been used in any previous studies. Although, the previous studies include many experimental investigations, these deal with specific shapes and dimensions that made the panels symmetric. However the third objective in this study covers curved panels with L-shape stiffeners which have asymmetric characteristics.

The last section of this chapter specified the main features of the VICONOPT program which is important to provide a better understanding of this software.

Chapter 4: Improving the Buckling Capacity of Composite Plates (Background and Method)

4.1 Introduction

This chapter presents a parametric study, which investigates the buckling behaviour of composite flat plates with different levels of anisotropy under a range of in-plane loading conditions. The aim is to determine a link between the plates' anisotropic characteristics, as defined in terms of lamination parameters and their buckling capacity, in order to tailor lay-ups to maximise performance. Critical buckling loads are calculated using the VICON analysis available in the VICONOPT software and finite element analysis using ABAQUS/Standard [156]. In recent years, reinforced composite structures have been used widely in large-scale, safety-critical structures for infrastructure and transport, (aerospace, energy and marine, see Figure 4.1). They provide huge weight savings whilst maintaining high stiffness and strength. Thin composite plates for example are used extensively in aerospace manufacturing (e.g. aircraft wings and fuselage structures) [157] replacing traditional metals with lighter weight alternatives with significant mass reductions offered, representing a major target in this industry.

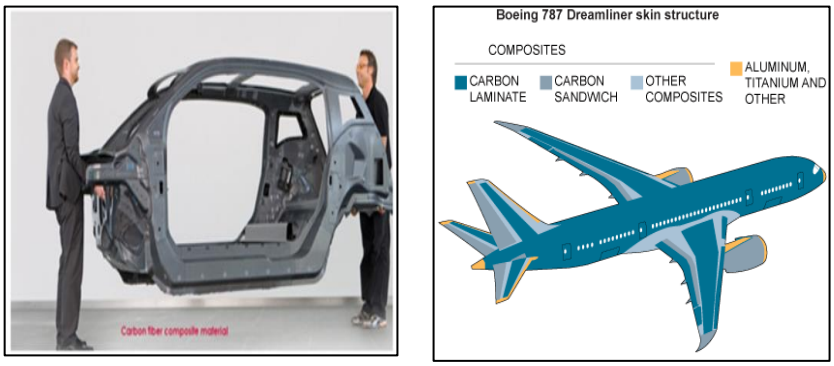

Figure 4.1: Composite materials use [157]

Thin plates however are sensitive to buckling failure when they are subjected to in-plane loading such as compression, shear or a combination of both. Over the last fifty years, many analytical, numerical and experimental studies related to the buckling of thin plates with varying levels of anisotropy have explored the behaviour of flat composite plates under different loading combinations. Williams and Kennedy [158] presented a theoretical procedure to include the effect of anisotropy in the exact strip method software VICONOPT. Nemeth [45] found that the effects of anisotropy are more pronounced in shear loaded plates than in those subject to compression. He showed this effect in terms of interaction curves. Loughlan [49] [159] utilised the finite strip method to examine the effect of bend-twist coupling on the buckling load and the mode shapes of buckled plates. His main conclusion was that for large aspect ratio plates, bend- twist coupling could cause a complete change in mode shape. Featherston and Watson [48] included the effect of anisotropy in the theoretical part of their study demonstrating its substantial effect in plates with relatively small thickness. Weaver [51] [52] suggested a solution to maximise the buckling load for different load combinations for long anisotropic composite plates. Selyugin [160] who studied flexural anisotropic plates under combined loading used a special Galerkin-type solution and compared it with a high accuracy numerical solution, for cases of composite laminates under combined in-plane compression, shear and bending.

The work described in this and the following chapter, unlike many previous studies which have sought mainly to incorporate the effect of anisotropy in their calculations, will outline an approach (which will use these properties through the relevant lamination parameter) to optimise the buckling load. The optimisation procedure suggested provides a direct and simple approach based

on a single factor to increase the buckling capacity depending on bending-twisting coupling parameters in the laminate stiffness matrix.

4.2 Composite materials

A composite is a structural material that consists of two or more constituents that are combined at a macroscopic level but remain separate and distinct and not soluble in each other. One part of the composite is called the reinforcing phase, and this is embedded in the other which is called the matrix. The reinforcing phase material may be in the form of fibres, particles, or flakes. The matrix phase materials are generally continuous. Examples of composite systems include concrete reinforced with steel and laminates made from epoxy reinforced with graphite fibres, see Figure 4.2.

The basic building blocks of a composite are the lamina, which are flat (or curved in the case of a shell) arrangements of unidirectional fibres or woven fibres in a matrix. These lamina are combined to form a laminate, a bonded stack of lamina with various orientations of principal material direction. The direction of the fibres in each of the lamina determines most of the features and behaviours of the composite under loading. Composite materials, like any other materials have strengths and weaknesses.

The advantages of composites include their high strength to weight ratio (weight reduction approximately 20-50% as compared with metal), high fatigue and creep resistance, high tensile strength at elevated temperature and corrosion resistance. On the other hand, there are disadvantages such as high material and manufacturing costs and susceptibility to damage including non- or barely- visible (BVID) impact damage which is difficult to detect, yet can cause significant reductions in in plane stiffness, and hence critical buckling loads and post buckling behaviour.

(a)

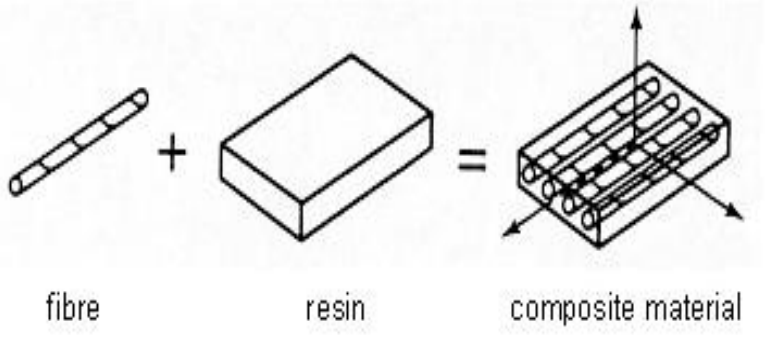

(b)

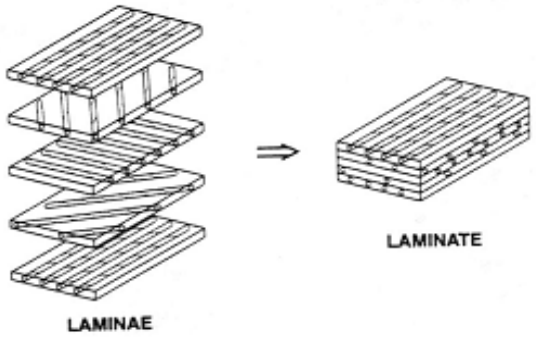

Figure 4.2: Composite materials,
a- composite composition, b- tailored Composite [161]

4.3 Stress-strain relations for a lamina

The plate equations presented in Chapter 2 can be extended to describe the behaviour, including buckling behaviour of laminated composites. For the lamina shown in Figure 4.3, the stress–strain relations in the global x and y directions are:

$$\begin{bmatrix}\sigma_x\\ \sigma_y\\ \tau_{xy}\end{bmatrix} = \begin{bmatrix}Q_{11} & Q_{12} & Q_{16}\\ Q_{12} & Q_{22} & Q_{26}\\ Q_{13} & Q_{26} & Q_{66}\end{bmatrix}\begin{bmatrix}\varepsilon_x^0\\ \varepsilon_y^0\\ \gamma_{xy}^0\end{bmatrix} + \begin{bmatrix}Q_{11} & Q_{12} & Q_{16}\\ Q_{12} & Q_{22} & Q_{26}\\ Q_{13} & Q_{26} & Q_{66}\end{bmatrix}\begin{bmatrix}k_x\\ k_y\\ k_{xy}\end{bmatrix} \tag{4.1}$$

where **ε** and **k** are the strain and curvature respectively at the middle surface of the laminate:

$$Q_{11} = q_{11}C^4 + 2(q_{12} + 2q_{66})S^2\,C^2 + q_{22}S^4 \tag{4.2}$$

$$Q_{12} = (q_{11} + q_{22} - 4q_{66})S^2\,C^2 + q_{12}(S^4 + C^4)$$

$$Q_{22} = q_{11}S^4 + 2(q_{12} + 2q_{66})S^2\,C^2 + q_{22}C^4$$

$$Q_{16} = (q_{11} - q_{12} - 2q_{66})SC^3 + (q_{12} - q_{22} + 2q_{66})CS^3$$

$$Q_{26} = (q_{11} - q_{12} - 2q_{66})CS^3 + (q_{12} - q_{22} + 2q_{66})SC^3$$

$$Q_{66} = (q_{11} + q_{22} - 2q_{12} - 2q_{66})C^2S^2 + q_{66}(S^4+C^4)$$

$S = \sin\boldsymbol{\theta}$ & $C = \cos\boldsymbol{\theta}$

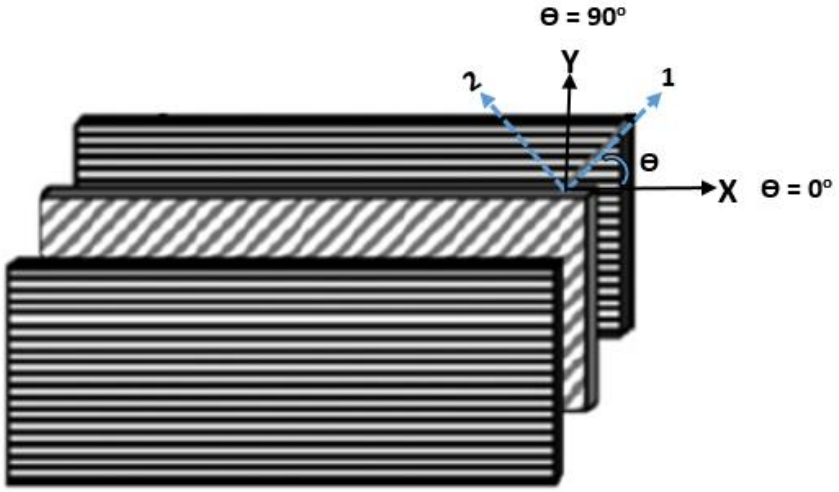

Figure 4.3: Fibre orientation with respect to global composite direction

In addition, q terms are defined as:

$$q_{11} = \frac{E_1}{1 - \nu_{12}\,\nu_{21}}$$

$$q_{22} = \frac{E_2}{1 - \nu_{12}\,\nu_{21}} \tag{4.4}$$

$$q_{12} = \frac{\nu_{12}E_2}{1 - \nu_{12}\,\nu_{21}} = \frac{\nu_{21}E_1}{1 - \nu_{12}\,\nu_{21}}$$

$$q_{66} = G_{12}$$

Assuming that the laminate's thickness is very small compared to its other dimensions, the layers of the laminate are perfectly bounded, the lamina and the laminate are linear elastic and the stresses and strains through thickness are negligible, Equation (2.9) for an isotropic plate can then be modified for a laminate:

$$\begin{Bmatrix} N_{xx} \\ N_{yy} \\ N_{xy} \end{Bmatrix} = \sum_{l=1}^{n} \int_{h_{l-1}}^{h_l} \begin{bmatrix} \sigma_{xx} \\ \sigma_{yy} \\ \tau_{xy} \end{bmatrix} dz \tag{4.5}$$

$$\begin{Bmatrix} M_{xx} \\ M_{yy} \\ M_{xy} \end{Bmatrix} = \sum_{l=1}^{n} \int_{h_{l-1}}^{h_l} \begin{bmatrix} \sigma_{xx} \\ \sigma_{yy} \\ \tau_{xy} \end{bmatrix} z dz \tag{4.6}$$

Where n is the total number of layers and h is the layer thickness. Substituting equation (4.1) in equations (4.5) and (4.6):

$$\begin{Bmatrix} N_{xx} \\ N_{yy} \\ N_{xy} \end{Bmatrix} = \sum_{l=1}^{n} \int_{h_{l-1}}^{h_l} \left\{ \begin{bmatrix} Q_{11} & Q_{12} & Q_{16} \\ Q_{12} & Q_{22} & Q_{26} \\ Q_{13} & Q_{26} & Q_{66} \end{bmatrix} \begin{bmatrix} \varepsilon_x^0 \\ \varepsilon_y^0 \\ \gamma_{xy}^0 \end{bmatrix} + \begin{bmatrix} Q_{11} & Q_{12} & Q_{16} \\ Q_{12} & Q_{22} & Q_{26} \\ Q_{13} & Q_{26} & Q_{66} \end{bmatrix} \begin{bmatrix} k_x \\ k_y \\ k_{xy} \end{bmatrix} \right\} dz \tag{4.7}$$

$$\begin{Bmatrix} M_{xx} \\ M_{yy} \\ M_{xy} \end{Bmatrix} = \sum_{l=1}^{n} \int_{h_{l-1}}^{h_l} \left\{ \begin{bmatrix} Q_{11} & Q_{12} & Q_{16} \\ Q_{12} & Q_{22} & Q_{26} \\ Q_{13} & Q_{26} & Q_{66} \end{bmatrix} \begin{bmatrix} \varepsilon_x^0 \\ \varepsilon_y^0 \\ \gamma_{xy}^0 \end{bmatrix} + \begin{bmatrix} Q_{11} & Q_{12} & Q_{16} \\ Q_{12} & Q_{22} & Q_{26} \\ Q_{13} & Q_{26} & Q_{66} \end{bmatrix} \begin{bmatrix} k_x \\ k_y \\ k_{xy} \end{bmatrix} \right\} z dz \tag{4.8}$$

Since the mid-surface strain and curvature are not functions of *z* (because at the middle surface *z=0*), they need not be included in the integration. Moreover, the laminate stiffness matrix is constant for a given ply. Hence, equations (4.7), (4.8) can be simplified as:

$$\begin{Bmatrix} N_{xx} \\ N_{yy} \\ N_{xy} \end{Bmatrix} = \sum_{l=1}^{n} \left\{ (h_l - h_{l-1}) \begin{bmatrix} Q_{11} & Q_{12} & Q_{16} \\ Q_{12} & Q_{22} & Q_{26} \\ Q_{13} & Q_{26} & Q_{66} \end{bmatrix} \begin{bmatrix} \varepsilon_x^0 \\ \varepsilon_y^0 \\ \gamma_{xy}^0 \end{bmatrix} + \frac{(h_l^2 - h_{l-1}^2)}{2} \begin{bmatrix} Q_{11} & Q_{12} & Q_{16} \\ Q_{12} & Q_{22} & Q_{26} \\ Q_{13} & Q_{26} & Q_{66} \end{bmatrix} \begin{bmatrix} k_x \\ k_y \\ k_{xy} \end{bmatrix} \right\} \tag{4.9}$$

$$\begin{Bmatrix} M_{xx} \\ M_{yy} \\ M_{xy} \end{Bmatrix} = \sum_{l=1}^{n} \left\{ \frac{(h_l^2 - h_{l-1}^2)}{2} \begin{bmatrix} Q_{11} & Q_{12} & Q_{16} \\ Q_{12} & Q_{22} & Q_{26} \\ Q_{13} & Q_{26} & Q_{66} \end{bmatrix} \begin{bmatrix} \varepsilon_x^0 \\ \varepsilon_y^0 \\ \gamma_{xy}^0 \end{bmatrix} + \frac{(h_l^3 - h_{l-1}^3)}{3} \begin{bmatrix} Q_{11} & Q_{12} & Q_{16} \\ Q_{12} & Q_{22} & Q_{26} \\ Q_{13} & Q_{26} & Q_{66} \end{bmatrix} \begin{bmatrix} k_x \\ k_y \\ k_{xy} \end{bmatrix} \right\} \tag{4.10}$$

And since the middle surface strains and curvatures are not a part of the summations, the laminate stiffness matrix and the $\boldsymbol{h_l}$ terms can be combined to form new matrices, defined as:

$$A_{ij} = \sum_{l=1}^{n} \left[Q_{ij}\right]_l (h_l - h_{l-1}) \tag{4.11}$$

$$B_{ij} = \frac{1}{2} \sum_{l=1}^{n} \left[Q_{ij}\right]_l (h_l^2 - h_{l-1}^2) \tag{4.12}$$

$$D_{ij} = \frac{1}{3} \sum_{l=1}^{n} \left[Q_{ij}\right]_l (h_l^3 - h_{l-1}^3) \tag{4.13}$$

where **A**, **B** and **D** represent the membrane, coupling and bending stiffness matrix respectively. This allows the constitutive equations to be written in matrix form as:

$$\begin{bmatrix} N_x \\ N_y \\ N_{xy} \\ M_x \\ M_y \\ M_{xy} \end{bmatrix} = \begin{bmatrix} A_{11} & A_{12} & A_{16} & B_{11} & B_{12} & B_{16} \\ A_{12} & A_{22} & A_{26} & B_{12} & B_{22} & B_{26} \\ A_{16} & A_{26} & A_{66} & B_{16} & B_{26} & B_{66} \\ B_{11} & B_{12} & B_{16} & D_{11} & D_{12} & D_{16} \\ B_{12} & B_{22} & B_{26} & D_{12} & D_{22} & D_{26} \\ B_{16} & B_{26} & B_{66} & D_{16} & D_{26} & D_{66} \end{bmatrix} \begin{bmatrix} \varepsilon_x^0 \\ \varepsilon_y^0 \\ \gamma_{xy}^0 \\ k_x \\ k_y \\ k_{xy} \end{bmatrix} \tag{4.14}$$

In the case of symmetric laminates, the elements of the **B** matrix will equal to zero. For orthotropic plates, D_{16} and D_{26} will be equal to zero.

4.4 Laminate buckling

The buckling equation, presented in Chapter Two equation (2.17), can be reproduced for composite plates as:

$$D_{11}\frac{\partial^4 w}{\partial x^4} + 4D_{16}\frac{\partial^4 w}{\partial x^3 \partial y} + 2(D_{12}+2D_{66})\frac{\partial^4 w}{\partial x^2 \partial y^2} + 4D_{26}\frac{\partial^4 w}{\partial x \partial y^3} + D_{22}\frac{\partial^4 w}{\partial y^4}$$
$$= N_x\frac{\partial^2 w}{\partial x^2} + 2N_{xy}\frac{\partial^2 w}{\partial x \partial y} + N_y\frac{\partial^2 w}{\partial y^2} \quad (4.15)$$

4.5 Buckling optimisation

It is clear that from equation (4.15), that the out of plane matrix **D** which changes depending on the stacking sequence of the lamina, has a significant effect on the buckling capacity of a laminate. Because of this, most of the optimisation studies carried out on the problem of buckling in composite plates have focused on the optimisation of the stacking sequence. These studies have considered the directions of the fibres in each ply of the composite laminates as an essential parameter in improving their buckling resistance [162][163][164]. Calculations are usually complicated due to the large number of design variables, which make these investigations computationally expensive. To address this, the stiffness matrix of the laminates can be re-written in terms of parameters, known as lamination parameters, which simplify the optimisation process. The next section will briefly describe these lamination parameters and how they are used to represent the laminate's stiffness and hence solve the optimisation problem.

4.6 Lamination Parameter (LP)

Lamination parameters [165] [166] provide a compact representation of the stacking sequence of a laminate. For a composite in which all the plies are

made of the same material, the constitutive matrices for the different lamina are identical except for their orientation. For two dimensional elasticity problems, twelve lamination parameters can be used to characterise the laminate's in plane, coupling and out of plane global stiffnesses (equations 4.16, 4.17 and 4.18 respectively).

The number of these parameters needed will be reduced to nine when using [0, 90, ±45], six in the case of symmetric laminates and five in the case of balanced symmetric laminates.

$$\begin{bmatrix} \xi_1^A \\ \xi_2^A \\ \xi_3^A \\ \xi_4^A \end{bmatrix} = \frac{1}{2} \int_{-1}^{1} \begin{bmatrix} \cos 2\theta(z) \\ \cos 4\theta(z) \\ \sin 2\theta(z) \\ \sin 4\theta(z) \end{bmatrix} dz_i \tag{4.16}$$

$$\begin{bmatrix} \xi_1^B \\ \xi_2^B \\ \xi_3^B \\ \xi_4^B \end{bmatrix} = \int_{-1}^{1} \begin{bmatrix} \cos 2\theta(z) \\ \cos 4\theta(z) \\ \sin 2\theta(z) \\ \sin 4\theta(z) \end{bmatrix} z_i dz_i \tag{4.17}$$

$$\begin{bmatrix} \xi_1^D \\ \xi_2^D \\ \xi_3^D \\ \xi_4^D \end{bmatrix} = \frac{3}{2} \int_{-1}^{1} \begin{bmatrix} \cos 2\theta(z) \\ \cos 4\theta(z) \\ \sin 2\theta(z) \\ \sin 4\theta(z) \end{bmatrix} z_i^2 \, dz_i \tag{4.18}$$

where $\theta(z)$ is the distribution function of the ply orientations through the normalised thickness coordinate $(2/h)\, z$.

Lamination parameters are independent of the number of the plies in a laminate, and in most applications, are normalised with respect to its total thickness. In the case of symmetric laminates, the four coupling parameters (4.17) disappear. By using these lamination parameters, stiffness optimisation problems can be substantially simplified. For example in the buckling case considered in section 4.4, it is now possible to rewrite the out of plane terms **D** in the form of lamination parameters:

$$
\begin{aligned}
D_{11} &= \frac{h^3}{12}(U_1+\xi_1^D U_2+\xi_2^D U_3)\\
D_{22} &= \frac{h^3}{12}(U_1-\xi_1^D U_2+\xi_2^D U_3)\\
D_{12} &= \frac{h^3}{12}(U_4-\xi_2^D U_3)\\
D_{66} &= \frac{h^3}{12}(U_5-\xi_2^D U_3)\\
D_{16} &= \frac{h^3}{12}(\frac{\xi_3^D}{2}U_2+\xi_4^D U_3)\\
D_{26} &= \frac{h^3}{12}(\frac{\xi_3^D}{2}U_2-\xi_4^D U_3)
\end{aligned}
\tag{4.19}
$$

where the material invariants can be defined as:

$$
\begin{aligned}
U_1 &= \frac{1}{8}(3q_{11}+3q_{22}+2q_{12}+4q_{66})\\
U_2 &= \frac{1}{8}(q_{11}+q_{22})\\
U_3 &= \frac{1}{8}(q_{11}+q_{22}-2q_{12}-4q_{66})\\
U_4 &= \frac{1}{8}(q_{11}+q_{22}+6q_{12}-4q_{66})\\
U_5 &= \frac{1}{8}(q_{11}+q_{22}-2q_{12}+4q_{66})
\end{aligned}
\tag{4.20}
$$

4.7 Anisotropic properties of the laminate

The anisotropic properties of composite plates are represented in the flexural/twisting coupling terms D_{16} and D_{26} which are equal in cases where [0,90,±45] orientation angles are used. Many previous studies (some of them mentioned in Chapter 3, section 3.2) have considered only symmetric and balanced laminates and hence have been able to neglect the effect of anisotropy and treat the laminates as orthotropic plates, assuming that the values of D_{16} and D_{26} are small compared to the other terms and can therefore be neglected. Jones however [161] found that the D_{16} and D_{26} values depend on

the number of plies in the laminate, and that the anisotropy terms are large for a plates consisting of small numbers of plies and become smaller in comparison to other coefficients as the number of plies is increased. Since, in the aerospace industry, the composite plates used can have a relatively small number of plies this indicates that D_{16} and D_{26} should not be ignored and still have an important effect on the behaviour of the laminate.

4.8 Increasing the buckling load of plates using anisotropy

4.8.1 Effect of anisotropy and shear in the laminate buckling mode

When a composite plate is subjected to in-plane loading, buckle. The nodal lines (lines of zero out-of-plane displacement) are straight and perpendicular to their longitudinal edges if they have orthotropic properties (D_{16}=D_{26}=0) and there is no shear load, see Figure 4.4a.

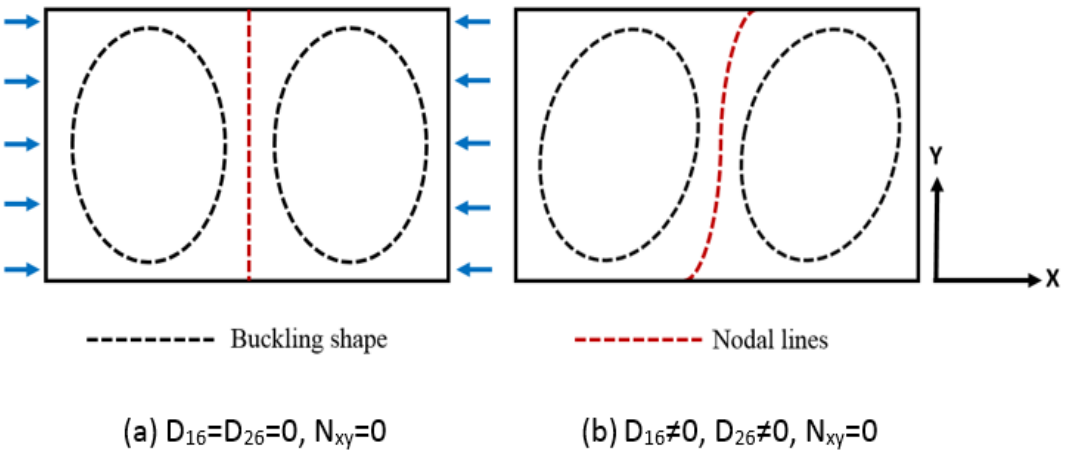

Figure 4.4: Buckling mode shape, a) without or b) with skewing

These nodal lines will become skewed however, if the laminate is anisotropic (even in the absence of shear load) or when shear load is present, see

Figure 4.4b. Theoretical and experimental investigations have shown that nodal line skewing decreases buckling loads [167] [51] [168].

The main objective of the approach presented in this chapter is a numerical proposal that aims to maximise the buckling load by altering the anisotropic properties of the laminates. These properties are introduced through the use of particular lay-ups to induce skewing behaviour, which oppose that due to the application of shear load and hence maximise the plate's buckling capacity under specific in plane loading. Therefore, the result of this process is to improve the buckling capacity of the composite plates. This in turn will lead to a reduction in the mass of the laminates required to carry a specific design load. The approach will be based on the use of the lamination parameters, which control the flexural-twisting coupling for particular in plane loading conditions. The main stages of this approach is expanded below as shown in Figure 4.5.

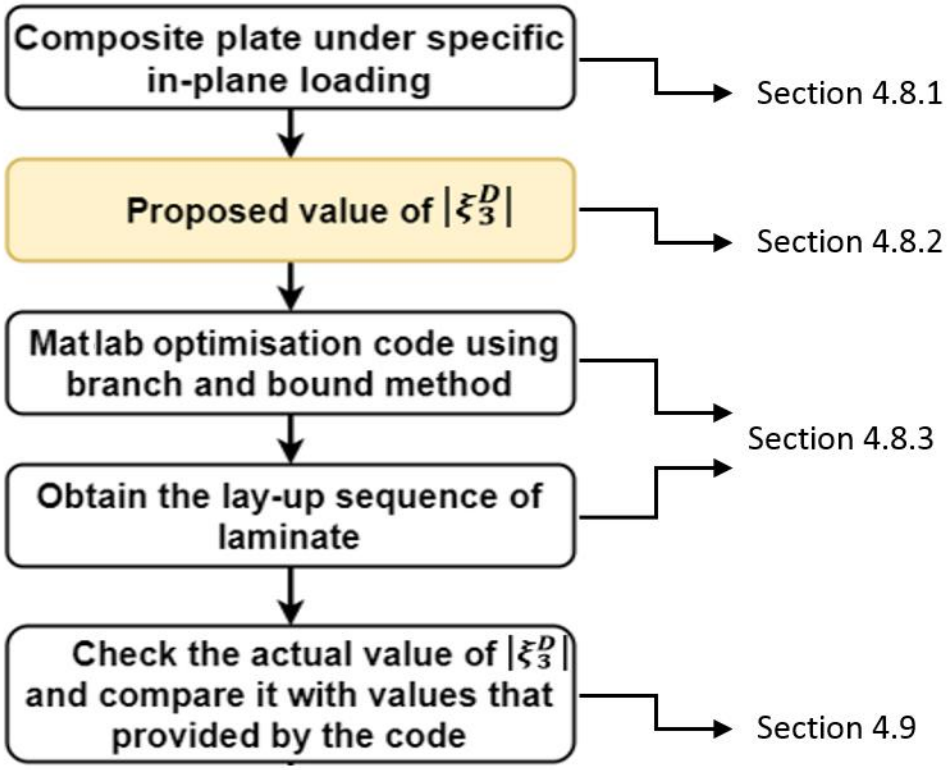

Figure 4.5: The suggested approach for layup optimisation

In this way, the anisotropy terms D_{16} and D_{26} will be utilised through the lamination parameter ξ_3^D to maximise the buckling load. Laminates will be designed with appropriate values of D_{16} and D_{26} which will cause skewing (and hence shear strain) in the opposite direction to that induced by the applied shear load reducing the effect of the applied shear strain and decreasing the nodal line skewing. Consequently, the critical buckling load will increase.

4.8.2 Application of the lamination parameter ξ_3^D for anisotropy level control

The first stage of the process proposed is to determine clear relationships between the level of anisotropy as characterised by the lamination parameter and the buckling behaviour of plates subject to different loading combinations (compression, shear and a combination of the two). This will be achieved through a parametric study, which is presented in chapter five. This study will use laminates with (±45°) layer orientations, which are balanced and symmetric, decreasing the number of the lamination parameters of interest to six. Five of the lamination parameters will be either -1 or zero while the parameter ξ_3^D will be varied, controlling the D_{16} and D_{26} terms in the laminate stiffness matrix responsible for the anisotropy properties. The value of ξ_3^D will be changed from 0.0 to a maximum value of 0.75 to determine that which results in the highest buckling load. Once the optimal value of ξ_3^D for a particular set of in plane loading conditions has been determined, a lay-up with the required lamination parameter needs to be found.

4.8.3 Optimum lay-up sequence extraction using branch and bound method

The process for determining a suitable lay-up with the proposed lamination parameter ξ_3^D is based on the branch and bound code developed by Liu et al

which is programmed into Matlab and incorporates a layer-wise approach to maximise efficiency [169].

The code output is restricted to four choices of ply angle (0°, 90°, and ±45 °) to ensure the recommended designs conform to manufacturing limitations. The Matlab program can be used to constrain the layers to be symmetric, balanced or both. The ply orientations are successively altered, working inwards from the outer plies, because they make the greatest contributions to the flexural lamination parameters. Initially, only the two outer plies are altered as shown in Figure 4.6a, followed by the four outer plies Figure 4.6b, and so on until in the final cycle all of them can be altered. This layer-wise approach helps to obtain the optimum layup efficiently thereby achieving a reduction in computational cost.

Run	1	2	3	4
θ1	**θ1**	θ1	θ1	θ1
θ2	θ2	**θ2**	θ2	θ2
θ3	θ3	θ3	**θ3**	θ3
θ4	θ4	θ4	θ4	**θ4**
θ5	θ5	θ5	θ5	**θ5**
θ6	θ6	θ6	**θ6**	θ6
θ7	θ7	**θ7**	θ7	θ7
θ8	**θ8**	θ8	θ8	θ8

(a)

Run	1	2
θ1	**θ1**	θ1
θ2	**θ2**	θ2
θ3	θ3	**θ3**
θ4	θ4	**θ4**
θ5	θ5	**θ5**
θ6	θ6	**θ6**
θ7	**θ7**	θ7
θ8	**θ8**	θ8

(b)

Figure 4.6: Branch and bound with layer-wise optimisation techniques [169], (a) cycle 1, (b) cycle 2. Each run optimises only the variables shown bold.

4.9 Selection of lay-ups for the parametric study

The same branch and bound process was used to design lay-ups with differing values of the lamination parameter ξ_3^D for the parametric study discussed in 4.8.2. As mentioned the aim was to vary this parameter between 0 and 0.75, and it was decided that this should be done in steps of 0.1 up until 0.7.A comparison between these desired lamination parameters and the lamination parameters calculated by the Matlab code for the selected lay-ups is given in Table 4.1 alongside the corresponding layups for laminates with different numbers of plies. The table shows that the difference between the two groups is relatively small and decreases as the number of layers is increased. The first column shows the proposed lamination parameter ξ_3^D, which is input into the code while the third column gives the values for the proposed lay-ups calculated using equation (4.18). The laminates designed in this way were then analysed for buckling under different loading conditions using the VICON analysis of exact strip method software VICONOPT and the finite element analysis program (ABAQUS).

4.10 Chapter summary

This chapter has presented a suggested method to optimise the buckling load of composite plates using different anisotropic configurations dependent on the applied in-plane loading. The main conclusions of this chapter are:

- The study used ±45 symmetric balanced laminates in order to focus on the lamination parameter ξ_3^D which controls the bend-twist coupling, and is responsible for the anisotropic properties of composite plates.
- A brief description of the Matlab code, which uses the branch and bound technique to extract the laminate layup angles, was presented.

- The differences between the proposed ξ_3^D parameter and the actual values calculated using the equations are acceptable and become smaller as the number of layers increased. The first part of the optimisation process is presented in form of a flowchart for simplicity.

Table 4.1: The layup of composite plates depending on $\boldsymbol{\xi_3^D}$values

$(\xi_3^D)_a$ target	Layup Sequences (Matlab code output)	$(\xi_3^D)_c$ optimised	$\|R\| = (\xi_3^D)_a - (\xi_3^D)_c$
0.0	[45 -45 -45 45 -45 45 45 -45]s	0.000	0.000
0.1	[45 -45 45 -45 -45 45 -45 45]s	0.0937	0.0063
0.2	[45 -45 45 -45 45 -45 45 -45]s	0.1875	0.0125
0.3	[45 45 -45 -45 45 -45 -45 45]s	0.3047	0.0047
0.4	[45 -45 45 45 45 -45 -45 -45]s	0.3948	0.0052
0.5	[45 45 45 -45 -45 -45 -45 45]s	0.5156	0.0156
0.6	[45 45 45 -45 -45 45 -45 -45]s	0.5859	0.0141
0.7	[45 45 45 -45 45 -45 -45 -45]s	0.6562	0.0438
0.75	[45 45 45 45 -45 -45 -45 -45]s	0.7500	0.0000
0.0	[45 -45 -45 45 -45 45 45 -45 45 -45 -45 45]s	0.0069	0.0069
0.1	[45 -45 45 -45 45 -45 45 -45 -45 45 -45 45]s	0.0972	0.0028
0.2	[45 -45 45 45 -45 45 -45 -45 -45 45 45 -45]s	0.2025	0.0025
0.3	[45 -45 45 45 -45 45 45 -45 -45 45 -45 -45]s	0.2986	0.0014
0.4	[45 45 45 -45 45 -45 -45 -45 45 -45 45 -45]s	0.4028	0.0028
0.5	[45 45 45 45 -45 -45 -45 45 -45 45 -45 -45]s	0.5000	0.0000
0.6	[45 45 45 45 -45 45 -45 -45 45 -45 -45 -45]s	0.5972	0.0028
0.7	[45 45 45 45 45 -45 45 -45 -45 -45 -45 -45]s	0.7083	0.0083
0.75	[45 45 45 45 45 45 -45 -45 -45 -45 -45 -45]s	0.7500	0.0000
0.0	[45 -45 -45 45 -45 45 45 -45 45 -45 -45 45 -45 45 45 -45]s	0.0000	0.0000
0.1	[45 -45 45 -45 45 -45 45 -45 45 -45 45 -45 45 45 -45 -45]s	0.0996	0.0004
0.2	[45 45 -45 -45 45 45 45 -45 -45 -45 -45 45 45 -45 45 -45]s	0.1992	0.0008
0.3	[45 45 45 -45 45 -45 -45 45 -45 -45 45 -45 45 45 -45 -45]s	0.2988	0.0012
0.4	[45 45 45 45 -45 -45 45 -45 45 -45 -45 45 -45 -45 -45 45]s	0.4014	0.0014
0.5	[45 45 45 45 45 -45 45 -45 -45 -45 -45 -45 45 -45 -45 45]s	0.5010	0.0010
0.6	[45 45 45 45 -45 45 45 45 -45 -45 45 -45 -45 -45 -45 -45]s	0.6006	0.0006
0.7	[45 45 45 45 45 45 -45 45 45 -45 -45 -45 -45 -45 -45 -45]s	0.7002	0.0002
0.75	[45 45 45 45 45 45 45 45 -45 -45 -45 -45 -45 -45 -45 -45]s	0.7500	0.0000

Chapter 5: Improving the buckling Capacity of Composite Plates (Results and Discussion)

5.1 Introduction

This chapter presents the results of the optimisation approach described in Chapter 4. Composite flat plates with different aspect ratios, subject to different in-plane loading conditions from pure compression to combined loading to pure shear are studied to determine the effect of their lay-up sequences and the number of plies used on their critical buckling loads and hence derive design rules for optimisation of these panels under different conditions. Critical buckling loads are calculated using the VICON analysis available in the VICONOPT software and finite element analysis using ABAQUS/Standard [156].

5.2 Material properties and boundary conditions

The study used laminates comprising of carbon fibre epoxy plies [170], of thickness 0.125 mm with Young's moduli E_1=181 GPa, E_2= 10.3 GPa, shear modulus G_{12}=7.17 GPa and Poisson's ratio ν_{12}= 0.28. All laminates were symmetric and balanced and consisted of [±45] orientated layers. Consequently, the coupling lamination $\xi^B_{[1,2,3,4]} = 0$.

The in and out of plane lamination parameters for these lay-ups are $\xi^A_1 = \xi^D_1 = \xi^A_3 = \xi^A_4 = \xi^D_4 = 0$ and $\xi^A_2 = \xi^D_2 = -1$, while the parameter, which controls the twisting-bending properties of the laminates ξ^D_3 was the target of the optimisation and was varied $\xi^D_3 = 0$ to 0.75. The plan dimensions of the plates were length a=0.5, width b=0.5 m and length a=0.8, width b=0.5 m for the square and rectangular laminates respectively.

The plates were simply supported along all four edges. The finite element models, which were used to validate the VICON results, consisted of 20 x 20 and 20 x 32, S4R linear shell elements [156].

Figure 5.1 shows the mesh sensitivity for a square laminate with different number of elements which explain the chosen number of elements that provide efficient converged results in this study. Three types of loading were applied namely: pure compression, combined in-plane compression and shear (with increasing levels of shear and vice versa) and pure shear. The loading and boundary conditions for both the exact strip and finite element methods are shown in Figure 5.2.

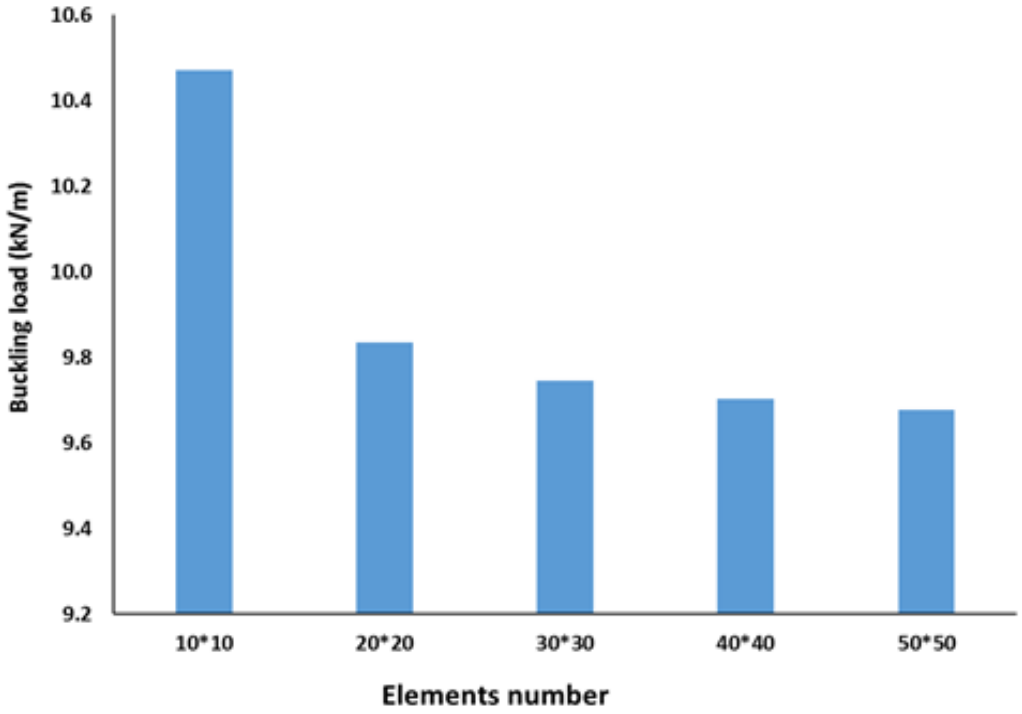

Figure 5.1: Mesh sensitivity

The layup sequences of the laminates analysed were generated by the Matlab code described in Chapter 4 to find lamina orientation angles corresponding to the desired values of the lamination parameters. As the study used only [±45], and the laminates were all symmetric and balanced, the only value that could be changed was that of ξ_3^D. The value of this parameter, which controls the bend-twist properties, was varied from an initial value of 0.0 to 0.75 in steps of 0.1. The highest value of ξ_3^D possible is 0.75 and rather than 1.0 because each of the laminates is required to be balanced.

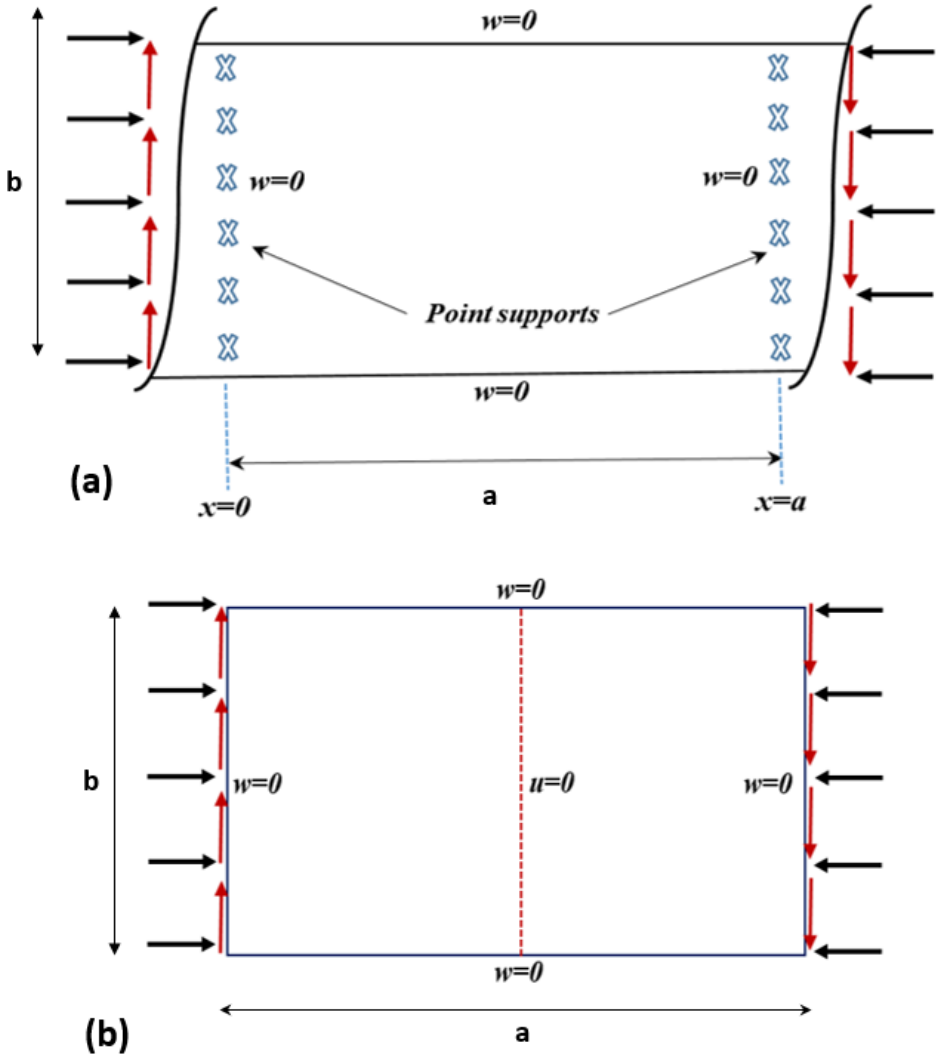

Figure 5.2: Laminate edge boundary conditions,
a- VICONOPT, b- ABAQUS

5.3 Laminates under in-plane loading

5.3.1 Uniaxial in-plane compression

For laminates subjected to a compressive load in the length *x*-direction, results are presented in terms of the relationship between the critical buckling load and the lamination parameter ξ_3^D. The anisotropy of the composite plates was increased gradually from zero to its maximum value by varying ξ_3^D and the buckling loads were calculated for each laminate using both VICON and finite element analysis. Both analyses showed that the maximum buckling capacity was obtained when the buckling mode shapes have no skewing (the nodal lines are perpendicular to the longitudinal edges of the laminates) which is achieved at $\xi_3^D = 0$. Figure 5.3, shows the buckling load to anisotropy level relationship for laminates with *a/b*=1.0. The critical buckling load (normalised with respect to its maximum value when the laminate has no anisotropy) calculated using VICON analysis decreases significantly from 1.0 to 0.8748 as the value of ξ_3^D is increased from 0 to 0.75 for a square laminates with 16 layers. The same behaviour is repeated, again with normalised buckling loads reducing when the number of layers is increased to 24 and then 32. However, when critical loads are calculated instead using ABAQUS greater reductions are seen as the bend twist coupling increases. In this case, the buckling load decreases from 1.0 to 0.7644, 0.7649 and 0.7655 for laminates with 16, 24 and 32 layers respectively as ξ_3^D is increased from 0.0 to 0.75.

The relatively higher buckling loads calculated by the VICON analysis are assumed to be because of the different assumptions applied in the two programs. VICON analysis assumes that the plate has infinite length and the buckling mode is repeated over a particular length as explained previously in Chapter 3, so there is no requirement for zero bending moment at the end of the plate. VICON and ABAQUS analyses of rectangular laminates show a

greater level of agreement compared with square plates. However, the results still follow the same overall trend.

The critical buckling loads drop from 1.0 to 0.7739 (0.7242) for VICON (for ABAQUS) analyses respectively when anisotropy is increased to its maximum level for rectangular laminates with 16 layers, see Figure 5.4a. The results 0.7739 (0.7250) for those with 24 layers and 0.7739(0.7259) for laminates with 32 layers, see Figure 5.4b and 5.4c. The results appear to show the effect of increasing the number of layers is marginal, with similar trends seen in the behaviour of laminates of different thickness. Since all the plates considered show the same tendencies it can be concluded that when a plate is subjected to compressive load conditions, its anisotropic properties should be minimised producing less skewing and consequently increasing the buckling load.

This observation is supported by examining the buckling mode shapes of the laminates analysed which are presented as contours of the out-of-plane displacements. All the mode shapes are for the laminates with 16 layers, laminates with different numbers of layers have the same buckling configurations. Figure 5.5 shows the buckling modes predicted by VICON and ABAQUS for square laminates, which buckle with one-half wavelength and increasing the levels of skew as anisotropy increases. The rectangular plates studied buckled with two half waves as seen in Figure 5.6. The VICON mode shapes are very close to those predicted by ABAQUS and gradually skewed due to the increased level of bend-twist coupling. Although the ABAQUS mode shape is seen to display slightly higher skewing as compared with the VICON mode when the value of $\xi_3^D = 0.4$ this could be due to the effect of the different plate modelling methods used in the two programs (such as the use of a series solution in VICON analysis). The skewing of the buckling mode shapes is directly proportional to the value of ξ_3^D while it is inversely proportional to the buckling load factors.

(a)

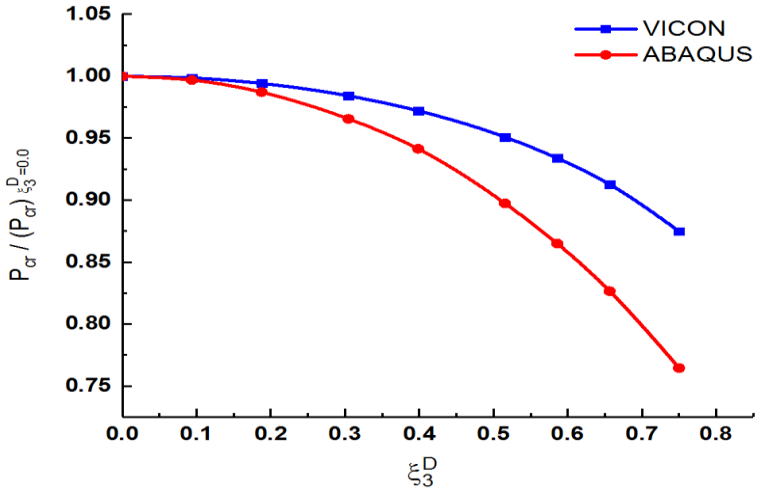

(b)

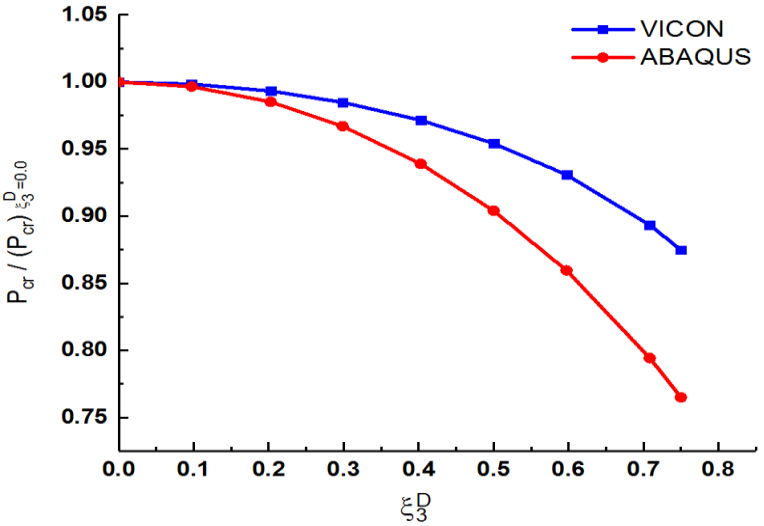

(c)

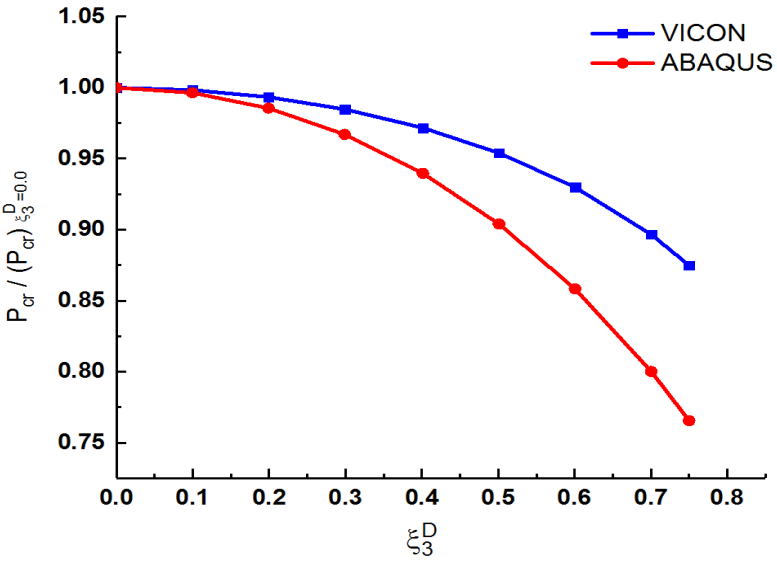

Figure 5.3: Buckling load to anisotropy level relationships for laminates with *a/b* =1.0, Number of plies = (a) 16, (b) 24, (c) 32

(a)

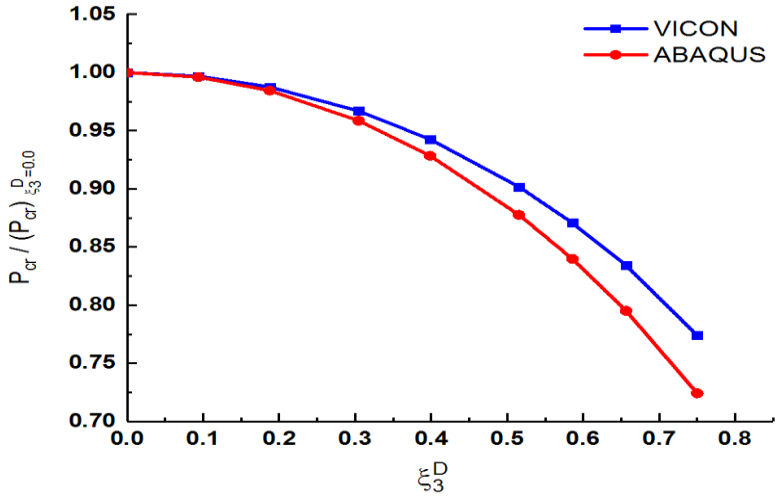

(b)

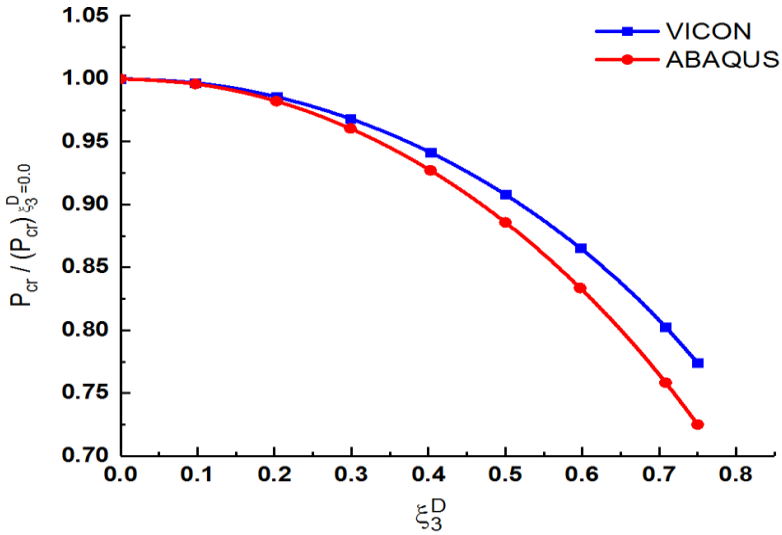

(c)

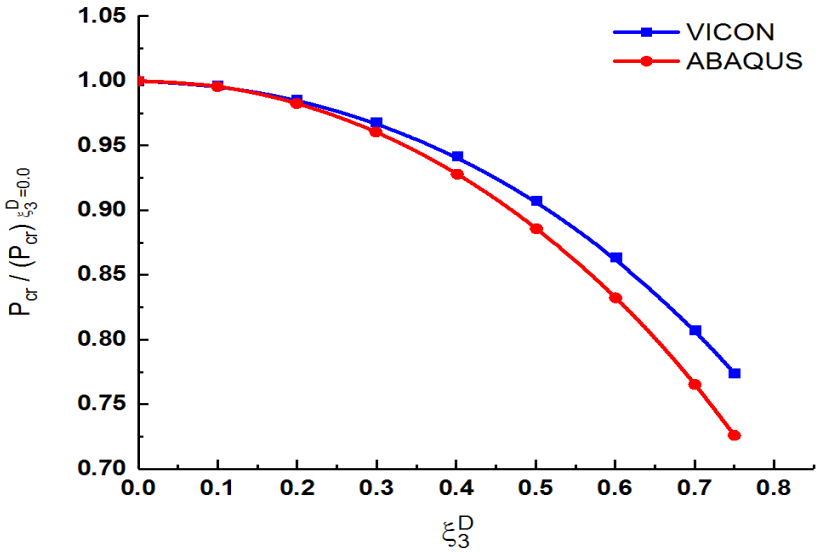

Figure 5.4: Buckling load to anisotropy level relationships for laminates with *a/b* =1.6, Number of plies = (a) 16, (b) 24, (c) 32

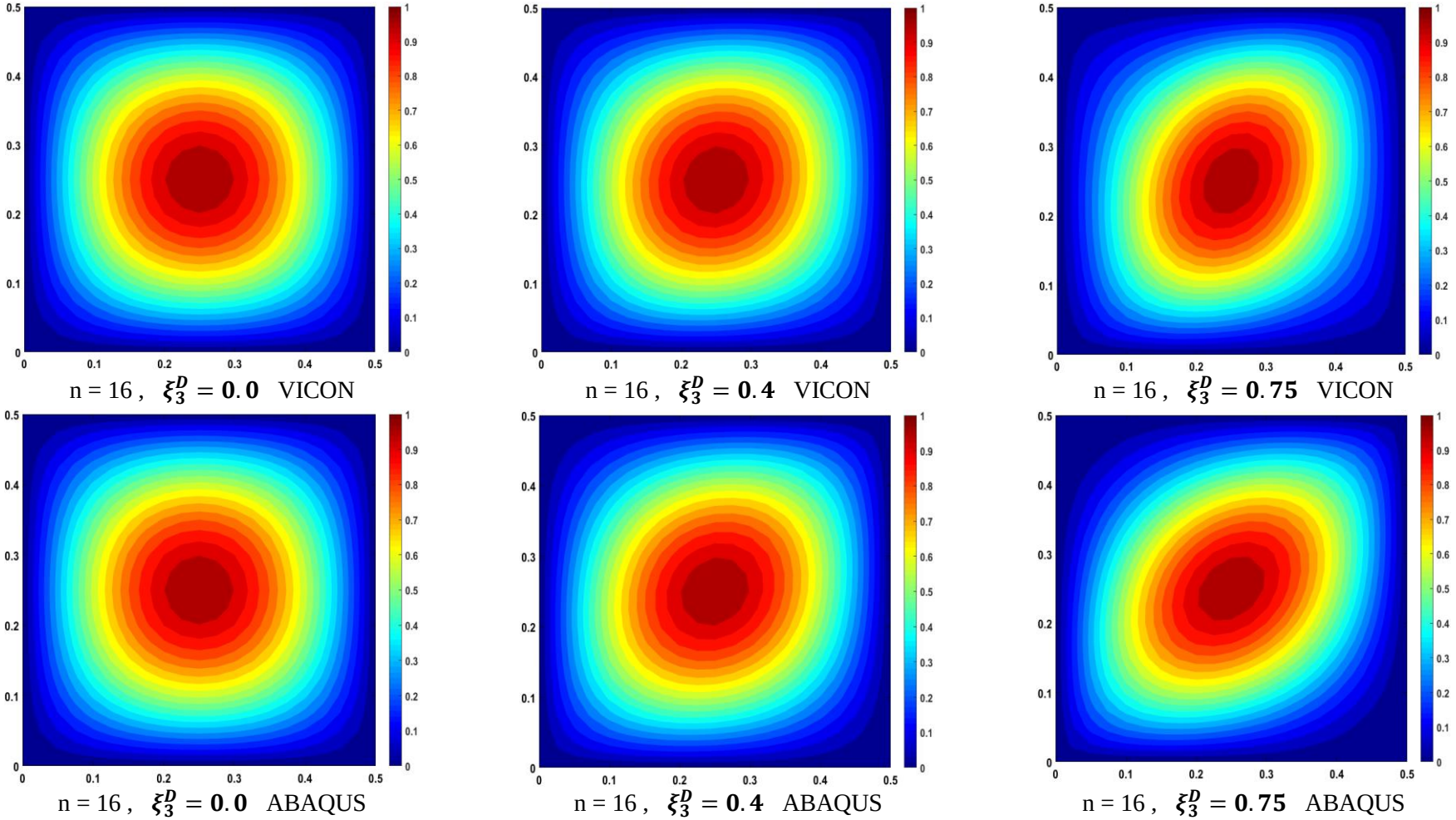

Figure 5.5: Laminates with *a/b* = 1.0, normalised buckling modes

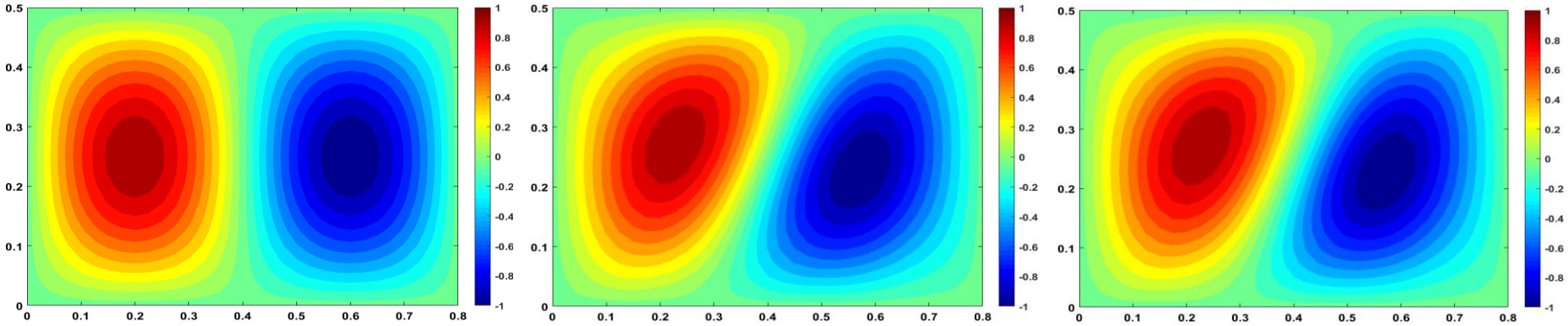

n = 16 , $\boldsymbol{\xi_3^D = 0.0}$ VICON

n = 16 , $\boldsymbol{\xi_3^D = 0.4}$ VICON

n = 16 , $\boldsymbol{\xi_3^D = 0.75}$ VICON

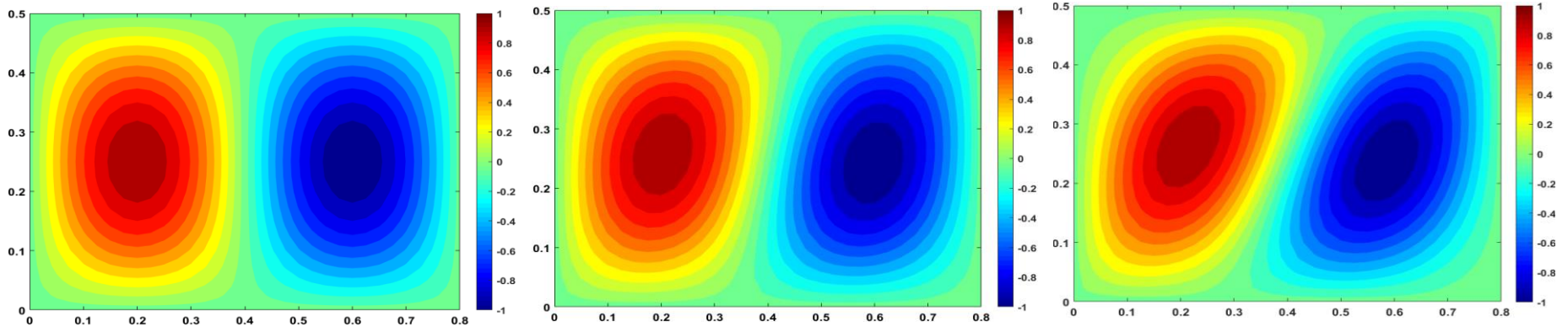

n = 16 , $\boldsymbol{\xi_3^D = 0.0}$ ABAQUS

n = 16 , $\boldsymbol{\xi_3^D = 0.4}$ ABAQUS

n = 16 , $\boldsymbol{\xi_3^D = 0.75}$ ABAQUS

Figure 5.6: Laminates with *a/b* = 1.6, normalised buckling modes

5.3.2 Combined in-plane loading (compression load dominates)

The study of composite plates under combined loading is more complicated than under uniaxial load since the behaviour is dependent on whether the compression or shear load is dominant. This section will focus on laminates subjected to combined in-plane compression and shear load when the compression dominates. This compressive load is applied as the main constant load (destabilising load) while the shear load (subcritical load) is increased in steps N_{xy}/N_x = 0.1 starting from 0.0 and increasing to 1.0. In each case, the laminate stacking sequence is varied depending on the lamination parameter ξ_3^D . The results are presented in the form of the relationship between the critical buckling load and the combined loading ratio $\frac{N_{xy}}{N_x}$ for laminates with different levels of anisotropy. Buckling load values are normalised with respect to the load calculated at $\xi_3^D = \frac{N_{xy}}{N_x} = 0$. For all of the lay-ups studied, the maximum buckling load occurred when the load ratio $\frac{N_{xy}}{N_x} = \xi_3^D$. This trend was repeated for laminates with different thickness (different number of plies). For example, the results for a square laminate (16 plies) with $\xi_3^D = 0.1$ show that, the buckling load factor increases from 0.9986 to 0.9995 as the load ratio increases from 0 to 0.1. It then decreases to 0.9979 when the load ratio changes to 0.2. This dropping in the buckling load continues as the shear load is increased as shown in Figure 5.7. The same behaviour is observed for laminates with ξ_3^D=0.4, for which the buckling load factor is raised from 0.97212 at a load ratio of zero to its peak value of 0.99036 at $\frac{N_{xy}}{N_x} = 0.4$. It then starts to decrease as the load ratio increases. Finally for a laminate with $\xi_3^D = 0.75$ the value of buckling load increases gradually with increasing load ratio until $\frac{N_{xy}}{N_x} = 0.7$ and then moves down. The mode shapes for the square laminates examined are shown in Figure 5.9.

All of the plates buckled with one-half wavelength. The contour plots show laminate skewing due to anisotropy when the load ratio is zero and due to a combination of shear and anisotropy for other values of $\frac{N_{xy}}{N_x}$. Moreover laminates with $\xi_3^D = 0.0$ show higher skewing (in the presence of shear load) than laminates with $\xi_3^D = 0.4$ and $\xi_3^D = 0.75$. The explanation of such behaviour is that the skewing is decreased because of the opposing effects of the anisotropy and the shear component of the loading.

The rectangular laminates (16 layers) show similar trends. For laminates with $\xi_3^D = 0.2$, the critical load was increases from 0.98758 to 0.99609 and then to 0.99774 as load ratio increases from 0.0 to 0.1 and then 0.2 respectively and then decreases after $\frac{N_{xy}}{N_x} = 0.2$. For a laminates with $\xi_3^D = 0.4$ the critical buckling load increases (while logically we might expect it to decrease because the buckling load factor normally has inverse proportion with the applied load) as the load ratio increases until $\xi_3^D = \frac{N_{xy}}{N_x}$ and then decreases after this point. For instance the load factor is 0.94262 when $\frac{N_{xy}}{N_x} = 0.0$, 0.99037 at $\frac{N_{xy}}{N_x} = 0.4$ and then 0.98536 at $\frac{N_{xy}}{N_x} = 0.5$ with this reduction continuing as the load ratio is increased. The results for laminates with $\xi_3^D = 0.75$ show exactly the same behaviour with the buckling load increasing as the load ratio increases until $\frac{N_{xy}}{N_x} = 0.7$ after which it starts to decrease. Results for rectangular laminates with different numbers of plies are shown in Figure 5.8. Laminates with aspect ratio 1.6 buckled with two half waves, see Figure 5.10. Plate skewing can be seen to be higher when the plate has no bend-twist coupling. The anisotropy is useful in this case because the bend-twist coupling generates a skewing effect, which decreases the external shear load skewing. Consequently, the critical buckling load increases.

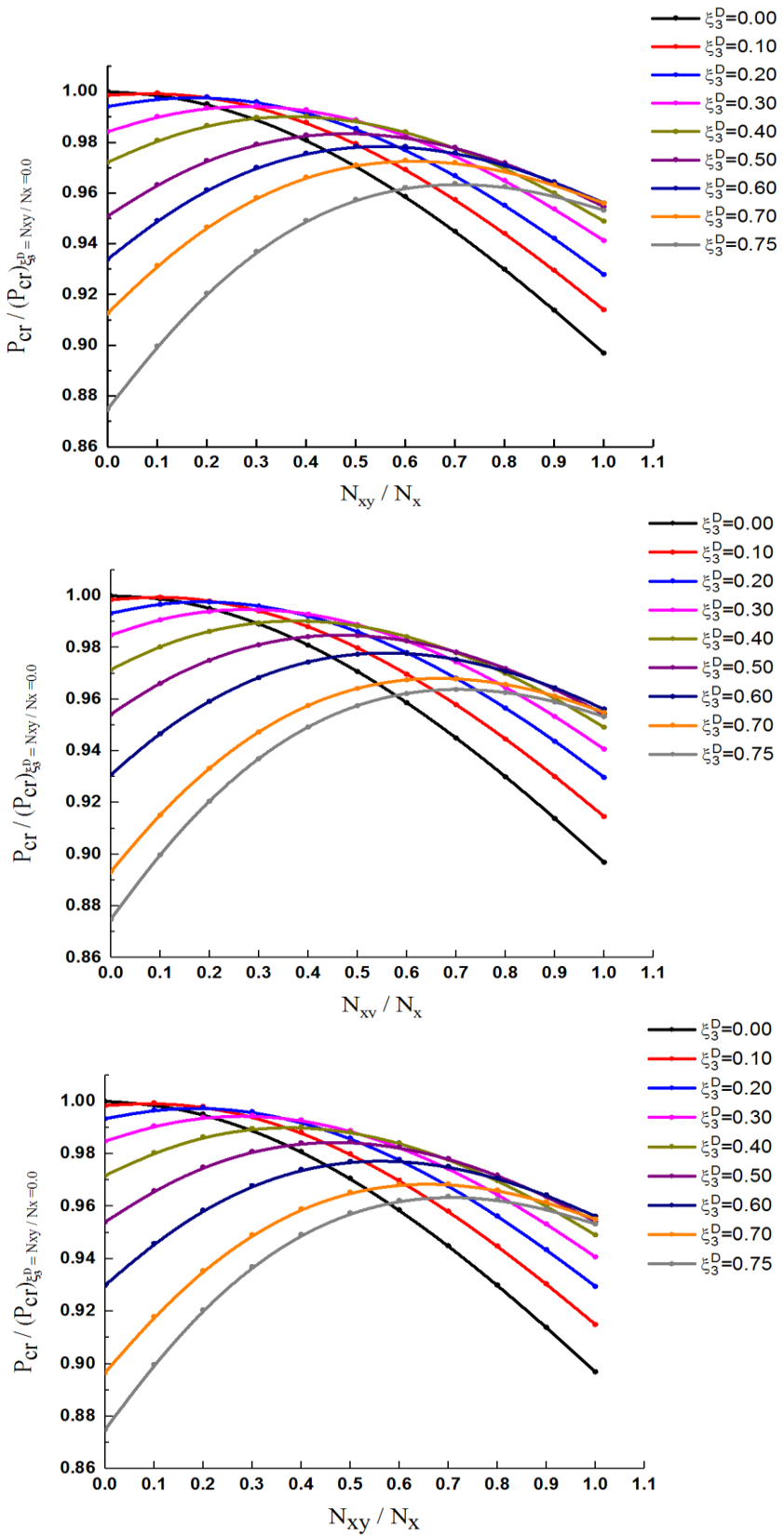

Figure 5.7: Normalised buckling load factor to load ratio relationships for laminates with *a/b* =1.0, Number of plies = (a) 16, (b) 24, (c) 32

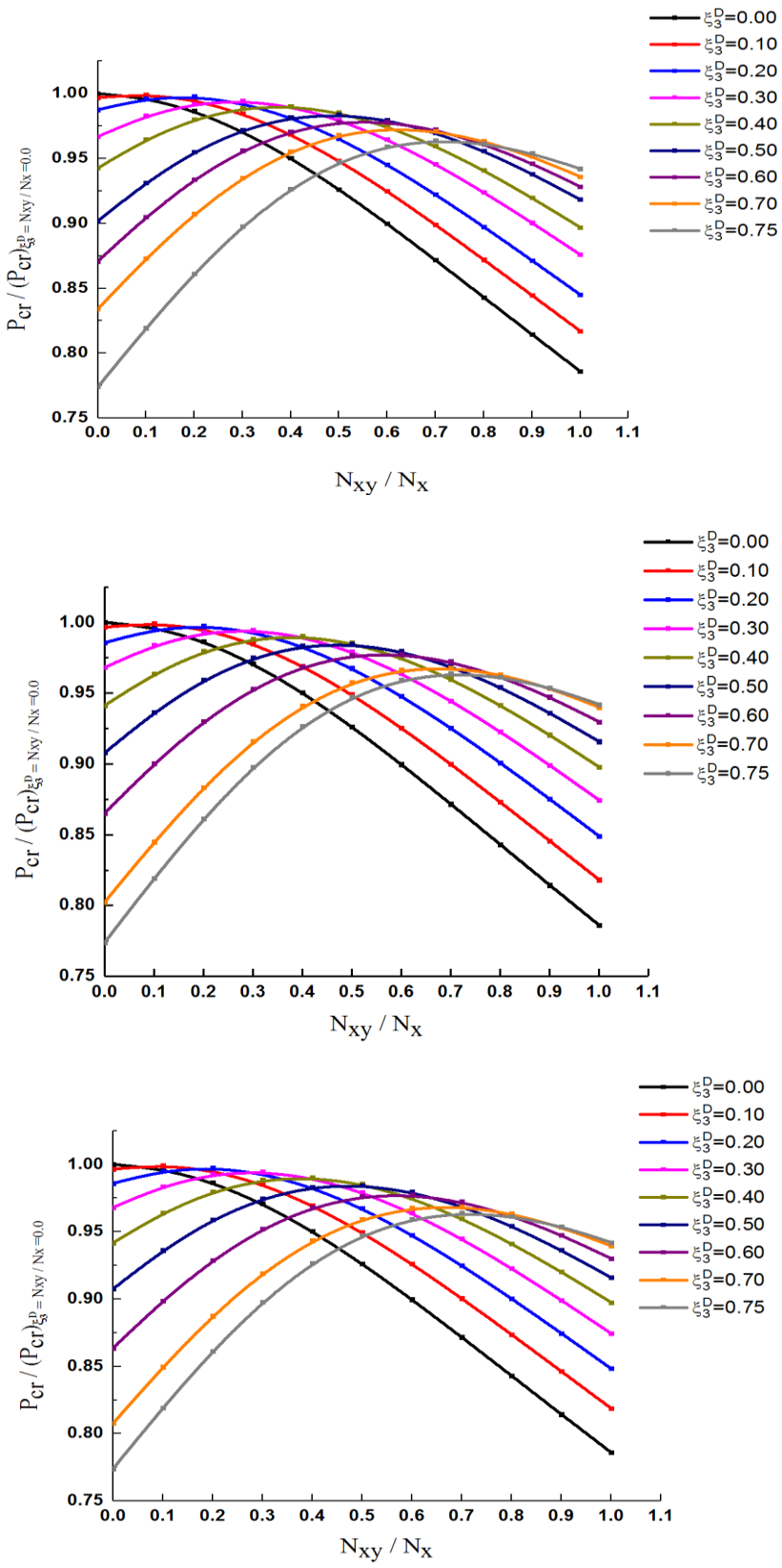

Figure 5.8: Normalised buckling load factor to load ratio relationships for laminates with *a/b* =1.6, Number of plies = (a) 16, (b) 24, (c) 32

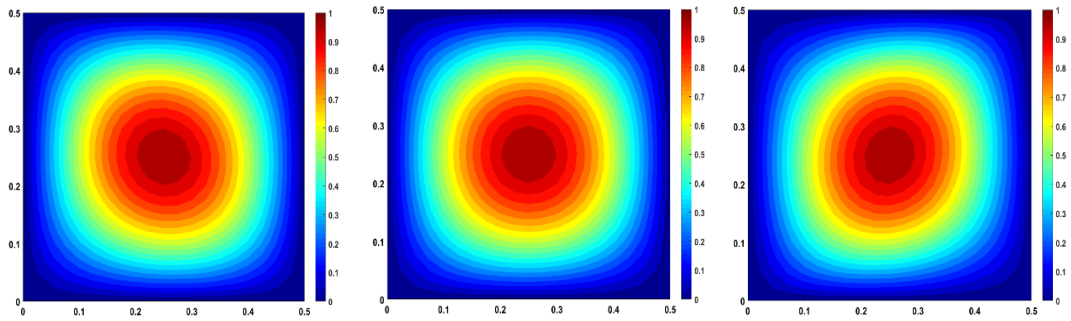

$\xi_3^D = 0.0$, $\frac{N_{xy}}{N_x} = 0.3$ $\xi_3^D = 0.4$, $\frac{N_{xy}}{N_x} = 0.3$ $\xi_3^D = 0.75$, $\frac{N_{xy}}{N_x} = 0.3$

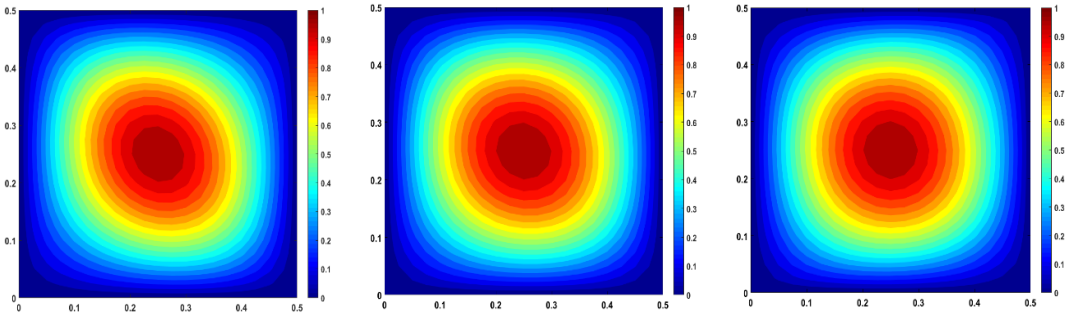

$\xi_3^D = 0.0$, $\frac{N_{xy}}{N_x} = 0.6$ $\xi_3^D = 0.4$, $\frac{N_{xy}}{N_x} = 0.6$ $\xi_3^D = 0.75$, $\frac{N_{xy}}{N_x} = 0.6$

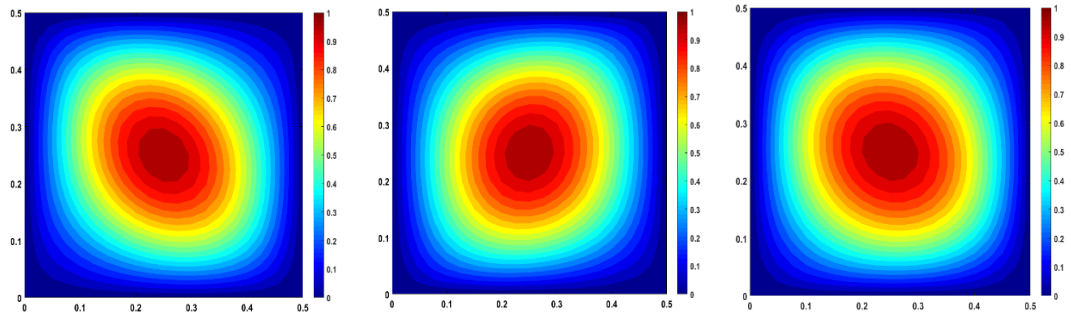

$\xi_3^D = 0.0$, $\frac{N_{xy}}{N_x} = 0.9$ $\xi_3^D = 0.4$, $\frac{N_{xy}}{N_x} = 0.9$ $\xi_3^D = 0.75$, $\frac{N_{xy}}{N_x} = 0.9$

Figure 5.9: Laminate mode shapes under combined loading with compression loading dominant , *a/b* =1.0

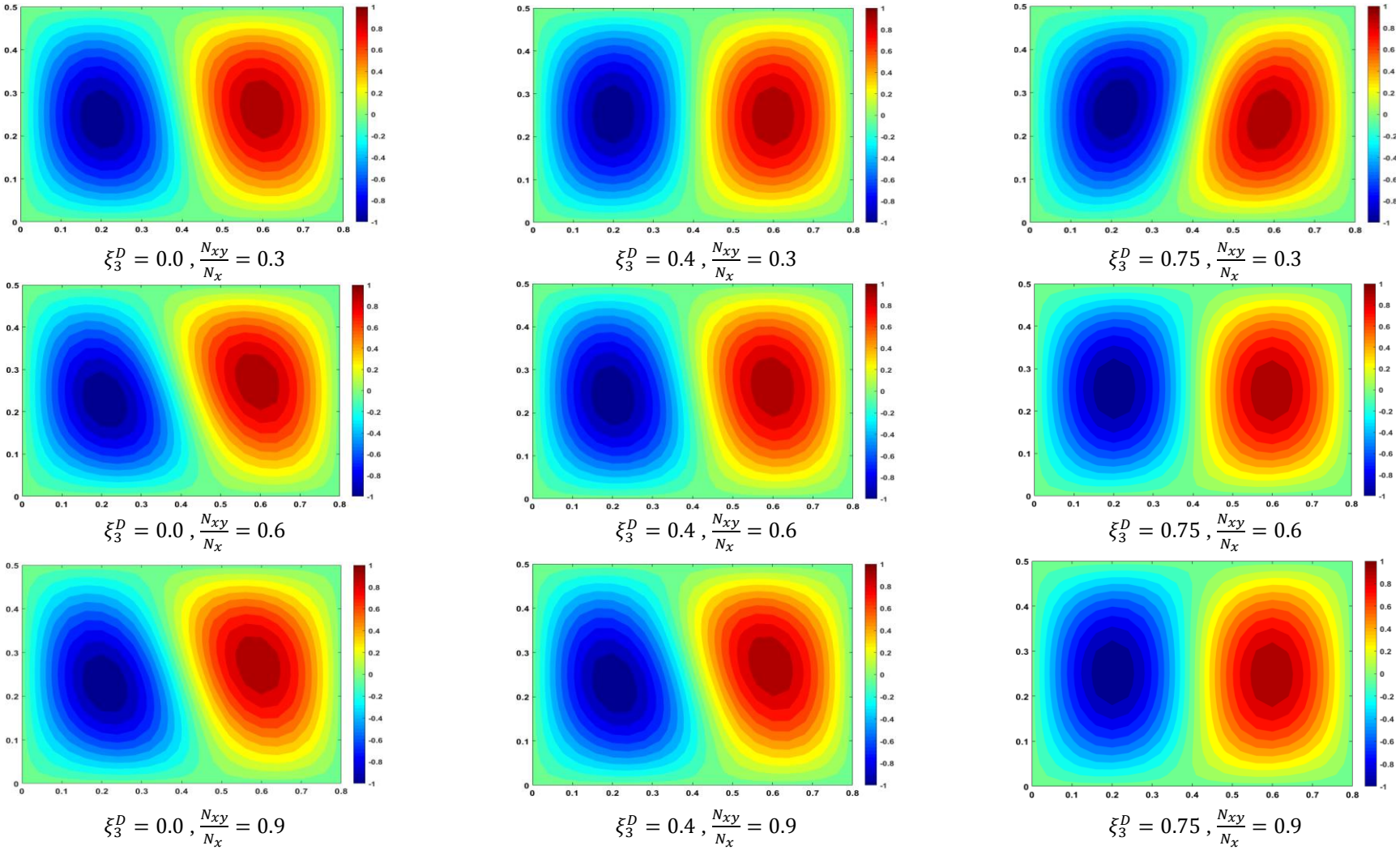

$\xi_3^D = 0.0$, $\frac{N_{xy}}{N_x} = 0.3$ | $\xi_3^D = 0.4$, $\frac{N_{xy}}{N_x} = 0.3$ | $\xi_3^D = 0.75$, $\frac{N_{xy}}{N_x} = 0.3$

$\xi_3^D = 0.0$, $\frac{N_{xy}}{N_x} = 0.6$ | $\xi_3^D = 0.4$, $\frac{N_{xy}}{N_x} = 0.6$ | $\xi_3^D = 0.75$, $\frac{N_{xy}}{N_x} = 0.6$

$\xi_3^D = 0.0$, $\frac{N_{xy}}{N_x} = 0.9$ | $\xi_3^D = 0.4$, $\frac{N_{xy}}{N_x} = 0.9$ | $\xi_3^D = 0.75$, $\frac{N_{xy}}{N_x} = 0.9$

Figure 5.10: Laminate mode shapes under combined loading with compression loading dominant, *a/b* =1.6

5.3.3 Combined in-plane loading (Shear load dominates)

In the case of shear load dominating, a constant shear load is applied as the main load (destabilising load) which causes the buckling, whilst increasing levels of compressive load (subcritical load) are applied simultaneously. Critical buckling loads are calculated using the VICON analysis in the VICONOPT software and presented in the form of the relationships between compression and shear loads for different levels of anisotropy. All of the results show that the buckling load is at its maximum when high levels of anisotropy are present and N_x=0. Therefore, all the results are normalised with respect to the bucking load when $\xi_3^D = 0.75 \; and \; \frac{N_x}{N_{xy}} = 0.0$.

Both square and rectangular laminates show the same trends which are that the critical buckling load decreases with increasing load ratio $\frac{N_x}{N_{xy}}$ however the effect of the bend twist coupling is still clear and can be noticed is the results. For example, composite plates with $\xi_3^D = 0.0$ have the lowest buckling loads and buckling capacity increases gradually as the value of ξ_3^D increases. The maximum load is obtained when the value of $\xi_3^D = 0.75$.

This can be explained by the fact that the skewing caused by the anisotropy works in opposition to the shear load skewing, increasing the buckling load. For a load ratio $\frac{N_x}{N_{xy}} = 0.2$ the buckling load increases from 0.598 to 0.760 when the value of ξ_3^D changes from 0.0 to 0.75 for square laminates with 16 plies, while it increases from 0.572 to 0.853 for rectangular plates under the same load ratio as shown in Figure 5.11a and 5.12a . Corresponding results for plates with 24 and 32 layers are shown in Figure 5.11b, 5.12b, 5.11c and 5.12c respectively clarifying the effect of the bend twist coupling on the buckling load. Mode shapes in the form of contour plots are presented in Figure 5.13 and 5.14.

It can be seen from the plots for the square plates that laminates with $\xi_3^D = 0.4$ show less skewing than laminates with $\xi_3^D = 0.0$ under the same load ratio. The same trends are repeated when the load ratio is increased to 0.9. In this case laminates with higher $\xi_3^D = 0.75$ show the least buckling mode skewing which explains why these plates have higher buckling load.

The rectangular plate's mode shapes demonstrate a similar relationship between the level of anisotropy and the amount of skewing with the latter reducing as the level of anisotropy increases. However, there are some important differences, most notably a change in mode shape as the load ratio increases. For example, in the case where $\xi_3^D = 0.0$, when the load ratio is relatively low, laminates buckle with one-half wavelength. However when the load ratio increases above 0.6 the mode changes to two half wavelengths. As the level of anisotropy increases, this transition occurs earlier i.e. at lower load ratios. For example, for laminates with lamination parameter $\xi_3^D = 0.4$ and $\xi_3^D = 0.75$ the transition between one and two buckles occurs at a load ratio of 0.3.

In general, both square and rectangular laminates show similar behaviour, when subjected to combined loading where shear is dominant. This is different from the previous case in which compression is dominant. Consequently, the effect of an isotropy is clearer for this case because the transverse skewing produced by the bend-twist coupling cancels part of the skewing effect caused by the applied shear in the opposite direction. This explains why the curve for $\xi_3^D = 0.75$ is the upper curve while the plate with $\xi_3^D = 0.0$ is the lower as shown in Figure 5.11 and 5.12.

(a)

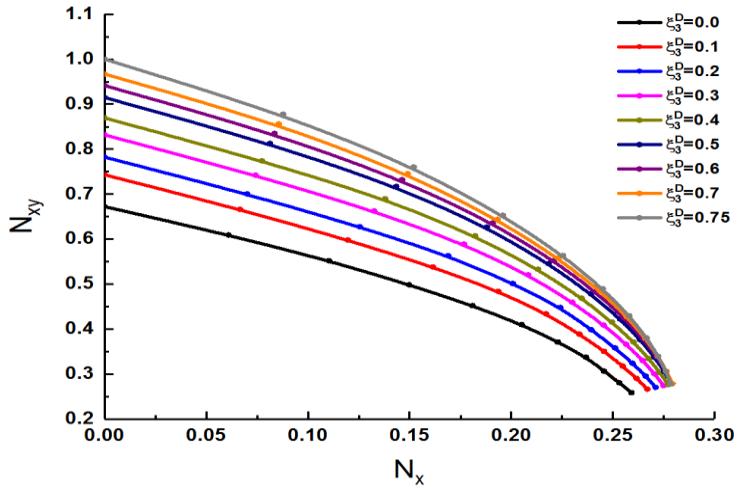

(b)

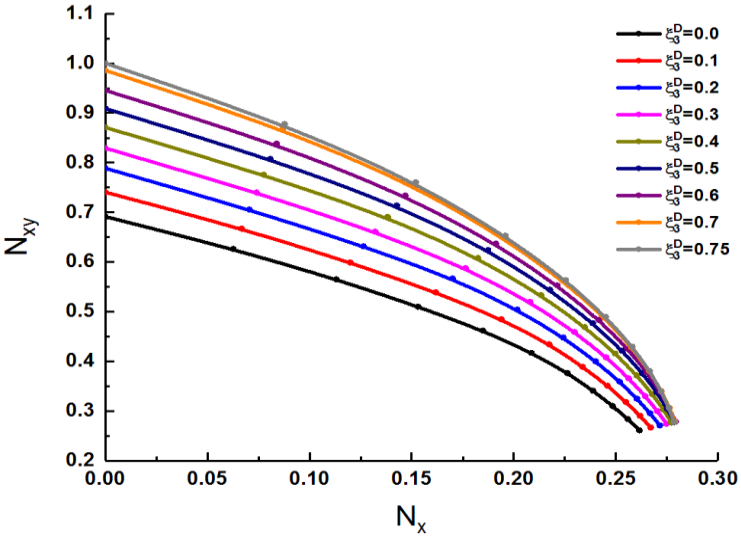

(c)

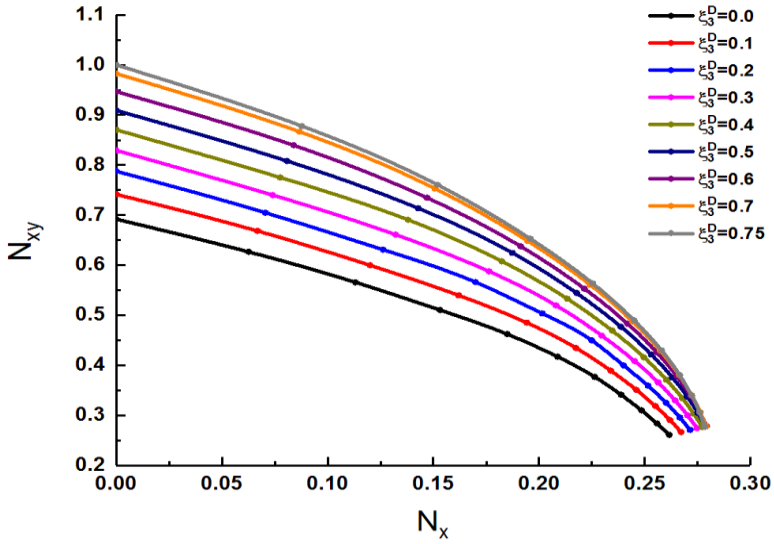

Figure 5.11: Normalised shear against compression relationships for laminates with *a/b* =1.0, Number of plies = (a) 16, (b) 24, (c) 32

(a)

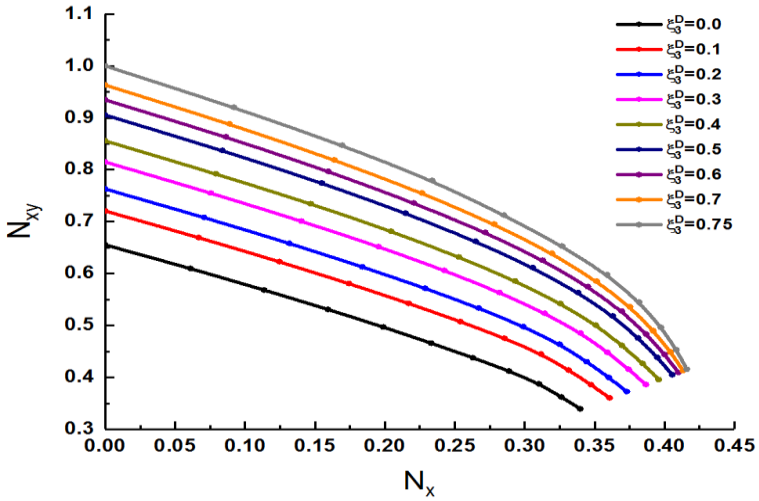

(b)

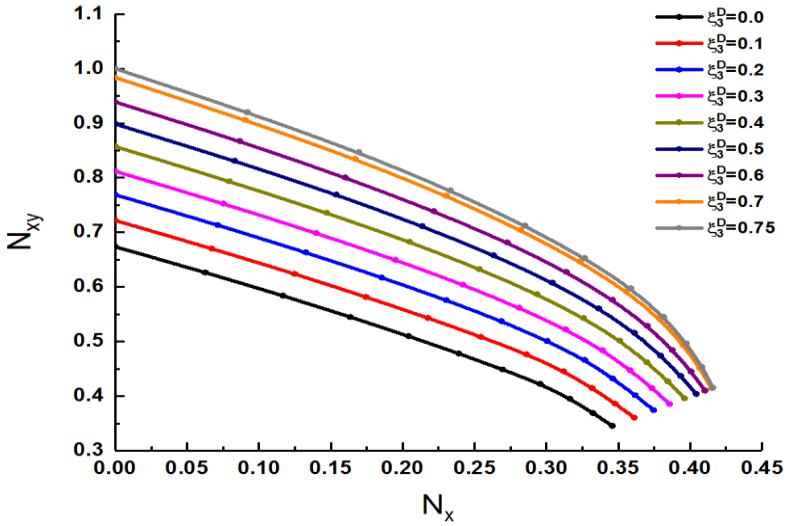

(c)

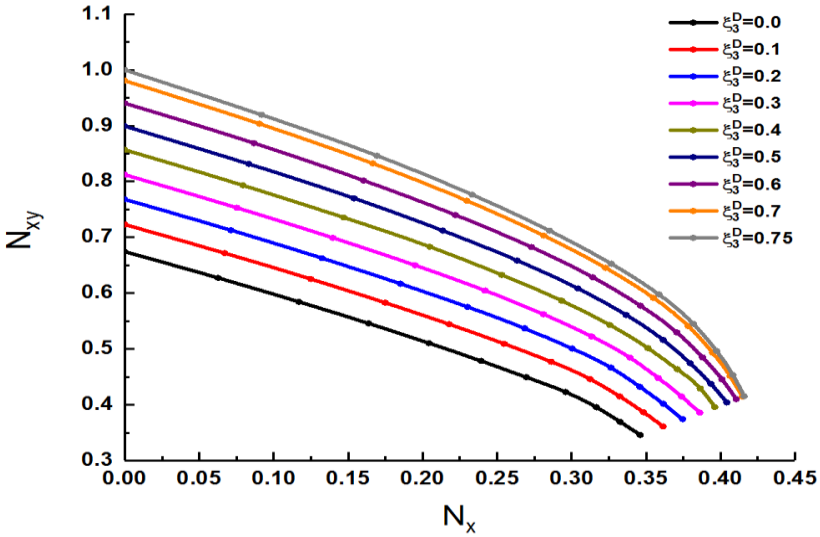

Figure 5.12: Normalised shear against compression relationships for laminates with *a/b* =1.6, Number of plies = (a) 16, (b) 24, (c) 32

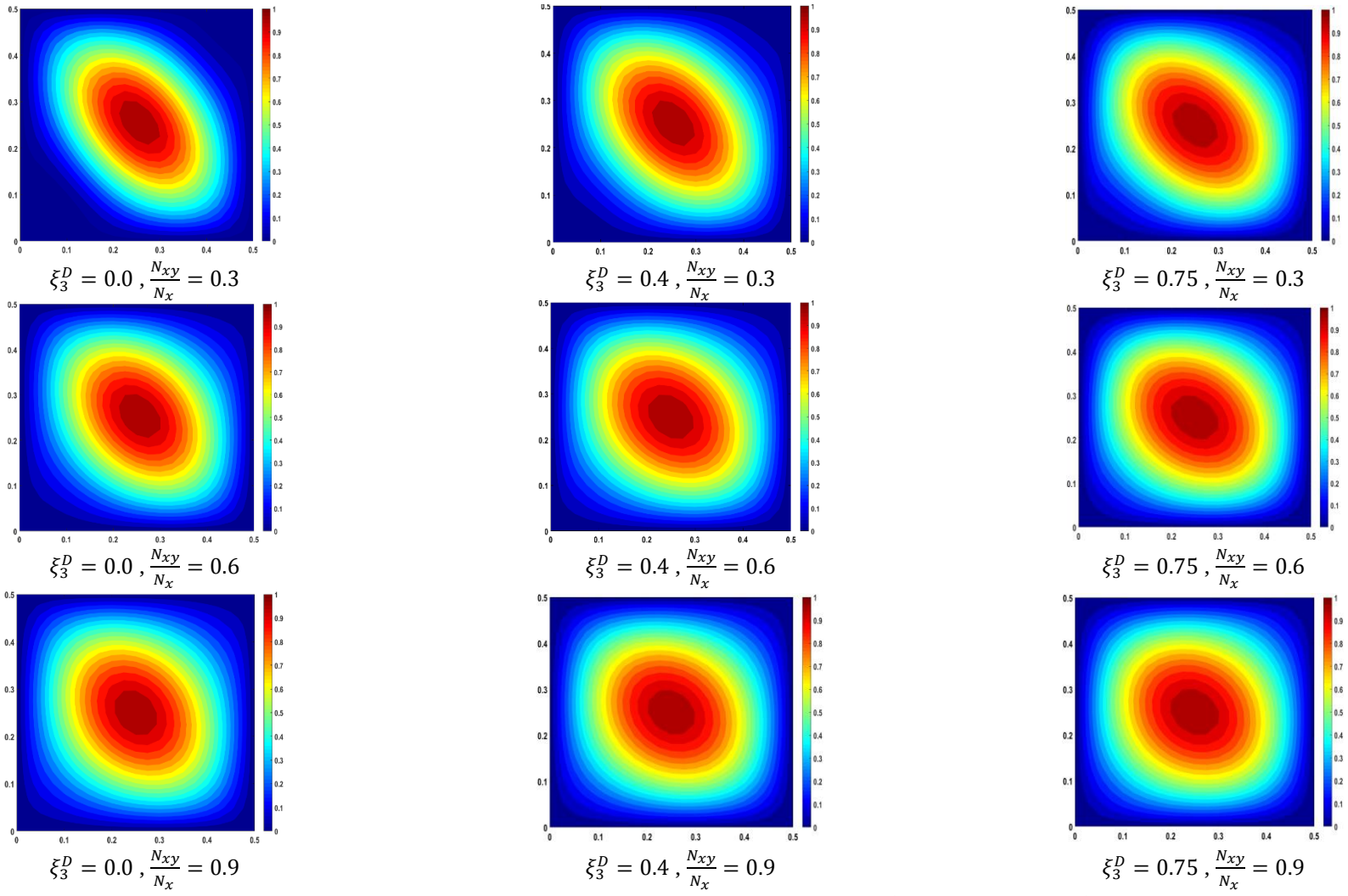

$\xi_3^D = 0.0$, $\frac{N_{xy}}{N_x} = 0.3$ | $\xi_3^D = 0.4$, $\frac{N_{xy}}{N_x} = 0.3$ | $\xi_3^D = 0.75$, $\frac{N_{xy}}{N_x} = 0.3$

$\xi_3^D = 0.0$, $\frac{N_{xy}}{N_x} = 0.6$ | $\xi_3^D = 0.4$, $\frac{N_{xy}}{N_x} = 0.6$ | $\xi_3^D = 0.75$, $\frac{N_{xy}}{N_x} = 0.6$

$\xi_3^D = 0.0$, $\frac{N_{xy}}{N_x} = 0.9$ | $\xi_3^D = 0.4$, $\frac{N_{xy}}{N_x} = 0.9$ | $\xi_3^D = 0.75$, $\frac{N_{xy}}{N_x} = 0.9$

Figure 5.13: Laminate mode shapes under combined loading (shear dominant), *a/b*=1.0

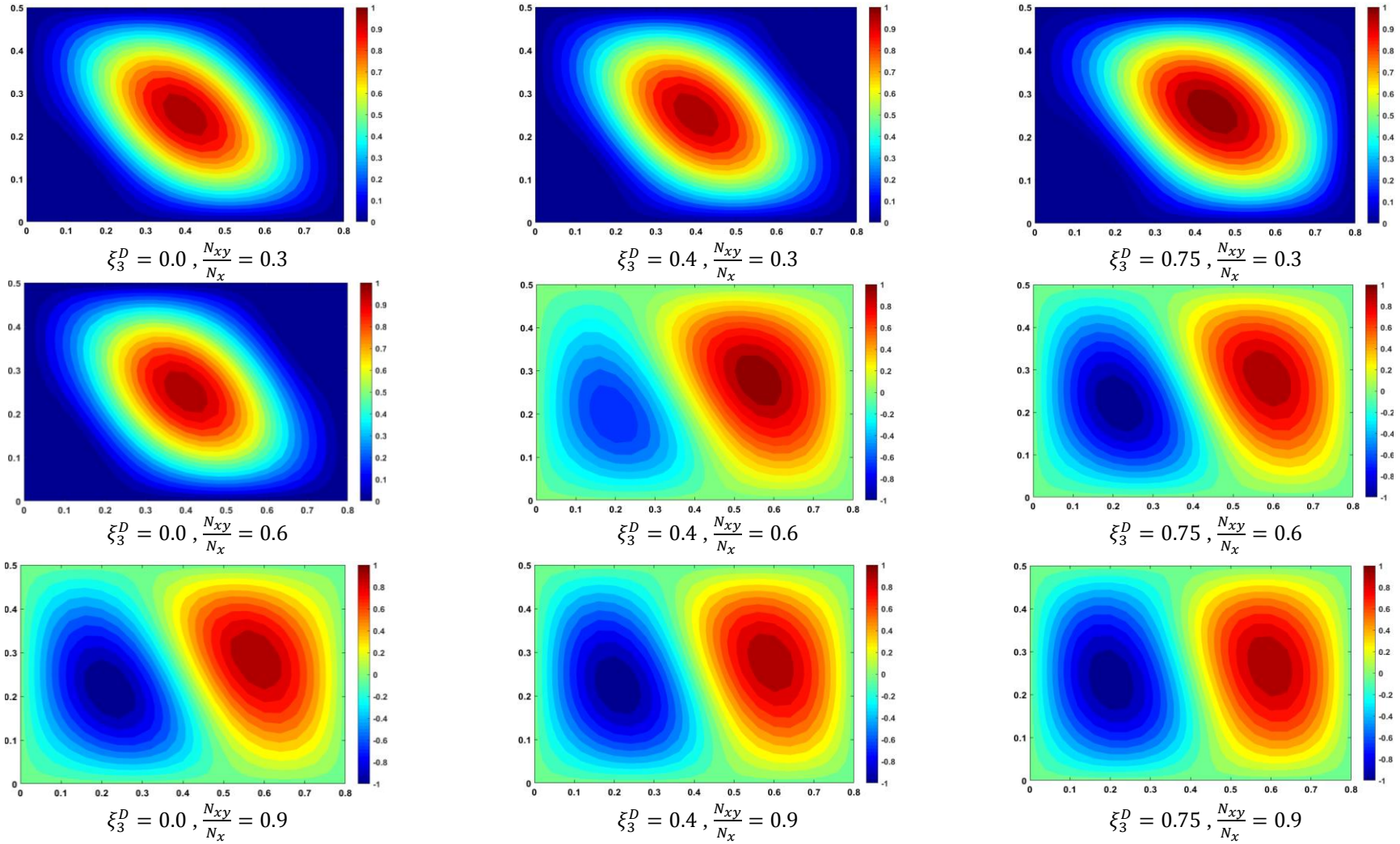

$\xi_3^D = 0.0$, $\frac{N_{xy}}{N_x} = 0.3$ | $\xi_3^D = 0.4$, $\frac{N_{xy}}{N_x} = 0.3$ | $\xi_3^D = 0.75$, $\frac{N_{xy}}{N_x} = 0.3$

$\xi_3^D = 0.0$, $\frac{N_{xy}}{N_x} = 0.6$ | $\xi_3^D = 0.4$, $\frac{N_{xy}}{N_x} = 0.6$ | $\xi_3^D = 0.75$, $\frac{N_{xy}}{N_x} = 0.6$

$\xi_3^D = 0.0$, $\frac{N_{xy}}{N_x} = 0.9$ | $\xi_3^D = 0.4$, $\frac{N_{xy}}{N_x} = 0.9$ | $\xi_3^D = 0.75$, $\frac{N_{xy}}{N_x} = 0.9$

Figure 5.14: Laminate mode shapes under combined loading (shear dominant), *a/b*=1.6

5.3.4 Pure shear loading

This section will examine the buckling response of composite laminates, with differing levels of bend-twist coupling (controlled by the lamination parameter ξ_3^D) subject to pure in plane shear. Under this type of loading anisotropy can have a significant effect on the buckling behaviour, which is dependent on the shear load direction. The results obtained for square laminates are presented here in two groups depending on this load direction.

The first group is subject to shear acting in the opposite direction to the anisotropic skewing effect. This leads to an increase in the bucking load factor from 0.6949 to 1.0 as the value of ξ_3^D is increased from 0.0 to 0.75 for composite plates consisting of 16 plies as shown in Figure 5.15a and from 0.6948 (0.6965) to 1.0 for laminates with 24(32) plies, see Figure 5.15b and 5.15c. This behaviour is completely reversed for the second group where the shear and the anisotropy act in the same direction leading to severe skewing in the buckling mode shape. Consequently the buckling load drop substantially from 1.0 to 0.4471 (0.4492, 0.4473) for laminates with 16 (24, 32) plies respectively based on VICON analysis. Finite element analysis results showed similar trends for both groups, although the results from the VICON analysis where slightly higher than the ABAQUS results due to the differences in the models mentioned previously. In ABAQUS the value of the buckling load factor was raised from 0.68798 (0.68741, 0.68705) for laminates with 16(24, 32) plies when the value of ξ_3^D was increased from 0.0 to 0.75 for the case where the load acts against the anisotropy effect. This trend is reversed completely when the shear load is applied in the opposite direction, when the load factor decreases significantly. Figure 5.15a, 5.15b and 5.15c show the details of the results.

The buckling loads for the first case (left y-axis) are normalised with respect to its maximum value when $\xi_3^D = 0.75$, whereas for the second group the results

(right y-axis) are normalised with respect to the critical buckling load for laminate when $\xi_3^D = 0.0$. Rectangular composite plates with aspect ratio 1.6 are shown to have approximately the same behaviour as square plates using both VICON and ABAQUS analyses. These results are displayed in terms of the relationship between the normalised buckling load and the lamination parameter ξ_3^D in Figure 5.16a, 5.16b and 5.16c with the shear load again applied in the same two directions, firstly in the opposite to the anisotropy effect and then the same. For the first load case, the buckling load increases significantly, when the bend twist coupling is higher, 31.2% when the value of ξ_3^D increases from 0.0 to 0.75 using finite element analysis and 32.3% in VICON analysis. This is again due to part of the effect of the shear strain being cancelled by the effect of the anisotropy, leading to a decrease in plate skewing. Conversely, the values of buckling load decreases by more than 50% when the laminate is subjected to the shear loading in the reverse direction due to the coupling effect of the shear load and the anisotropy, which causes substantial skewing, and hence a high reduction in the buckling load. The results for both square and rectangular laminates show the number of layers has only a slight effect on the buckling load values because composite plates with different thickness all showed the same behaviour under this load conditions.

Figure 5.17 and 5.18 shows the buckling modes for laminates with aspect ratios 1.0 and 1.6 respectively. In both cases, the plates buckles with one half-wave along the length in contrast to the other load conditions where the rectangular plates buckled with two half-wave lengths. Contour plots demonstrate the level of skewing with the irregular shape around the edges of the buckles being caused by the opposing effects of the shear strain due to the external load and the anisotropy.

(a)

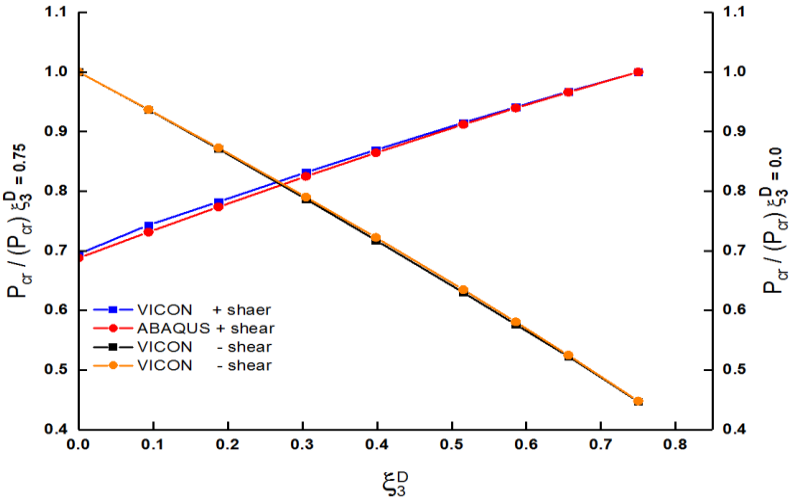

(b)

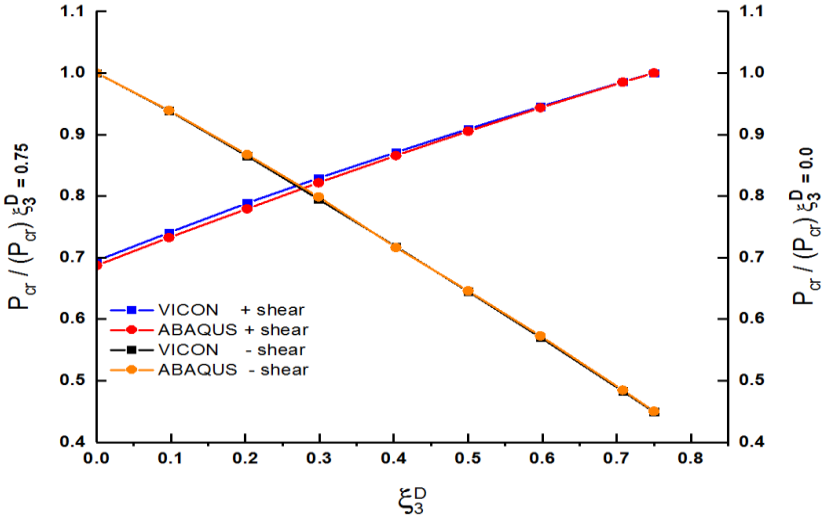

(c)

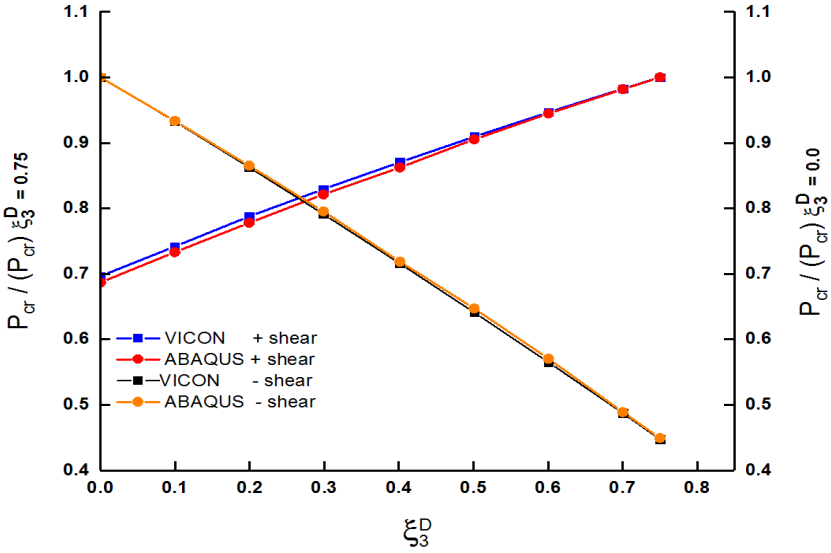

Figure 5.15: Load-anisotropy level relationship for laminates with *a/b* =1.0, Number of plies = (a) 16, (b) 24, (c) 32

(a)

(b)

(c)

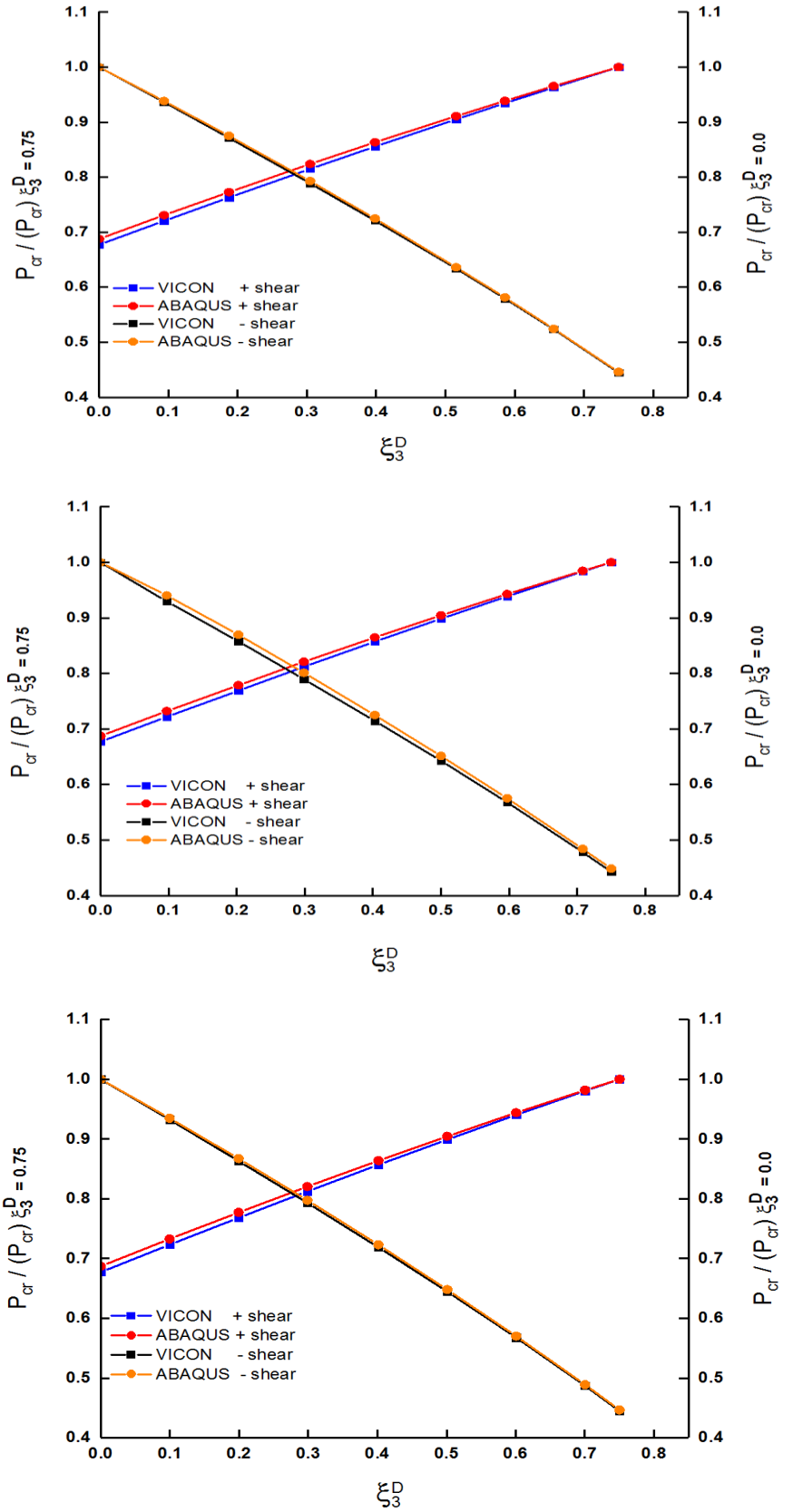

Figure 5.16: Load-anisotropy level relationship for laminates with *a/b* =1.6, Number of plies = (a) 16, (b) 24, (c) 32

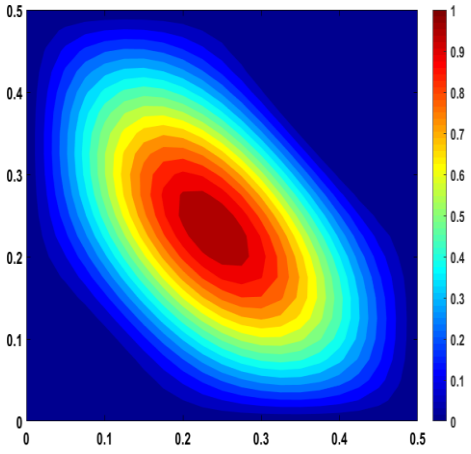

n = 16 , $\boldsymbol{\xi_3^D = 0.0}$ VICON

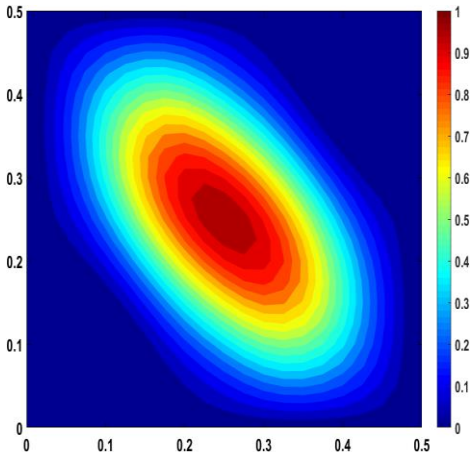

n = 16 , $\boldsymbol{\xi_3^D = 0.0}$ ABAQUS

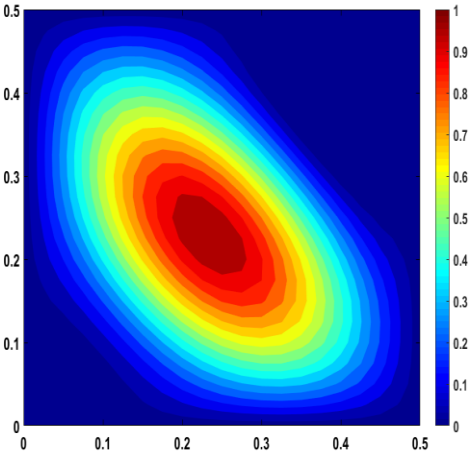

n = 16 , $\boldsymbol{\xi_3^D = 0.4}$ VICON

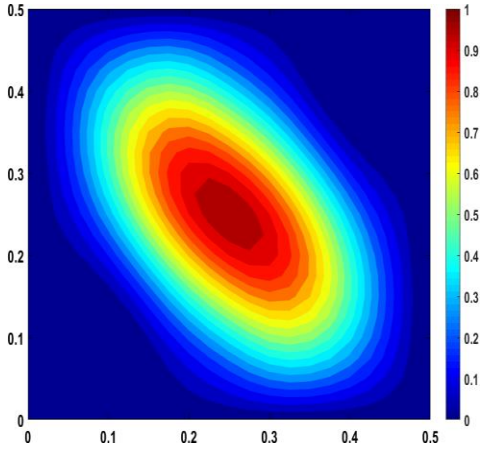

n = 16 , $\boldsymbol{\xi_3^D = 0.4}$ ABAQUS

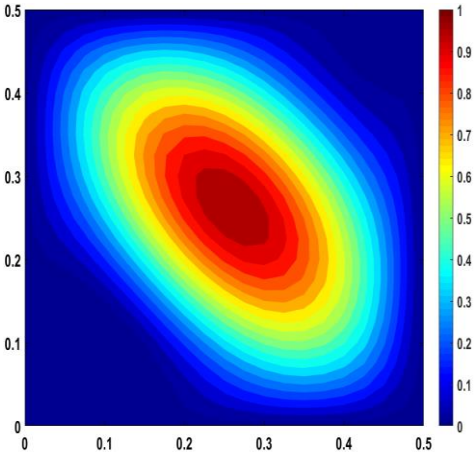

n = 16 , $\boldsymbol{\xi_3^D = 0.75}$ VICON

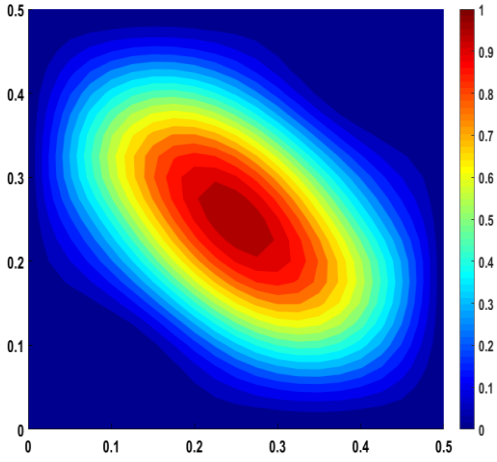

n = 16 , $\boldsymbol{\xi_3^D = 0.75}$ ABAQUS

Figure 5.17: Buckling modes for laminates with *a/b* =1.0

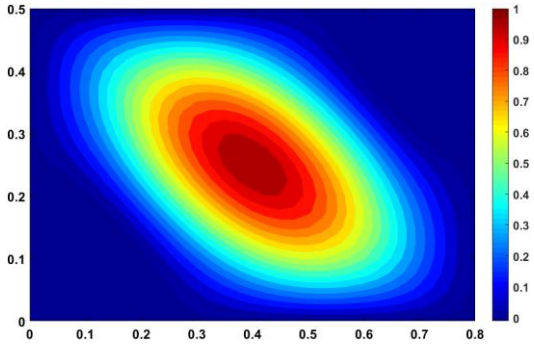

n = 16 , $\boldsymbol{\xi_3^D = 0.0}$ VICON

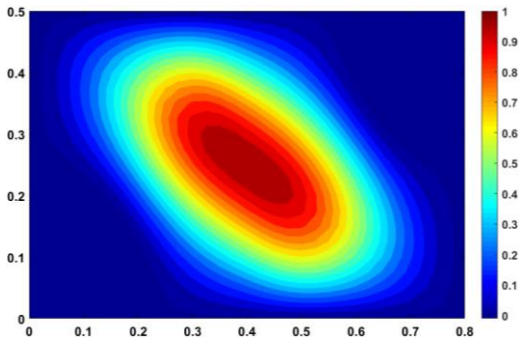

n = 16 , $\boldsymbol{\xi_3^D = 0.0}$ ABAQUS

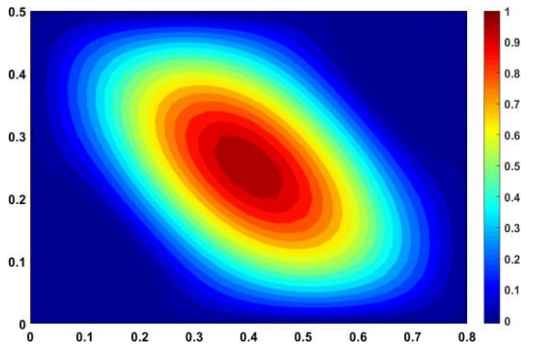

n = 16 , $\boldsymbol{\xi_3^D = 0.4}$ VICON

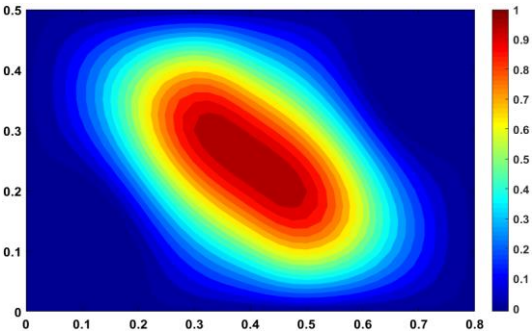

n = 16 , $\boldsymbol{\xi_3^D = 0.4}$ ABAQUS

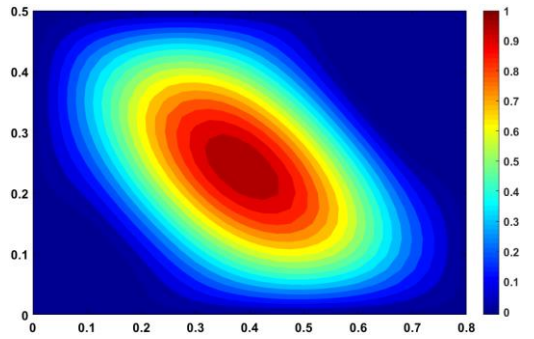

n = 16 , $\boldsymbol{\xi_3^D = 0.75}$ VICON

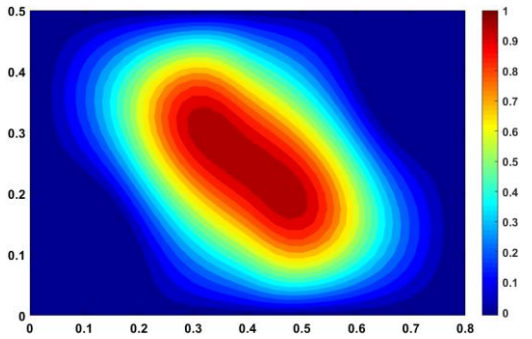

n = 16 , $\boldsymbol{\xi_3^D = 0.75}$ ABAQUS

Figure 5.18: Buckling modes for laminates with *a/b* =1.6

5.4 Chapter summary

Chapter 5 has presented the results of the parametric study outlined in Chapter 4 and carried out to determine relationships between the level of anisotropy (described using the lamination parameter ξ_3^D) and the buckling load of a series of composite plates under different load conditions in order to develop a set of design rules for optimising buckling behaviour. Contour plots of the buckling mode shapes have been used to demonstrate the effect that this anisotropy has on the skewing of the buckling modes. The main conclusions of this study can be summarised as:

- Plates subjected to uniaxial loads showed severe degradation in their buckling load factor with increases in ξ_3^D. Therefore, the use of laminates with $\xi_3^D = 0.0$ is recommended for these load conditions.
- For the laminates under combined in-plane loading (buckled because of the compression load), the best layup sequence is that for which $\xi_3^D = \frac{N_{xy}}{N_x}$, where $\frac{N_{xy}}{N_x}$ is the combined in-plane load ratio.
- In case of the composite plates under combined in plane loading shear and compression (where shear dominates), it is better to design the laminates with the maximum value of $\boldsymbol{\xi_3^D}$.
- When laminates are subjected to pure in plane shear load, the design of the layup sequence will depend on the direction of the applied load. In these cases, it is recommended to use laminates, which have the maximum value of $\boldsymbol{\xi_3^D}$ which produces an opposite skewing effect to the external load deformations.
- The laminates with different number of layers (16, 24, and 32) showed a similar trends under various in plane loading when using both VICONOPT and finite element method (ABAQUS).

Using these design rules, we can optimise the layup of a range of composite plates subject to differing load conditions using the process outlined by the flow chart in Figure 5.19.

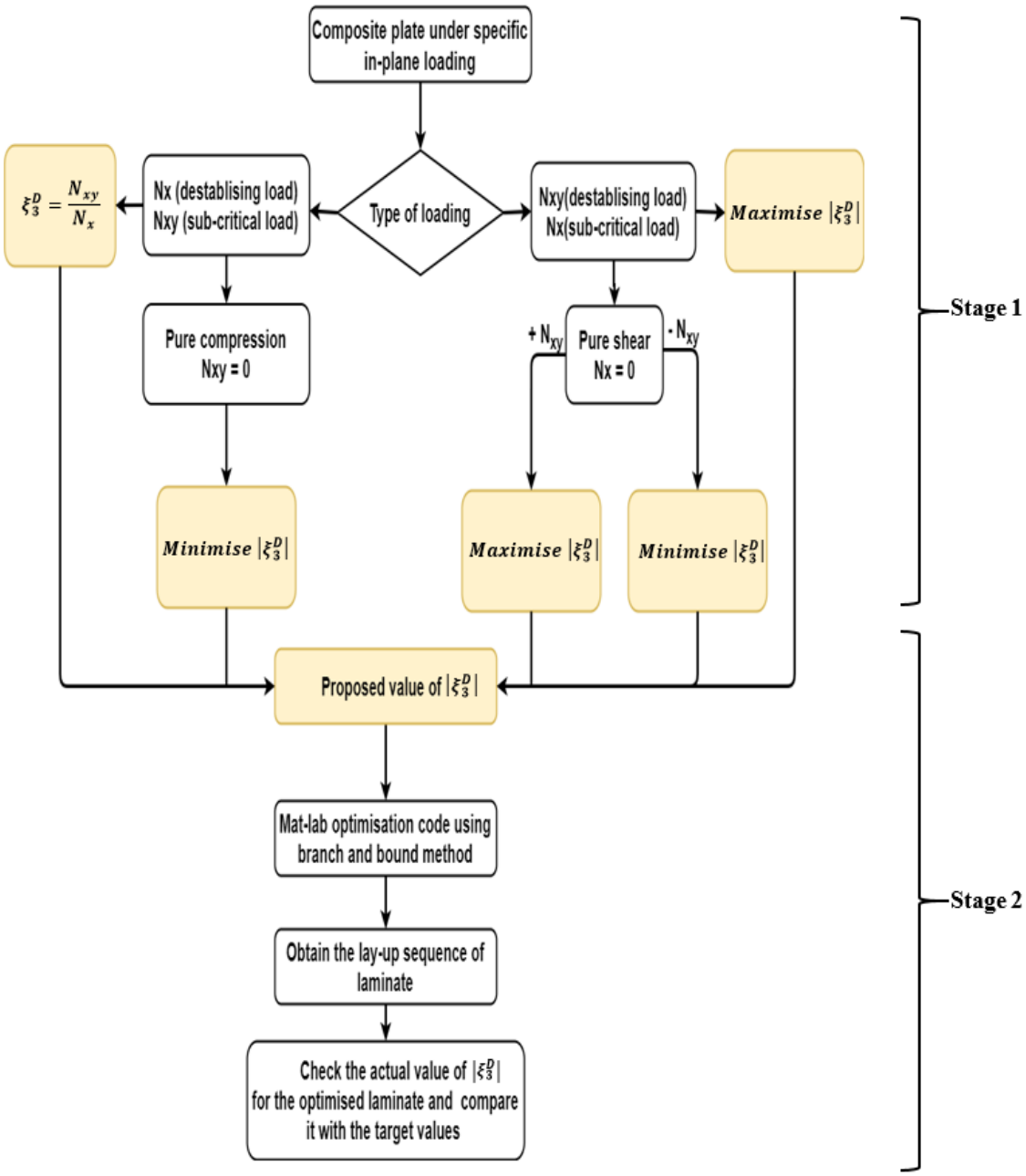

Figure 5.19: Optimisation procedure steps

Chapter 6: Mode Jumping in Thin-Walled Structures (Theoretical Approach)

6.1 Motivation

This chapter presents a theoretical investigation of the mode jumping phenomena in flat plates and stiffened panels. The study presents two suggested approaches to specify the jumping point between equilibrium paths utilising different proposals. The target of the investigation is to improve the post-buckling analysis in the exact strip analysis software VICONOPT by including the mode change in the post-buckling analysis. Consequently, the results will be more reliable and accurate in comparison to both experiments and other numerical methods. VICONOPT, as outlined previously, is a powerful software, which uses the exact stiffness method to calculate the natural frequencies and buckling load factors for different structural configurations, Figure 6.1.

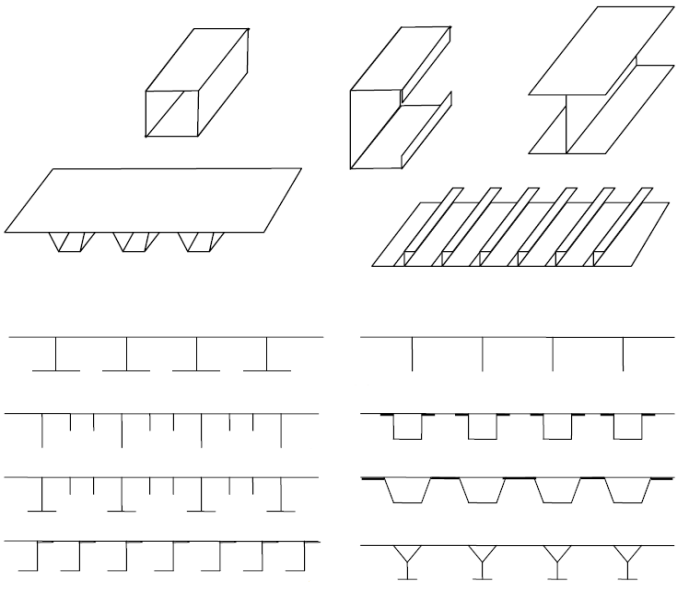

Figure 6.1: Range of prismatic plates assemblies to which VICONOPT applies

The exact strip methods VICONOPT provides a computationally efficient post-buckling analysis with substantial reduction in time and cost compared with other analysis methods such as finite element analysis. The post-buckling analysis uses the VIPASA [37] analysis option. Thus, the critical buckling mode shape retains the same sinusoidal shape in the length direction during the post-buckling analysis. This limitation will be overcome in this investigation, leading to more reliable and accurate results. The results will be compared with finite element analysis using the ABAQUS/CAE [156] program in order to validate and check the accuracy of the proposed solutions.

6.2 Mode jumping phenomenon

Mode jumping can occur as the buckling mode changes through the post-buckling region. This phenomenon occurs at any time and in some cases, it can happen violently and lead to panel failure. Previously in Chapter 3 (section 3.4), some factors were mentioned that affect the occurrence of mode changes such as boundary conditions, aspect ratio, load rates, initial imperfections and materials. When the initial buckling mode jumps to a new buckling configuration, the number of buckles (half wavelengths) over the plate length usually increases by one.

The position of this jump during the equilibrium path could occur early or late depending on the plate characteristics. Moreover, it is also affected by the gap between the sequential buckling loads. Before introducing the mechanism of how this phenomenon may occur, it is essential to start with a brief explanation about the reasons for such behaviour. After the plate or panel has initially buckled, the structure will move to a new equilibrium stage, which is called post-buckling.

In this case, the structure tries to adapt to the new equilibrium state due to large deformations and bending which leads to a decrease in the overall

stiffness. However, the initial post-buckling equilibrium path is still relatively stable so that plated structures can safely carry loads after initial buckling.

The post-buckling region can be divided into two main zones in term of the equilibrium state. The first is the region of geometrical non-linearity in which the source of nonlinear is large deformations, while the second is the region of material nonlinearity in which the material properties are modified to include the plastic properties. The work in this study will focus on the first post-buckling zone because the main aim is to improve VICONOPT post-buckling analysis by including mode jumping in the non-linear analysis. This software currently includes geometrical non-linear post-buckling analysis only. The main stages in the post-buckling analysis are shown below in Figure 6.2.

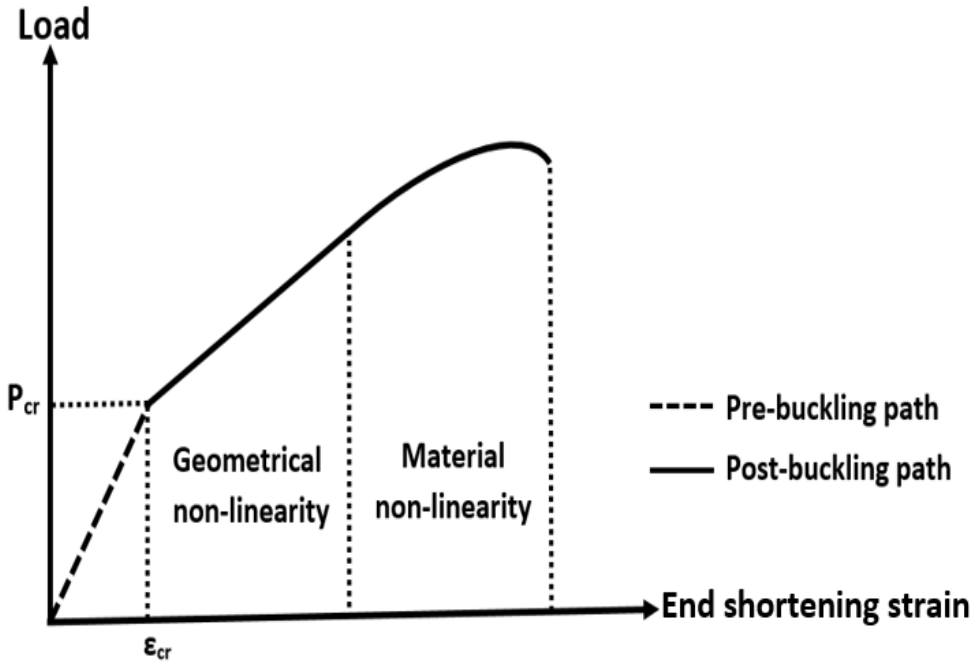

Figure 6.2: Pre-buckling and post-buckling behaviour explaining the nonlinear structural behaviour sources.

6.3 Mode jumping mechanism

When buckling first occurs, the structure starts to follow the most stable post-buckling path from many others depending on many factors such as edge boundary conditions, aspect ratio and initial imperfections. However, as the structure continues to carry more load, the deformations in the geometry gradually become large. Consequently, the initial post-buckling path becomes unstable. The structure tends to leave the current path and move to a more stable equilibrium path, which will lead to a possible jump from one post-buckling path to another.

According to the above explanation, the occurrence of mode jumping can lead us to divide the geometrical non-linear post-buckling equilibrium zone into two parts. The former is the initial post-buckling path, which has the initial critical buckling mode configuration. The post-buckling path remains relatively stable at this stage, see Figure 6.3.

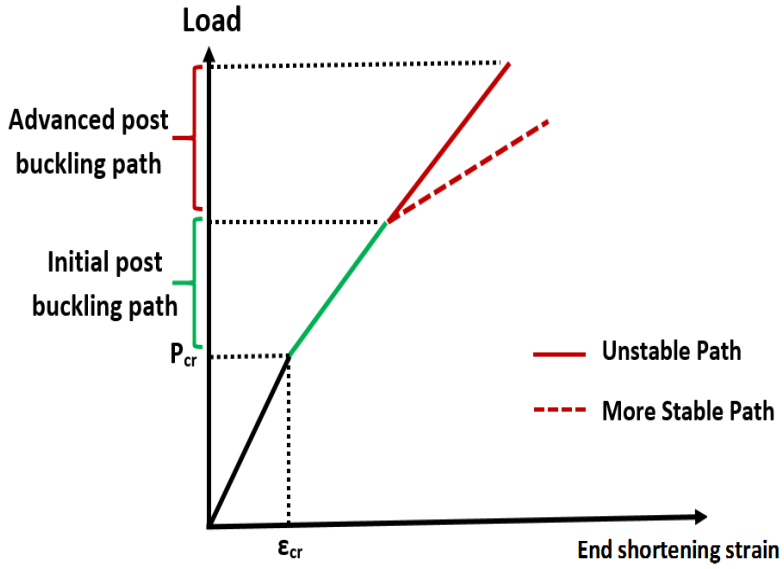

Figure 6.3: Load-end shortening curves which clarify the mode jumping mechanism in post-buckling analysis considering the virtual post-buckling stages.

Thus there is no expected jump in this part of the path. The latter is the advanced post-buckling equilibrium path, which becomes unstable due to the large deformations in the current mode. Hence, the jump from the initial buckling mode to others could occur at any time and these two stages can extend or shrink depending on many parameters like the aspect ratio, boundary conditions and the initial imperfections.

6.4 Mode jumping types

The jump from one buckling mode to another can occur in two different ways depending on the analysis or test techniques. The first is called the load jump, which may occur under a stress (or load) control test, while the second is the strain jump caused when the test is under strain (or displacement) control. To explain these two types of jumps in terms of the load-end shortening curve, a horizontal jump occurs when the structure jumps from one mode to another under the same load values, whereas a vertical jump will occur from one path to another at the same level of strain. Both jumping types are shown in Figure 6.4.

Therefore, if the jump occurs from point A to point B, it is a strain (displacement) jump. Otherwise, if it occurs from A to D it is a stress (load) jump. In some cases, especially when two equilibrium paths are close, the jump may occur in more smooth transitions. The current study will assume the strain jumping type to specify the jumping point and the value of jumping strain. The suggested theoretical techniques will be based on two well-known concepts in thin-walled structure theory, namely the effective width concept and the energy principle for different post-buckling equilibrium paths. The following sections will deal with proposed solutions to predict the jumping point (in terms of strains).

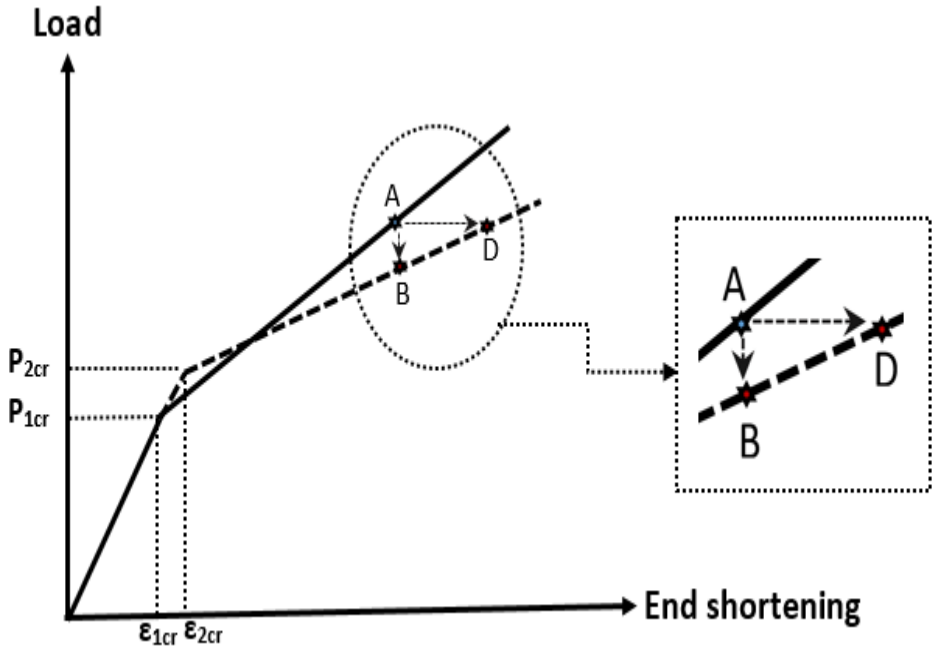

Figure 6.4: Mode jumping types:
stress (load) jumping: point A to D, strain (displacement) jump: point A to B

6.5 Effective width concept

It is essential to introduce the effective width concept before starting to explain the proposed solution approach which is based on it. In 1932, von Karman [15] published a theoretical study of a simply supported rectangular plate, in which a relationship for the effective width was developed. The effective width was simply defined as the virtual width of the buckled plate loaded edges, which is reduced due to the geometrical deformations. The assumption of this principle depends on load (stress) redistribution on two strips near the supported edges that carry the load applied beyond buckling, see Figure 6.5.

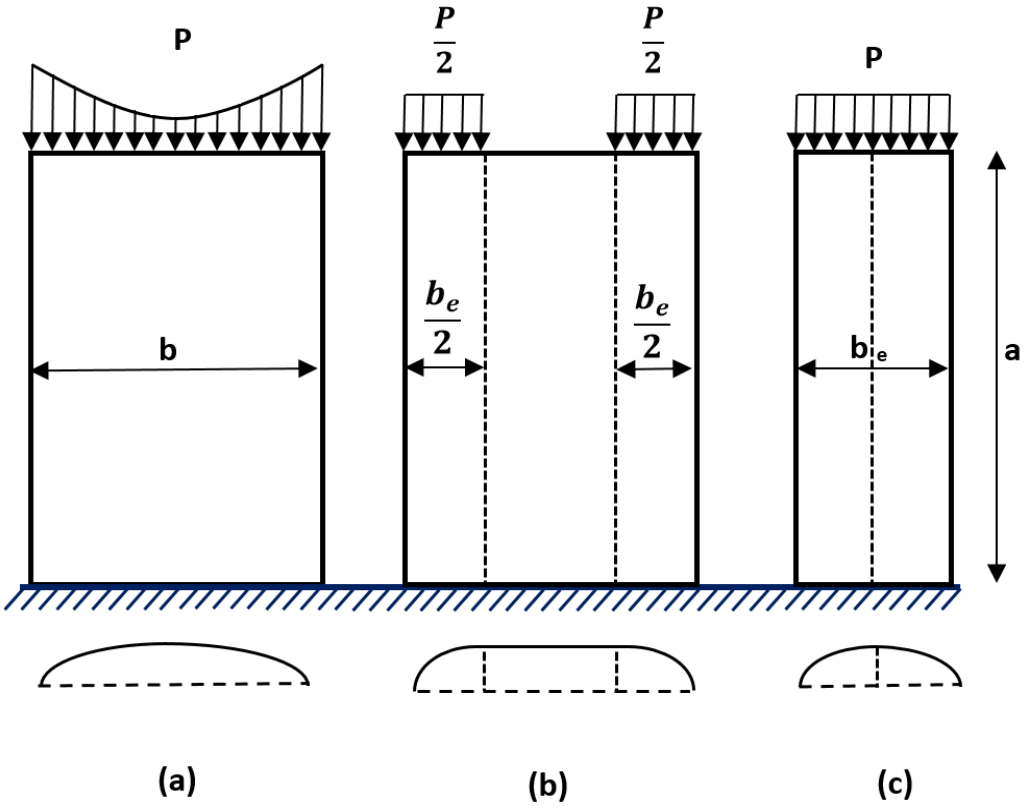

Figure 6.5: von Karman's effective width concept (a) non-uniform stress distribution after initial buckling, (b) stress redistribution according to effective width principle, (c) equivalent plate configuration.

Figure 6.5a shows the plate at the initial post-buckling stage, while the assumed loaded edge stress redistributions are represented in Figure 6.5b according to von Karman's effective width principle. The plate geometry consists of three strips, the middle strip that is assumed to carry zero load and two edge strips that carry an equal amount of load. Consequently, it is possible to represent the new configuration of the plate in the loaded parts (a x b_e) instead of the original dimensions (a x b) as shown in Figure 6.5c. This assumption is approximate because the middle strip still carries a load in the early post-buckling steps; however, that amount of load is relatively small when compared to the edge loads. Moreover, this amount will be decreased gradually as the deformation of the middle strip increases.

The principles of the effective width concept will be utilised in the next section to provide the value of jumping strain where the mode change may occur for flat isotropic and composite plates. The relationship between the original plate width and the effective width was first proposed by von Karman as:

$$\frac{b_e}{b} = \sqrt{\frac{\sigma_{cr}}{\sigma}} \tag{6.1}$$

The investigations that explored the effective width of buckled plates are followed by many studies to improve and produce an accurate approximation for the hypothetical width of plates subjected to uniform stress which will be summarised below.

6.5.1 Marguerre effective width equations

In 1937, Marguerre [171] studied the post-buckling behaviour of the buckled plate by incorporating the principle of minimum potential energy into von Karman's large deflection equations. He proposed the following boundary conditions:

- $w(y = 0, y = b) = w(x = 0, x = a) = 0$
- The edge moments to be zero, $\frac{\partial^2 w}{\partial y^2}(y = 0, y = b) = \frac{\partial^2 w}{\partial x^2}(x = 0, x = a) = 0$
- The edges are constrained to remain straight
- The longitudinal edges are free to expand as a straight line.
- The shear stress at the edge to be zero.

He then introduced approximations to calculate the effective width by the following two alternative equations:

$$\frac{b_e}{b} = 0.81\sqrt{\frac{\varepsilon_{cr}}{\varepsilon}} + 0.19 \tag{6.2}$$

$$\frac{b_e}{b} = \sqrt[3]{\frac{\varepsilon_{cr}}{\varepsilon}} \tag{6.3}$$

He recommended equation (6.3) as a better approximation to the exact formula under condition $1 \leq \frac{\varepsilon_{cr}}{\varepsilon} \leq 20$.

6.5.2 Winter effective width equations

After von Karman, some further studies provided a better accurate estimation for the effective width. Winter [172] added some modifications to von Karman effective width formula.

$$\frac{b_e}{b} = \sqrt{\frac{\sigma_{cr}}{\sigma}}\left(1 - 0.22\sqrt{\frac{\sigma_{cr}}{\sigma}}\right) \tag{6.4}$$

Also, he proposed in 1970 another formula, which he recommended for unstiffened elements.

$$\frac{b_e}{b} = 1.19\sqrt{\frac{\sigma_{cr}}{\sigma}}\left(1 - 0.298\sqrt{\frac{\sigma_{cr}}{\sigma}}\right) \tag{6.5}$$

6.5.3 Stein effective width equation

Stein is one of the researchers who proposed a solution for elastically buckled rectangular plates [76]. He expanded the displacement functions *u, v* and *w* in power series in terms of arbitrary parameters. He imposed the boundary conditions as below:

- w (0, y) = w (a, y) = w (x, 0) = w (x, b) = 0.
- The bending moments at all edges were equal to zero.
- $\partial u/\partial y\ (0,\mathrm{y}) = \partial u/\partial y\ (\mathrm{a},\mathrm{y}) = \partial v/\partial x(\mathrm{x},0) = \partial v/\partial x(\mathrm{x},\mathrm{b}) = 0.$
- $\partial v/\partial x(0,\mathrm{y}) = \partial v/\partial x\ (\mathrm{a},\mathrm{y}) = \partial u/\partial y(\mathrm{x},0) = \partial u/\partial y(\mathrm{x},\mathrm{b}) = 0.$
- $\int_0^a \sigma_y\ (x,0) = \int_0^a \sigma_y\ (x,b) = 0.$

The solution suggests the following calculation to evaluate the effective width:

$$\frac{b_e}{b} = \frac{\frac{\sigma}{\sigma_{cr}}}{\frac{\sigma}{\sigma_{cr}} + J^2\,\frac{\beta^2}{2} + J^4\, w_3\, \beta^2} \tag{6.6}$$

$$J^2 = \frac{\beta^2\,\frac{P\,b}{D\pi^2} - (\,\beta^2 + n^2\,)^2}{(\beta^4 + n^4)} \tag{6.7}$$

$$\beta = \frac{m\,b}{a} \tag{6.8}$$

$$w_3 = \frac{3}{2}\,\frac{\beta^4\, w_{13}^{(3)} + n^4\, w_{31}^{(3)}}{\beta^4 + n^4} \tag{6.9}$$

$$w_{13}^{(3)} = \frac{n^4}{(\beta^2 + 9n^2)^2 - (\beta^2 + n^2)^2} \tag{6.10}$$

$$w_{13}^{(3)} = \frac{n^4}{(\beta^2 + 9n^2)^2 - (\beta^2 + n^2)^2} \tag{6.11}$$

6.5.4 Koiter effective width equation

Koiter was one of the pioneer researchers who introduced an effective width solution for infinitely long, initially flat elastic plate [173]. He utilised the principle of total strain energy in his calculations. He assumed the following boundary conditions for his model:

- The longitudinal edges are constrained to remain straight $\frac{\partial v}{\partial x}(\mathrm{x}, 0) = \frac{\partial v}{\partial x}(\mathrm{x}, \mathrm{b}) = 0$.
- $\int_0^{\ell} \sigma_y\,(x, 0) = \int_0^{\ell} \sigma_y\,(x, b) = 0$. where is the length of longitudinal of half wave the buckling mode.

The effective width according to Koiter's solution can be calculated from the following equation when $1 \leq \frac{\varepsilon_{cr}}{\varepsilon} \leq 100$:

$$\frac{b_e}{b} = 1.2\left(\frac{\varepsilon_{cr}}{\varepsilon}\right)^{0.4} - 0.65\left(\frac{\varepsilon_{cr}}{\varepsilon}\right)^{0.8} + 0.45\left(\frac{\varepsilon_{cr}}{\varepsilon}\right)^{1.2} \quad (6.12)$$

Some other researchers suggested formulas to predict the value of effective width more accurately which will be summarised in the next section.

6.5.5 Other effective width equations

Cox [64] assumed that no transverse load or shear acts on the plates and the longitudinal plate edges are not forced to remain straight.

$$\frac{b_e}{b} = 0.8\left(\frac{\varepsilon_{cr}}{\varepsilon}\right) + 0.9 \quad (6.13)$$

Bengston [174] imposed a constant axial strain condition at the longitudinal edges, and used the total potential energy of the assumed displacement functions:

$$\frac{b_e}{b} = 0.483 + 0.517\left(\frac{\varepsilon_{cr}}{\varepsilon}\right) \qquad when \quad \frac{\varepsilon_{cr}}{\varepsilon} \leq 9 \quad (6.14)$$

$$\frac{b_e}{b} = \left[0.483 + 0.517\left(\frac{\varepsilon_{cr}}{\varepsilon} - 9\right)\right]\left[0.483 + 0.517\left(\frac{\varepsilon_{cr}}{\varepsilon}\right)\right] for \ \frac{\varepsilon_{cr}}{\varepsilon} > 9 \quad (6.15)$$

From the above, it is seen that many equations can be used to calculate the value of the effective width for buckled plates as a function of the original width of the plate at the pre-buckling stage.

6.6 Effective width approach (E. W.)

6.6.1 Solution assumptions

The main motivation of this approach as mentioned previously is to find the value of strain where the mode jump may occur. Although this approach includes some approximated calculations and assumptions, it still provides an acceptable fast technique and sufficient accuracy to predict the jumping strain when examined for different plate aspect ratios.

When the plate is subjected to axial compression and with the first sign of buckling, the plate will be deformed, and these deformations are considered to obey the large deformation theory. Consequently, stress redistribution will occur. The plate is divided into a middle strip (M.S.) and two similar edge strips (E.S.), if the two longitudinal edges have the same boundary conditions. The effective width principle assumes that the edge strips carry the load after buckling. This approach outlines that the dimensions of the middle and edge strips will be changed as the applied load increases due to deflection increases across the plate. Hence, the plate will consist of the unloaded middle strip (M.S.), and two edge strips (E.S.) loaded and will behave sequentially as shown in Figure 6.6. The edge strips will carry the same load if the original boundary conditions of the longitudinal are the same. The dimensions of the middle strip are (b-be) x a while those of the edge strips are (b_e x a).

The value of b_e will reduce gradually on progressing through the post-buckling region. This assumption will be the main basis of the effective width approach to predict the mode jumping point. First, the plate is assumed to have new configurations, and then new suggested boundary conditions are applied.

The investigation will focus on the two edge strips Figure 6.7a, because they are the parts that carry the loads. The edge strips are assumed to have a boundary condition that is partially free where they connect with the middle strip, and all other edges are simply supported as shown in Figure 6.7b.

These boundary conditions for the edge strips are explained in detail in Figure 6.7c, in which the free edge is assumed to have zero rotation because it is still connected to the middle strip. Therefore, the edge deflection is free but there are no rotations about the longitudinal axis. The other three edges of the E.S. remain the same as the initial boundary conditions of the plate which were simply supported conditions.

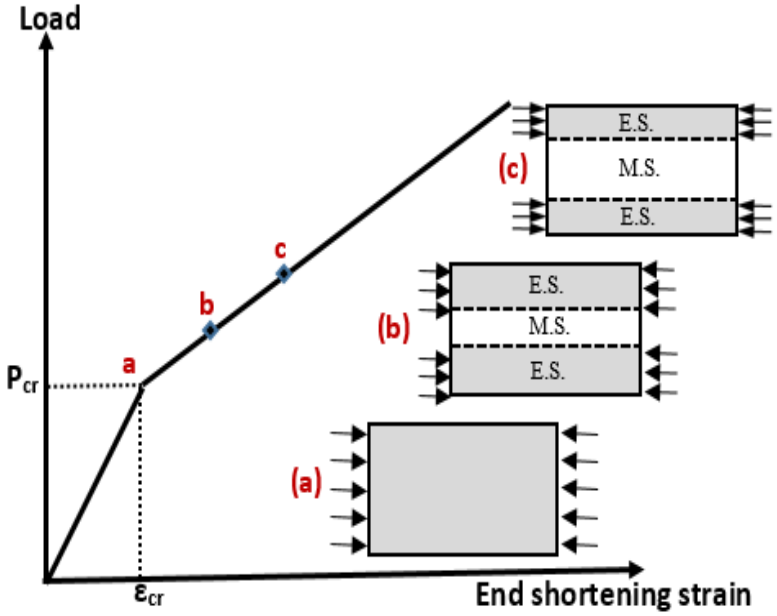

Figure 6.6: Load redistribution in post-buckling analysis of plated structures according to the effective width principle

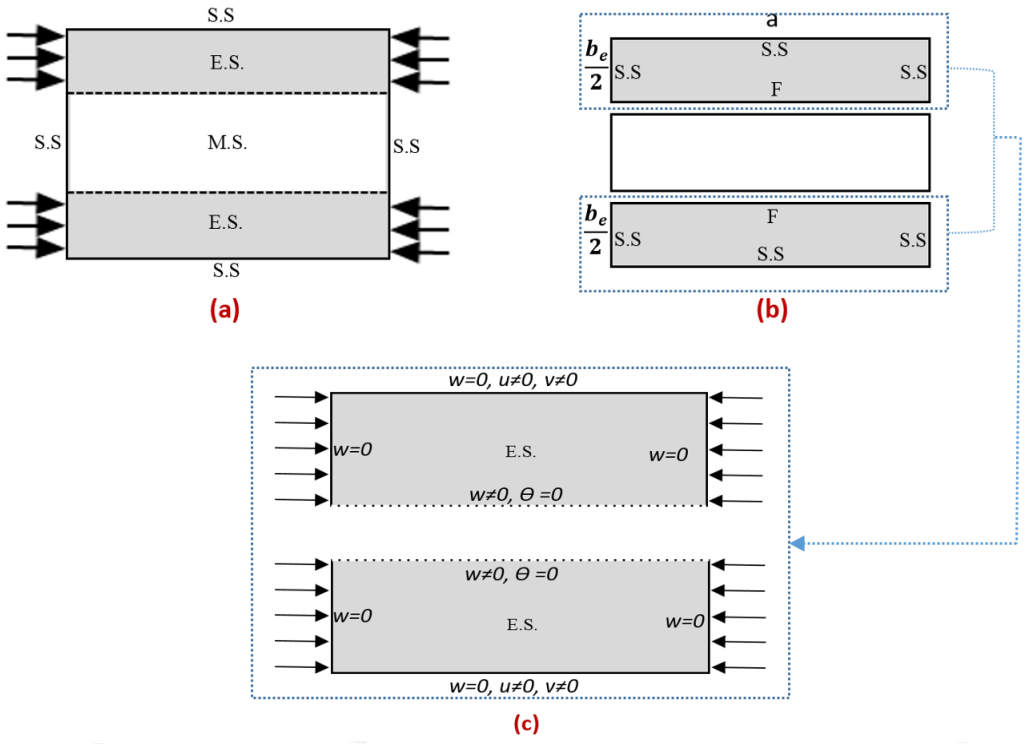

Figure 6.7: Effective width approach hypothesis, a) load distributions, b) edge strip boundary conditions, c) boundary conditions details.

6.6.2 Mathematical formulations

The mathematical expressions of (E. W.) will be derived in this section. The first step of the buckling problem is to assume an out of plane displacement function, which represents the key that will lead to calculating the buckling load of the thin plates.

The plate in this problem will be a flat plate representing one of the edge strips and which has the following boundary conditions.

- Three simply supported edges with w=0, u≠0, v≠0
- Partially free edge with w≠0, θ=0.

The plate is under uniaxial load in the x-direction and the deflection function that satisfies these boundary conditions is assumed to be:

$$w(x,y) = w_0 \frac{y}{2b} (3b^2 - y^2) \sin\frac{m\pi}{a} x \tag{6.16}$$

For isotropic plates equation 6.16 is substituted into the buckling equation

$$\left(\frac{\partial^4 w}{\partial x^4} + 2 \frac{\partial^4 w}{\partial x^2 \partial y^2} + \frac{\partial^4 w}{\partial y^4} \right) = \frac{P}{D} \tag{6.17}$$

where

$$D = \frac{E h^3}{12(1-\vartheta^2)} \tag{6.18}$$

$$P = N_x \frac{\partial^2 w}{\partial x^2} \tag{6.19}$$

Then the minimum energy principle is applied by the following equations to calculate the buckling load.

$$\Delta T = \Delta U \tag{6.20}$$

ΔT is the work done by the external forces and is given by:

$$T = -\frac{1}{2}\int_0^a \int_0^b \left\{ N_x \left(\frac{\partial^2 w}{\partial x^2}\right)^2 + 2N_{xy}\left(\frac{\partial w}{\partial x}\frac{\partial w}{\partial y}\right) + N_y \left(\frac{\partial^2 w}{\partial y^2}\right)^2 \right\} dx\, dy \tag{6.21}$$

whereas ΔU is the strain energy of bending and is given by the equation

$$\Delta U = \frac{D}{2}\int_0^a \int_0^b \left\{ \left(\frac{\partial^2 w}{\partial x^2} + \frac{\partial^2 w}{\partial y^2}\right)^2 - 2(1-v)\left[\frac{\partial^2 w}{\partial x^2}\frac{\partial^2 w}{\partial y^2} - \left(\frac{\partial w}{\partial x \partial y}\right)\right] \right\} dx\, dy \tag{6.22}$$

Substituting equations (6.21) and (6.22) into equation (6.20) with $N_y = N_{xy} = 0$ (because there is no transverse or shear load), the critical buckling load is given by:

$$N_x = D\left[\frac{m^2\pi^2}{a^2} + \frac{105\,a^2}{17m^2\pi^2 b^4} + \frac{84}{17b^2}\right] \tag{6.23}$$

The same procedure has been performed for composite plates, and the final equation used to calculate the buckling load for the laminates was:

$$N_x = \frac{1}{b^2}\left[\frac{m^2\pi^2 b^2}{a^2}D_{11} + \frac{105\,a^2}{17m^2\pi^2 b^2}D_{22} + \frac{84}{17}D_{12} + \frac{168}{17}D_{66}\right] \tag{6.24}$$

where m is the number of half-waves through the length. Equations (6.23) and (6.24) are considered in calculations and applied for both isotropic and composite plates, and their derivations are presented in Appendix A.

6.6.3 Validation of equations

To validate the buckling load calculated in the previous section, examples of isotropic plates are considered to check equation (6.23) and laminates for equation (6.24). The plate mechanical properties used are E_{11}= 161 GPa, υ = 0.3 with density = 2300 kg/m^3 for the metal plates while they were E_{11}= 181 GPa, E_{12}= 10.3 GPa, G_{12}= G_{13}= G_{23}=7.17 GPa, υ_{12} = 0.28 for the laminates.

The laminates have three different lay-up sequences: [45 -45 -45 45 -45 45 45 -45]s, [45 -45 0 90 -45 45 90 0]s and [45 -45 -45 45 0 90 90 0]s. The dimensions are a = n x 300 mm where n = 1, 1.2, 1.4, 1.6 …, b = 300 mm, t = 1.5 mm for the isotropic plates and t = 2 mm for the laminates. The finite element model has

similar boundary conditions, to those assumed in the equation derivation. S4R shell elements are used with element size 10 mm, and a linear perturbation-buckle step is used to find the buckling load for the first five modes. The model was under shell edge loading type, which is applied in the x-direction as shown in Figure 6.8.

A comparison between the equation and ABAQUS results was made for different number of half waves *m* and they are presented as a relationship between the buckling load and the aspect ratio. The results for isotropic plates showed excellent agreement between the buckling load calculated by equation (6.23) and finite element analysis, as shown in Figure 6.9.

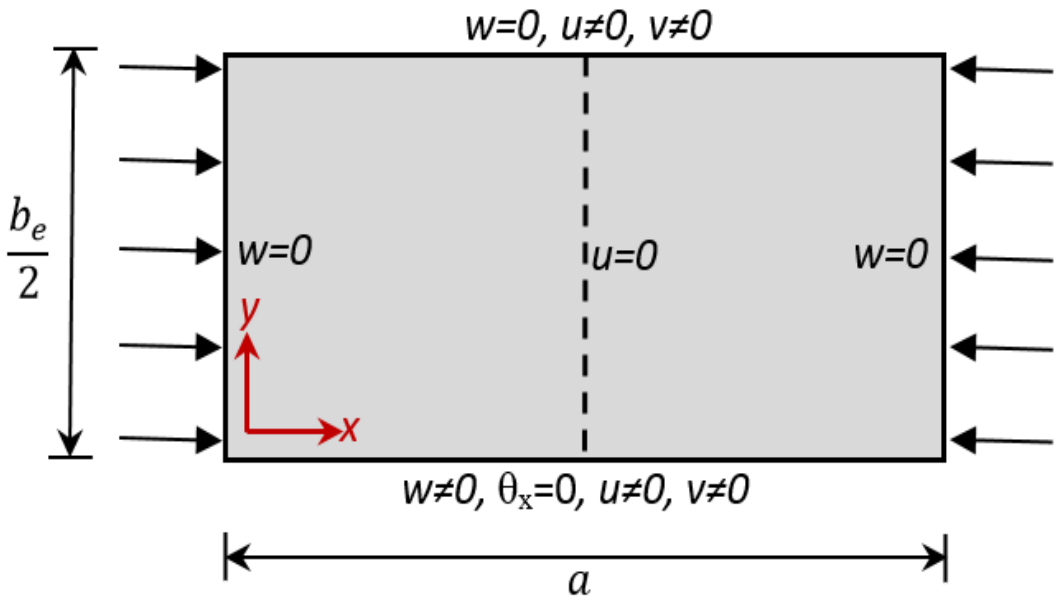

Figure 6.8: ABAQUS model boundary conditions

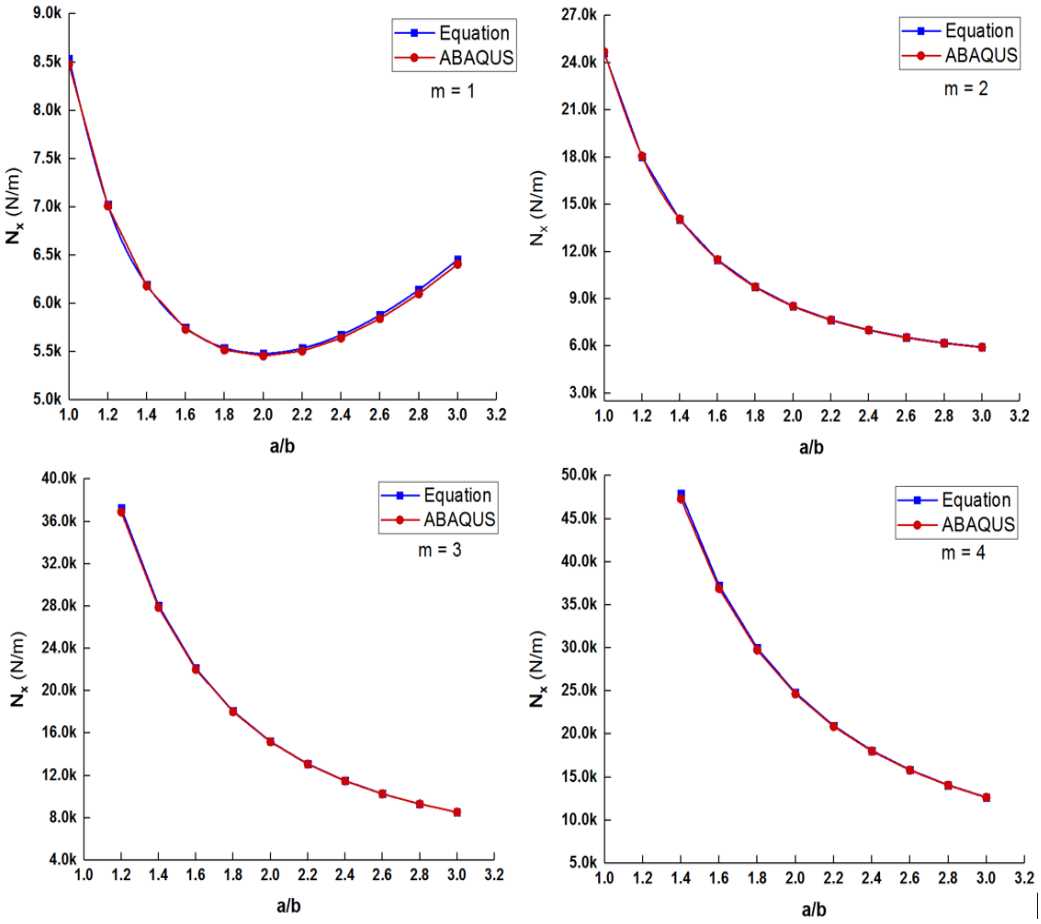

Figure 6.9: Equation (6.23) vs FE model comparison for isotropic plate

The first composite plate with lay-up sequence [45 -45 -45 45 -45 45 45 -45]s showed a good agreement with ABAQUS results. Equation (6.24) results showed a slightly higher buckling load when the plate buckled with one-half wave. However, the difference is small, and it did not appear for the higher values of *m* as shown in Figure 6.10.

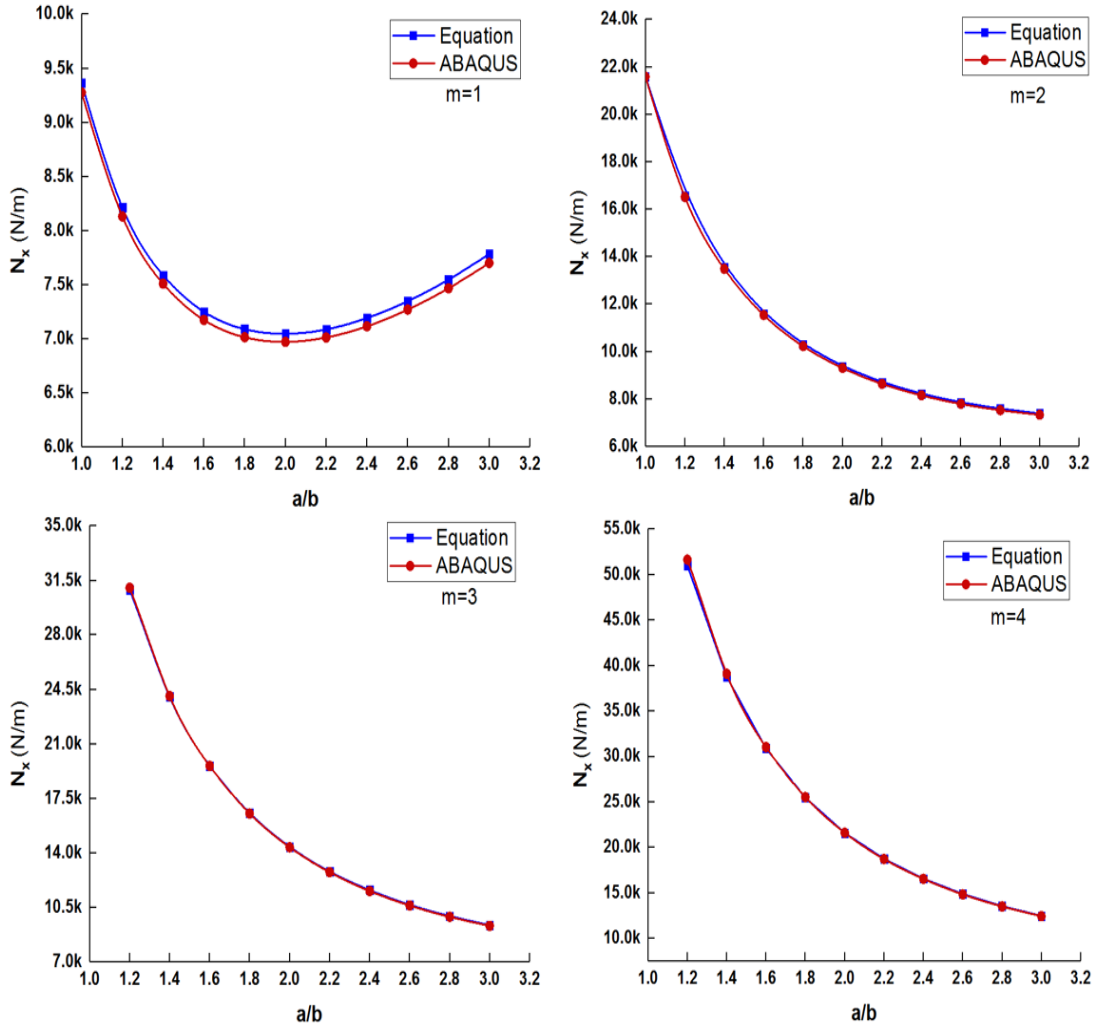

Figure 6.10: Equation (6.24) vs FE model comparison for laminate [45 -45 -45 -45 -45 45 45 -45]s

Another two composite plates with different lay-up sequences were examined to verify equation (6.24) presented in the previous section. The composite plate with [45 -45 0 90 -45 45 90 0]s lay-up shows a higher buckling load calculated by equation (6.24) for all values of m except those when m=1, which appeared to have a lower buckling load than finite element analysis beyond aspect ratio a/b =2, see Figure 6.11. Corresponding result for the [45 -45 -45 45 0 90 0 90]s laminate are shown in Figure 6.12.

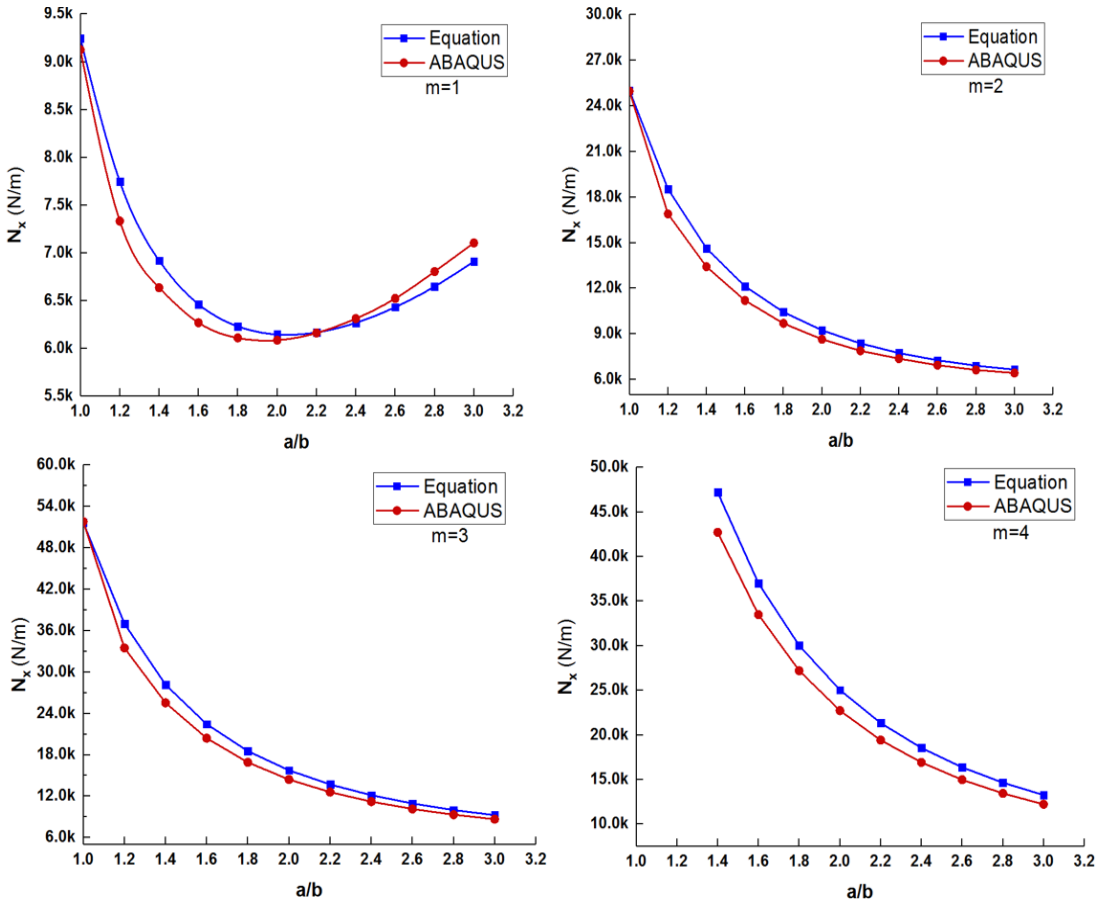

Figure 6.11: Equation (6.24) vs FE model comparison for laminate [45 -45 0 90 -45 45 90 0]s

All the buckling loads calculated by equation (6.24) have higher values than those from ABAQUS analysis for the laminate with [45 -45 -45 45 0 90 90 0]s stacking sequence except those for m=1 between aspect ratios 2.2 and 3.0.

The differences between the results for the second and third lay-up sequences are relatively higher than those for the first composite plate. These differences can be interpreted as follows. In equation (6.24) the effect of anisotropy was neglected to reduce the terms in the main buckling equations and hence simplify the calculations. Moreover, these differences did not appear in the first laminate results because of the values of D_{16} and D_{26} were equal to zero.

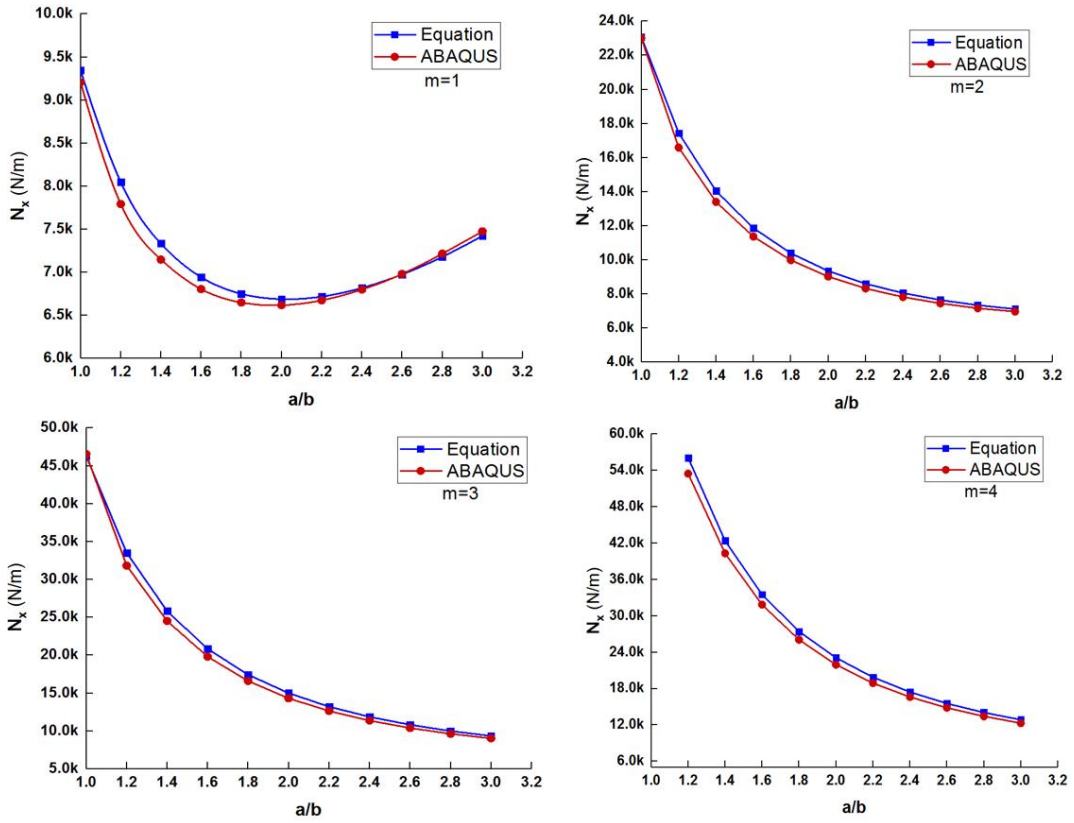

Figure 6.12: Equation (6.24) vs FE model comparison for laminate [45 -45 -45 45 0 90 0 90]s

6.6.4 Jumping strain determination

This section will outline the main hypothesis of this approach in order to predict the value of strain where a jump can occur. The first assumption is built on the fact that the value of effective width decreases as the load increases in the post-buckling stage. Consequently, the two edge strips have aspect ratio = $2a/b_e$ which increases because of the decreasing of b_e at each post-buckling step. This assumption will lead to the fact that the plate has a new aspect ratio at each load step and thus will reach a point where it tends to buckle with the next mode and leave the initial buckling configuration.

Hence the jump will occur. The next step in the approach is to find the value of the critical aspect ratio, which can be calculated at the point when the second critical load $(N_x)_2$ become less than the initial critical buckling load $(N_x)_1$. A Matlab program was written to find the value of the targeted aspect ratio (AR), which was found by applying the calculated value of effective width be in the following equation:

$$AR = \frac{2a}{b_e} \tag{6.25}$$

The final step is calculating the strain ε where the jumping point can occur by substituting the value of effective width calculated above in Koiter's effective width equation.

$$\frac{b_e}{b} = 1.2\left(\frac{\varepsilon_{cr}}{\varepsilon}\right)^{0.4} - 0.65\left(\frac{\varepsilon_{cr}}{\varepsilon}\right)^{0.8} + 0.45\left(\frac{\varepsilon_{cr}}{\varepsilon}\right)^{1.2} \tag{6.12}$$

The calculations use the Matlab program to predict the value of jumping strain. The reason behind choosing this equation among the many others reviewed in section 6.3 was that this equation gives better predictions of the jumping point (strain) for plates with different materials and aspect ratios when compared with the next proposed approach (energy approach) to detect the mode jumping. The steps of the effective width approach calculations to find the jumping strain are summarised in the flowchart in Figure 6.13.

Although the current approach includes many assumptions and some approximations, however, it provides a simple and fast way to predict the value of strain at which the mode jump will occur. The next section will describe another suggested approach to determine the value of jumping strain with two different mathematical techniques depending on the energy principle. The methods will be compared with numerical results in section 6.8.

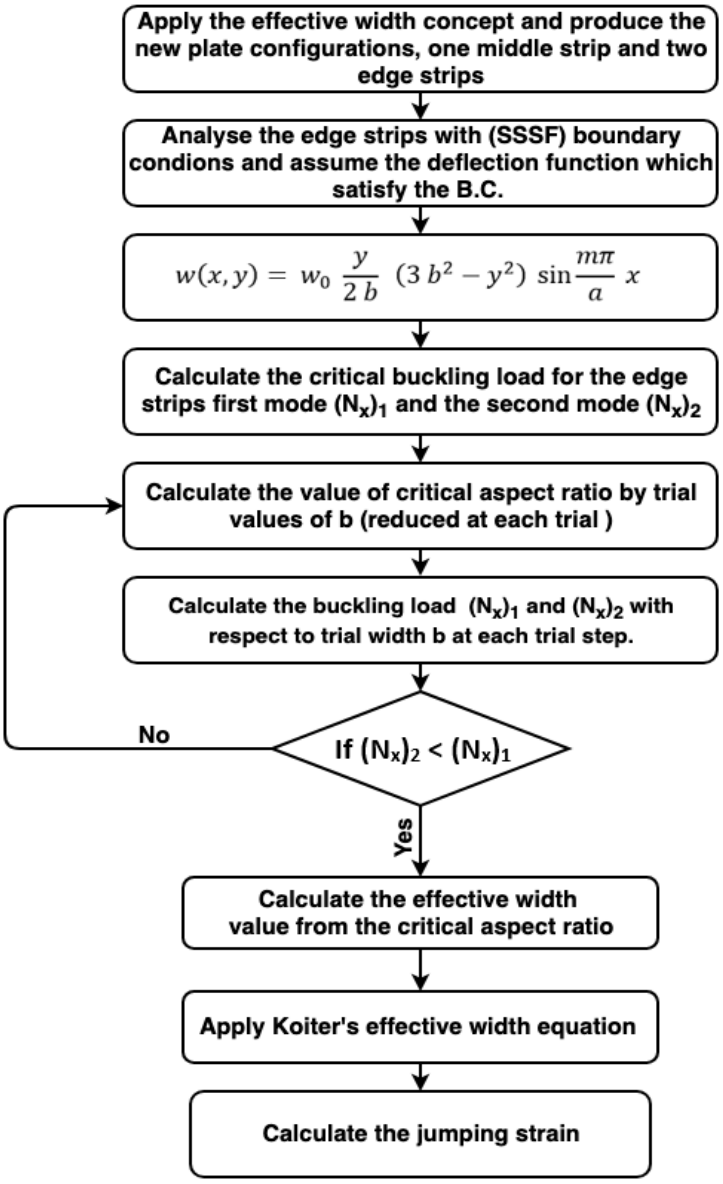

Figure 6.13: Effective width approach calculation procedure

6.7 Energy approach (E.A.)

The objective of this approach is to predict the strain value where a jump could occur. The proposed method to achieve that mainly considers the energy of the equilibrium path for both the initial post-buckling mode and the alternative buckling modes to which the structure tends to jump.

As mentioned previously at the beginning of this chapter (section 6.1), the motivation of this study is to improve the post-buckling analysis of VICONOPT software by including mode jumping. Consequently, the data for the energy calculation will be derived from the VICONOPT output.

The post-buckling analysis in VICONOPT is based on VIPASA analysis. Therefore, it is assumed that a jump will occur from one buckling mode to another by increasing the number of half wavelengths in the *x*-direction by one. An important inspiration for this approach came from previous work published as a conference paper by Watson and Kennedy [142] in 2004. The authors suggested an energy summation for the post-buckling equilibrium path to localise the possible jumping point in VICONOPT post-buckling analysis. Although this approach utilises the same concept, i.e. the strain energy, it uses completely different mathematical techniques to calculate the energy at different points on the post-buckling equilibrium path. Two mathematical procedures are employed to find the point where the mode (m+1) has lower energy than the initial buckling mode (m) and hence the jump will occur.

6.7.1 Third order polynomial method (3rd P.M.)

In this section, a simple mathematical method is proposed to calculate the energy of the different equilibrium paths in terms of the area under the post-buckling load-end shortening curve for initial and the second buckling mode curves. The method presented here assumes that the load-end shortening curve is a third order polynomial in the post-buckling region. The reason for choosing a third order polynomial is that this order gives acceptably accurate results which allow for the curvature which is frequently observed while avoiding complexity associated with higher order methods. The post-buckling curves will have the following form:

$$y = a_1 x^3 + a_2 x^2 + a_3 x + a_4 \tag{6.26}$$

Suppose the equation of the initial buckling (mode m) curve is:

$$P_1 = a_1 \mathcal{E}^3 + a_2 \mathcal{E}^2 + a_3 \mathcal{E} + a_4 \tag{6.27}$$

while that for the second (mode m+1) is:

$$P_2 = b_1 \mathcal{E}^3 + b_2 \mathcal{E}^2 + b_3 \mathcal{E} + b_4 \tag{6.28}$$

The value of constants a_n and b_n are calculated using Matlab least squares interpolation. To find the strain of the crossing point

$$P_1 = P_2 \tag{6.29}$$

Equation (6.29) is solved to calculate $\boldsymbol{\mathcal{E}} = \boldsymbol{\mathcal{E}}_c$ which represents the value of strain at the crossing point of the two curves. As mentioned previously, the jump will occur beyond this point when the energy associated with mode (m+1) equals the energy associated with mode (m).Therefore, it is required to solve the following equation to predict the value of jumping strain ($\boldsymbol{\mathcal{E}}_j$).

$$\frac{1}{2}\mathcal{E}_{cr1}P_{cr1} + \int_{\mathcal{E}_{cr1}}^{\mathcal{E}_j}(a_1 \mathcal{E}^3 + a_2 \mathcal{E}^2 + a_3 \mathcal{E} + a_4)d\mathcal{E} = \frac{1}{2}\mathcal{E}_{cr2}P_{cr2} + \int_{\mathcal{E}_{cr2}}^{\mathcal{E}_j}(b_1 \mathcal{E}^3 + b_2 \mathcal{E}^2 + b_3 \mathcal{E} + b_4)d\mathcal{E} \tag{6.30}$$

where $\boldsymbol{\mathcal{E}}_{cr1}$ and $\boldsymbol{\mathcal{E}}_{cr2}$ are, the initial buckling strain for mode m and m+1 respectively Equation (6.31) can be rewritten in a more simple form:

$$\int_{\mathcal{E}_{cr1}}^{\mathcal{E}_{cr2}}(K\mathcal{E} - a_1 \mathcal{E}^3 + a_2 \mathcal{E}^2 + a_3 \mathcal{E} + a_4)\, d\mathcal{E} + \int_{\mathcal{E}_{cr2}}^{\mathcal{E}_j}[(b_1 - a_1)\mathcal{E}^3 + (b_2 - a_2)\mathcal{E}^2 + (b_3 - a_3)\mathcal{E} + (b_4 - a_4)]d\mathcal{E} = 0 \tag{6.31}$$

$$K = \frac{P_{cr1}}{\mathcal{E}_{cr1}} = \frac{P_{cr2}}{\mathcal{E}_{cr2}} \tag{6.32}$$

Solving equation (6.32) will lead to determining the value of jumping strain $\boldsymbol{\mathcal{E}}_j$. Figure 6.14 illustrates the solution for the initial post buckling curve m and the secondary curve m+1. The full calculation of this method was performed using a Matlab program.

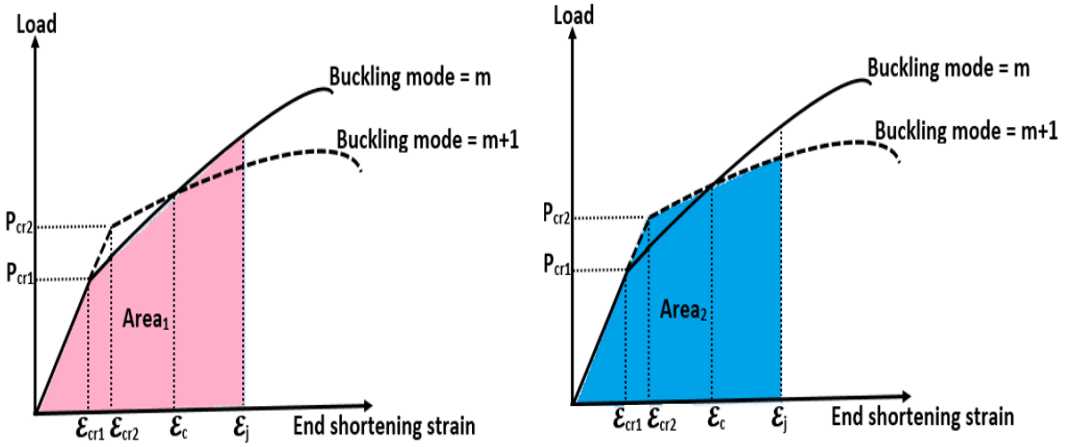

Figure 6.14: Area under the two equilibrium paths, which represent the strain energy, a- Energy for mode *m,* b- Energy for mode *m*+1

6.7.2 Trapezoidal method (T.M.)

This method is also based on the energy comparison between different post-buckling mode equilibrium paths. However, this mathematical technique has more accurate results because it evaluates the cumulative energy for the two post-buckling curves, see Figure 6.15.

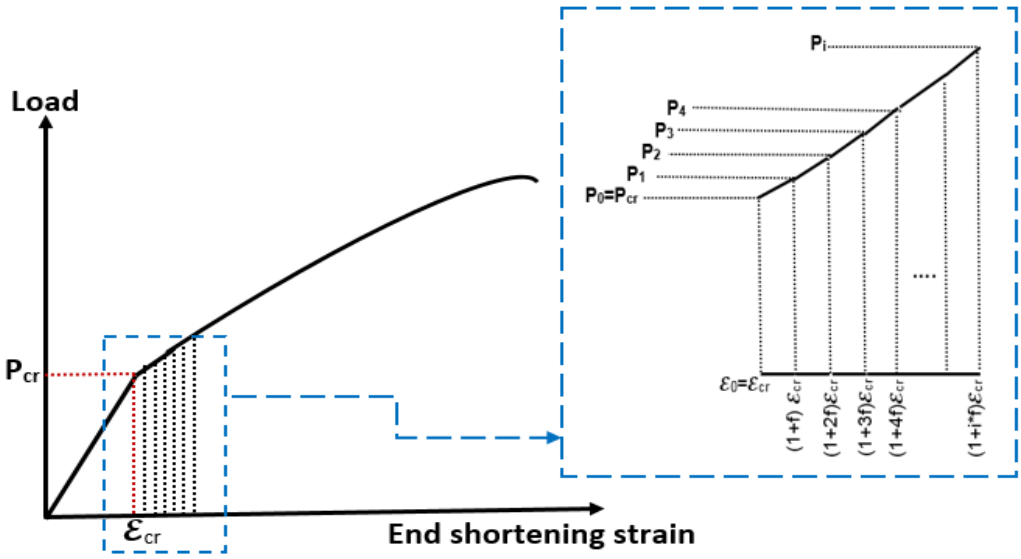

Figure 6.15: Trapezoidal method to calculate the area under VICONOPT post-buckling curves

Moreover, it compares the energy at each post-buckling cycle. The incremental energy at each cycle can be calculated by the trapezoidal rule using the following equation:

$$(Enr)_i = \frac{P_{i-1} + P_i}{2} \left(\mathcal{E}_i - \mathcal{E}_{i-1} \right) \tag{6.33}$$

where (i) is the cycle number. The load and strain values are imported from the VICONOPT post-buckling result file for modes m and m+1. The cumulative energy for initial buckling mode and the second mode are:

$$(Enr)_m = \sum_{i=1}^{i=n} \left[\frac{P_{i-1} + P_i}{2} \left(\mathcal{E}_i - \mathcal{E}_{i-1} \right) \right] \tag{6.34}$$

$$(\mathrm{Enr})_{\mathrm{m+1}} = \sum_{\mathrm{i=1}}^{\mathrm{i=n}} \left[\frac{\mathrm{P_{i-1}} + \mathrm{P_i}}{2} \left(\mathcal{E}_{\mathrm{i}} - \mathcal{E}_{\mathrm{i-1}} \right) \right] \tag{6.35}$$

The jump will occur when $(Enr)_{m+1} \leq (Enr)_m$. The mode jumping strain calculations are performed using a FORTRAN 77 program in order to be more compatible with VICONOPT, which is written in this language. As the current study assumes strain control mode jumping, the energy calculation will depend on the strain step at each post-buckling analysis cycle. VICONOPT uses equal strain increments at each step. This increment is a function of the initial buckling strain as shown in Figure 6.15. Consequently, the strain step at cycle i for the two equilibrium paths respectively will be:

$$(\mathcal{E}_{\mathrm{i}})_1 = (\mathrm{i} \times \mathrm{f} + 1)\mathcal{E}_{\mathrm{cr1}} \tag{6.36}$$

$$(\mathcal{E}_{\mathrm{i}})_2 = (\mathrm{i} \times \mathrm{f} + 1)\, \mathcal{E}_{\mathrm{cr2}} \tag{6.37}$$

The problem here is that an energy comparison at each post-buckling cycle is not possible because the strain increments are not equal. To tackle this problem, a transfer factor linking the initial buckling strain of both modes is needed to ensure the same strain increments are used for both modes.

This factor is derived from the linear part of the post-buckling load-shortening curves as below:

$$\frac{\mathrm{P_{cr1}}}{\mathcal{E}_{\mathrm{cr1}}} = \frac{\mathrm{P_{cr2}}}{\mathcal{E}_{\mathrm{cr2}}} \tag{6.38}$$

Substituting equation (6.39) into equation (6.38) leads to:

$$(\mathcal{E}_{\mathrm{i}})_1 = (\mathrm{i} \times \mathrm{f} + 1)\mathcal{E}_{\mathrm{cr1}} = \frac{\mathrm{P_{cr1}}}{\mathrm{P_{cr2}}}(\mathrm{i} \times \mathrm{f} + 1)\ \mathcal{E}_{\mathrm{cr2}} \tag{6.39}$$

After this transformation of the strain values for each mode. It is required to reproduce the load values for the new modified strain values $\mathcal{E}_t$. To achieve this, a linear interpolation is used to extract the transformed load values. According to the following equation:

$$P_t = P_i + \left[\left(\frac{\mathcal{E}_t - \mathcal{E}_i}{\mathcal{E}_{i+1} - \mathcal{E}_i}\right) \times (P_{i+1} - P_i)\right] \tag{6.40}$$

The total cumulative energy of the initial equilibrium path after r such strain increments is given by

$$(Enr)_{acc1} = \sum_{i=1}^{r} (Enr_1)_i \qquad i = 1, 2, 3, \ldots \ldots r \tag{6.41}$$

whereas the total energy for the secondary equilibrium path is

$$(Enr)_{acc2} = \sum_{i=1}^{r} (Enr_2)_i \qquad i = 1,2,3 \ldots \ldots r \tag{6.42}$$

Consequently, the mode jump will occur if

$$(\mathrm{Enr})_{\mathrm{acc2}} \leq (\mathrm{Enr})_{\mathrm{acc1}} \tag{6.43}$$

The FORTRAN code involves all the calculations and comparisons of the energy of the post-buckling paths with mode *m*, *m+1* and *m+2*. However, the study will focus on the first jump only. The complete procedure of the mode jumping strain by using the trapezoidal role through the FORTRAN code is summarised in flowchart presented in Figure 6.16.

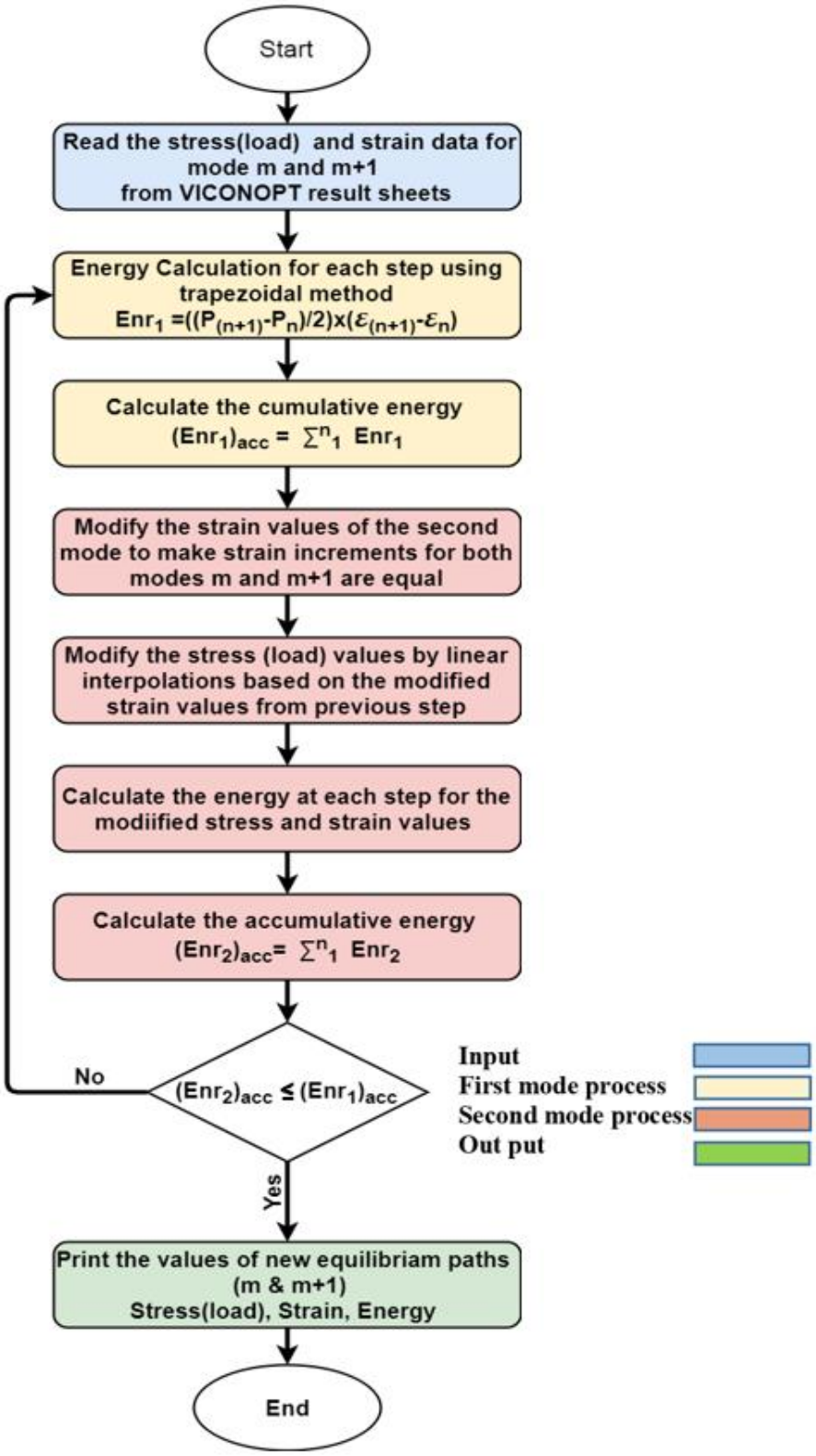

Figure 6.16: Fortran77 code flowchart for energy calculations

6.8 Flat plate results

The section will outline the analysis results for flat plates to predict the values of jumping strain by using the effective width and energy approaches discussed previously in this chapter. The results include flat plates with simply supported edge conditions. The study considers different aspect ratios and material properties (isotropic and composite), as mentioned previously in section 6.6.3. These plates will be sub-divided according to the initial buckling mode and the expected mode that the structure tends to jump to.

6.8.1 Example 1: Mode jumps from m = 1 to m = 2

This section will discuss the results for isotropic and composite simply supported plates which initially buckled with one-half wavelength m=1 and then jump to the second mode m =2, so that the buckling mode pattern will change at some point along the equilibrium path to buckle with two half waves instead of one. The results are described as load-shortening relationships of VICONOPT analysis which include two equilibrium paths that have two different modes. It was mentioned that the VICONOPT post-buckling depends on VIPASA analysis, which assumes that the plate buckles with an integer number of half wavelengths m in the longitudinal direction. The main objective of this chapter is to include mode jumping in VIPASA post-buckling analysis. Thus the jump will occur from m=1 to m=2, and the calculations will use strain control.

The results of VICONOPT are compared with finite element results using both ABAQUS standard and dynamic explicit analysis for validation. The finite element model consisted of two models, the first one using ABAQUS/Standard (version 6.14) [156]. Linear eigenvalue analysis was first conducted to evaluate the initial buckling modes and then these results were used in a second model that utilised the ABAQUS/Dynamic explicit step to estimate the post-buckling

behaviour depending on the buckling mode configuration provided from the linear model. The finite element dynamic explicit analysis provides a reliable source of nonlinearity such as geometric imperfection and material plasticity (which is not included here in order to match the exact strip analysis results).

The finite element mode boundary conditions are shown in Figure 6.17. The loaded edges are constrained to move in a straight line utilising multi-point constraints (MPC), which make the displacements at all the edge node equal. The model uses standard S4R shell elements for the linear buckling model while for the dynamic explicit step analysis model it was explicit shell elements which have the same element size for both models equal to 0.01m. A mesh sensitivity test was done to examine a range of element sizes to ensure the accuracy of the chosen element size as shown in Figure 6.18.

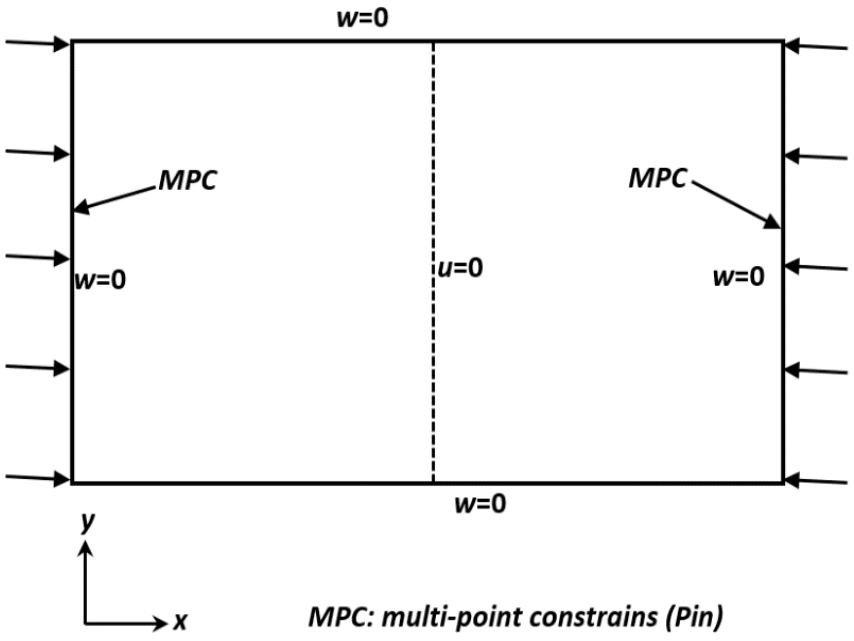

Figure 6.17: ABAQUS model boundary and load conditions

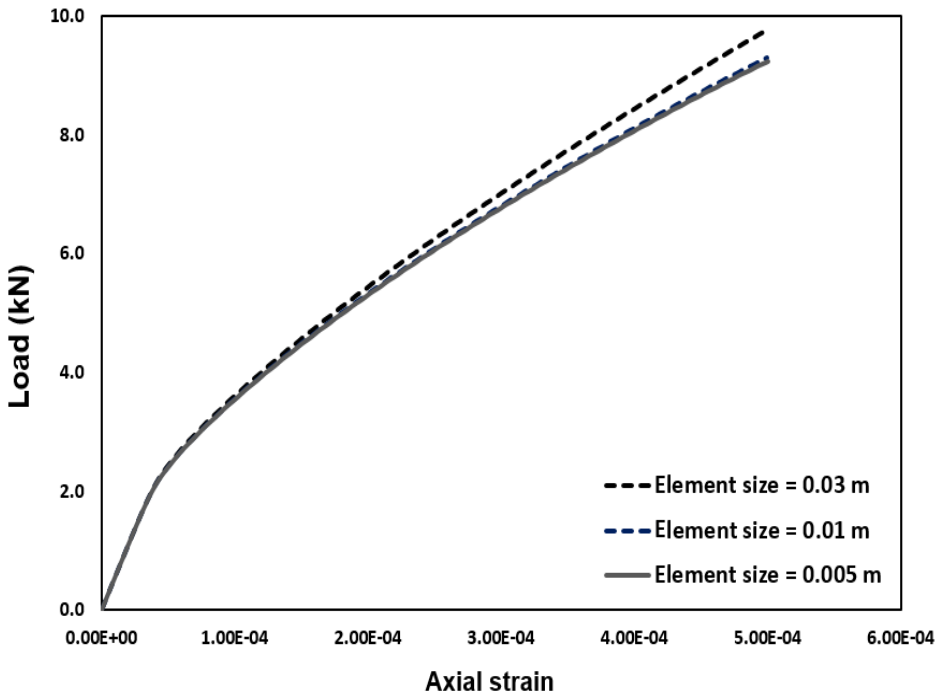

Figure 6.18: Mesh sensitivity for ABAQUS model

In order to include mode jumping in the analysis, it is essential to provide a geometrical imperfection for the first and second modes. Imperfections are usually introduced by perturbations in the geometry. These imperfections are provided as a linear superposition of buckling eigenmodes from the displacements of static analysis. The initial buckling mode imperfection will be slightly higher than the second mode imperfection to ensure that the buckling will start with the critical buckling mode recalled from the linear buckling mode. The maximum values of the geometrical imperfection were 20% of the plate thickness in case of the isotropic plate and 15% of the laminate thickness in case of composites (these imperfection amplitude values were chosen according to information extracted from the literature). The plates have a width of 300 mm, and different aspect ratios ranging from 1.0 to 1.4.

6.8.1.1 Isotropic plates

The load against axial strain curves are introduced for plates with *a/b* =1.2 and 1.4 to clarify the mode-jumping occurrence using two approaches: effective width (E.W) and energy calculations including two techniques, i.e. the trapezoidal method implemented in FORTRAN code (VICONOPT code) and the third order polynomial method (VICONOPT 3rd poly). The two curves (which represent the post-buckling analysis for buckling modes *m* and *m+1*) are compared with the finite element curve, which showed a gradual transition between modes.

The reason that the ABAQUS equilibrium path did not show a sudden jump was based on a transitional change in buckling pattern due to the two mode configurations provided by geometrical imperfections. The ABAQUS model was assembled by using shell element S4R with element size 0.01m for both standard and dynamic analysis. The flat plates all had the dimensions b=0.3 m with different aspect ratios from 1.0 to 1.4. The results for the isotropic plate with aspect ratio 1.2 are shown in Figure 6.19. The initial critical buckling load was 6.768 kN using VICONOPT. It was slightly less at 6.541 kN when using ABAQUS with an initial imperfection applied. The initial buckling mode has one half wavelength along the length.

The second buckling configuration with two half wavelengths has a buckling load equal to 8.411 kN. VICONOPT initial buckling strains were 9.342E-5. The effective width method estimates that the mode jump will occur at strain level 8.136E-4 where the load value will jump from 21.814 to 20.511 kN. The mode jump happens slightly later when utilising the energy calculations, i.e. at strain 8.968E-4 (9.012E-4 using the 3rd order polynomial method) and the load in this case dropped from 23.307 to 21.669 kN (23.383 to 21.730 kN) as shown in Figure 6.19.

ABAQUS results showed the plate started to buckle with a single buckle initially. However, the buckle was not exactly in the middle due to the two imperfections applied in the model, which showed the resultant of the two out of plane displacements of the two modes. After that a small buckle starts to initiate at strain level 2.231E-4 and grows gradually until the post-buckling pattern is fully changed from a single half wavelength to a new mode configuration consisting of full two buckles. The details of the buckling mode changes are shown in Figure 6.20.

The plate with aspect ratio 1.4 has interesting results due to very early occurrence of a jump. The plate initially buckled with one-half wavelength at load 7.317 kN and 1.010E-4 strain while the second buckling load with m=2 will be at 7.417 kN and 1.024E-4 strain. The energy calculations showed that the jump would occur in the early part of the equilibrium path when compared with the previous aspect ratio, see Figure 6.21. The energy approach predicts the jump at strain 2.606E-4 (2.780E-4 using the 3rd order polynomial method) where the load reduces from 11.052 to 10.938 kN (11.450 to 11.337 kN).

The effective width calculations showed relatively conservative value for jumping points at 5.696E-4 strain with a load jump from 17.772 to 16.566 kN. This was due to the assumptions used in that approach depending on effective width degradation. Therefore, for the expected early jump at this aspect ratio, this method estimates the jumping point quite late compared to other approaches. The finite element curve followed the same trends as the previous aspect ratio. The buckling mode started with one buckle and gradually changed partially to two half wavelength at strain 2.689E-4, and the new buckle expanded gradually so that at the end of analysis the plate buckled with a full wavelength mode as shown in Figure 6.22.

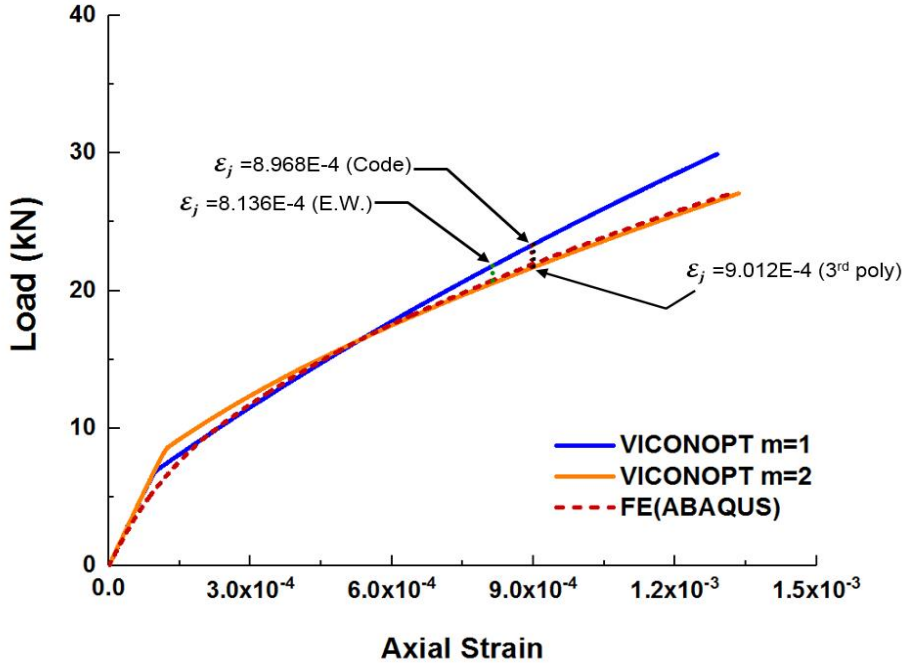

Figure 6.19: Load vs strain for isotropic flat plate, *a/b*=1.2

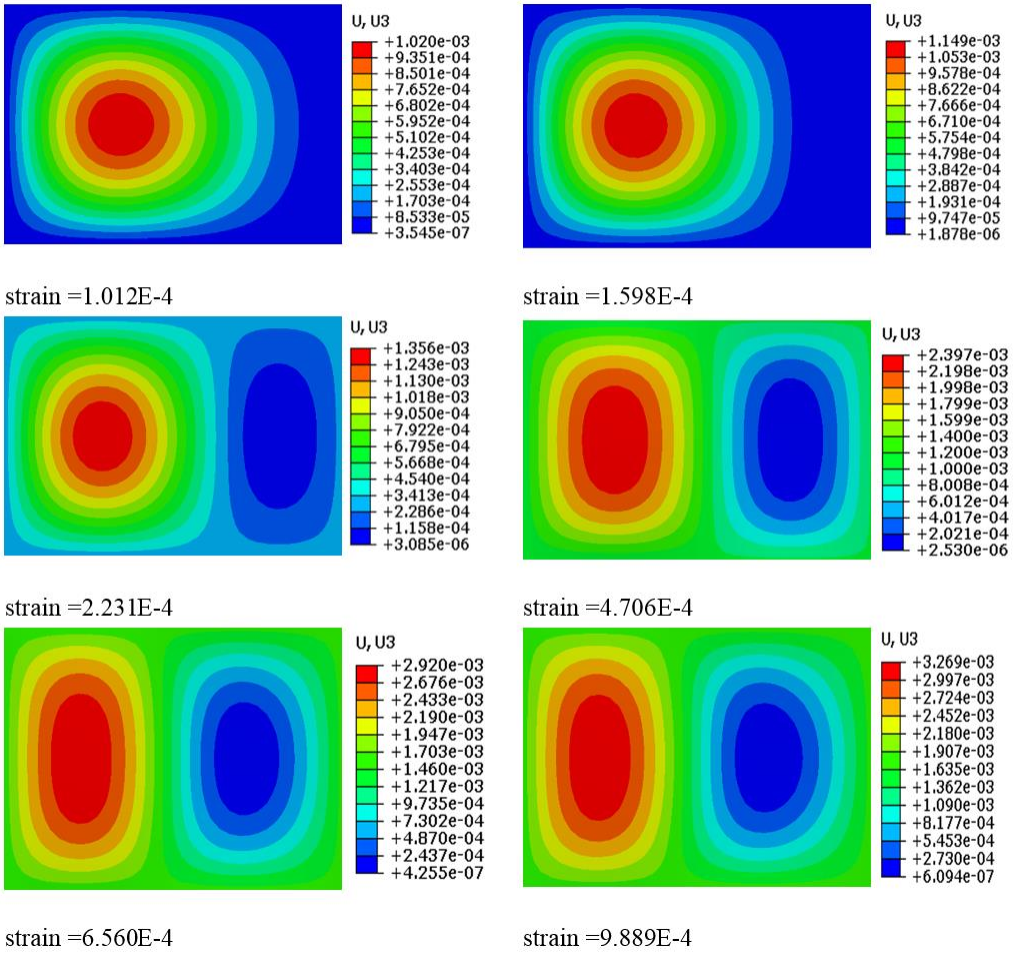

Figure 6.20: ABAQUS buckling mode for isotropic plate, *a/b* =1.2

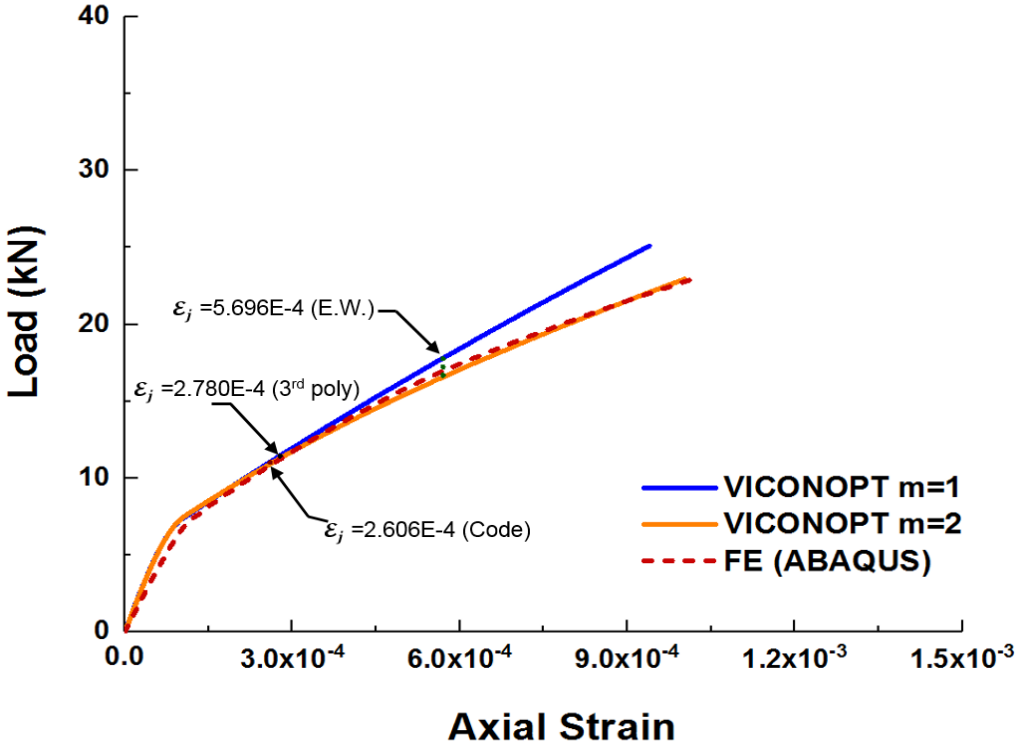

Figure 6.21: Load vs strain for isotropic flat plate, *a/b*=1.4

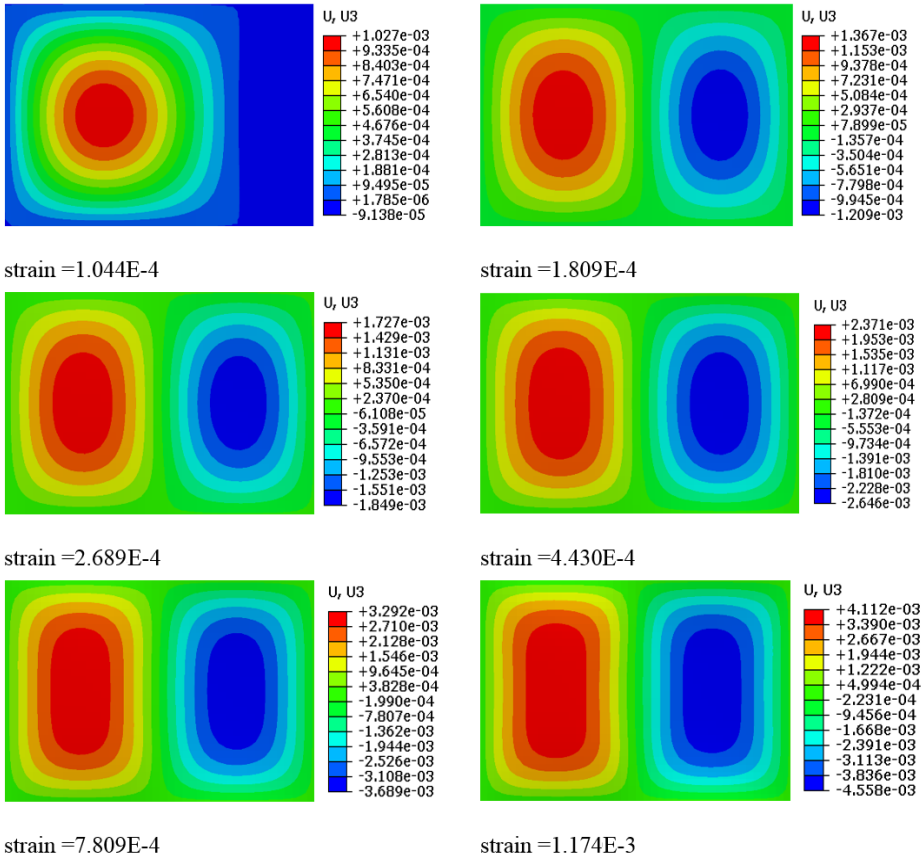

Figure 6.22: ABAQUS buckling mode for isotropic plate, *a/b* =1.4

6.8.1.2 Composite plates

The composite plate had a symmetric stacking sequence consisting of 16 layers of overall thickness 2mm with a [45 -45 -45 45 -45 45 45 -45]s ply sequence. The width of the laminates was 0.3 m and the length was varied to have different aspect ratios from 1.0 to 1.4. The results for the plate with a/b = 1.2 showed a similar trend to the isotropic plates but with some different features that will be discussed. The VICONOPT results showed that the plate buckled initially with one-half wavelength at axial strain 5.719E-4 while the second buckling mode had m=2 at strain 6.549E-4.

The jumping strain using the effective width approach (E.W.) calculations was 4.981E-3 in which the load jumps from 26.732 to 24.959kN. However the energy calculation showed that the jumping from mode m=1 to m=2 occurs slightly earlier at strain 4.347E-3 (4.333E-3 using the 3rd order polynomial method) in which the load will jump from 24.495 to 23.216 kN (24.446 to 23.178 kN) as described in Figure 6.23. The ABAQUS results gave a lower initial buckling load with m=1 than VICONOPT analysis due to the effect of imperfection. The buckling mode starts to change progressively as the load increases until jumping to a new buckling mode with m=2 as described in Figure 6.24.

The results for the composite plate with aspect ratio 1.4 will now be explained because the jump occurred at an early stage. For instance, the energy calculation predicts that the equilibrium path will change at strain 1.419E-3(1.516E-3) as the load reduces from 12.980 to 12.849 kN (13.433 to 13.261 kN).

The effective width approach estimates a late jump at 3.337E-3 because of the sudden early jump occurrence as the plate has very close post-buckling paths. This conservative value can be interpreted by the fact that the effective width approach depends on the stress redistributions and effective width concept, which assumed to decrease gradually while load increases.

This condition was not satisfied because the jump for this aspect ratio occurred relatively earlier than other cases due to the close values of the first and second critical buckling load. Therefore, the calculations of this approach failed to predict a jumping strain match the values conducted by the energy method.

The finite element model showed good agreement with VICONOPT results. It was possible to notice the effect of the small imperfections required in the ABAQUS non-linear analysis at the end of the linear buckling stage. However, the effect of it was small because the small values of the imperfection (15% of the laminate overall thickness).

The laminates buckled with m=1 and followed a path close to the exact strip method equilibrium path with m=1, see Figure 6.25, then gradually started to leave the previous path and curved significantly to match the VICONOPT post-buckling path for mode m=2 at a strain value of 1.389E-3. The transition between the modes in ABAQUS analysis is a superposition of two modes applied by the two imperfections of sinusoidal buckling modes with one and two half waves through the length, as shown in Figure 6.26.

In addition, the results showed that there was no obvious effect regarding the material properties in the mode change occurrence. However, in terms of the same material i.e. composites, the lay-up sequence of the laminate affects the initial buckling values and thus it definitely has an effect on the post-buckling behaviour and hence the mode jumping phenomena.

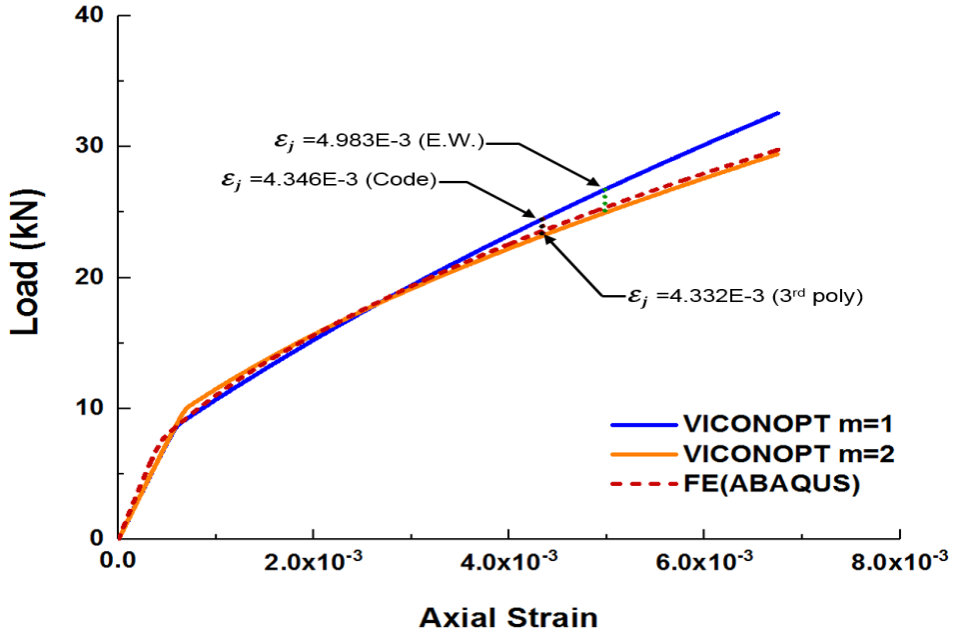

Figure 6.23: Load vs strain for laminate [45 -45 -45 45 -45 45 45 -45]s, *a/b*=1.2

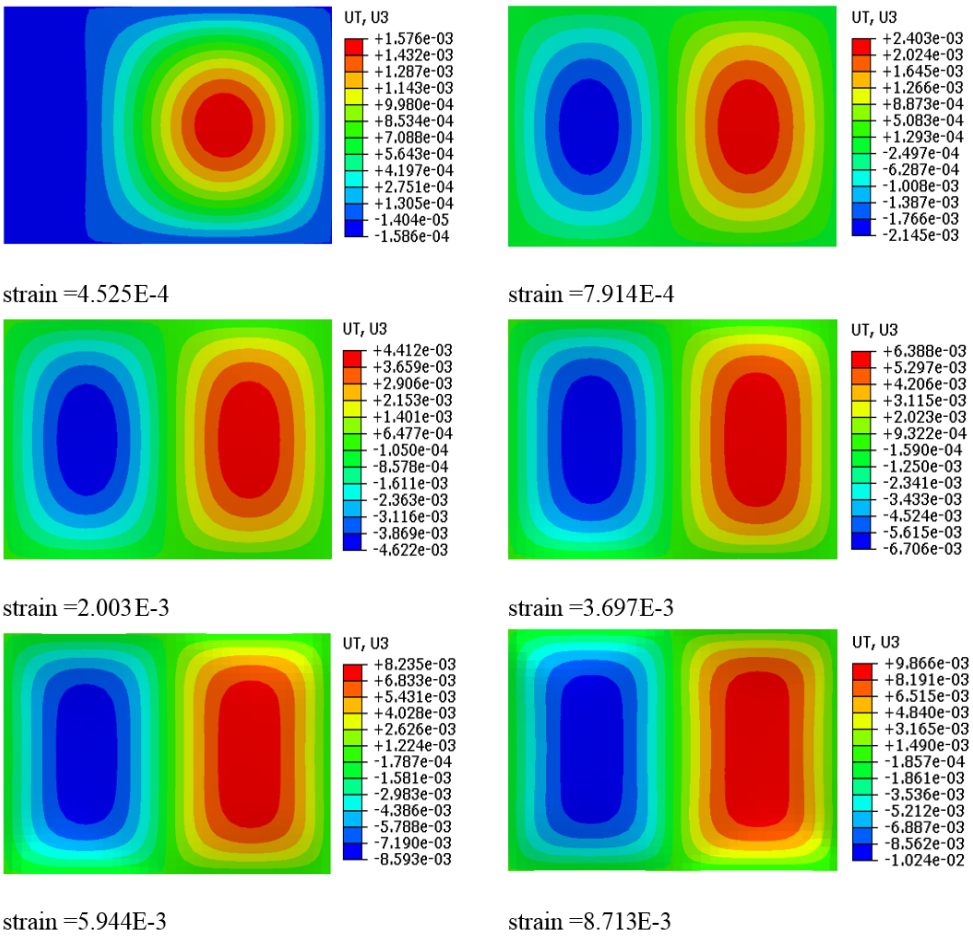

Figure 6.24: ABAQUS buckling mode for laminate [45 -45 -45 45 -45 45 45 -45]s, *a/b* =1.2

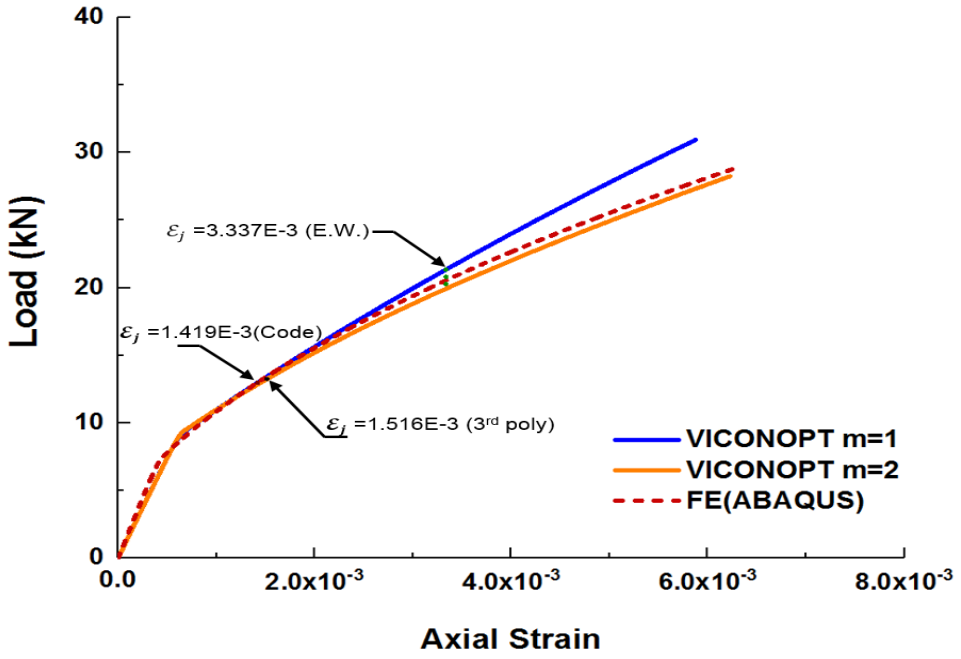

Figure 6.25: Load vs strain for laminate [45 -45 -45 45 -45 45 45 -45]s, *a/b*=1.4

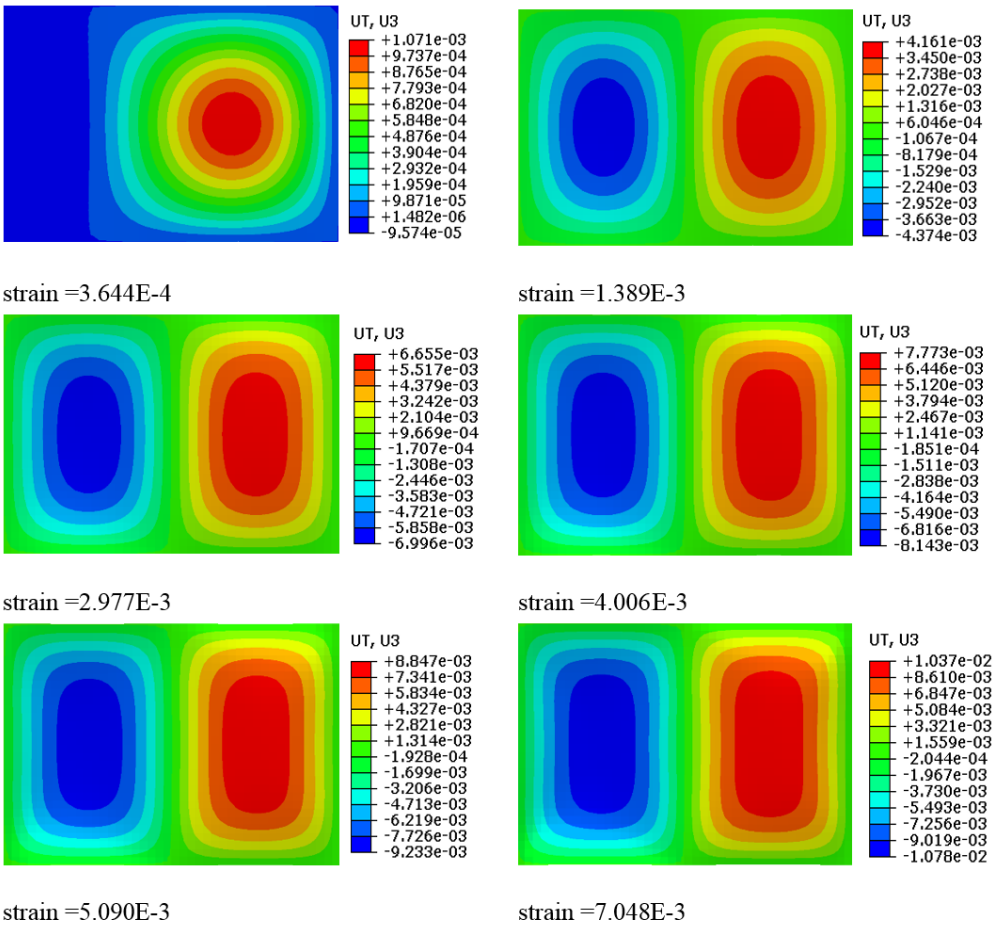

Figure 6.26: ABAQUS buckling mode for laminate [45 -45 -45 45 -45 45 45 -45]s, *a/b*=1.4

A range of isotropic and composite plates were examined for the mode jump strain prediction from m=1 to m=2 are presented in Figure 6.27 and Figure 6.28. Moreover, the results for a composite plate with different ply sequences are summarised in Appendix B.

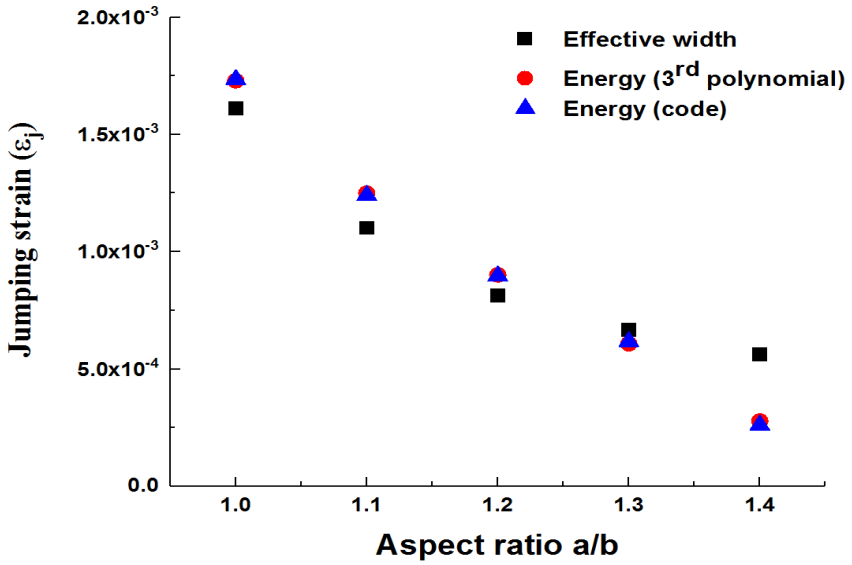

Figure 6.27: Mode jumping strain for isotropic plates (from m=1 to m=2)

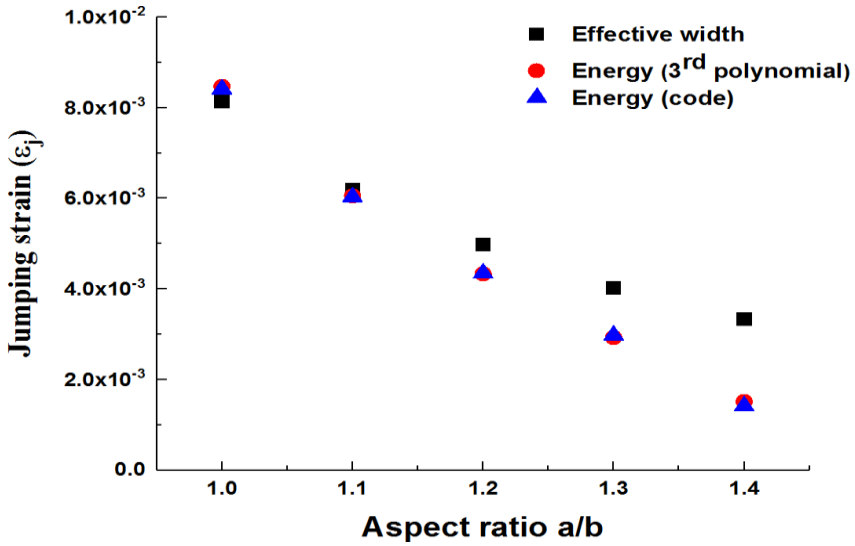

Figure 6.28: Mode jumping strain for laminates [45 -45 -45 45 -45 45 45 -45]s (from m=1 to m=2)

6.8.2 Example 2: Mode jumps from m = 2 to m = 3

6.8.2.1 Isotropic plate

The plate aspect ratio has a significant effect on the mode jumping phenomenon. Moreover, it is important to apply the two approaches introduced in this study for a wide range of plates to ascertain their applicability. Consequently, this section deals with flat plates buckling initially with two half wavelength m=2 and jumping to a new buckling mode m=3. The results will be discussed for a range of metal and composite flat plates with aspect ratios from a/b=1.5 to 2.4.

The aspect ratios 2.0 and 2.4 will be explained in detail and the rest will be presented as a mode jumping strains versus aspect ratios curves for the different proposed methods. In general, the plates showed similar trends to those discussed in the previous section. However, the effect of aspect ratio on the buckling and post-buckling behaviour are significant especially in terms of the out of plane mode shape. Therefore, these plates will be discussed here.

VICONOPT post-buckling analysis was performed for an isotropic plate with a/b =2.0 initially buckling with two buckles in the longitudinal direction at strain 9.038E-5. The calculations in order to predict the jumping point showed that the mode changed at strain level 9.806E-4 (9.885E-4 for the 3rd order polynomial method) where the load dropped from 23.815 to 22.708 kN (23.853 to 22.739 kN) as shown in Figure 6.29. The calculations based on the effective width method estimate a lower jumping strain at 8.816E-4 with load decrease from 22.125 to 21.293 kN. Generally, the results showed a relatively late jump along the post-buckling equilibrium path for this aspect ratio.

The finite element analysis showed that the plate buckled with mode m=2 and then the mode started to gradually change throughout the post-buckling region. The out of plane displacement pattern showed a third buckle initiated

after strain level 3.361E-4. The third buckle became more observable at strain 3.578E-4 as shown in Figure 6.30, which expanded step by step with a full change to a new mode m=3. The finite element model showed a gradual transition between modes, which made the post-buckling curve smooth with no sudden drop in load.

The isotropic plate with a/b=2.4 showed similar behaviour to that one with a/b=1.4. However the latter buckled first with mode m=1 and jumped to m=2, while the former buckled with mode m=2 and jumped to m=3. The effective width method predicts a late jump due to the early jump occurrence because the assumptions of this approach that discussed previously.

The energy method estimates that the mode changes at strain level 3.184E-4(3.186E-4) using the energy calculation in which the load jumps from 11.938 to 11.798 kN (11.944 to 11.803 kN) respectively as described in Figure 6.31. On the other hand, the finite element analysis showed a jump from m=2 to 3 started at strain level 1.885E-4, a third buckle grew and the mode changed gradually to have three half wavelength as shown in Figure 6.32.

There was a noticeable feature that can be observed in the ABAQUS analysis in terms of the out-of-plane contour which showed the first buckling mode shape not positioned equally along the length and it was close to either left or right side of the plate. This behaviour was due to including more than one mode by considering more than one imperfection. Thus the mode was a resultant of two modes imported from the linear buckling model and this appeared in all the cases investigated in this chapter.

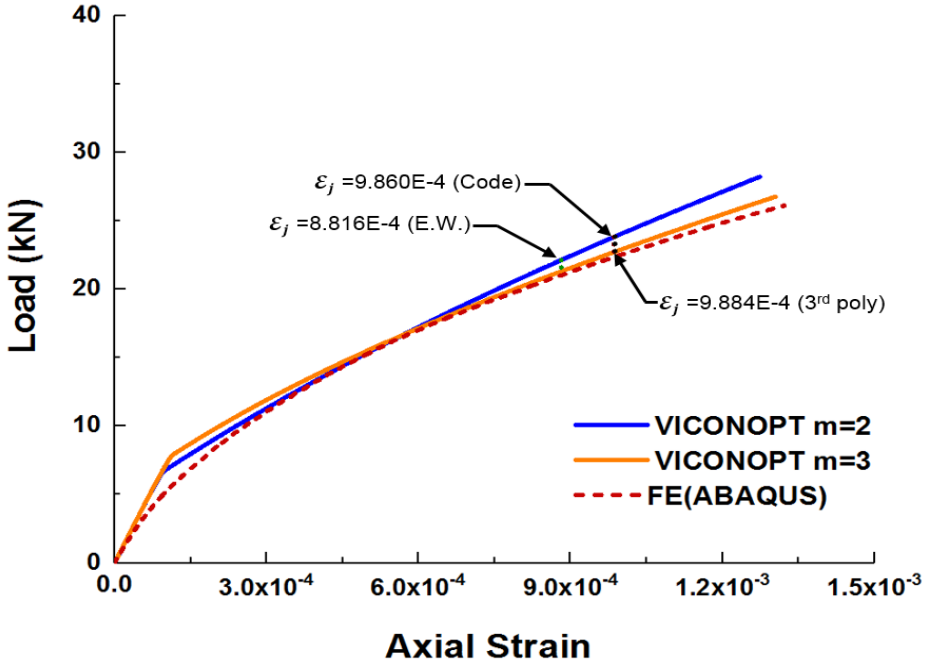

Figure 6.29: Load vs strain for isotropic flat plate, *a/b*=2.0

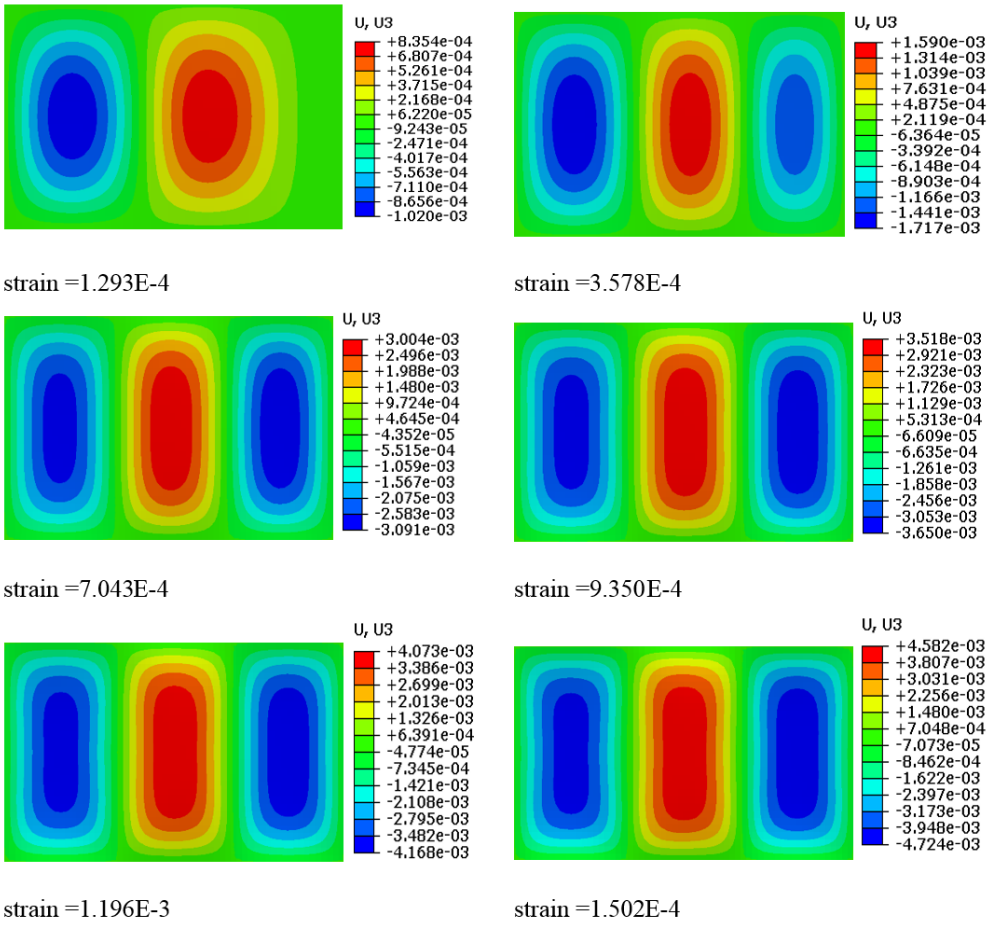

Figure 6.30: ABAQUS buckling mode at different strain for the isotropic plate, *a/b* =2.0

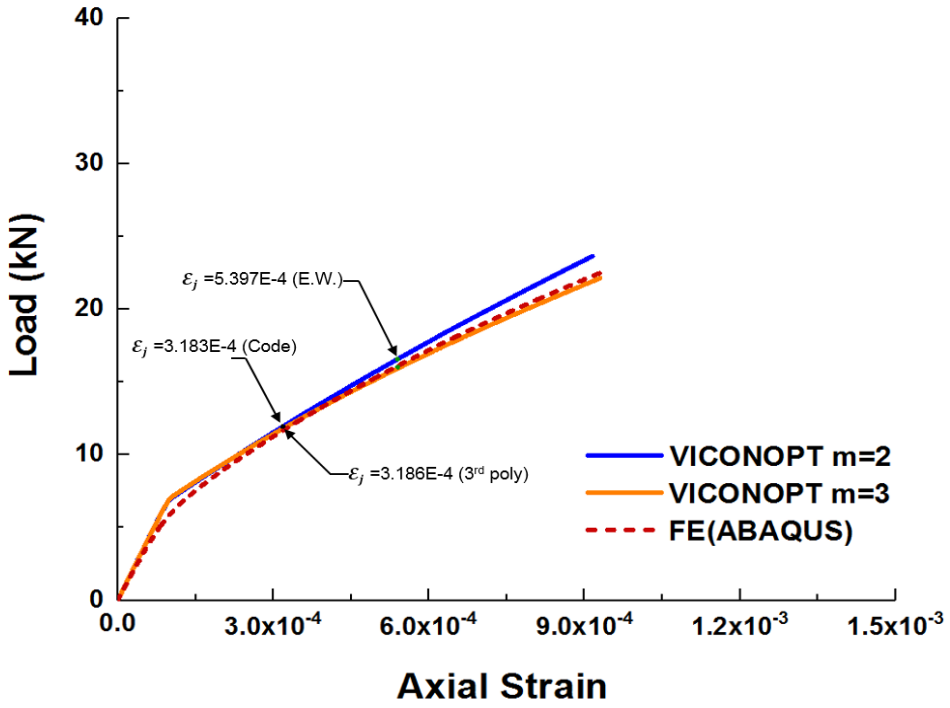

Figure 6.31: Load vs strain for isotropic flat plate, *a/b*=2.4

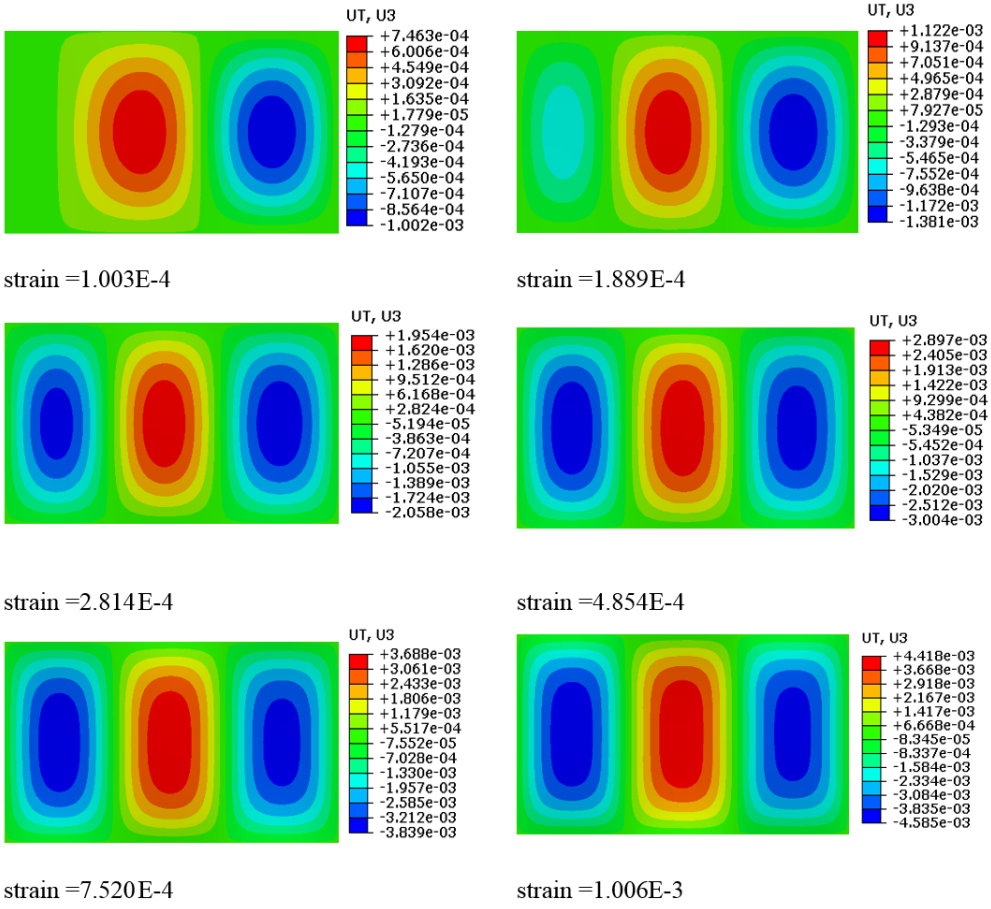

Figure 6.32: ABAQUS buckling mode for the isotropic plate, *a/b* =2.4

6.8.2.2 Composite plates

Composite plates that buckled initially with m=2 and changed to m=3 will be discussed in this section. The analysis shows a similar trend to the metal plates with the same aspect ratio but with some differences. For instance, the laminate with a/b =2.0 showed a relatively late jump when compared with that of aspect ratio 2.4. The effective width calculation estimates the change in the buckling mode will occur at a lower somewhat strain that predicted by the energy method as shown in Figure 6.33.

The ABAQUS results showed a gradual mode change started at strain level 1.425E-4, Figure 6.34. Conversely for the laminate with a/b=2.4, the effective width technique estimates again late jump at strain 3.305E-3 where the load moved down from 20.601 to 19.783 kN, compared with the strain values based on energy 1.545E-3 (1.693E-3) at which the load jumps from 13.225 to 13.134 kN (13.897 to 13.760 kN) as shown in Figure 6.35. The numerical results which were obtained from ABAQUS analysis showed that the mode switching started early at strain 8.527E-4 and continued as the load increased until there was a full change from mode m=2 to m=3 at strain level 2.167E-3 as presented in Figure 6.36.

The early jump occurrence in both VICONOPT energy calculation and finite element analysis was caused by the close values of the post-buckling paths for mode m=2 and m=3 which means the mode jumping was more likely to happen in comparison to other aspect ratios. For instance, the exact strip analysis showed that the buckling loads are closed, i.e. 8.596 kN (strain = 5.719E-4) for mode m=2 and 8.681kN (5.775E-4) for mode m=3. Thus, the two equilibrium post-buckling paths are very close compared with other plate cases. Hence, the mode change is more likely to happen in the initial post-buckling region as described above.

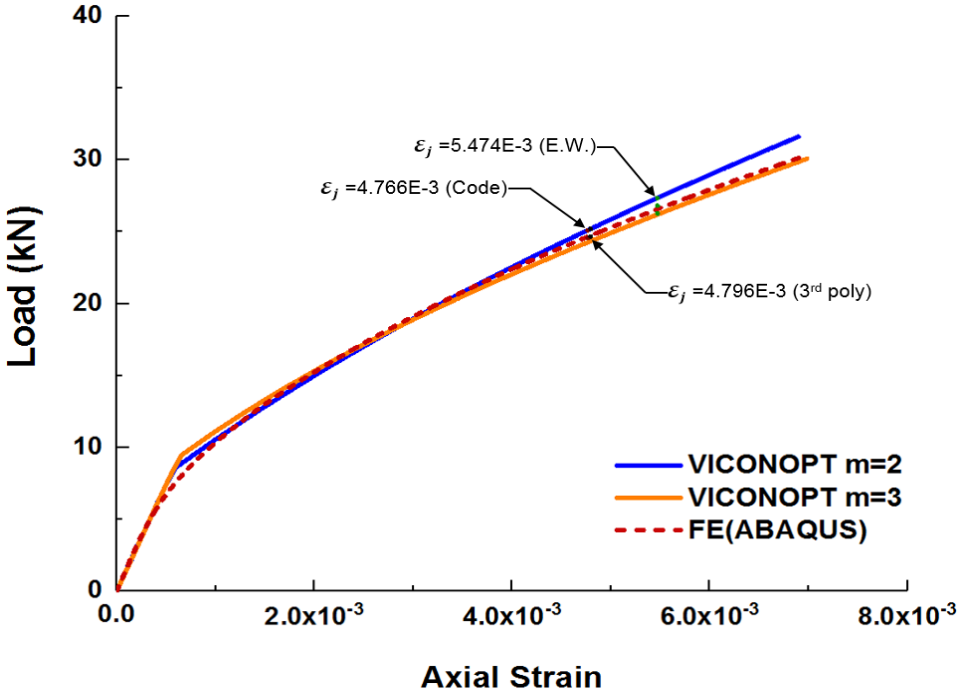

Figure 6.33: Load vs strain for laminate [45 -45 -45 45 -45 45 45 -45]s, a/b=2.0

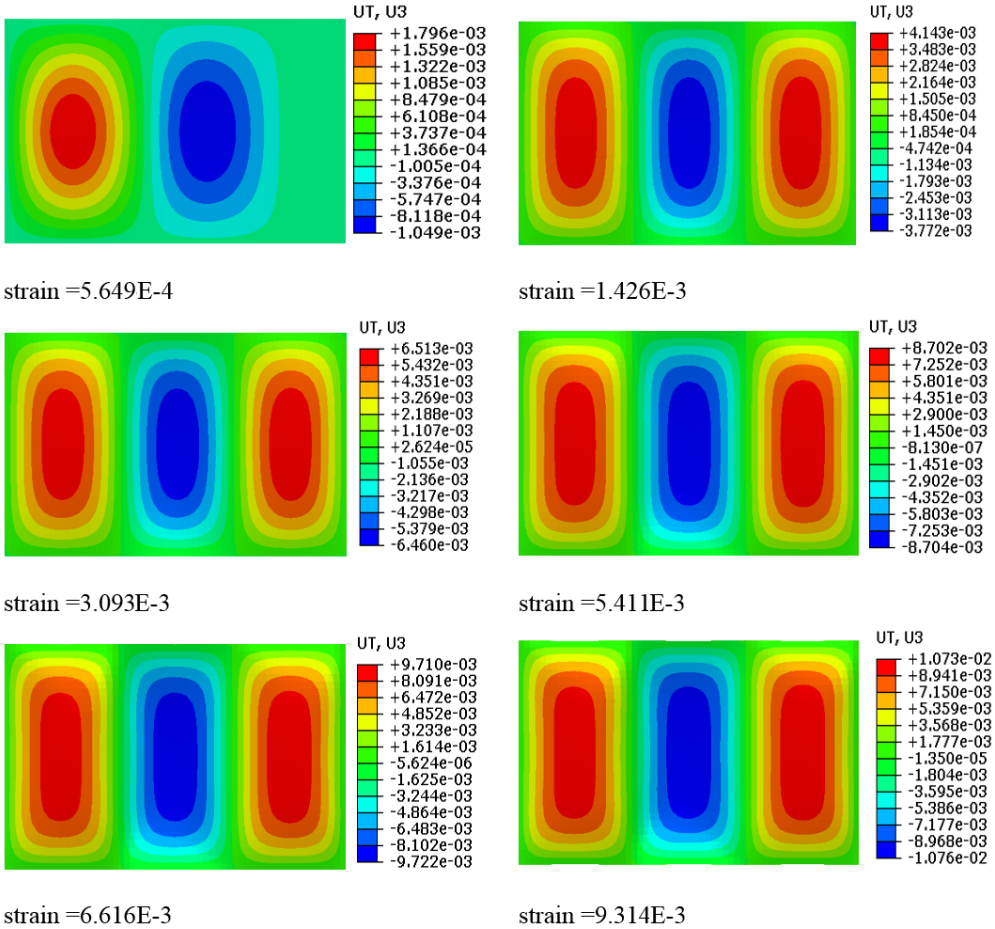

Figure 6.34: ABAQUS buckling mode for laminate [45 -45 -45 45 -45 45 45 -45]s, *a/b*=2.0

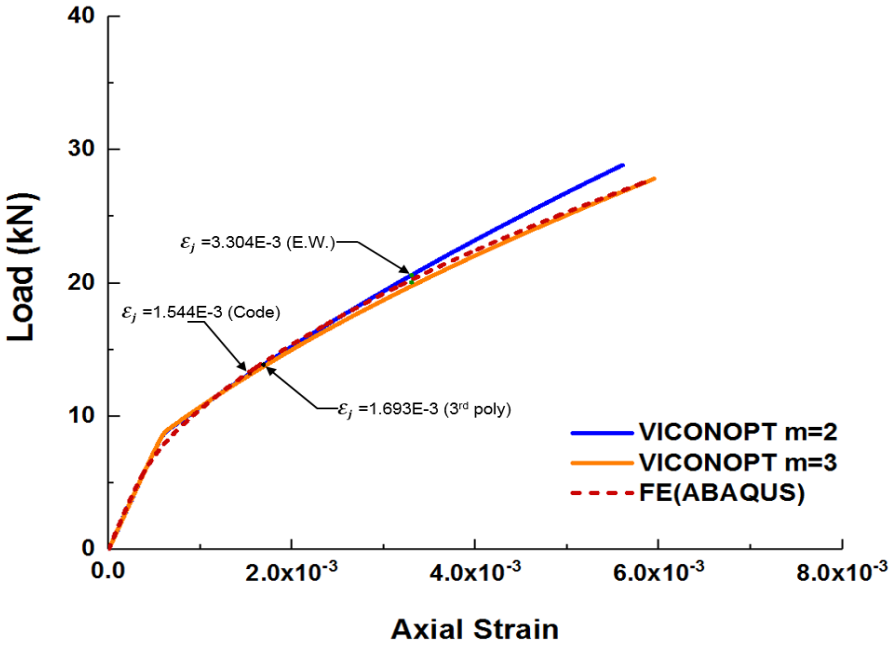

Figure 6.35: Load vs strain for laminate [45 -45 -45 45 -45 45 45 -45]s, *a/b*=2.4

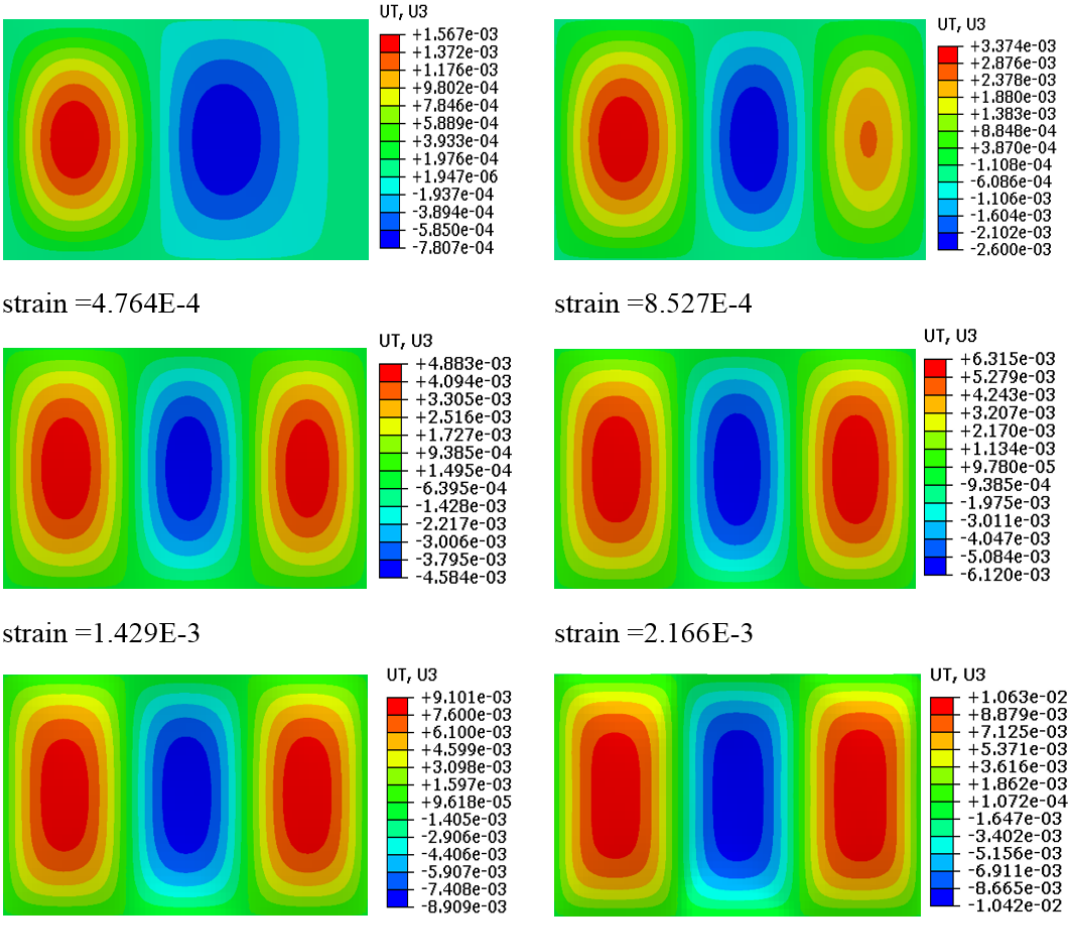

Figure 6.36: ABAQUS buckling mode for laminate [45 -45 -45 45 -45 45 45 -45]s, *a/b*=2.4

The other plates (metal and composite), with an aspect ratio between 1.5 and 2.4 were examined and their results are shown in Figure 6.37 and 6.38. The results for laminates with different stacking sequences and the results for plates jumping from *m*=3 to *m*=4 are highlighted in Appendix B.

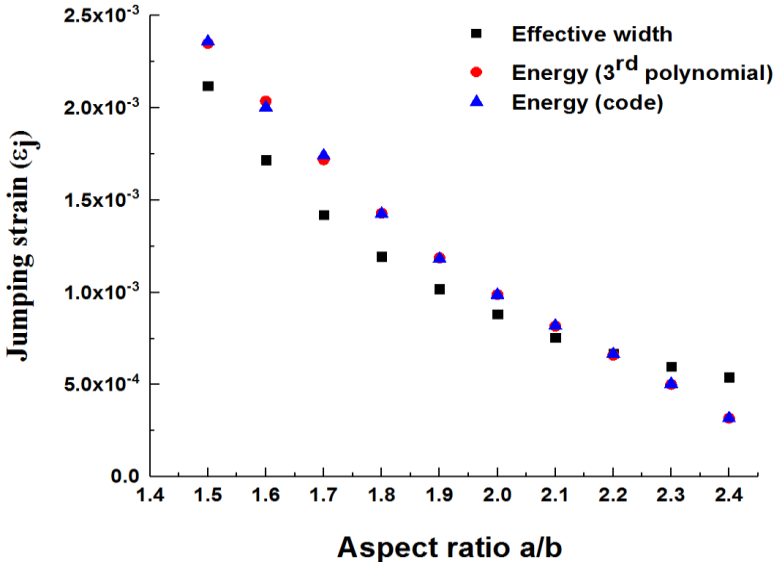

Figure 6.37: Mode jumping strain for isotropic plates (jump from *m*=2 to *m*=3)

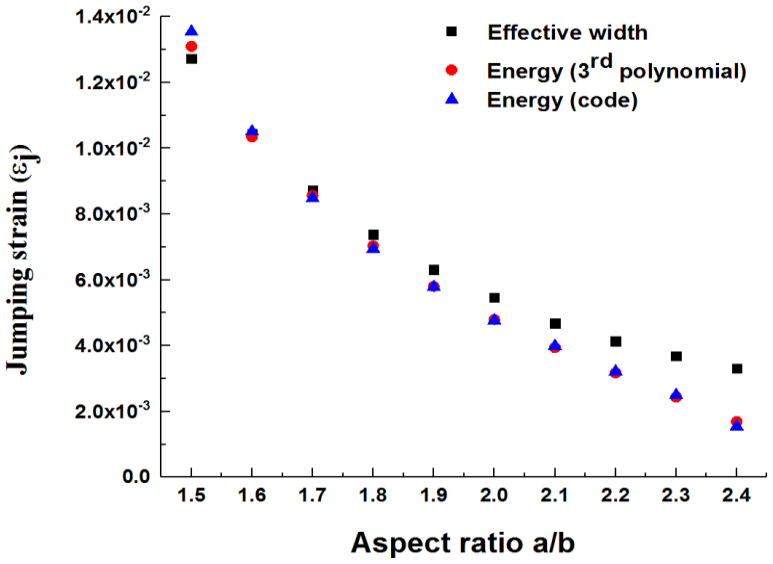

Figure 6.38: Mode jumping strain for laminates
[45 -45 -45 45 -45 45 45 -45]s (jump from *m*=2 to *m*=3)

6.9 Stiffened panel results

To move forward in examining mode changes in the post-buckling analysis for more complicated cases, this section will outline results for stiffened panels. Stiffened panels are very common in aircraft design. The use of stiffeners assists by dividing the skin into smaller plats which each carry a proportion of the load applied to the panel. Consequently, a numbers of stiffened panels were analysed using the exact strip program VICONOPT.

All the panels initially buckled locally (skin buckling) in order to illustrate the mode jumping phenomenon in which the number of half wavelengths through the length of the panel in a skin bay between stiffeners will increase by one when the jump occurs. The results were then compared with numerical analysis extracted from ABAQUS/CAE for validation. The panels had different isotropic and composite materials. Figure 6.39 shows a full description of the load and boundary conditions for the investigated panels.

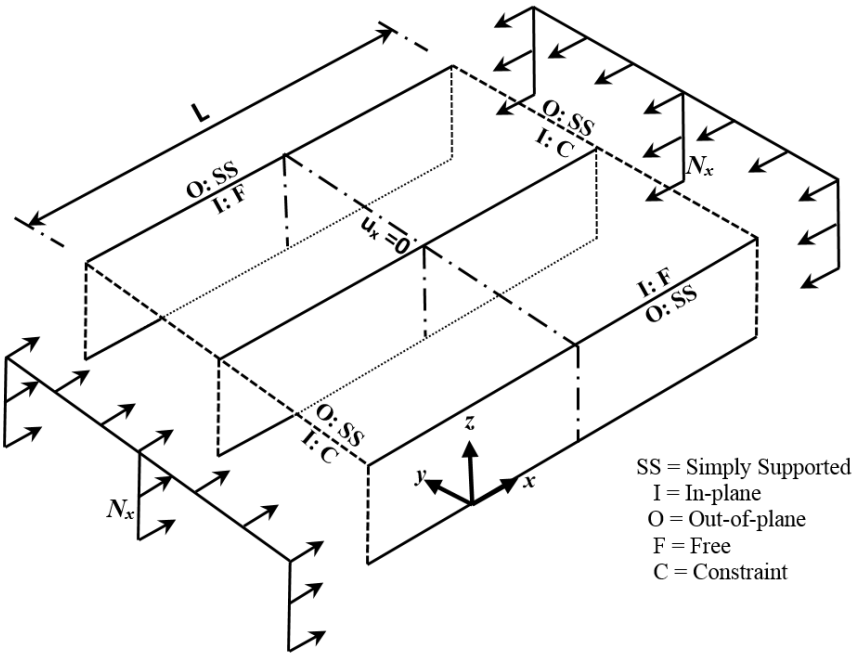

Figure 6.39: Proposed stiffened panels showing load and boundary conditions

The analysis was performed for two panels with metal and composite material respectively, the dimensions and material of those panels are shown in Table 6.1. The finite element analysis used the techniques used for a flat plate in the previous section using ABAQUS/CAE.

Table 6.1: Mechanical properties and dimensions of the examined panels

Property	Value	Units
Metal:		
Young's modulus, E_{11}	161	GPa
Poisson's ratio, υ_{12}	0.3	-
Mass density, ρ	2300	$kg.m^{-3}$
Composite:		
Young's modulus, fibre direction, E_{11}	181	GPa
Young's modulus, transverse direction, E_{22}	10.3	GPa
Poisson's ratio, υ_{12}	0.28	-
In-plane shear modulus, G_{12}	7.17	GPa
Mass density, ρ	1760	$kg.m^{-3}$
Panel width, b	240	mm
Panel length, a	260	mm
Skin thickness, t_{sk}	1.5	mm
Stiffener thickness, t_{st}	2.0	mm
Stiffener height, h_f	30	mm
Skin lay-up (composite),	[45, -45, 0, 90, -45, 45]s	
Stiffener lay-up (composite),	[45, -45, -45, 45, -45,45, 45, -45]s	

The ABAQUS analysis used two models, as before. The former was the linear buckling model created with ABAQUS/Standard using the step procedure type "linear perturbation/buckle" in order to provide the initial buckling load factors and mode shapes. The latter utilised the ABAQUS/Dynamic explicit step to provide the buckling and post-buckling analysis using geometrical nonlinearity concepts to evaluate the load-end shortening relationship after the initial buckling stage. A geometrical imperfection was applied in the model to provide a linear superposition between the linear buckling mode and

the dynamic analysis. Two imperfections were written in the second model representing the initial and second buckling modes targeted in the mode jumping investigation. The maximum values of the geometrical imperfection were 22% of the skin thickness, and as in the flat plate cases, the initial buckling mode had a slightly higher imperfection than the second mode that the panel tends to jump to. Also, "MPC" multi-point constraints were applied on the loaded edges to make the in-plane displacements are equal at all node of those edges, so that they moved as a line to match the VICONOPT analysis. The initial buckling mode was the same for both isotropic and composite panels namely a local buckling with two half wavelengths while the second critical mode had m=3. The first and second critical buckling modes are shown in Figure 6.40 in which the panel skin buckles locally in a sinusoidal mode along the length of the panel.

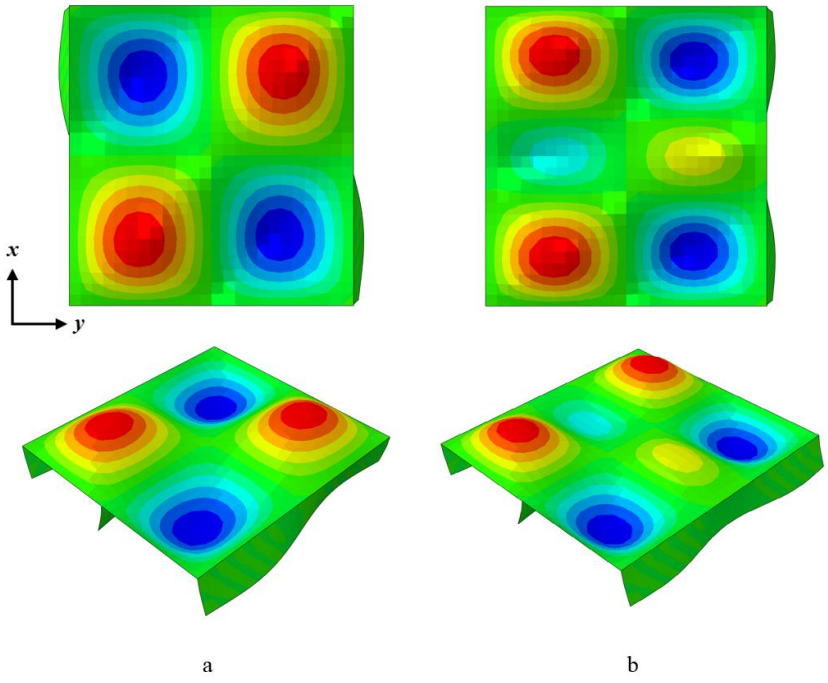

Figure 6.40: ABAQUS linear buckling mode shape for stiffened panel
(a) mode m=2, (b) mode m=3

6.9.1 Isotropic panel

The post-buckling analysis results for the isotropic stiffened panel using the exact strip method show that the initial critical buckling mode was a skin local buckling with *m*=2 at strain value 7.311E-04, while the second critical mode was *m*=3 at 7.593E-04. The energy calculation showed that the jumping strain was 7.261E-3 (7.174E-3 using the 3rd order polynomial method). However, the effective width method estimates the point of mode change is lower, occurring at strain level 5.868E-3, at which the load jumps from 218.40 to 221.54 kN. The two equilibrium paths *m*=2 and *m*=3 are close and grow side by side. The fact that the two approaches provided different strain jumping values was completely understandable due to the different assumptions and solution procedure used in the two approaches. The effective width results showed a early jumps at strain 5.868E-3 which considered that the skin bay between stiffeners is a simply supported plates and this assumptions could explain the early jump. The finite element non-linear analysis using the ABAQUS dynamic explicit analysis step showed mixed buckling mode curve depending on the modes (*m*=2 and *m*=3) exported from the linear buckling model. The ABAQUS post-buckling curve started to buckle with two half wavelengths and then a new buckle initiated and started to grow until there was a change to a new mode shape *m*=3 as shown in Figure 6.41. The mode change in finite element analysis is smooth, and there was no sudden jump because of the numerical solution techniques used in ABAQUS. Mode shapes, represented by out of plane deformations contour plot, at different strain levels through the post-buckling paths are illustrated in Figure 6.42. The figure shows that the initial buckling occurred at strain value 6.845E-4, which was lower than the buckling strain in VICONOPT analysis due to the effect of imperfection that make the panel buckle earlier, and the buckling point was mixed in the curves providing a smooth transition between buckling and post-buckling regions.

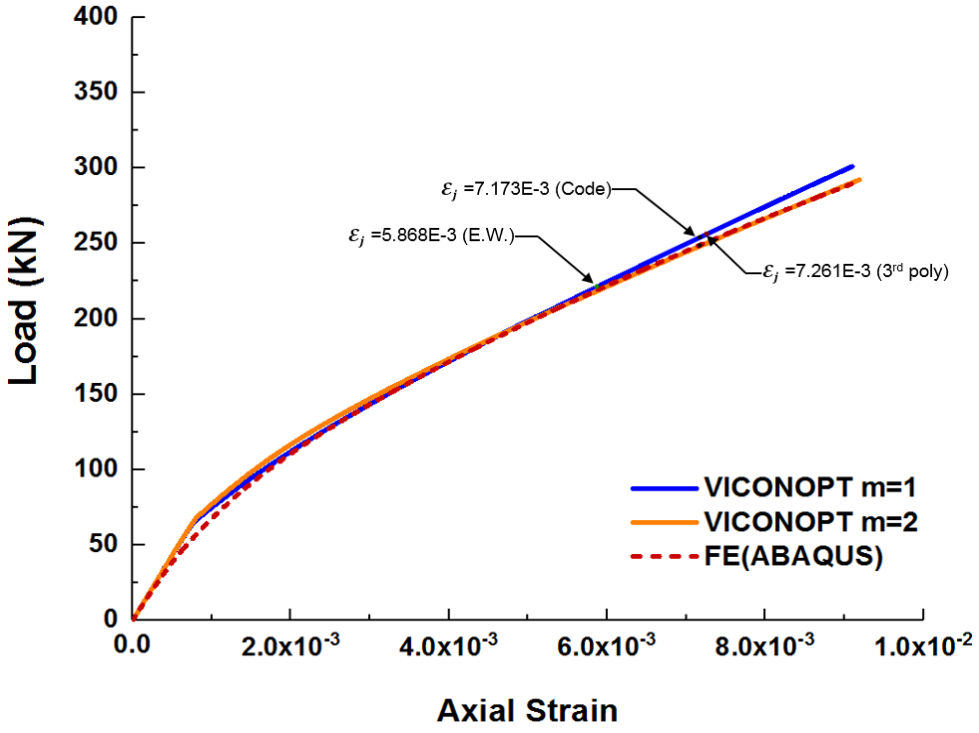

Figure 6.41: Load-strain curve for post-buckling analysis of isotropic stiffened panel

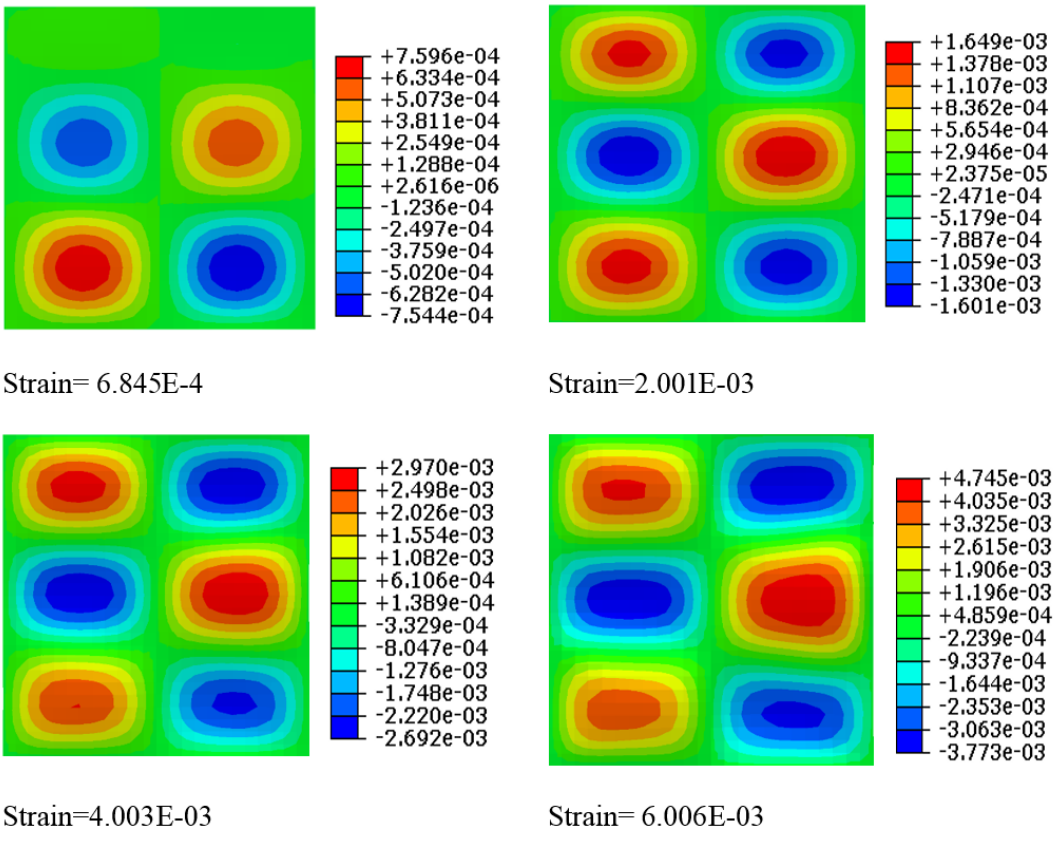

Figure 6.42: ABAQUS contour plot of out of plane displacement for the isotropic stiffened panel

6.9.2 Composite panel

The investigation of post-buckling analysis for a composite stiffened panel including mode jumping point detection will be discussed here. The panel has the same dimensions and boundary conditions of the isotropic panel studied previously. Exact strip analysis showed that the panel skin buckled locally with m=2 and the second buckling mode was m=3. The mode changing point was investigated as before in term of mode jumping strain. Unlike the metal panel, the results for the composite panel showed that the effective width methods estimated a relatively late jump at strain 5.872E-3 with load dropping from 84.325 to 82.836 kN, whereas the energy approach predicted that the jump happened at strain values 5.328E-3 (5.302E-3) in which the load jumped from 78.825 to 77.962kN (79.078 to 77.721 kN). The jump occurred at a strain level approximately nine times the initial buckling strain. This relatively late jump can be interpreted by the fact that a stiffened panel has a higher ability to carry loads after initial buckling. The results are presented in Figure 6.43. The finite element analysis showed almost the same behaviour as the previous panel. The ABAQUS analysis showed a gradual mode change and it is possible to describe the finite element analysis curve as a multi-mode post buckling equilibrium path. The gradual change in the out of plane displacement contour plot is presented in Figure 6.44, which shows a smooth mode jump through chosen stations along the post-buckling path at different strain levels. The differences in mode shape changing between VICONOPT and finite element analysis in terms of the switching time was clear due to many reasons such as the different methods of analysis, the effect of imperfections and the element size compared to strip size in VICONOPT. However, both softwares showed a similar behaviour and very close responses in terms of the load-end shortening relationships and the mode-jumping occurrence, which is a fact that could not be ignored despite the difference in the mode jumping mechanism.

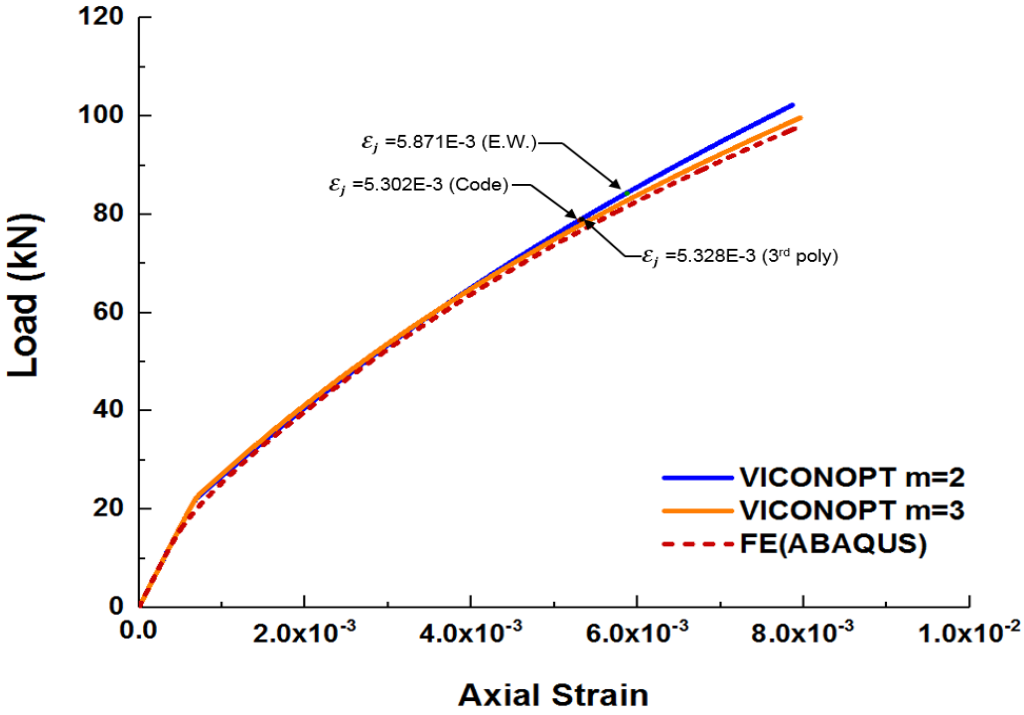

Figure 6.43: Load-strain curve for composite stiffened panel

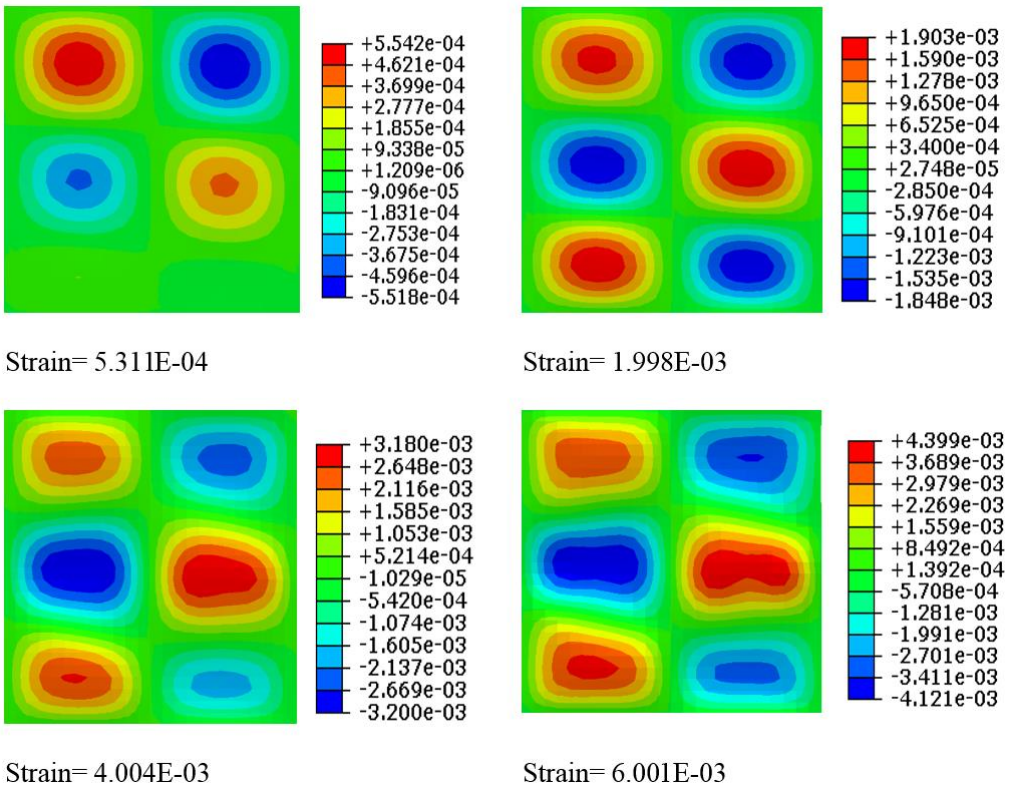

Figure 6.44: ABAQUS contour plot of out of plane displacement for the composite stiffened panel

6.10 Chapter summary

Chapter 6 illustrates a theoretical investigation to explore the mode-jumping phenomenon in post-buckling analysis of thin-walled structures. First, the motivation of this study was explained which was improving the post-buckling analysis of exact strip analysis software VICONOPT. An explanation about mode jump occurrence in the post-buckling region in terms of the cause, mechanism and type of jump was presented before introducing the proposed approaches to predict the jumping point.

The proposed solutions include two different methods, which are based on two well-known principles in the structural analysis of plated members. The former was an effective width approach based on von Karman's effective width concept. Consequently, a brief review of this concept was described before introducing the proposed solution method. The latter method depends on an energy comparison between different equilibrium paths by assuming that the jump can only occur from one path to another, which has lower strain energy.

Two mathematical techniques were used to calculate and compare the energy in order to specify the transformation point of mode change. The first one is called the third order polynomial method because it was assumed that the post-buckling path is a 3^{rd} order polynomial curve. Interpolation and integration techniques were used to evaluate the area under those curves. The procedure was coded in Matlab to find the target jumping strain. The second technique was based on the trapezoidal method to calculate the energy and compare it at each post-buckling cycle. This method was written as a code using FORTRAN 77. The code read the post-buckling stress and strain values from VICONOPT result sheets, and then used the energy comparison to find the strain at which the mode jump occurs. The results are compared with finite element analysis using ABAQUS/CAE software utilising the dynamic explicit step analysis for validation. Then a number of isotropic and composite flat plates and stiffened

panels were analysed to prove the ability of the proposed solution approaches to specify the jumping point (strain). The main conclusions of this chapter are:

- The first proposed approach based on effective width concept provides a simple and fast mathematical method to evaluate the jumping strain. The method showed an acceptable prediction in most of the examined plates and panels except some cases with specific aspect ratios. This is due to the approximations included in the calculations procedure such as the assumption that the middle strip carried zero load, which is in fact not completely true.
- The second proposal which was used to predict the mode jumping point (strain) utilised the energy principle to compare the strain energy stored in different equilibrium paths in order to capture a point where the mode jump might occur. The calculations use a Matlab program to provide the jumping strain. The first calculation method assumes that the post buckling paths are curves with third polynomial equations. The energy was calculated using interpolation and integration techniques to compare and predict the jumping point. The second method used the trapezoidal integration method to calculate the energy for different post buckling equilibrium paths. This method was written as FORTRAN code which uses the VICONOPT post buckling data for different modes to estimate the mode jumping strain.
- When compared with ABAQUS/Dynamic explicit nonlinear finite element buckling analysis, the results of post-buckling analyses produced by VICONOPT for both flat plates and stiffened panels showed better agreement when mode jumping was accounted for.

Chapter 7: Mode Jump in Post-buckling Analysis of Stiffened Panels (Experimental Approach)

7.1 Introduction

This chapter focuses on examining by experimental testing the effect of mode jumping phenomenon on the post-buckling response of isotopic stiffened curved and flat panels. This type of structure is of significant interest to the aerospace industry, and it is therefore necessary to understand its behaviour under real loading conditions through experiments. The panels tested were subject to in-plane compression and monitored using digital image correlation (DIC) to visualise three-dimensional field deformations and strain gauges to measure the axial displacement in the direction of loading at different locations on the panels. The experimental results were compared with finite element (FE) analysis results, which used to validate the exact strip method discussed in the previous chapter.

7.2 Specimen material and manufacturing

7.2.1 Skin material

The stiffened panel specimens were manufactured from two parts, the skin and the stiffeners. The skins were manufactured from aluminium alloy 6082-T6 sheet [175] of 1.0 mm thickness. They were cut to the required size of the available test rig using a BAILEICH Guillotine as shown in Figure 7.1a, and then rolled in the rolling machine shown in Figure 7.1b. Rivet holes were then drilled at a spacing of 25mm (c/c) using an EDGE3000 as shown in Figure 7.1c, to enable attachment of the rivets. Finally, the skins were cleaned to prepare them for assembly.

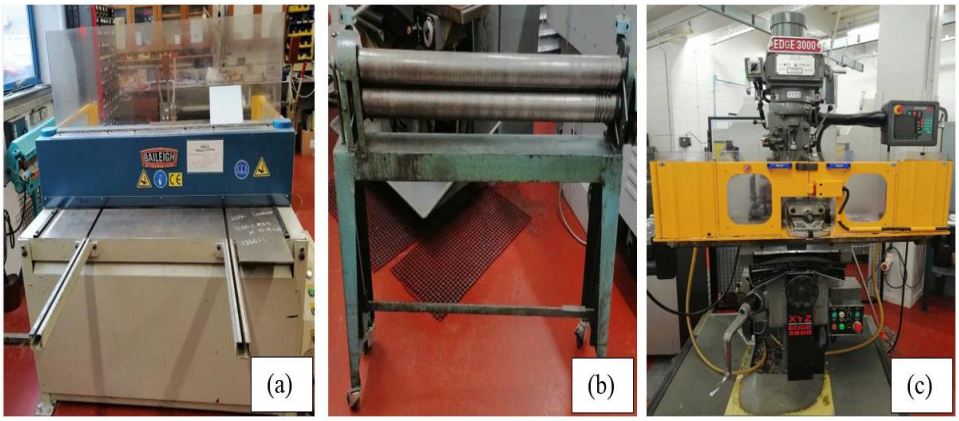

Figure 7.1: Specimen manufacturing machines (mechanical workshop)

7.2.2 Stiffeners material

The stiffeners were made from 6082-T6 aluminium angle (50 mm x 50 mm x 1.5 mm) which was used to generate L-shape stiffeners with dimensions 50 mm x 20 mm x1.5 mm. Each panel had five identical stiffeners, which were attached to the skin using Loctite Multi-bond 330 adhesive bond metal and 25 rivets, see Figure 7.2. The panels were then left at room temperature for 48 hr for the adhesive to cure.

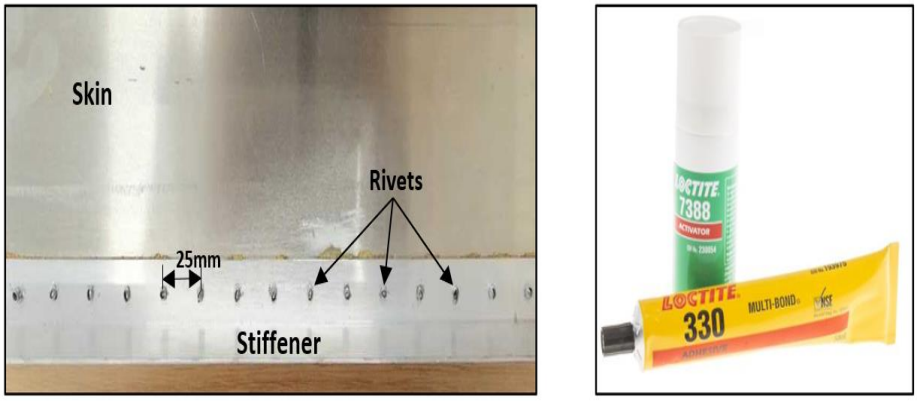

(a) (b)

Figure 7.2: Stiffener- skin connections,
(a) The skin-stiffener rivet connection, (b) Adhesive

7.2.3 Material properties test

The aluminium sheets and angles, which were used to manufacture the stiffened panels, were tested to provide accurate mechanical properties particularly with respect to the onset of plasticity to be used in the finite element models developed. Tests were carried out according to British Standard 6892 [176]. Three samples from the skin and the stiffeners were tested. Specimen dimensions are provided in Figure 7.3.

Test were carried out using a Zwick/Roell testing machine as shown in Figure 7.4a. Specimens before and after the test are shown in Figure 7.4b, and 7.4 c respective. All the specimens failed due to a fracture which occurred approximately at the mid length of the web. The results of the test in terms of stress strain curves are illustrated in Figure 7.5.

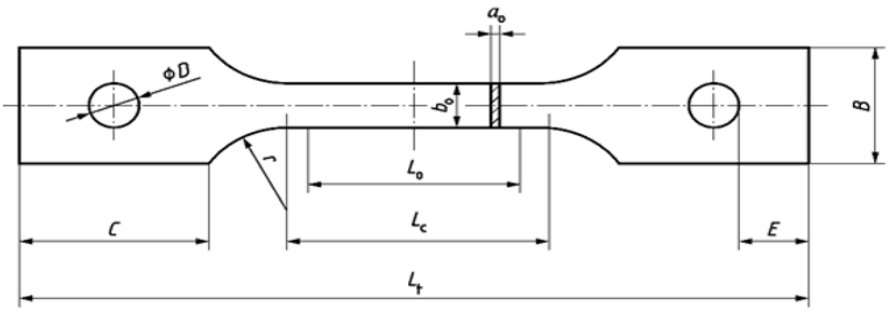

a_o	original thickness	L_o	original gauge length ($L_o = 50$ mm)
b_o	original width of the parallel length	L_c	parallel length ($L_c \geqslant L_o + b_o$)
r	transition radius	L_t	total length of test piece
B	width of the gripped ends	D	diameter of the hole
C	length of the gripped ends	E	distance from the test piece end to the hole

Dimensions in millimetres

a_o ⩾	a_o ⩽	b_o	L_o	r	B	C	D	E	L_c min.	L_t min.[a]
0,1	3,0	12,5	50	25	35	50	15	17	62,5	205

[a] The minimum value is only sufficient when the parallel length L_c is the minimum value.

Figure 7.3: Tensile strength specimen dimensions according to B.S. 6892

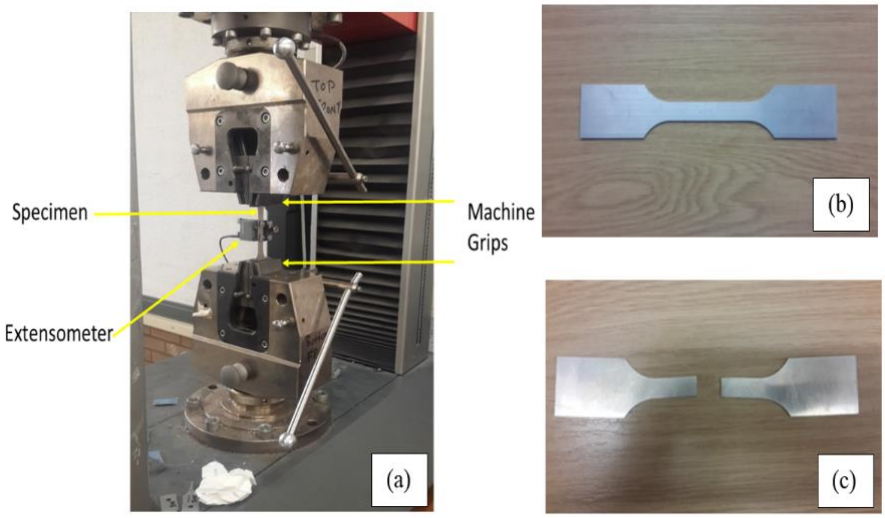

Figure 7.4: Material properties tensile test,
(a) Test set-up, (b) Specimen before test, (c) Specimen after test

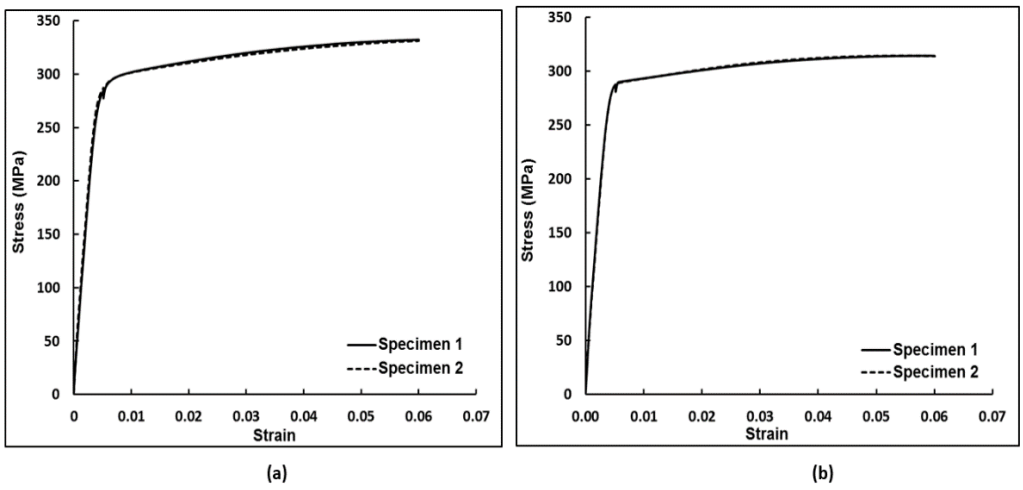

Figure 7.5: Stress-strain curves for the aluminium used in panel manufacturing, (a) Skin sheet, (b) Stiffener angle

Table 7.1: Mechanical properties

Property	Value	Units
Young's modulus, E_{11} (material sheet)	70.0	GPa
Young's modulus, E_{11} (experimental), skin	72.2	GPa
Young's modulus, E_{11} (experimental),stiffener	72.6	GPa
Poisson's ratio, ν_{12}	0.3	-
Mass density, ρ (material data sheet)	2700	$Kg.m^{-3}$

7.3 Stiffened panel specimens details

The stiffened panels investigated had three different geometries. The panels were similar except for their radii of curvature. The tested specimens were chosen with specific dimensions and boundary conditions for the following reasons:

- Stiffened panels are usually able to carry the additional load after initial buckling which provides relatively stable post-buckling behaviour and crucially the opportunity to capture the mode jump.
- Despite their simple geometry, the panels were representative enough to enable the post-buckling behaviour of real aircraft components in both geometry and proportion.
- The number of studies which have been carried out to investigate the behaviour of stiffened panels with L stiffeners is relatively small.
- A suitable test rig was already available.

Based on the these considerations, six stiffened panels were manufactured, two with radii of curvature 400 mm, two with 800 mm, and two ∞ (flat). Stiffeners were fixed with the 20 mm section flush against the main panel and 50mm perpendicular to the skin. These were equally spaced; however due to their orientation (see Figure 7.6) this resulted in a panel consisting of three skin bays with 80 mm of unsupported skin and a fourth in which only 60 mm was unsupported. The surface of the panels was spray painted white, using a white primer, with a black speckled pattern applied for use with the DIC system as will be explained in section 7.4.2.

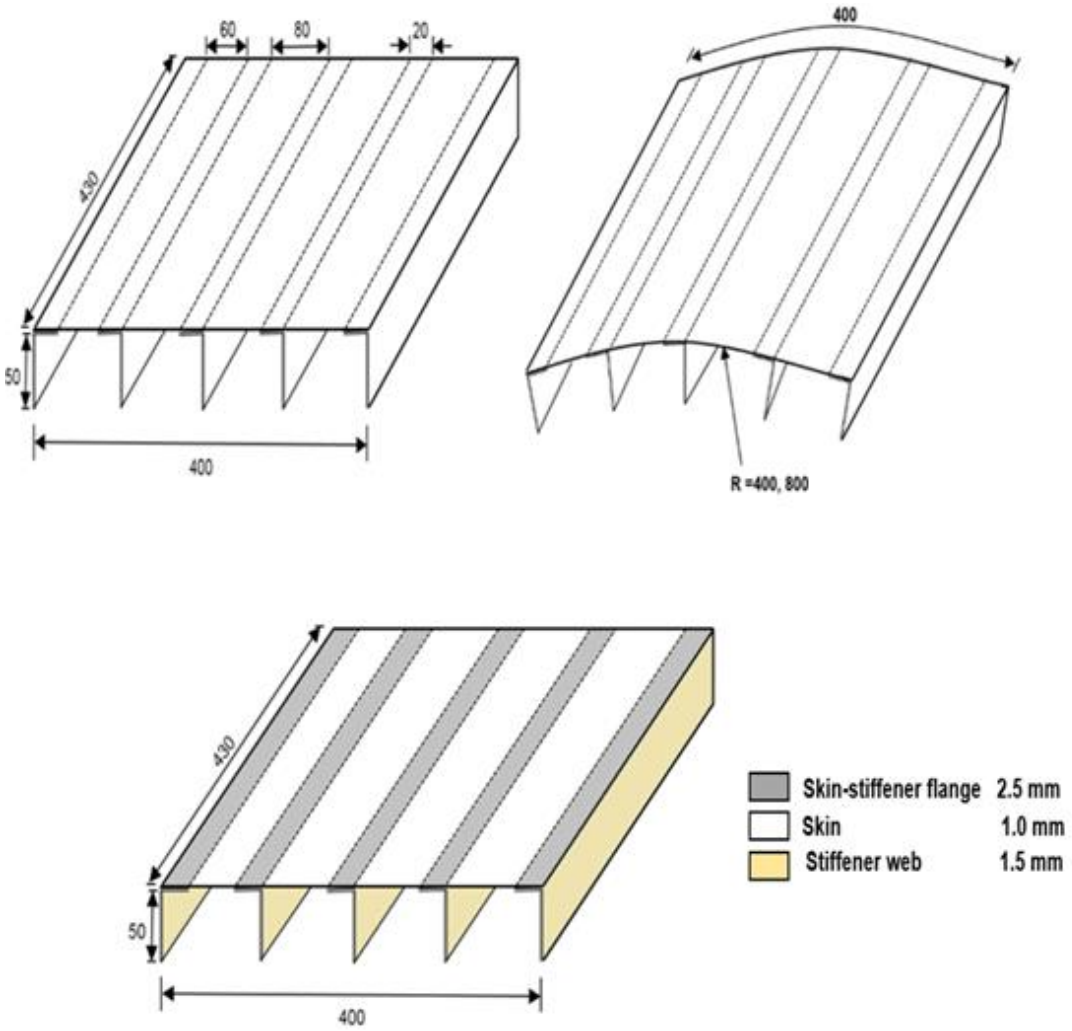

Figure 7.6: Panel dimensions (all dimensions in mms)

7.4 Test monitoring techniques

In this study, two systems were used to monitor the responses of the panels under load: strain gauges to record axial strains of both skin and stiffeners and digital image correlation (DIC) to monitor 3D skin surface deformations.

7.4.1 Strain gauges system

Twelve strain gauges were attached in different positions on the skin and stiffeners. The gauges were sliver-clad copper KFGS-5-120-C1 produce by

KYOWA company [177], see Figure 7.7. Six gauges were located on the two skin panels in locations selected to coincide with the peaks of the buckles at different points during the post buckling process whilst the others were distributed over the three central stiffeners as shown in Figure 7.8.

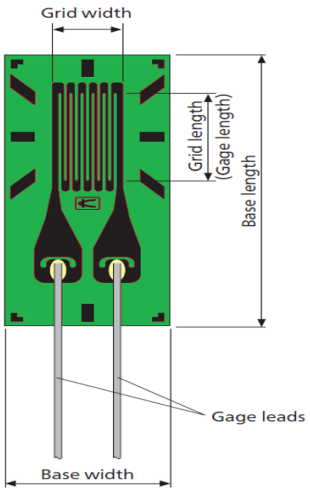

KFGS-5-120-c1-23 (Dimensions)		
Grid		
length	5	mm
width	1.4	mm
Base		
length	9.4	mm
width	2.8	mm

Figure 7.7: Strain gauges type KFGS-5-120-c1-23

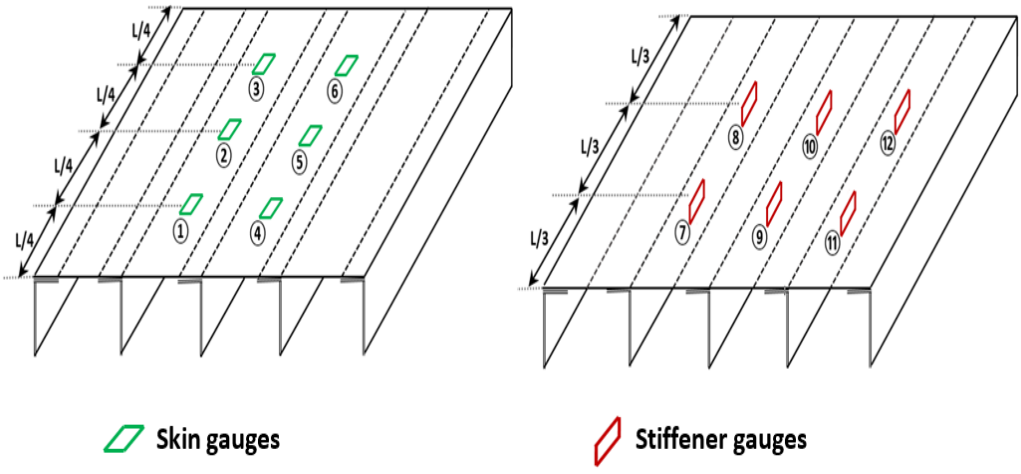

Figure 7.8: Strain gauges locations

7.4.2 Digital image correlation (DIC) system

Digital image correlation is an optical measurement technique used to carry out full field, non-contact, two or three-dimensional measurement of the shape, displacements and strains in a specimen during testing. The system determines the targeted surface's displacement from digital images of a random speckle pattern applied to the surface using a process of pattern recognition tracking. Images captured from the surface as it deforms are compared with a reference image taken from the undeformed surface before load application.

7.4.2.1 La-Vision (DIC) system

The Strain Master DIC system used in this work is shown in Figure 7.9. This system was programed to captures an image every 2.0 seconds (user defined) automatically through the system set-up.

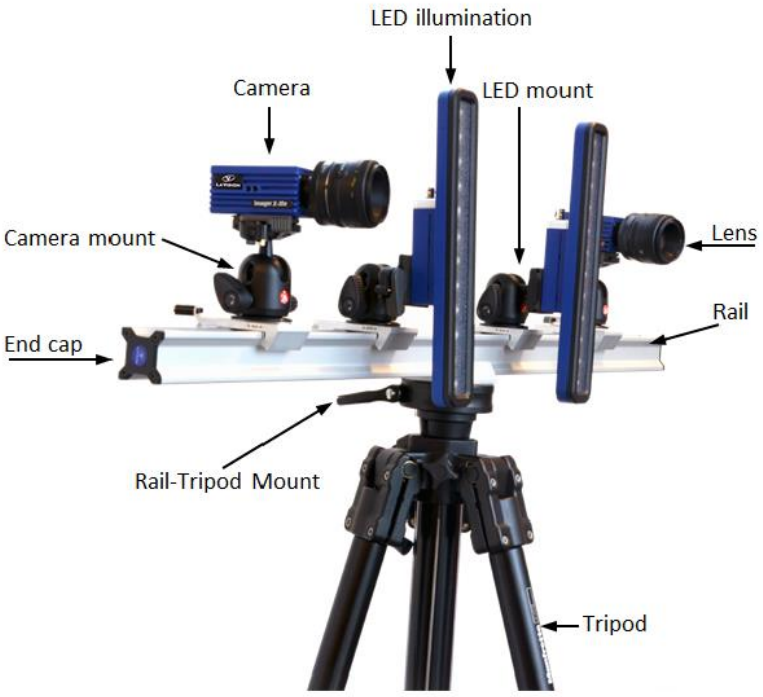

Figure 7.9: La-Vision DIC system components

7.4.2.2 Speckle pattern

Before testing, each specimen was prepared for DIC by applying a speckle pattern. The optimum pattern is a random, rich in contrast, speckle pattern, which is typically created using spray paint. To achieve this, the samples were first cleaned carefully and then painted in two stages. First, two thin layers of white primer were applied to improve the contrast and then the speckle pattern was added which was made by black paint in a random arrangement as shown in Figure 7.10.

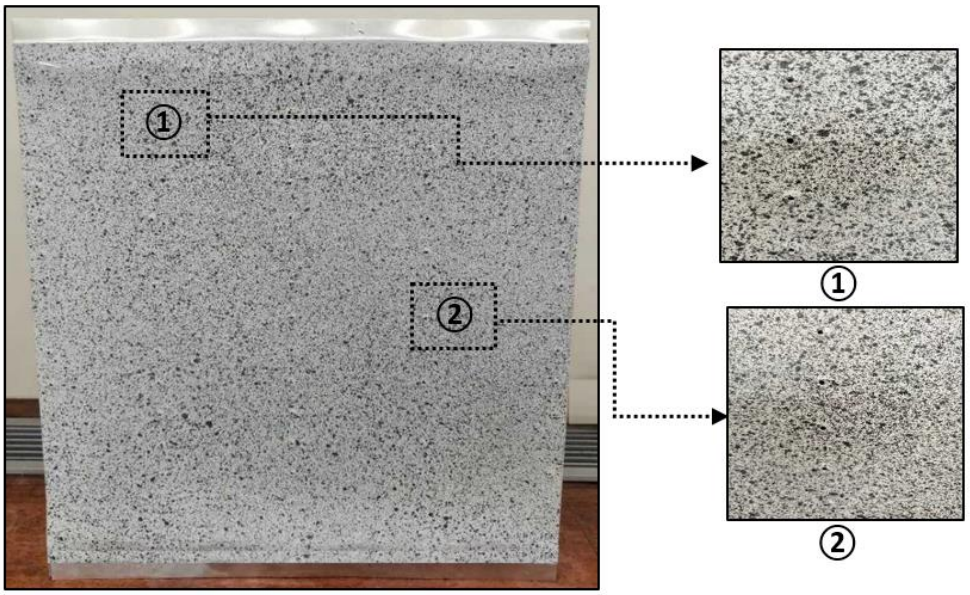

Figure 7.10: Speckle pattern

7.4.2.3 DIC calibration and set-up

The system setup used is shown in Figure 7.11. A pair of Imager X-lite 8M CCD cameras fitted with 24 mm F/2.8 lenses were used. These are progressive scan, fully programmable cameras, with a resolution of 3312 x 2488 pixels. Calibration was performed using calibration plate number 058-5 shown in Figure 7.12 by a fully trained technician, who also supervised the system during the test.

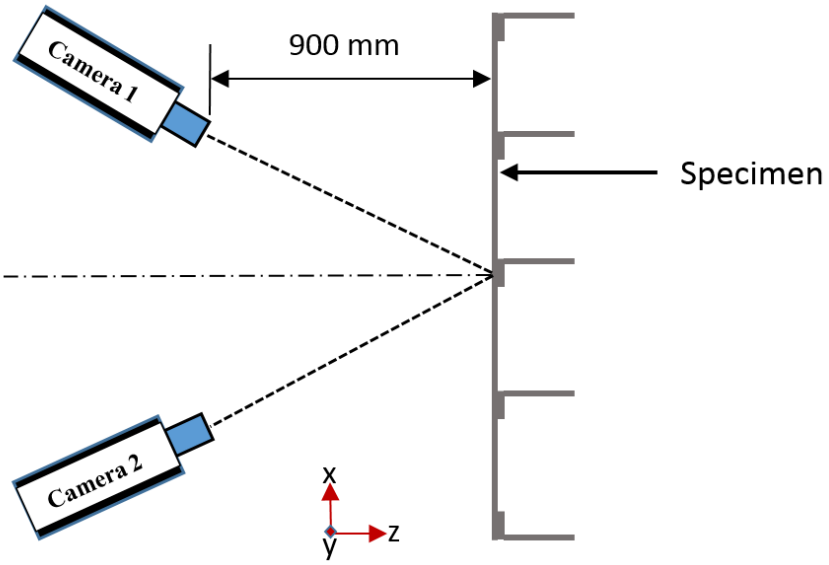

Figure 7.11: DIC system set-up

Figure 7.12: (a) LaVision X-lite 8M DIC camera, (b) calibration target plate

7.5 Test set-up

The test utilised a specially designed test rig shown in Figure 7.13, manufactured from stainless steel to apply a uniformly distributed compression load. The rig was mounted in a 500 kN Zwick servo-hydraulic testing machine. Axial alignment was maintained by four guide rods running

on linear bearings in the plate. The six specimens tested were fixed in the rig using full clamps inserted into the top and bottom frame, which prevent any rotation in the specimen horizontal ends as shown in Figure 7.14a and 7.14b. These edges provided fully clamped boundary conditions along the bottom edge, with the top edge having the same condition except for the axial movement, Figure 7.14. The test was performed under displacement control with a crosshead velocity of 0.15 mm/min.

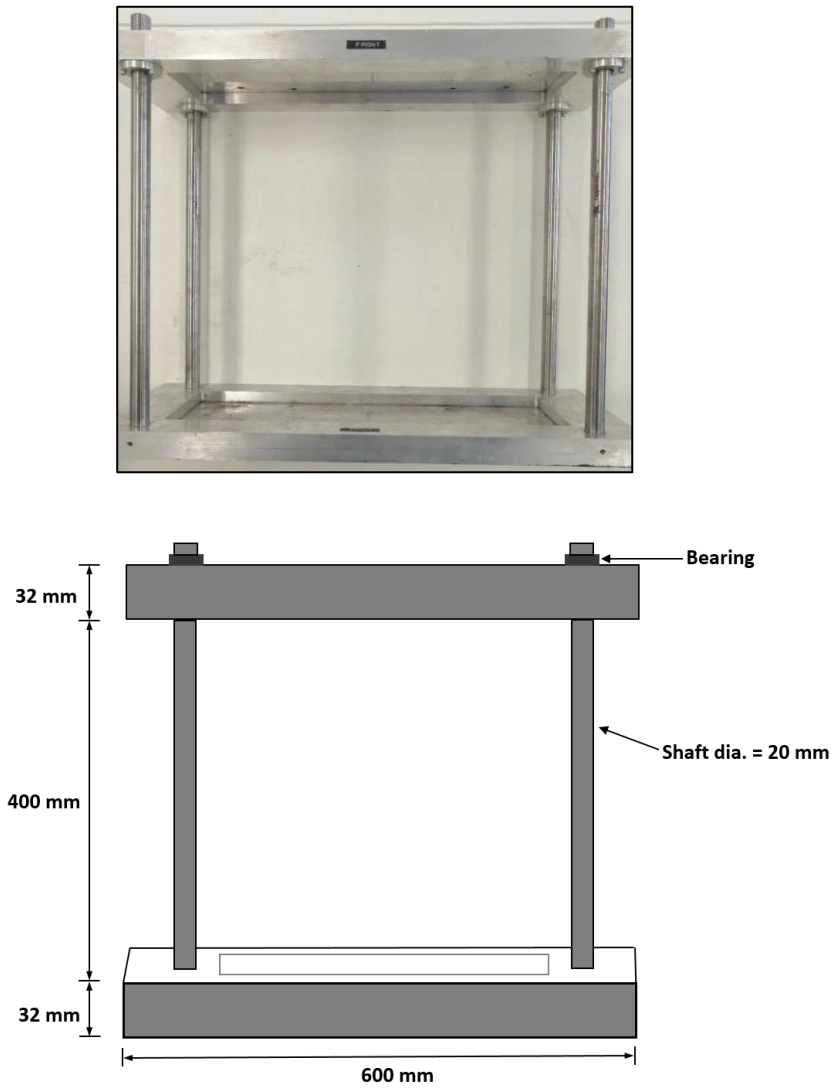

Figure 7.13: Test rig used in the stiffened panel experiment

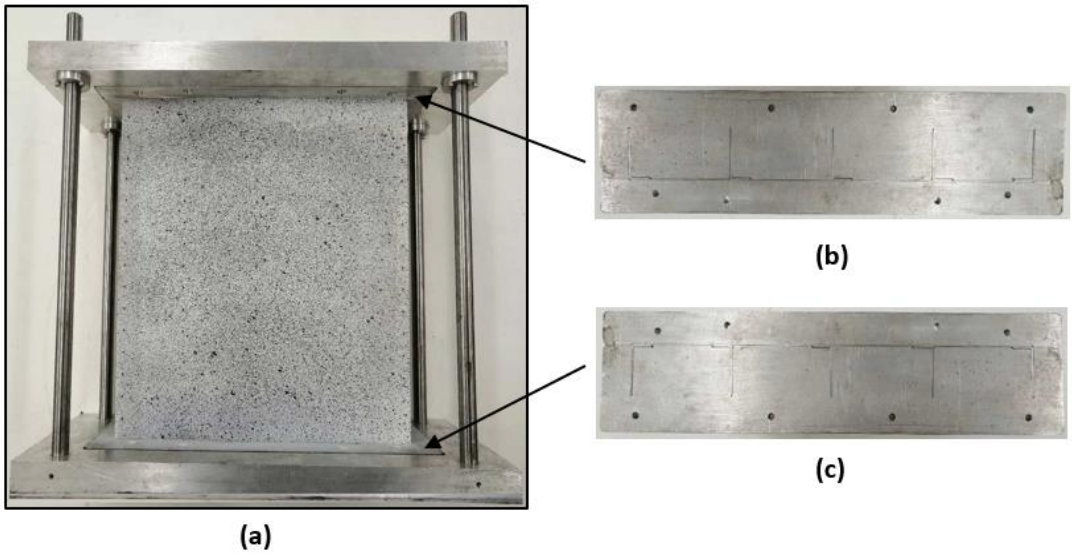

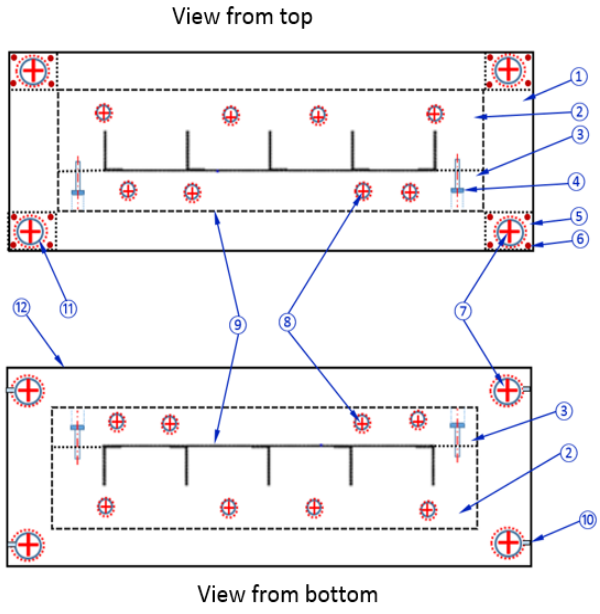

Item	Part name	Part number
1	Rig top plate	1
2	Panel clamp 1	2
3	Panel clamp2	2
4	(M6x40) caphead machine screws	4
5	Bearing clamp	4
6	(M3x6) bottom head machine screws	16
7	Shaft	4
8	(M6x25) countersunkmachinescrew	16
9	Specimens (stiffened panel)	1
10	(M4x10) grub screw	4
11	Bearing	4
12	Rig bottom plate	1

(d)

Figure 7.14: (a) Specimen mounted in the test rig, (b) Top clamp with specimen inserted, (c) Bottom clamp with specimen inserted, (d) clamp details

The complete test set-up including strain gauging and DIC is shown in Figure 7.15 and 7.16.

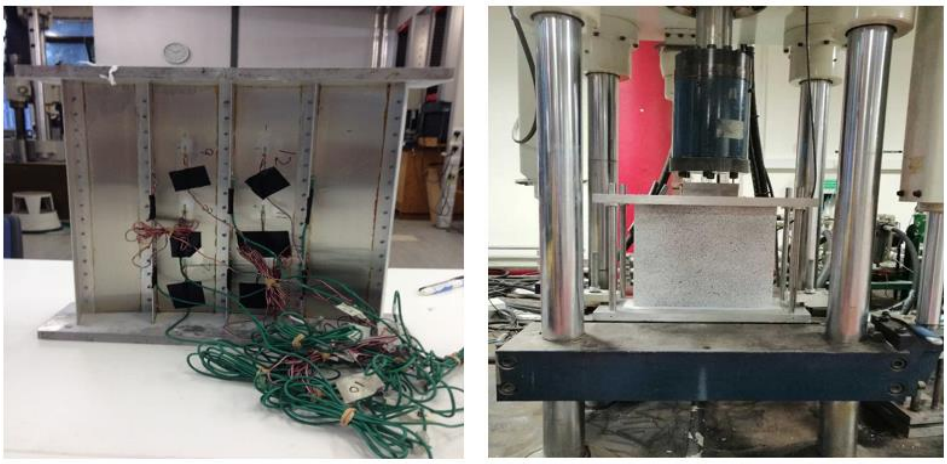

Figure 7.15: (a) Strain gauges positions, (b) test set up

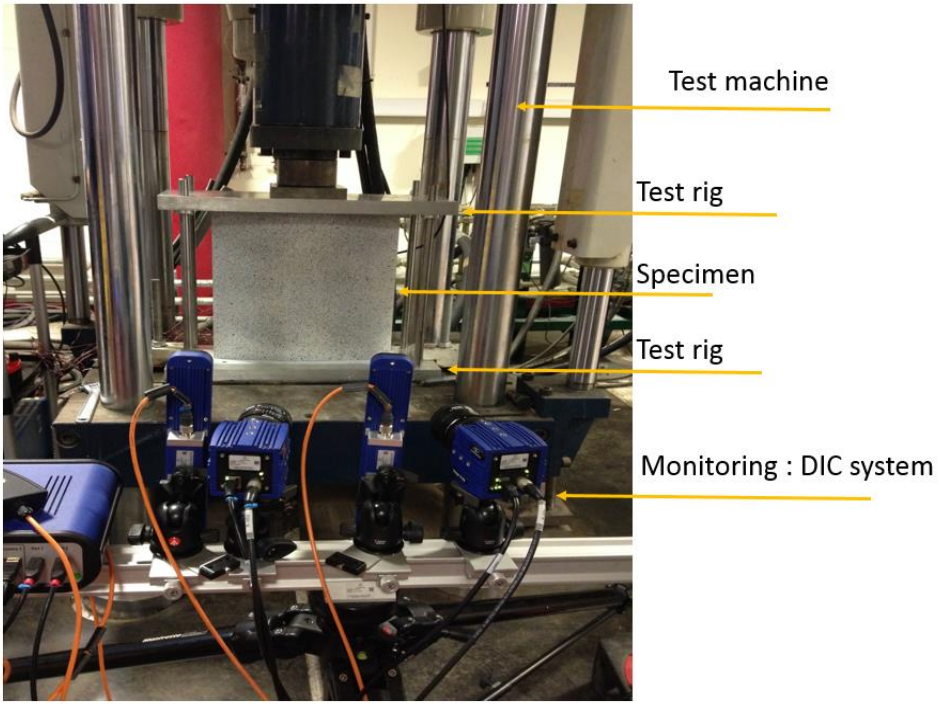

Figure 7.16: DIC set-up

7.6 Experimental results and discussion

7.6.1 Stiffened panels with 400mm radii of curvature

Figure 7.17 shows the load versus in-plane displacement curves for the two panels with radii of curvature 400 mm. The curves show that for the first specimen (400-1) significant displacement occurs initially with only a small increase in load. This is thought to be due misalignment between the ends of the stiffeners and the panel as shown in Figure 7.18 due to some of the stiffeners being slightly longer than the skin. Thus, a load eccentricity is generated with some of the stiffeners taking the whole of the load initially, resulting in relatively large deformations in these stiffeners, until their edges become aligned with the skin, after which the loading process continues normally across the whole of the specimen's loaded edge.

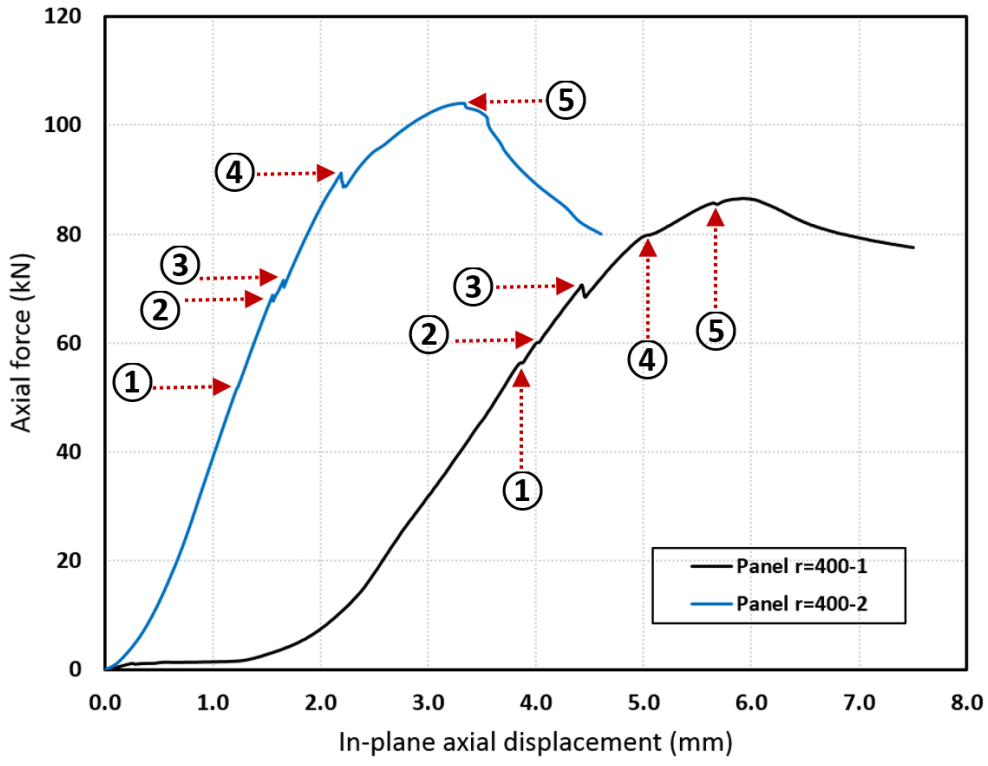

Figure 7.17: Axial load versus in-plane axial displacement for curved stiffened panels with a radius of curvature = 400 mm

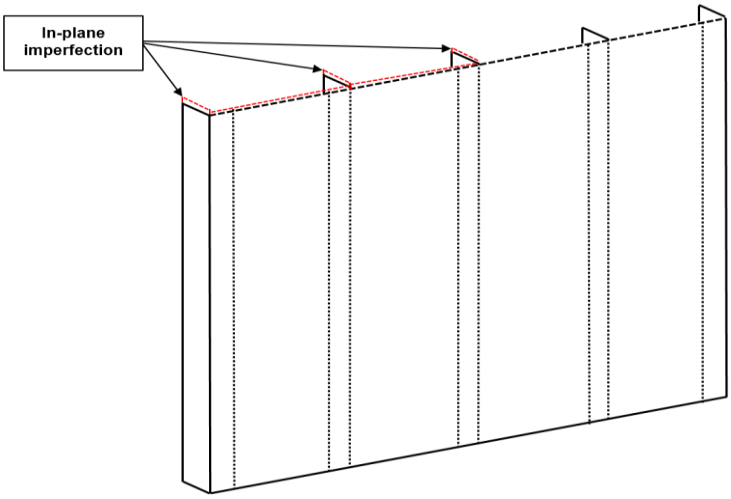

Figure 7.18: Initial manufacturing imperfection

This imperfection was significantly reduced in the second panel (400-2), which showed a significant decrease in this in-plane imperfection effect. The results for each panel will be discussed separately, starting with the first panel, for which DIC data is only available for the central part of the panel due to the position of the DIC cameras, as shown in Figure 7.19. This issue was solved in the three panels which were tested later.

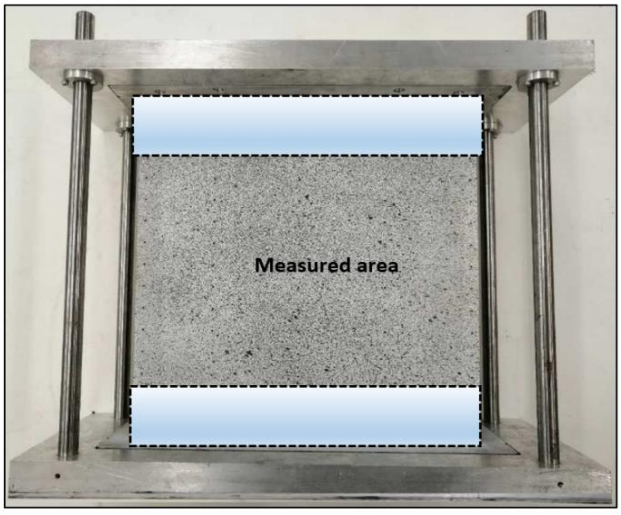

Figure 7.19: The area of panel 400-1,800-1, flat 1 captured by the DIC cameras

The load-shortening curves in Figure 7.17 can be described in relation to five key points. For the first panel (400-1) initial buckling occurs at a load of 56.344 kN with the skin in the first three bays between the stiffeners buckling with two half-wavelengths as shown in Figure 7.20a. wich represents point 1 on the curve. The fourth bay buckles slightly later at point 2 on the load-end shortening curve when the load was 60.091 kN, see Figure 7.20b.

A dramatic change occurs at point 3 with the panel jumping from its initial buckling mode to a new configuration with three buckles per bay and a corresponding drop in load from 69.947 to 68.420 kN. Unfortunately, this change is not very clear due to the missing part in the DIC images extracted from the test; however, the third buckle can just be seen at the bottom of the first and second skin bays in Figure 7.20c. The equilibrium path showed a sudden drop at point 4 which is when that the panel jumps to a new configuration and the skin buckled with four half wavelengths as shown in Figure 7.20d.

The final stage, starts at point 5 on the load-shortening curve, represents the beginning of the collapse stage at a load of 85.379 kN. Figure 7.20e and 7.20f show the blue buckles joining together in the lower part of the panel while the red ones in the upper part are due to severe bending with the skin and stiffeners failing due to high deformations. The specimen's failure configurations presented in Figure 7.21 showed a skin-stiffeners debonding near the loaded edge in which the separation occurred in different positions of the five stiffeners. The debonding of the longitudinal boundary stiffeners combined with a crashing noise and severe deformations in those stiffeners.

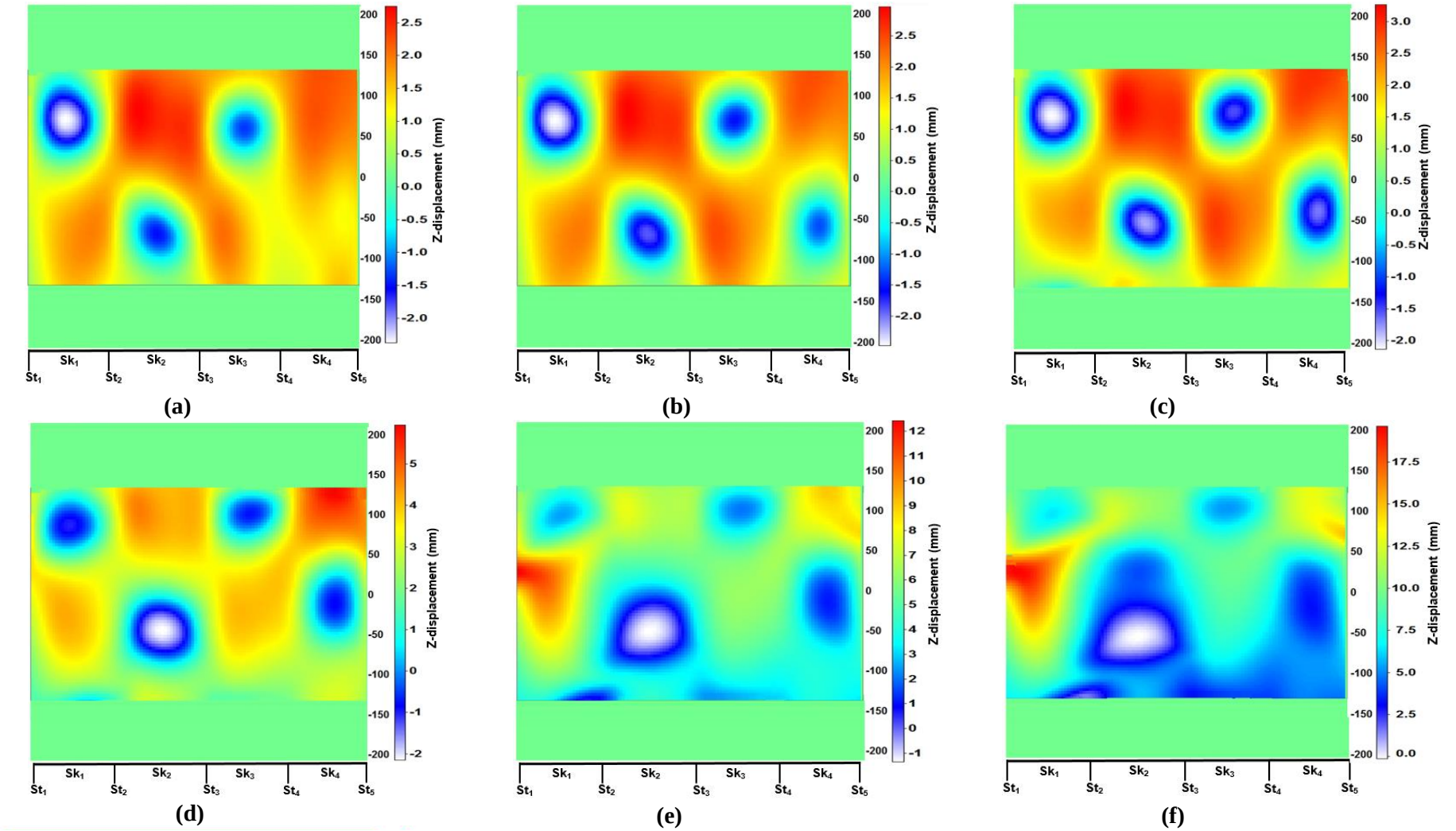

Figure 7.20: Panel 400-1 contours of out-of-plane displacement (DIC images)

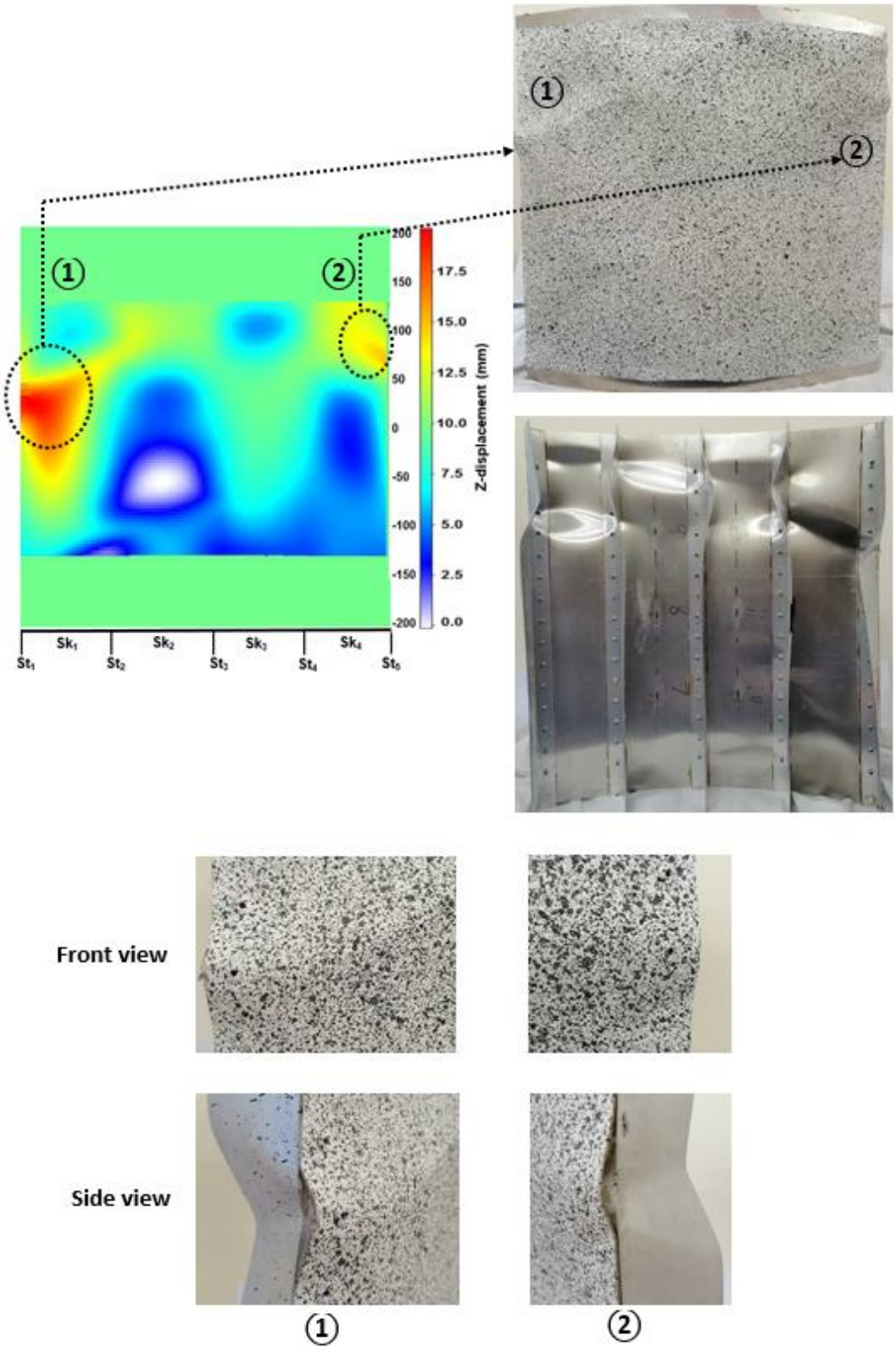

Figure 7.21: Panel 400-1 failure configurations

As discussed earlier the misalignment between the ends of the skin and stiffeners was significantly reduced in the second 400-2 panel although it was not eliminated. This panel started to show signs of initial buckling at 51.471 kN with a single buckle being observed near the top of the second bay at point 1 as shown in Figure 7.22a. This buckle transformed into two half-wavelength buckles at point 2 when the load reaches 68.135 kN, Figure 7.22b.

This mode becomes clearer as the out of plane deformation increases, with two buckles being observed in all four skin bays in Figure 7.22c. Although the load - shortening curve showed a potential mode jump at point 3, the DIC results showed that this is due to a further buckle appearing only in the third skin bay.

The full jump from the buckling mode *L/2* to mode *L/3* occurs at point 4, with the DIC images showing that the panels move to a completely new mode at this stage and all bays now contain three buckles. The jump from mode *L/2* to L/3 again does not occur in the four skin bays at the same time as shown in Figure 7.22d. This is potentially due to different imperfections in each bay and the fact that these imperfections have a significant effect on the mode-jumping occurrence. Moreover, the load eccentricity effect could be a reason for this behaviour.

A second jump occurred and the skin bay started to move to a new buckling mode that had four buckles instead of three at point 5, as shown in the DIC output data in Figure 7.22e. The stage after point 5 can be considered the start of the failure stage with the load dropping significantly from 102.89 to 82.221 kN by the end of the test as shown in Figure 7.22f. The failure features of this panel are illustrated in Figure 7.23 which showed a realtively late skin-stiffener debonding compared with the other panels.

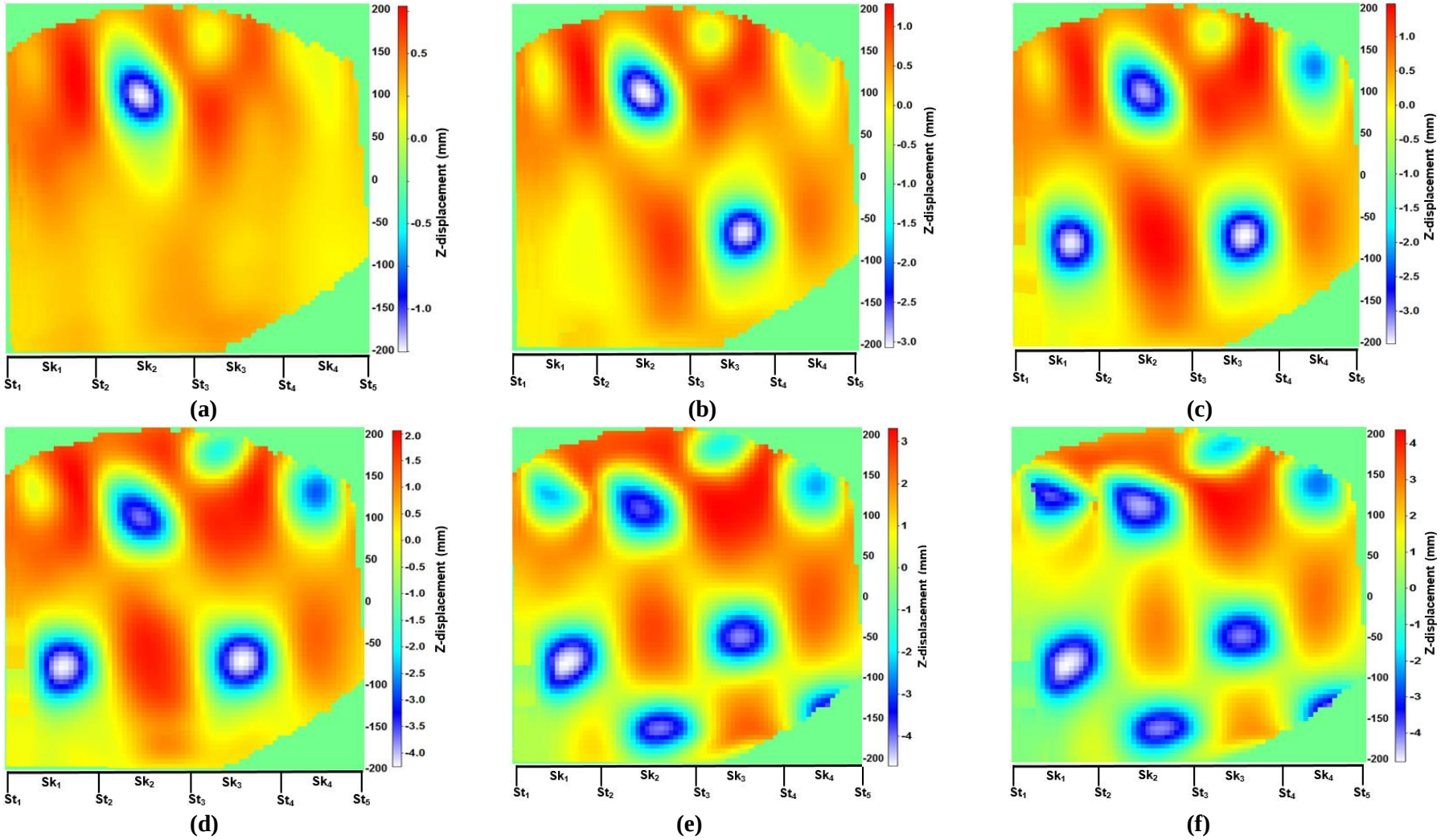

Figure 7.22: Panel 400-2 contours of out-of-plane displacement (DIC images)

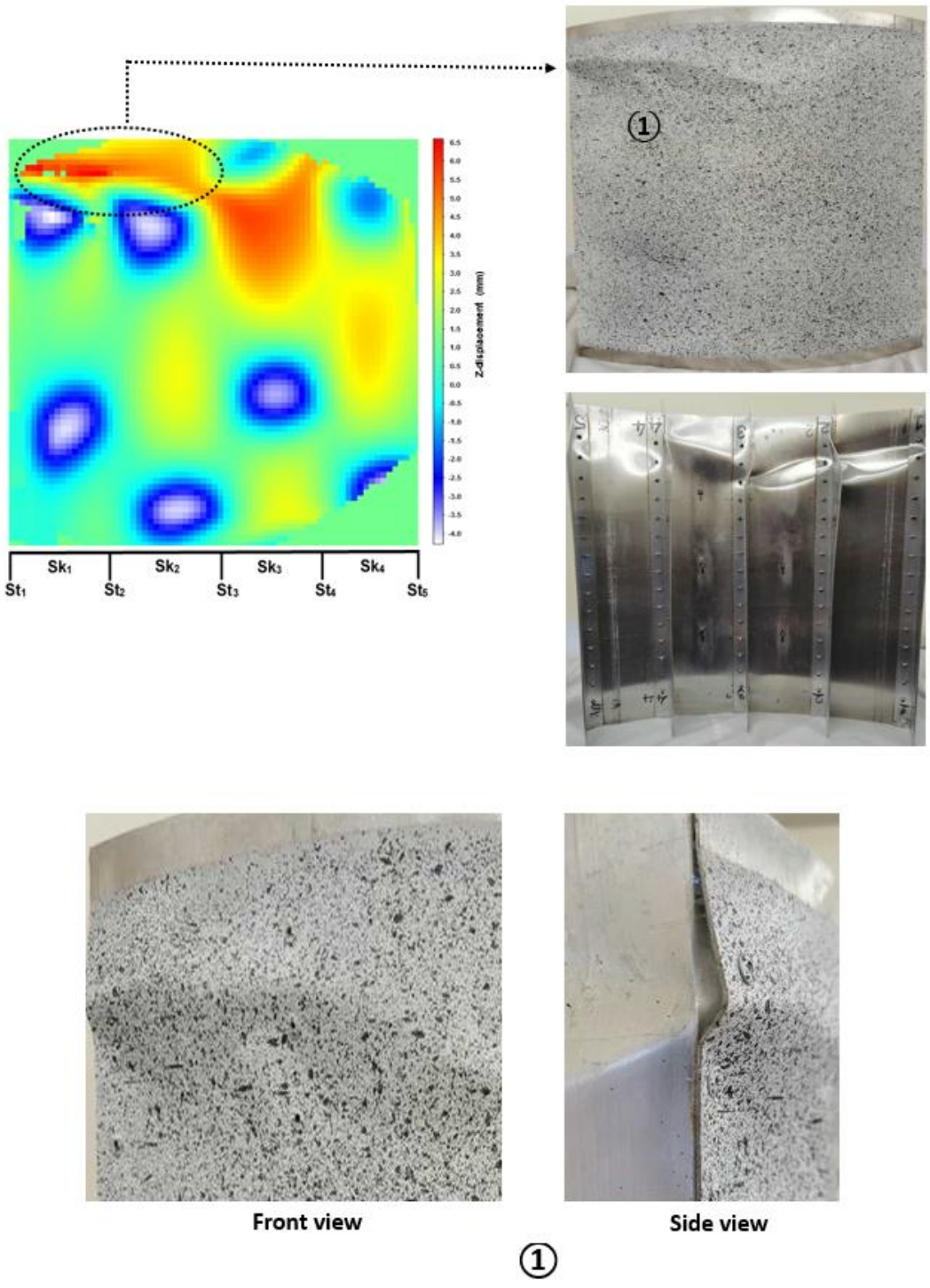

Figure 7.23: Specimen 400-2 failure configurations

7.6.1.1 Strain gauge results

This section will illustrate the strain gauge results and match them with results extracted from test machine and the DIC. More focus will be placed on the gauges positioned on the skin for two main reasons:

- The two 400 mm panels exhibited local buckling of the skin with the stiffener following the deformations in the skin due to the potential rigid skin-stiffener connection.
- Only the skin was observed by the DIC system, with the stiffeners fixed on the other side. Data for comparison with the strain gauges was therefore available for the skin side only. Observation of the stiffener behaviour would have required a more sophisticated system with more cameras than was available.

The stiffeners strain gauge data for the three middle stiffeners is however useful, and will therefore be presented here, since it provides some insight into the level of support provided by those stiffeners to the skin. As described earlier, two gauges were attached to each stiffener. Figure 7.24 and 7.25 show both the skin and stiffener gauge output data with the points corresponding to those highlighted on the end-shortening curves marked for comparison. The strain gauge data is presented as the relationship between load and micro-strain. The gauges are renamed from Figure 7.8 as outlined in Table 7.2, to facilitate interpretation.

The strain gauge readings for panel 400-1 are presented in Figure 7.24. The skin gauges show clear changes in behaviour at the same points as observed in the load-shortening curves, giving further insight into what is happening at these points.

Table 7.2: Strain gauges names according to positions

Gauge number	Position (Figure 7.8)	Gauge name
1	skin second bay	sk_1
2	skin second bay	sk_2
3	skin second bay	sk_3
4	skin third bay	sk_4
5	skin third bay	sk_5
6	skin third bay	sk_6
7	Stiffener 2	st_1
8	Stiffener 2	st_2
9	Stiffener 3	st_3
10	Stiffener 3	st_4
11	Stiffener 4	st_5
12	Stiffener 4	st_6

The results are divided into two sub-groups depending on their position. The first three sets of results, corresponding to the second skin bay, are shown in Figure 7.24a. These show that gauges sk_1, sk_2 and sk_3 all exhibit the same behaviour, deforming in the same direction although to different degrees until point 1 when there is a sudden change. At this point, the reading for sk_3 changes from negative (compression) to positive (tension) due to the occurrence of a buckle in the area of the gauge, sk_1 and sk_2 showed a reaction at the same load level although they continue to be in compression albeit at a reduced level.

Other points of change observed previously in the load-shortening curve also appeared in the strain gauges results. Figure 7.24b shows the results for the third skin bay. The level of compression in gauge sk_5 can be seen to start to decrease after point 2 and gradually change to tension after point 3 which is considered to be the point at which the jump from *L/2* to *L/3* occurs.

The same type of behaviour is shown by gauge sk_4 however this reading remains compressive after point 3. The stiffeners gauges showed in Figure 7.24c, 7.24d and 7.24e, display three interesting trends. Firstly, the data shows sudden changes occur at the same load levels as those highlighted in both the load shortening curves and the skin strain gauges showing these responses are linked as might be expected. Potentially there are two reasons for this: either the skin buckled locally first and affected the stiffener or the stiffeners buckled first reducing the level of support in the skin and hence causing it to buckle. The second reason could be more acceptable.

Secondly, the strain gauges which was fixed near the bottom of the three mid stiffeners showed a change in strain from compression to tension, although these changes occurred in different points while the top gauges continued to record compressive strains even though the level of compression decreased at particular salient points. Finally, the results recorded by gauges st_4 and st_6 showed early sudden deformation (buckling) at a load level of 23.54 kN before the other components. This behaviour is likely to be because of the initial manufacturing imperfections discussed earlier and the fact that these two stiffeners were longer than the rest of the panel. Consequently, they would have carried the load first and then deformed before the other part of the panel. The shape of the deformations in the panel could lead to the conclusion that the panel has a mixed failure mode; the main one being the local mode due to the skin buckling with the other was being a stiffener buckling mode.

The difficulty in capturing the stiffener's behaviour using the DIC system was a limitation in the test. However, the strain gauges still give reliable information on the behaviour at particular points and in particular are able to highlight points at which sudden changes occur.

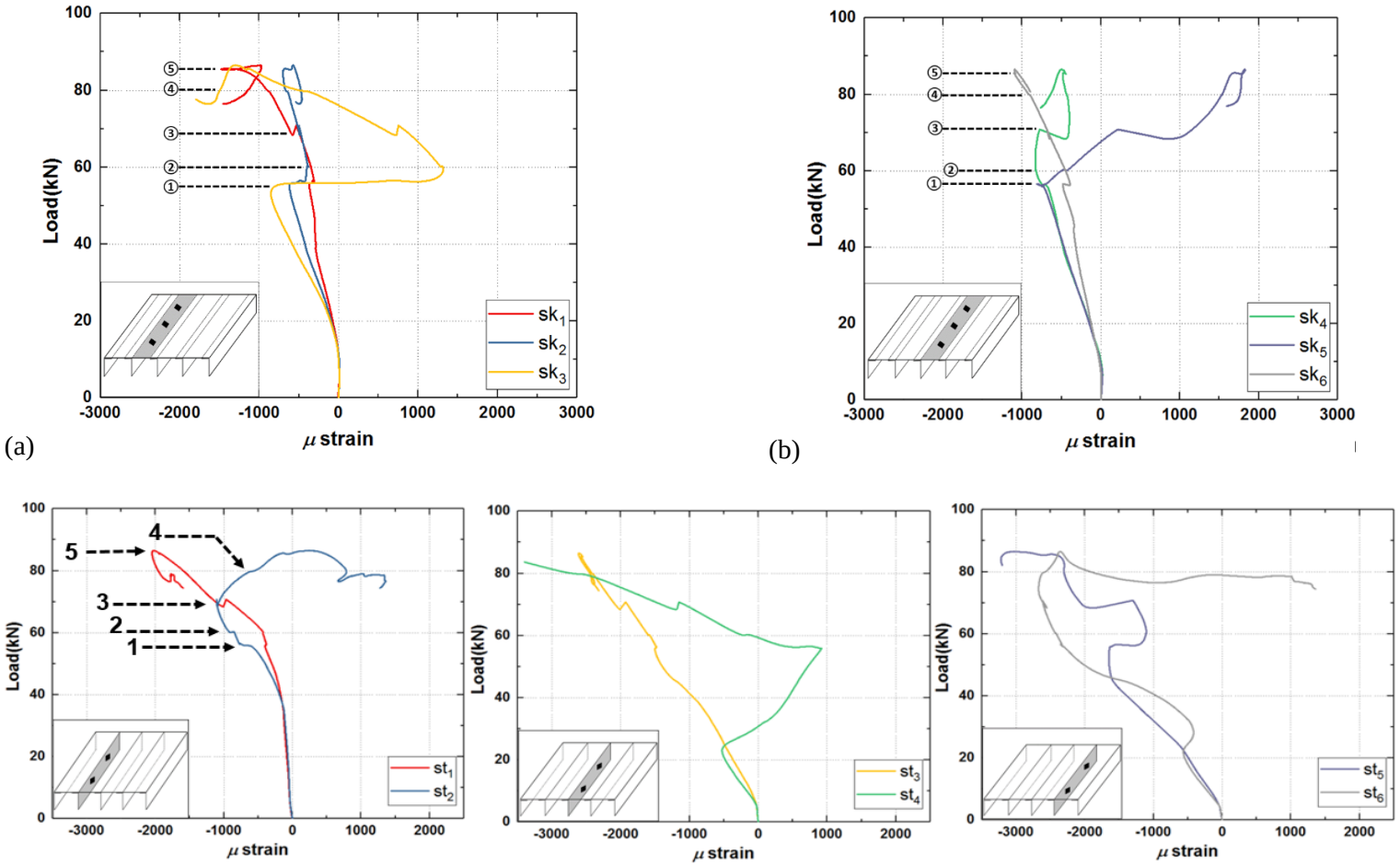

Figure 7.24: Strain gauge data for panel 400-1 (a) skin bay 2, (b) skin bay 3, (c) stiffener 2, (d) stiffener 3, (e) stiffener 4

The results for panel 400-2 results are presented in Figure 7.25. Considering bay 2 first, sk_2 and sk_3 show a sudden change at point 1, unlike sk_1. The loading in sk_2 reverses after point 1 with the gauge reading a positive strain until the failure of the panel. All three gauges show changes at points 2, 3 and 4 on the curve in Figure 7.25a, and the strain in all three gauges decreases at point 5 at a load level of 104.1 kN. The gauges mounted in the next skin bay (3) highlight changes at point 1, the initial local buckling on the skin, and then at points 2 and 3, where the mode change from two to three half-wavelengths occurs at point 3. As with the neighbouring bay, the strain decreases after point 5 before the panel collapses, and all the gauges in this bay give a compressive reading throughout, see Figure 7.25b.

The stiffener gauges are displayed in a similar way as for the previous panel. Stiffener 2 top and bottom gauges show approximately inverse behaviour; however, both gauges indicate compression throughout the test. The gauge st_1 in Figure 7.25c shows early deformation occurs at a load of 33.6 kN which is again because this stiffener was slightly longer than the loaded edge of the panel which resulted in it carrying all the load and hence deforming before the rest of the panel.

Similarly, gauge st_6 on stiffener four shows earlier buckling at a load of 19.547 kN for the same reason although the initial imperfection for this stiffener was higher which could explain its considerably lower buckling load (Figure 7.25e). The reading from gauge st_5 changes from positive to negative after the mode jump at point 3 which is explained by the appearance of a buckle near it which would make the gauge move in the reverse direction.

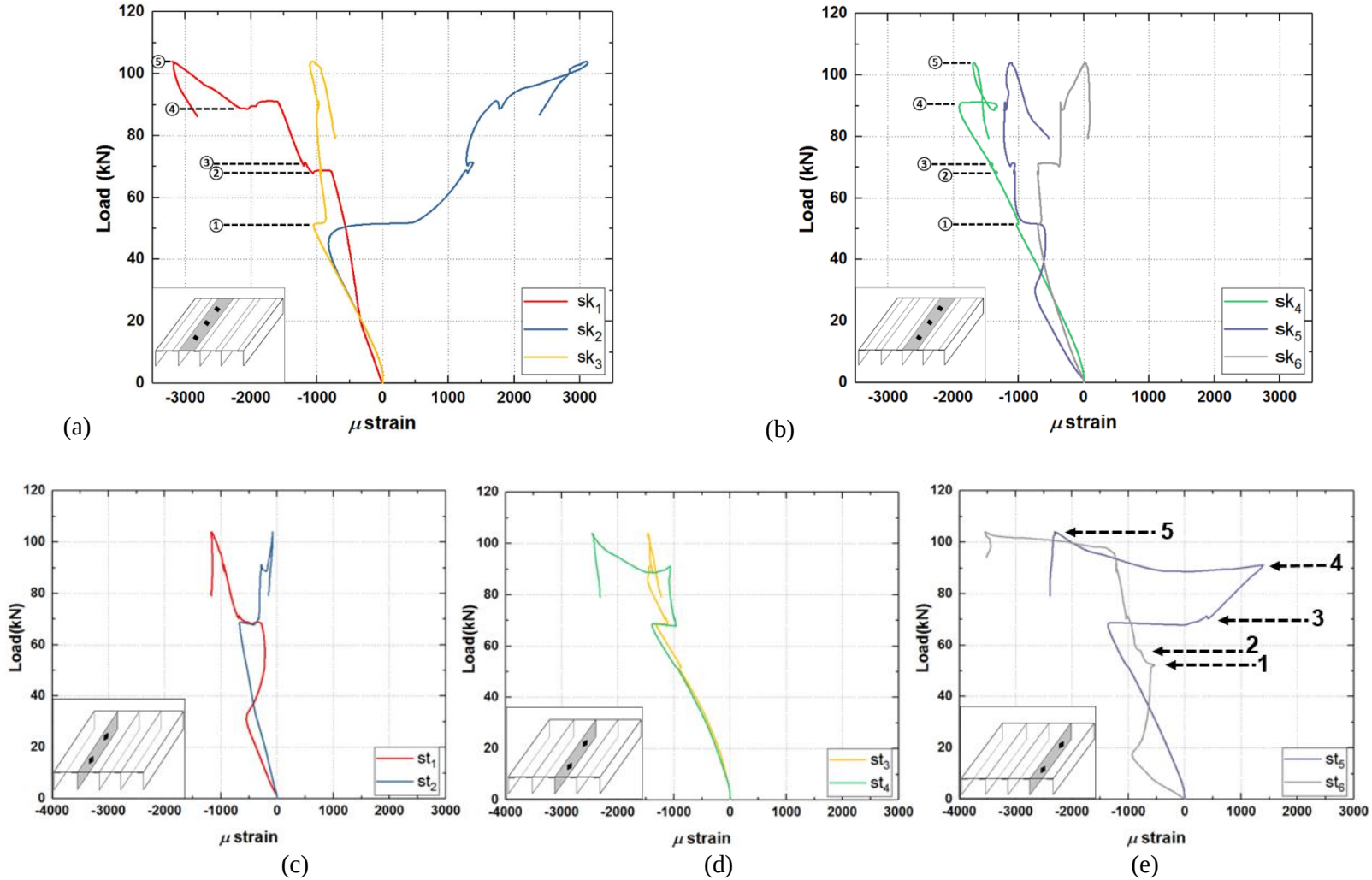

Figure 7.25: Strain gauge data for panel 400-2 (a) skin bay 2, (b) skin bay 3, (c) stiffener 2, (d) stiffener 3, (e) stiffener 4

7.6.2 Stiffened panels with 800mm radii of curvature

7.6.2.1 Load –shortening behaviour and DIC results

The load-displacement relationships for the two 800mm radius panels are presented in Figure 7.26. In a similar way to panel 400-1, the graph shows the effect of initial imperfections generated during the panel's manufacture on 800-1 which was manufactured and tested alongside panel 400-1. Again due to some stiffeners being longer than others, these were loaded first with the result that there was a rapid increase in displacement initially, which became less rapid once the load was more evenly distributed, effectively increasing the stiffness of the panel.

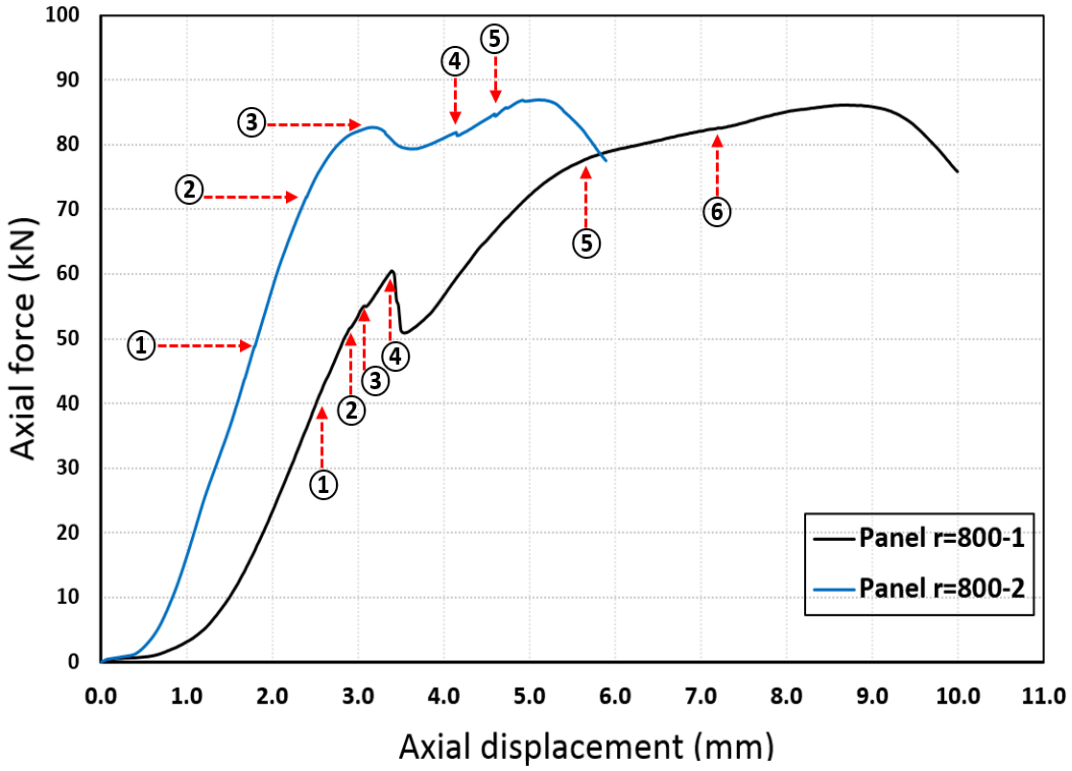

Figure 7.26: Axial load versus in-plane axial displacement for curved stiffened panels with a radius of curvature = 800 mm

The behaviour of panel 800-1 will again be discussed in relation to six salient points which are marked on Figure 7.26. Following the initial sharp increase in deformation due to manufacturing imperfections, the panel behaves linearly until point 1 (at a load of 40.434 kN) at which the middle skin bays first buckle with a clear *L/2* mode as shown in Figure 7.27a. Then, at point 2, the right hand side bay follows the mid skin bays at a load of 50.853 kN (Figure 7.27b).

At point 3 there is a jump from mode *L/2* to a new buckling configuration with three buckles along the length, which only partially appears in the DIC images due to the omission of the bottom section (Figure 7.27c, 55.506 kN). At load level 60.506 kN the curve shows (at point 4) a significant drop in load to 50.998 kN which seems to be a jump. However, it can be seen that this happens because the left hand skin bay is stiffer than the others due to the two facing stiffener flanges in that bay providing additional support, and so the transition to 3 buckles is delayed until this point, at which a loud noise also occurs (Figure 6.27d). The curve then takes a relatively stable path until point 5 when the positive out of plane buckles start to join together in the upper half of the panel which can be considered the beginning of the failure stage.

This failure continues after point 6 when the slope changes due to the negative buckles in the lower part of the panel beginning to join together before failure at a load 86.033 kN as shown in Figure 7.27e and 7.27f. The panel showed skin-stiffener separation at some points during failure accompanied by a relatively load noise and the area near the loaded edges showed severe damage and bent with significant stiffener deformations. The positive out of plane displacement increased significantly up to 9 mm in the top part of the panel while the negative deformation decreases to -1.5 mm. The failed panel images are presented in Figure 7.28, which shows the large deformations in the panel and the stiffeners separation.

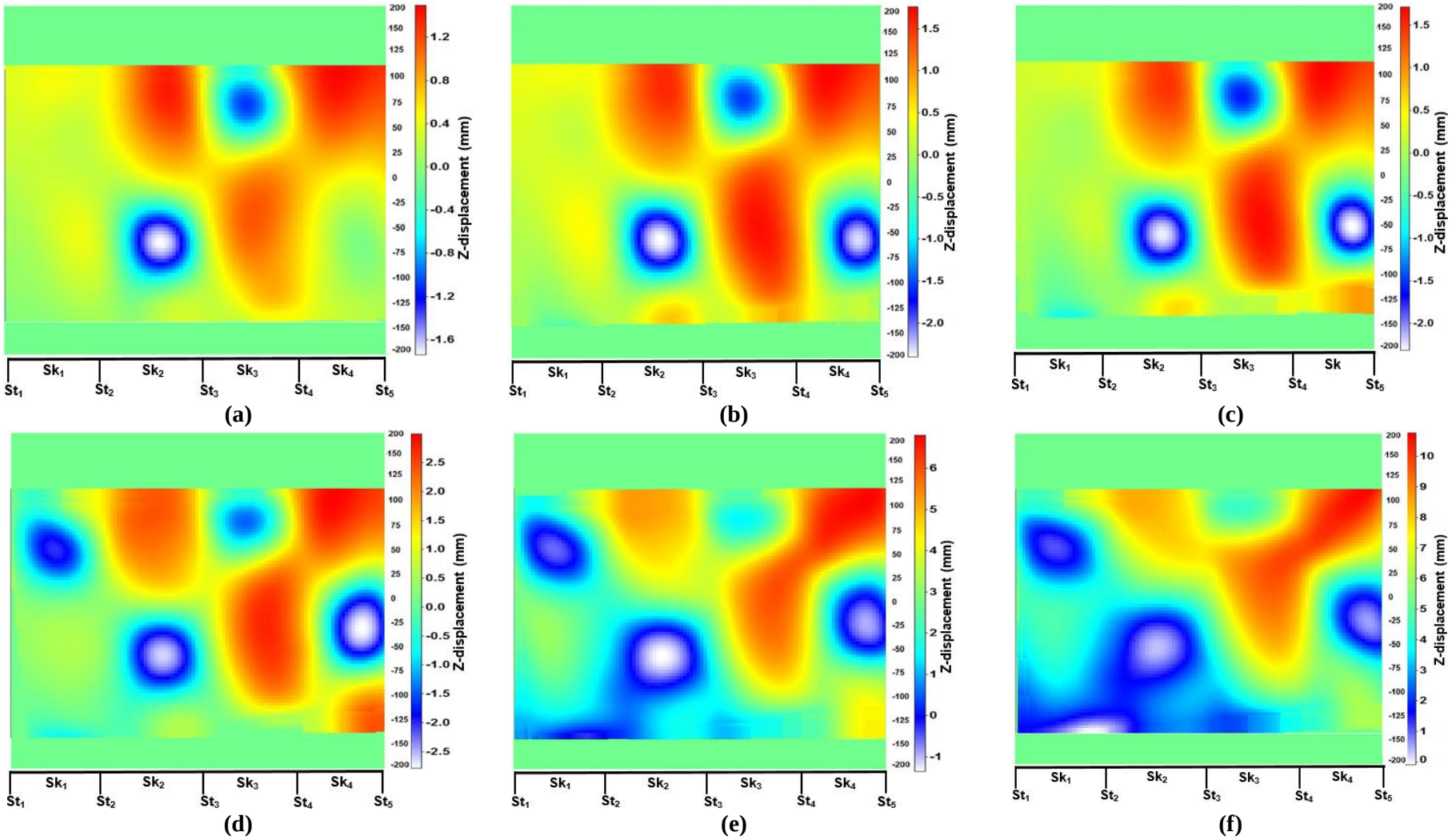

Figure 7.27: Panel 800-1 contours of out-of-plane displacement (DIC images)

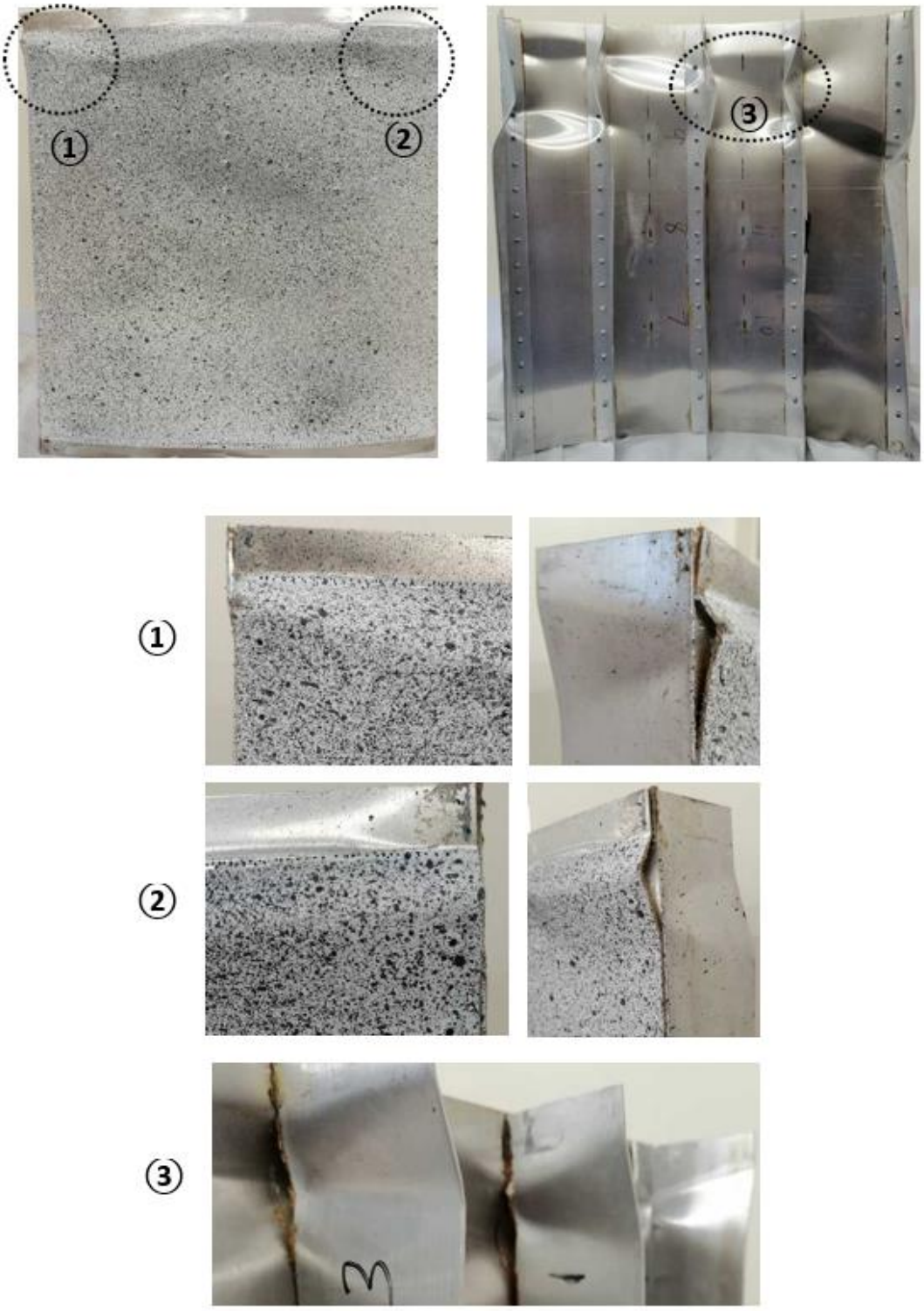

Figure 7.28 : Panel 800-1 failure configurations

The second panel 800-2 showed similar trends but with some differences. The most significant of these was that the effect of in-plane imperfections was significantly decreased. At point 1 local buckling occurred, with three half-wavelengths appearing in the middle skin bays as shown in Figure 7.29a.

Then, at point 2 the outer skin bays followed, buckling relatively late compared with the middle bays, potentially due to smaller imperfections in the bays, the higher level of support provided by the stiffener orientation in the left hand skin bay reducing the unsupported width or the variations in loading caused by uneven stiffener lengths, see Figure 7.29b.

A significant jump occurred at point 3 as shown in Figure 7.29c with the skin bays jumping to four buckles with the exception of the left hand bay, after which the panel continued with the same buckling mode configurations until point 4. At this point the panel started to show a high rate of overall bending with the buckles with negative out of plane displacement (blue) starting to move down the panel while the buckles with positive out of plane displacement (red) moving to the upper half of the panel near the loaded edge. This point can be considered the start of the failure stage, Figure 7.29d.

As the load increased past this point, the panel showed significant deformation until at point 5, when the area near the loaded and opposite edges creased before the panel failed completely and the load dropped, see Figure 7.29e and 7.29f. This drop off in load was accompanied by stiffener-skin separation in a number of locations, further reducing the panel's ability to carry load. The failure images of the panel 800-2 are presented in

Figure 7.30.

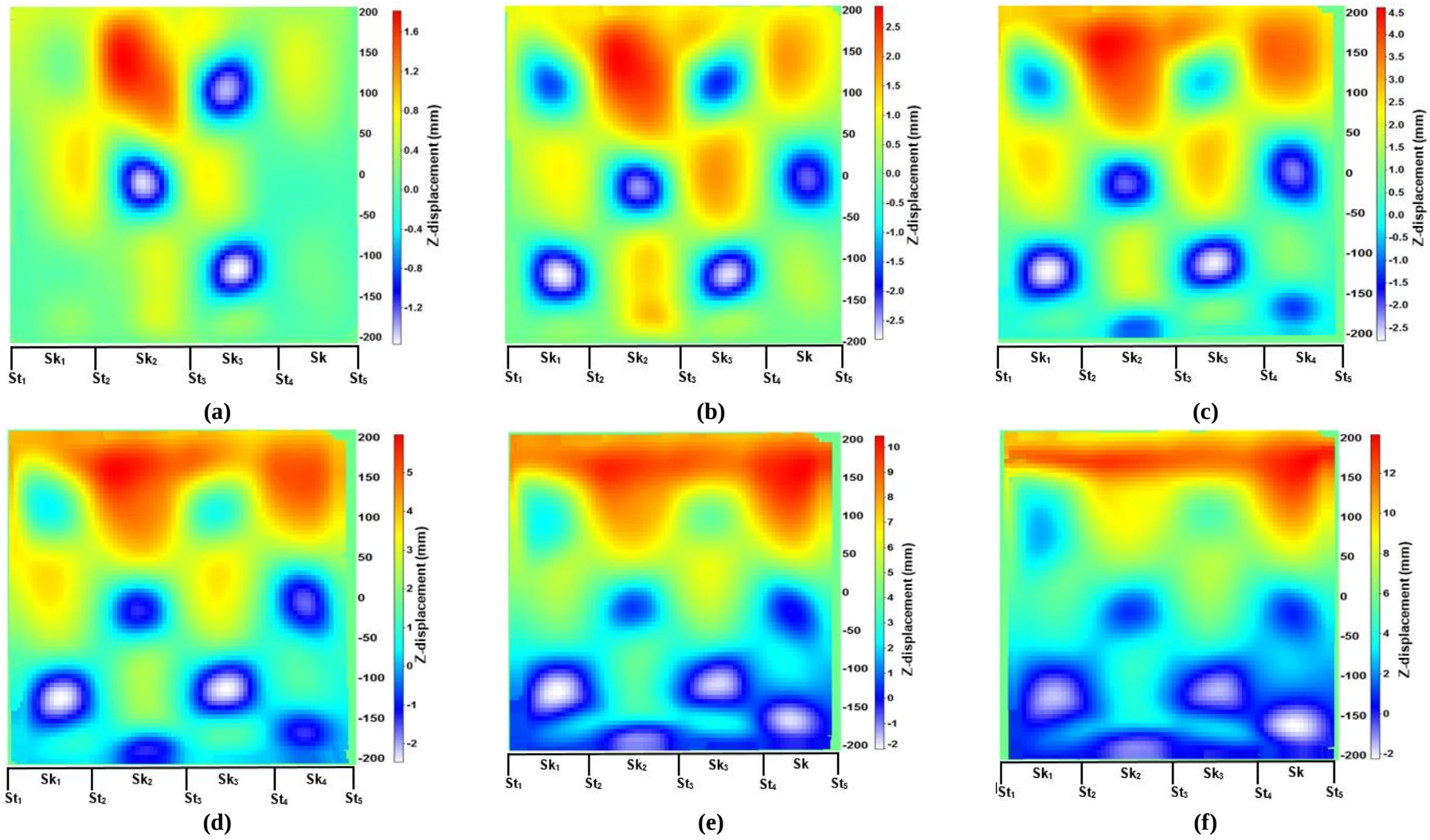

Figure 7.29: Panel 800-2 contours of out-of- plane displacement (DIC images)

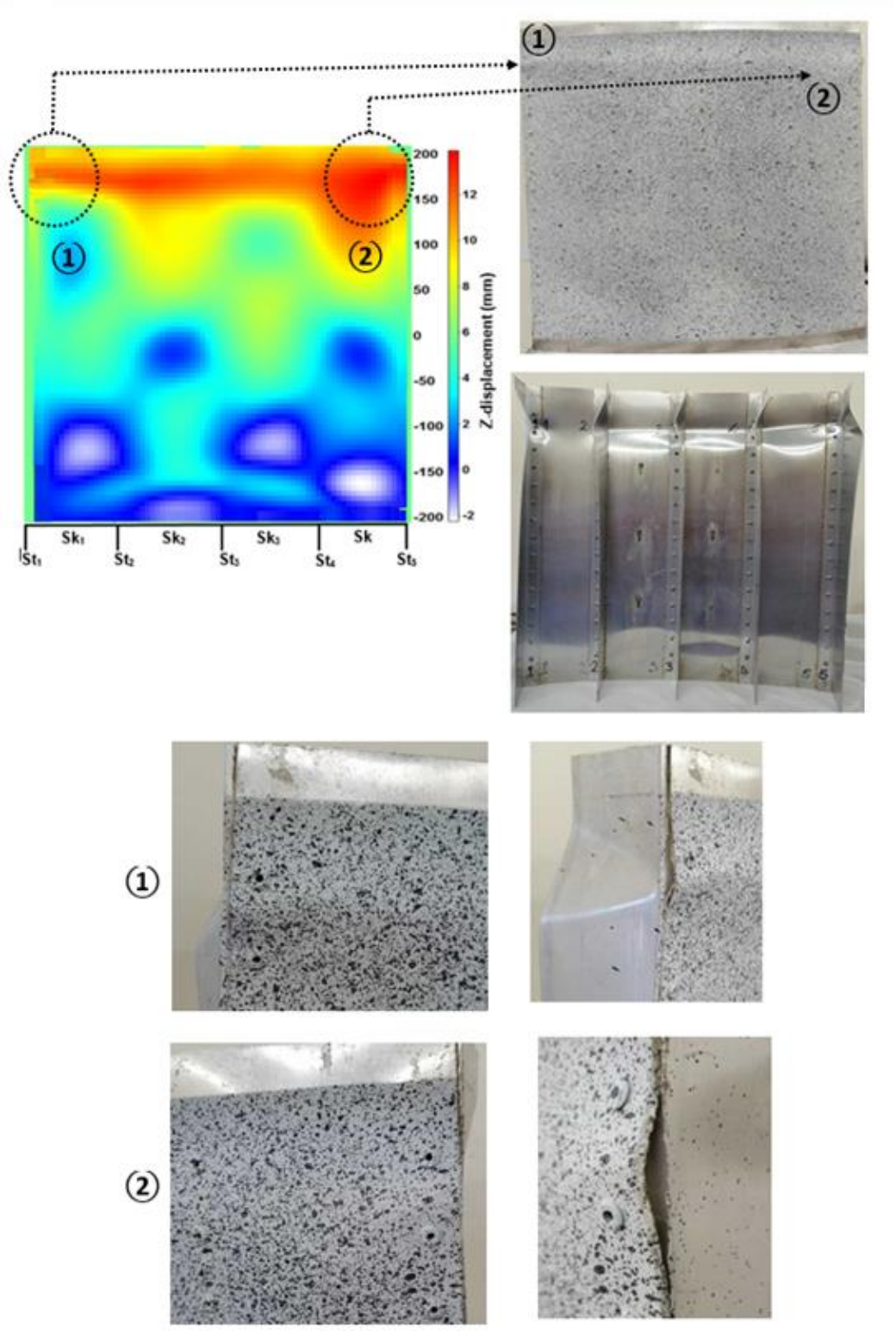

Figure 7.30: Panel 800-2 failure configurations

7.6.2.2 Strain gauge results

The strain gauge results for panel 800-1 are presented in Figure 7.31, again divided into two groups: skin and stiffener gauges. The skin results are separated into two groups of three gauges fixed in the same skin bay and are presented as relationships between load and micro-strain. Results for bay 2 show a change for gauge sk_1 at a load level slightly before point 1 marked on the curve. A sudden reduction in strain is then detected by all three gauges at point 2, potentially due to a new buckle appearing suddenly at the last skin bay on the right.

The most interesting feature in Figure 7.31a, however, occurs at point 4, where a sudden change from compression to tension in gauge sk_1 supports the presence of a mode jump at the same load level as seen in the load-shortening curve discussed previously. The load drops after point 6 at which there is evidence of panel failure close to 90 kN. Similar trends are observed in bay 3 as shown in Figure 7.31b, with gauges again indicating a considerable reaction to the mode jump at point 4. Gauges sk_1 and sk_5 show a transformation from compression(negative) to tension (positive) at loads of 60kN (point 4) and 40 kN (point 1) respectively. This is caused in each case by buckle initiating at the location at which they are mounted. Results for the three central stiffeners are illustrated in Figure 7.31c, 7.31d and 7.31e. All stiffeners showed observable changes at a load level of 60 kN where a mode jump occurs. The gauge st_4, which is located in the middle stiffener, also shows early deformations at load level 39.52 kN due to the in-plane imperfection as appeared in skin gauge sk_1 at point 1. All the stiffener gauges demonstrate the same behaviour as the load drops close to load 88.74 kN (point 6) showing good agreement with the load-shortening curve, although the reading for gauge st_2 stop at load level 80 kN as shown in Figure 7.31c.

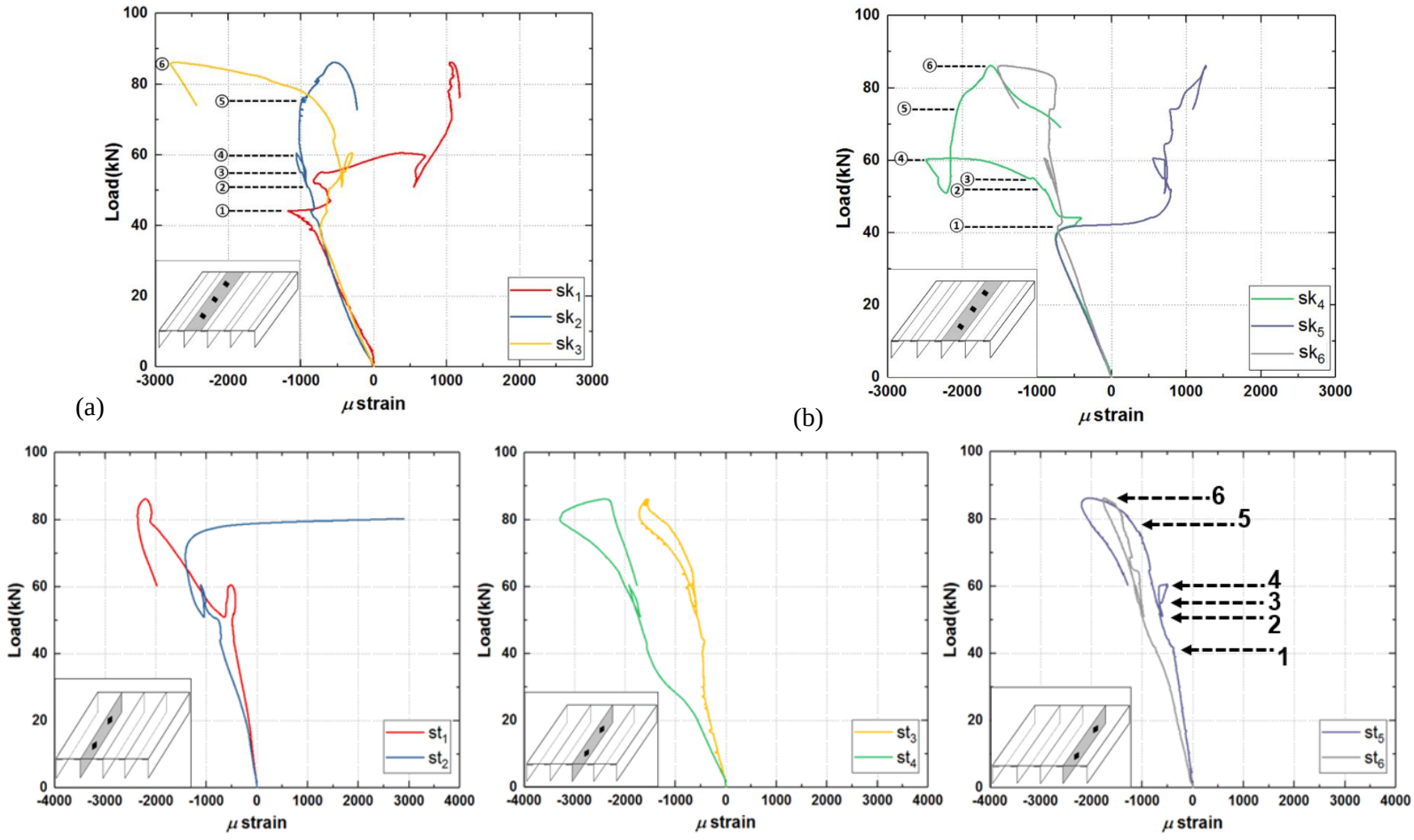

Figure 7.31: Strain gauge data for panel 800-1 (a) skin bay 2, (b) skin bay 3, (c)stiffener 2, (d) stiffener 3, (e) stiffener 4

Results for the panel 800-2 strain gauges are presented in Figure 7.32. Notably for this panel Figure 7.32a and 7.32b show an early reaction at point 1 at load level 39.1 kN. This is due to deformation in the stiffeners near the gauges as a result of the extra-load applied on those stiffeners due to the manufacturing imperfections applied on stiffener 3 (0.5mm) and stiffener 4 (0.4 mm) and stiffener 5 (0.5 mm). The skin buckled locally at load 49.21 kN marked as point 1 on the curve in Figure 7.32a and again at point 2 accompanied by sudden jumps in strain gauge data. The gauge responses occurring before point 1 at load 38.65 kN were potentially caused due to the stiffener deformations shown in Figure 7.32d and 7.32e in gauges sk_3, sk_4, sk_5, sk_6 respectively.

All the skin gauges register a sudden drop at point 3 where a further jump occurs at a load of 83.6 kN, after which the curves recover until panel failure at a load of 88.5 kN. The stiffener gauge readings are presented in Figure 7.32c, 7.32d and 7.32e. All gauges except st_2 are seen to change suddenly at a load of 39.1 kN, with st_3 and st_5 changing from a negative (compression) to a positive reading (tension). This is due to the stiffeners buckling relatively early compared with the skin for two reasons; firstly as the stiffeners have a higher stiffness than the skin bays due to their geometry they will carry more load and secondly, due to particular stiffeners taking all the load initially because of the imperfections generated through panel manufacturing. In fact, the significant effect of either in or out of plane manufacturing imperfections cannot be ignored. At the same time, it is difficult to avoid imperfections despite great attention to detail during manufacture. Therefore, the effect of imperfections must be considered in design because of the level of effect they have on the non-linear behaviour of the thin-walled shells particularly in terms of post-buckling and the mode jumping phenomenon.

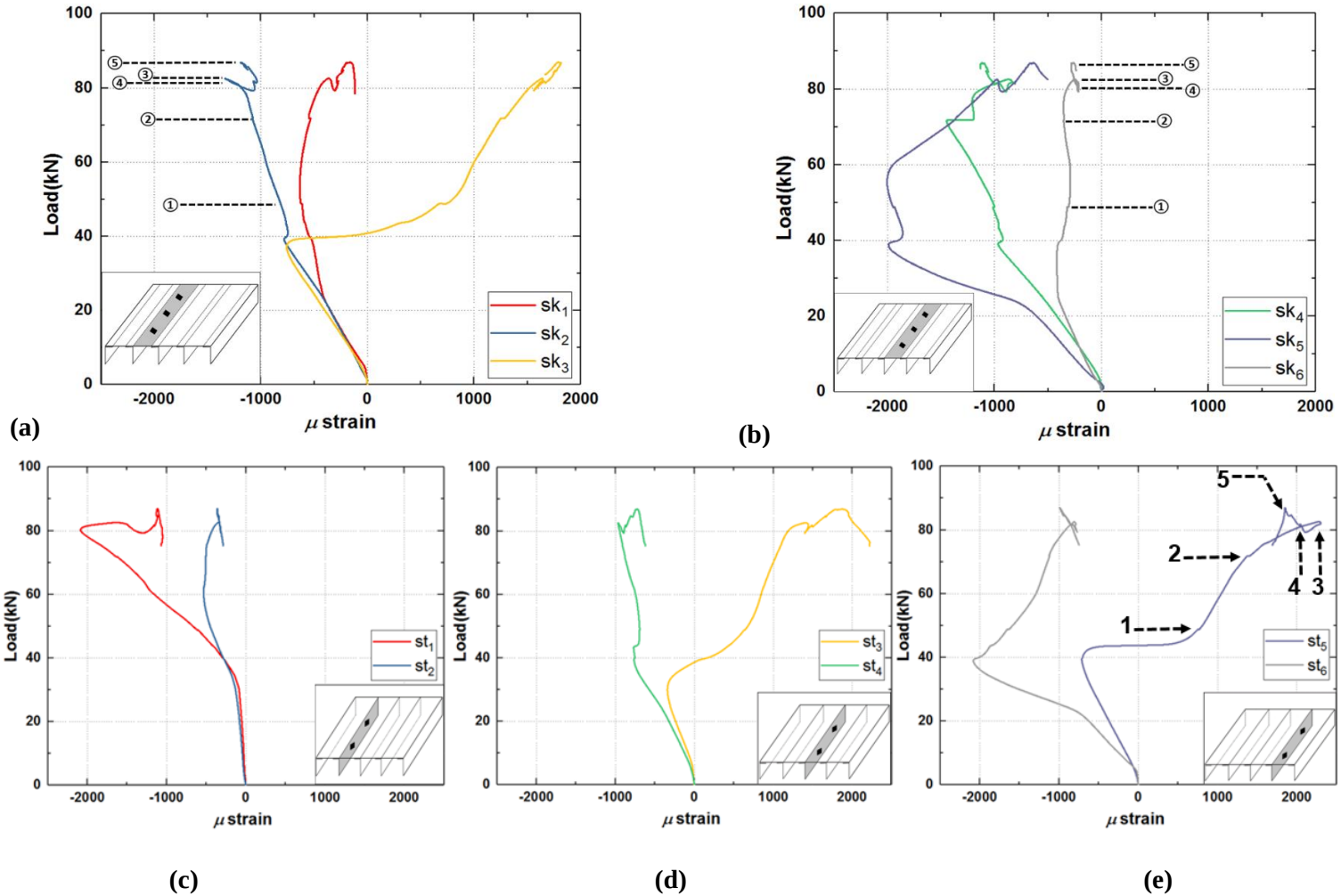

Figure 7.32: Strain gauge data for panel 800-2 (a) skin bay 2, (b) skin bay 3, (c) stiffener 2, (d) stiffener 3, (e) stiffener 4

7.6.3 Flat stiffened panels

7.6.3.1 Load-shortening behaviour and DIC results

This section highlights the results for the flat stiffened panels beginning with the load shortening relationships illustrated in Figure 7.33.

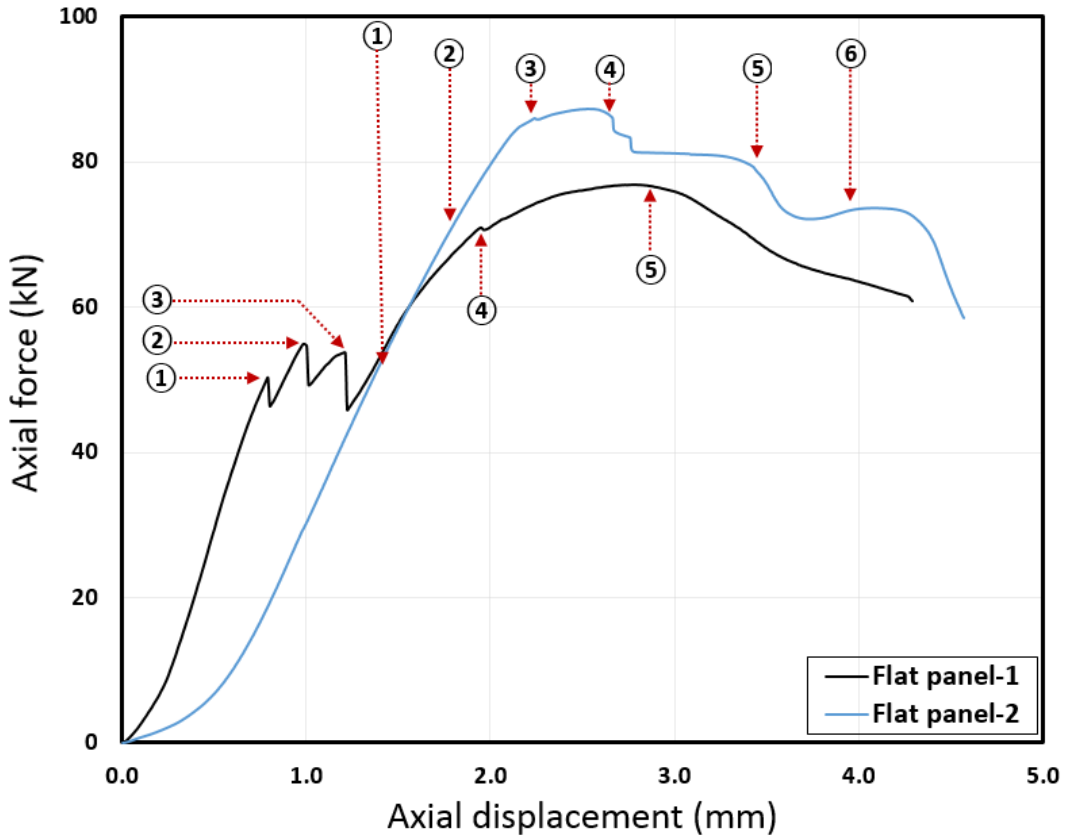

Figure 7.33: Axial load versus in-plane displacement for flat stiffened panels

The curve for Flat panel-1 highlights again the effect which in-plane imperfections can have on the buckling behaviour of the plate, in this case in the initial stages of the loading regime. We first notice a sudden drop in the load-displacement curve at a load 50.229 kN with the panel buckling locally with four buckles in bay 2 and five buckles in bay 3 as illustrated in Figure 7.34a, which shows the out of plane displacement contour plots at the

start and end of the load drop. A further load drop occurs when the load reaches 54.854 kN at which point bay 1 jumps from *L/4* to *L/5* as shown in Figure 7.34b. At the same time, bay 4 shows a noticeable change in the out of plane displacement amplitude (particularly for the negative out of plane buckle (blue). Finally, as the curve starts to recover and rise again, a substantial drop in load from 53.678 to 44.931 kN occurs at point 3. This behaviour is due to further jump in bay 1 with the skin jumps from *L/5* to *L/6* with a significant corresponding change in the out of plane displacement in bay 4, see Figure 7.34c.

The curve then follows a smooth path until it reaches a load level of 70.593 kN marked as point 4. Figure 7.34d shows the panel is subject to a considerable increase in the deflection amplitude without clear evidence of a new mode jump. The delay in buckling in bay 1 and its ability to sustain six local buckles reflect its increased stiffness in comparison to the other bays due to reduced unsupported width because of the orientation of the stiffeners. Hence, load can redistribute, particularly from bay 4, which has the lowest stiffness due to it being adjacent to an unsupported boundary. The effect of the different stiffnesses is more clearly seen in the flat panel where the additional stiffness the bays possess due their curvature, present in the previous two geometries, is not present.

Point 5 on the curve represents the beginning of the failure stage in which high levels of deformation occurred in the stiffeners as well as the skin. This is particularly clear in the top right hand side of the panel near the loaded edge where out of plane displacements reach 4 mm as shown in Figure 7.34e, and 14 mm in Figure 7.34f. The failure features and images for panel Flat-1 including the skin-panel debonding near the loaded edge, are presented in Figure 7.35.

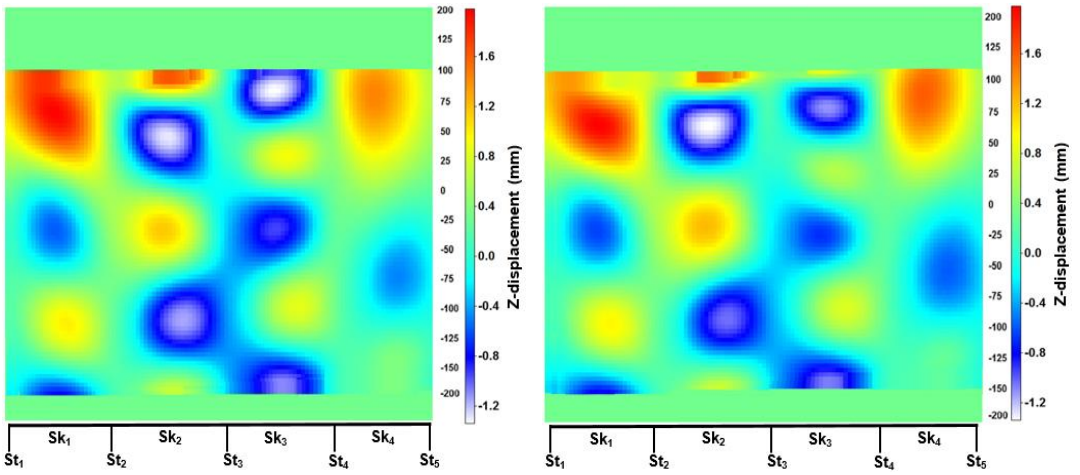

Start End

(a)

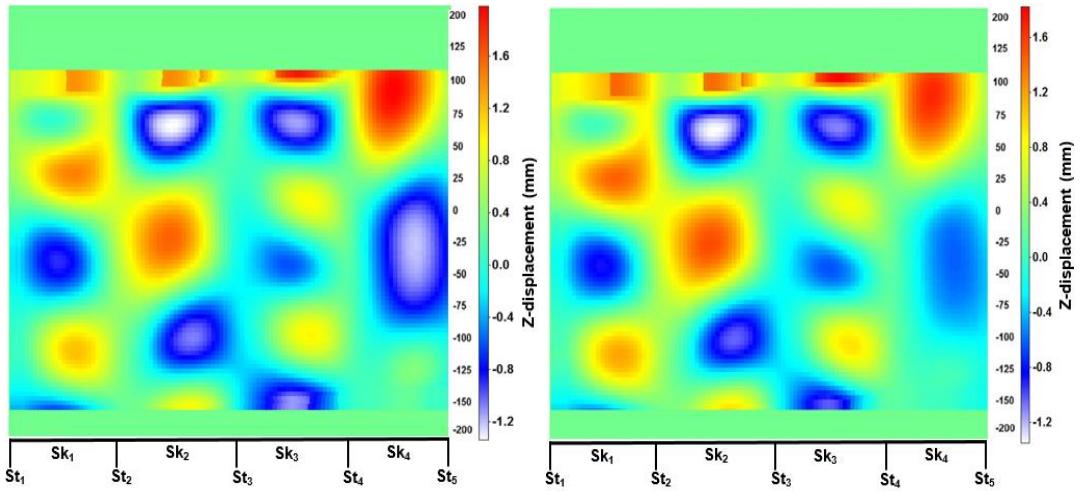

Start End

(b)

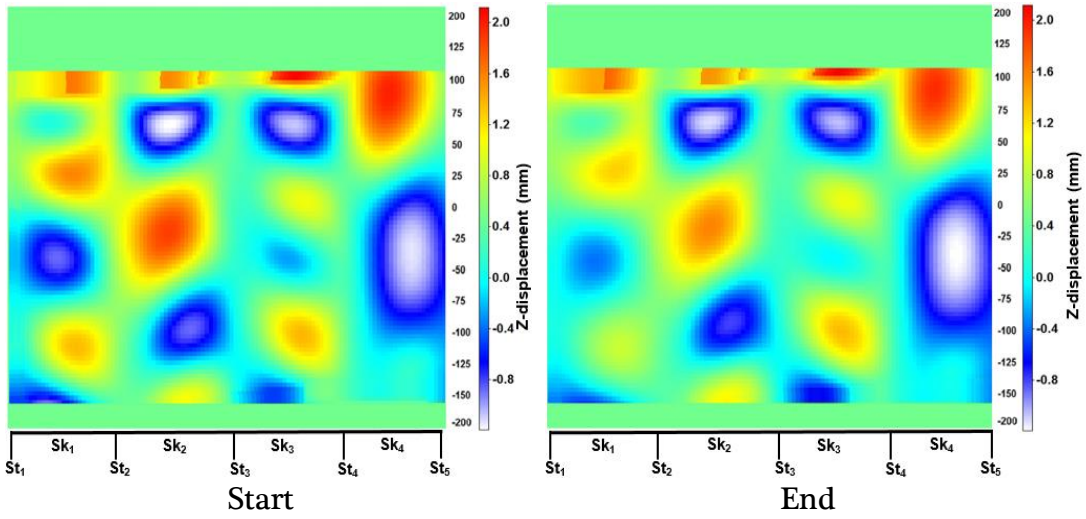

Start End

(c)

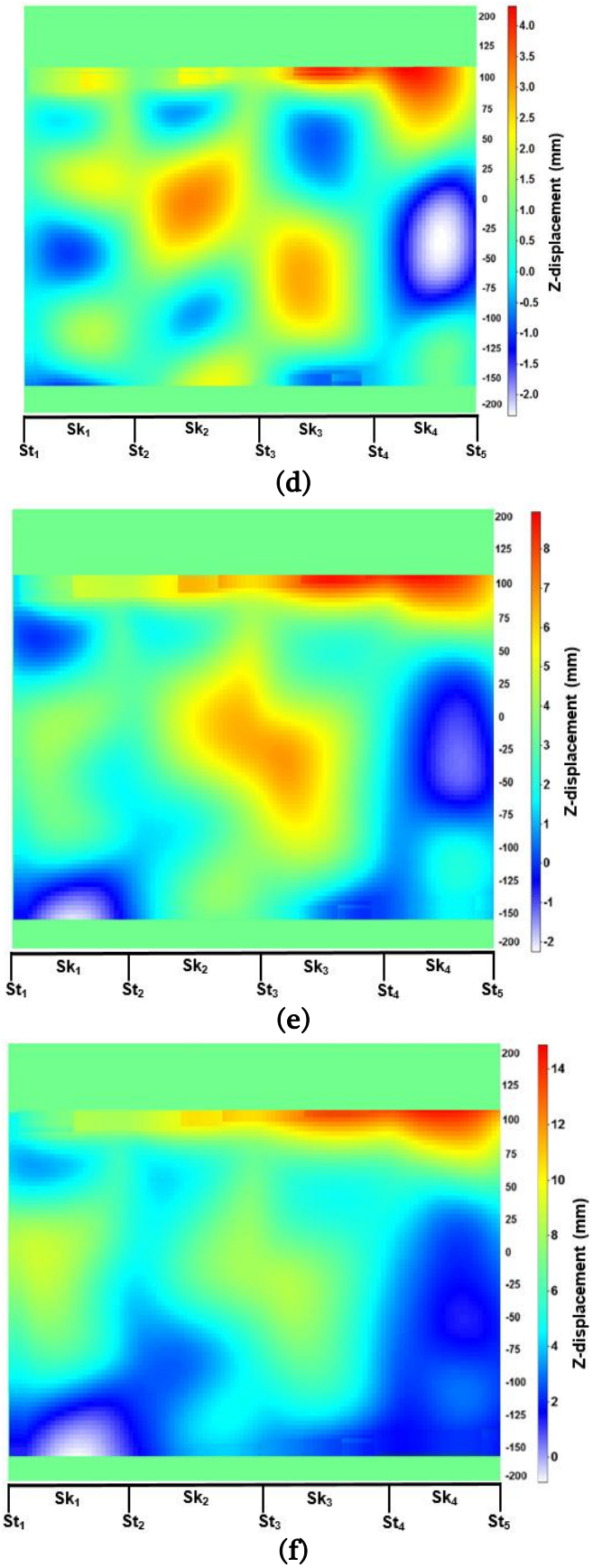

Figure 7.34: Flat panel-1 contours of out-of- plane displacement (DIC images)

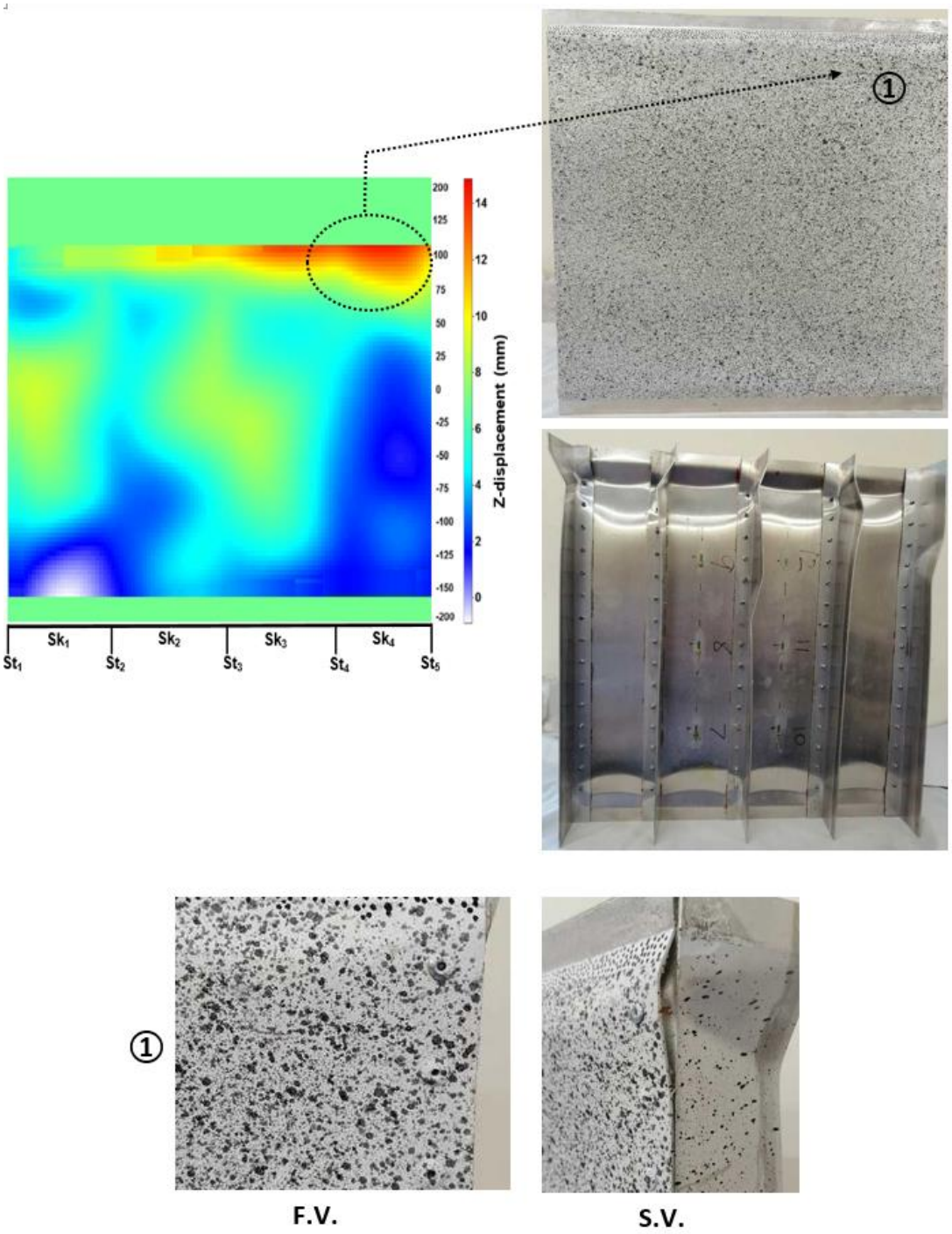

Figure 7.35: Panel Flat-1 failure configurations

Flat-2 panel behaves totally differently compared with the first flat panel especially in the early stages of post buckling region. This could be due to different manufacturing imperfections in the skin and stiffeners, slight differences in the boundary conditions at the loading edges due to variations in the level of packing used and finally the load eccentricity, which could have differed between one specimen and another. For this reason, ideally the number of specimens tested would have been increased in order to understand the level of scatter and its causes, however due to time and resource restrictions this was not possible. For this panel, local buckling occurs at point 1 with an *L/3* mode for the first skin bays (from left to right) while the fourth one buckled with a mode close to *L/5* as shown in Figure 7.36a. The independent behaviour of the neighboured skin bays can be explained due to the different initial imperfection for each bay and the differing levels of stiffness due to the orientation of the stiffeners and the free axial edges which provide less support than a neighbouring bay. The panel (unlike other specimens) makes a smooth transition between loads of 52.532 and 73.730 kN with the buckling configuration changing and the panel buckling with mode *L/4* (Figure 7.36b). After point 2 at load 73.730 kN the fourth bay retains the *L/5* mode.

There is then a very small drop in load at point 3, corresponding to bay 3 jumping to five buckles (Figure 7.36c). At a load level of 86.60 kN, high levels of deformation were observed in the panel with a consequent large reduction in load carrying capability due to the stiffeners buckling (Figure 7.36d). This deformation was particularly severe near the loaded edge. Point 5 can be considered the final stage before the panel fails (Figure 7.36e), at which the panel showed severe bending and the out of plane displacement increased rapidly and the load dropped off further. This behaviour was in part at least due to separations between the skin and the stiffener flanges in some locations and was accompanied by high levels of noise (Figure 7.36f).

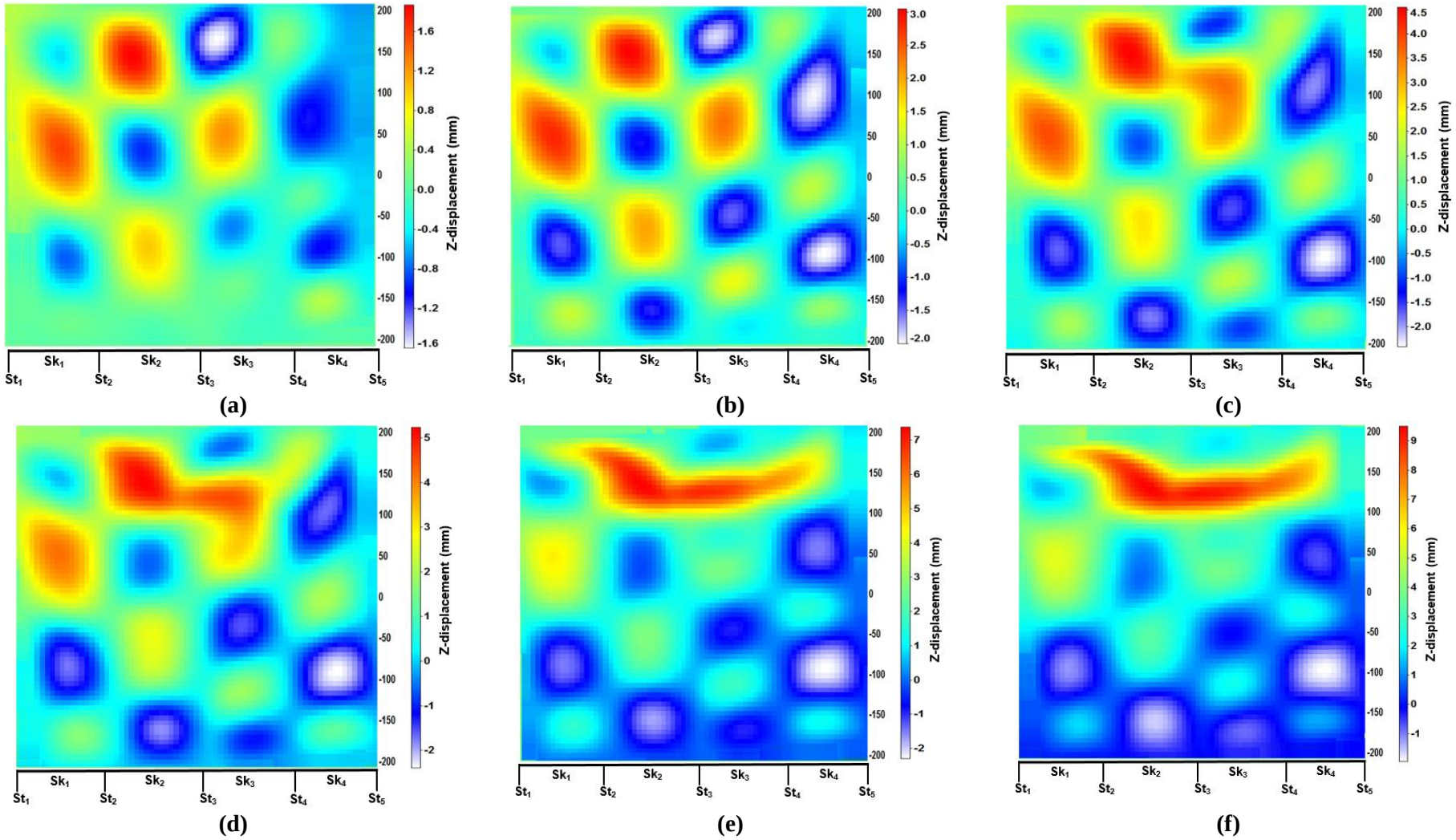

Figure 7.36: Flat panel-2 contours of out-of- plane displacement (DIC images)

The failure images for panel Flat-2 are shown in Figure 7.37 below which illustrate the damage in the specimen after test.

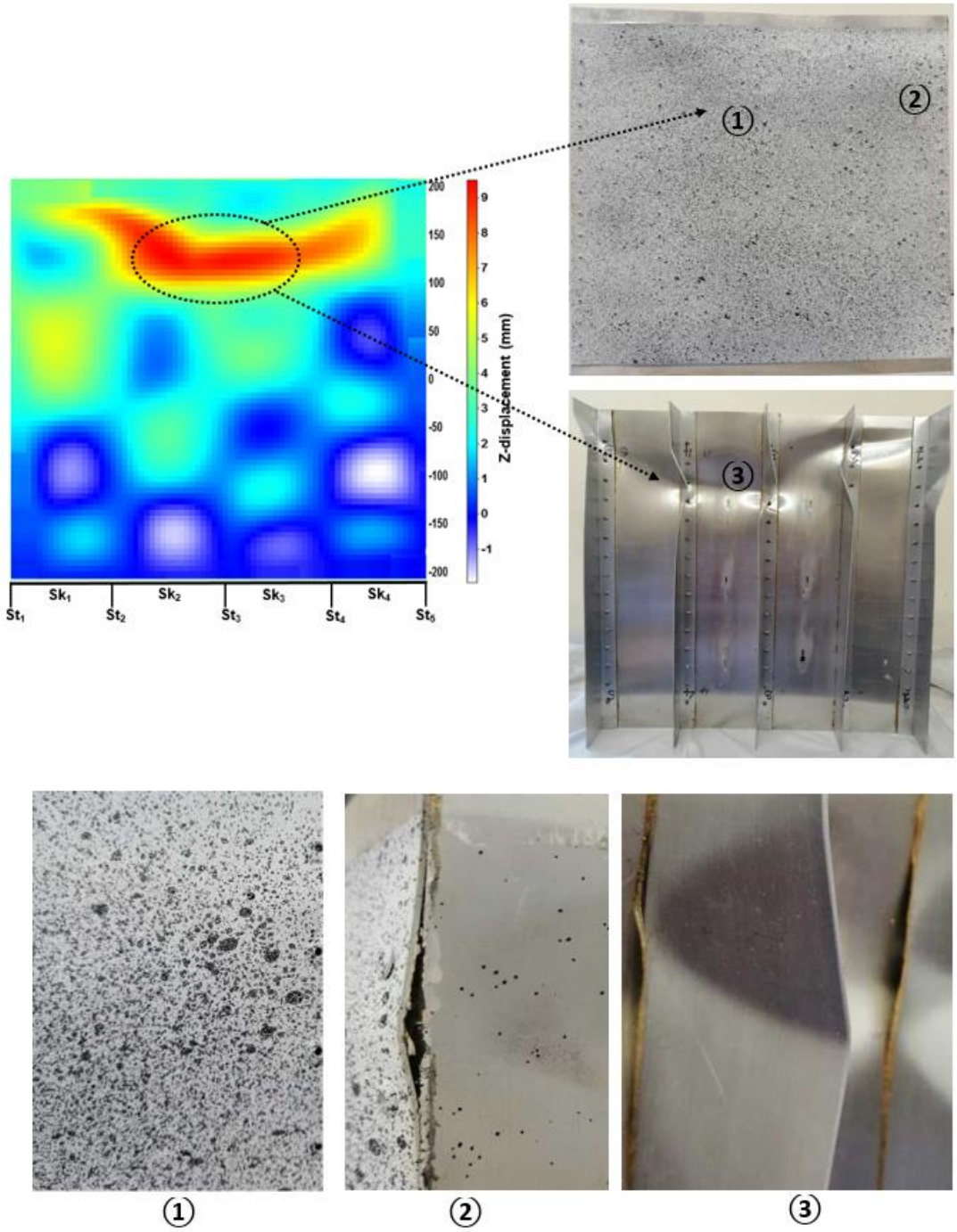

Figure 7.37: Panel Flat-2 failure configurations

7.6.3.2 Strain gauge results

Strain gauge results for panel Flat-1 are presented in Figure 7.38. The skin results in Figure 7.38a and 7.38b show an early reaction at point 1 in bays 2 and 3 at a load level close to 30 kN with the sk_1 reading for example transformed from negative (compression) to positive (tension).

This corresponds to a small buckle appearing near the loaded edge where this gauge is located which can be defined as the start of initial local buckling as shown Figure 7.38a. The effect of this buckle is not however significant enough to be observable in the load-shortening curve because of the relatively small out of plane amplitudes recorded. Other significant points on the output of the gauge correspond to points 2, 3 and 4, validating changes in the load-shortening relationships illustrated previously.

Gauge sk_5 which is in middle of bay 3 starts to give a positive reading after point 3. This behaviour could be explained as a result of the out of plane displacement amplitude generally increasing after point 3 in which the DIC results showed that bay 3 has a jump from 4 to 5 buckles as shown in Figure 7.36c.

Unfortunately gauge sk_6 stopped working at this point and no further results were therefore able to be captured to determine what was happening towards the bottom of this bay. The stiffener gauges displayed changes in behaviour at the same points mentioned above reinforcing the strong interaction between the two, as expected. Noise is apparent in the data from gauges st3 and st5, however they continued to provide readings and showed reactions similar to other stiffener gauges. The full details of the strain readings from the stiffener gauges are described in Figure 7.38c, 7.38d and 7.38e, respectively.

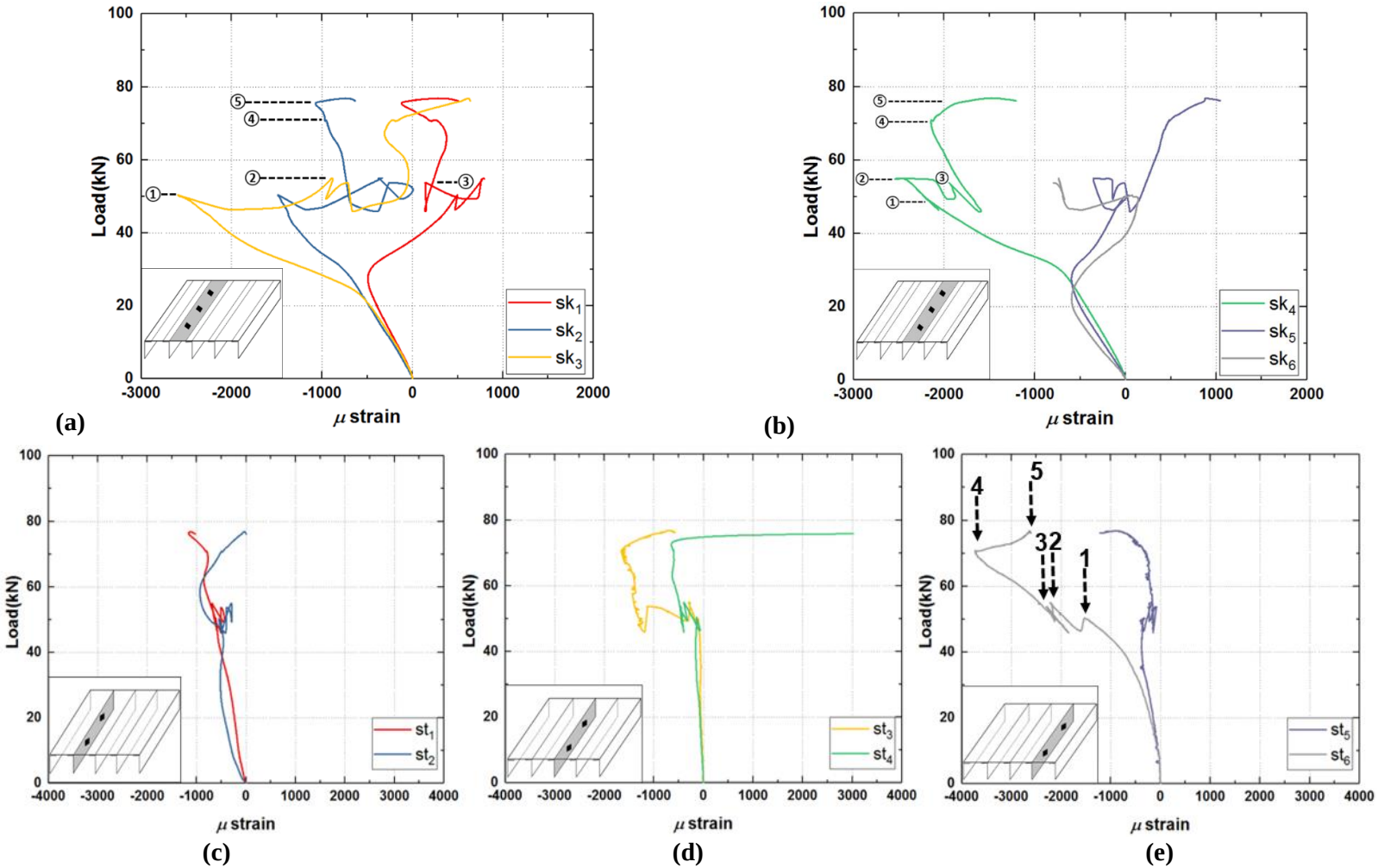

Figure 7.38: Strain gauge data for panel flat-1 (a) skin bay 2, (b) skin bay 3, (c) stiffener 2, (d) stiffener 3, (e) stiffener 4

The Flat-2 panel strain gauge results are shown in Figure 7.39. In bay 2, gauges sk_2 and sk_3 showed similar trends up to point 2. After this however, sk_2 continued to indicate increased levels of compression whilst sk_3 maintained only a very small compressive strain. The cause of this is the opposing directions of the buckles in the locations of these gauges as presented previously in the DIC output (Figure 7.39a). These results were in contrast to those for the neighbouring bay sk_4 and sk_6 in which the buckles are reversed. All six gauges located on the skin reacted at the same points of change marked on the load-shortening curve, demonstrating a good level of agreement between the machine and the strain gauge results. However all the gauges (with the exception of sk_1 and sk_6) stopped providing readings shortly after point 4 at a load of 83.6 kN due to substantial deformations occurring in the panel.

The stiffener results showed some interesting features through their load-strain relationship curves although unfortunately stiffener gauge st_4 stopped working at a load of 60 kN due to an electrical problem. Gauges st_1 and st_6 responded early in the loading cycle due to the stiffeners on which they were mounted being slightly longer than the rest of the panel and hence carrying all of the load during this period causing them to deform until they became level with the panel loaded edges. Consequently, these stiffeners were expected to show early signs of buckling due to these in-plane manufacturing imperfections. This is consistent with the effect of the in-plane imperfections during the initial stages of the load-shortening curves for this panel as discussed in section 7.6.3.1. Gauge st_1 stopped working above a load of 83.5 kN due to the high deformation in the effective area of this gauge. Figure 7.39c, 7.39d and 7.39e below describe the results of the stiffener gauges.

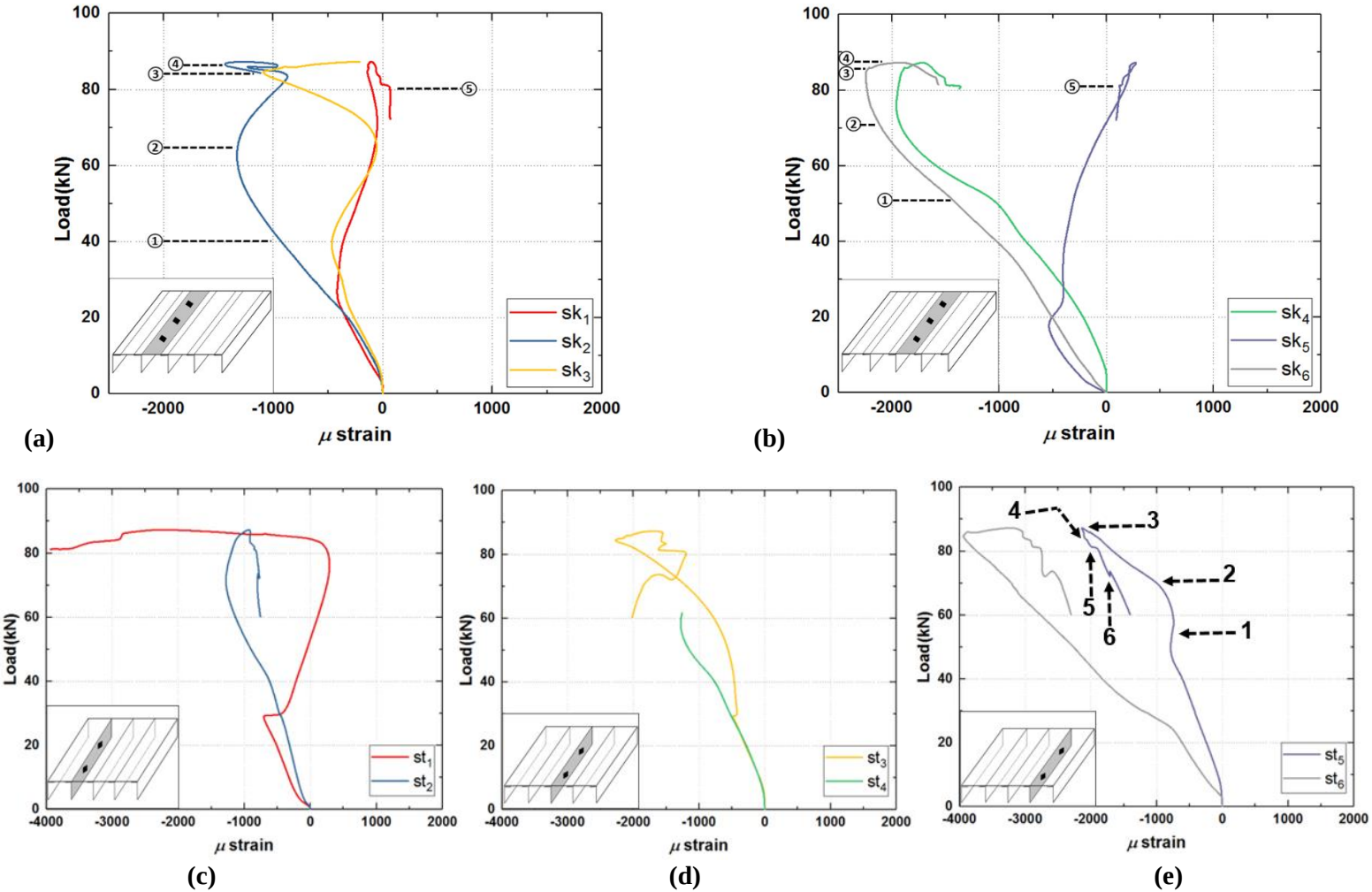

Figure 7.39: Strain gauge data for panel flat-2 (a) skin bay 2, (b) skin bay 3, (c) stiffener 2, (d) stiffener 3, (e) stiffener 4

7.7 Finite element models

This section will describe the numerical analysis of the tested specimens and provide a comparison between the finite element (FE) models developed and the experimental results. This work utilises the commercial software ABAQUS incorporating both implicit ABAQUS/Standard and explicit ABAQUS/Explicit analyses.

7.7.1 Models geometry

Models were created for each of the three geometries tested. Since the ends of each panel were built-in during the test, only the unsupported length was modelled, giving a length of 400 mm (shown for the flat panel in Figure 7.40). The models assumed the interface between the skin and stiffener flat was perfect.

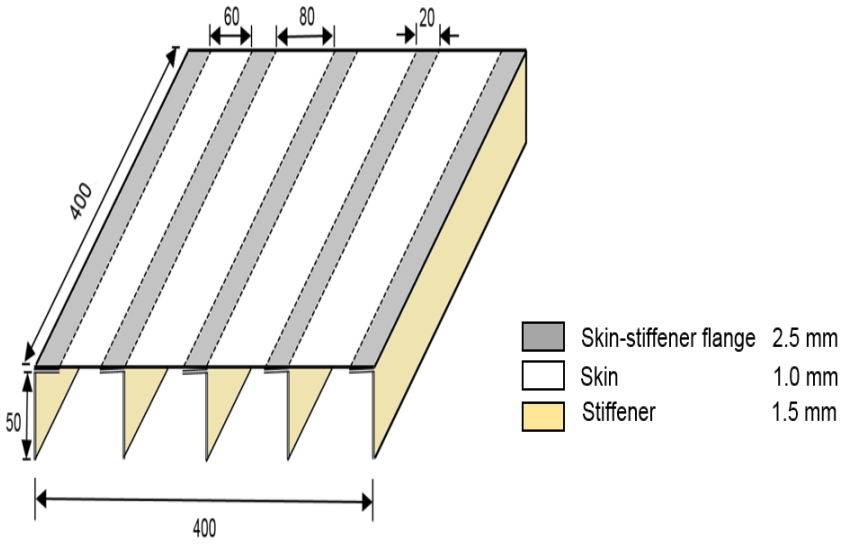

Figure 7.40: Flat panel geometry and dimensions

7.7.2 Finite element meshes

Models were generated using 2600 shell elements (for both Standard and Explicit analysis). The elements used were linear S4R elements from the ABAQUS/CAE element library. According to the ABAQUS user guide [156] using a reduced integration element (denoted by 'R') often significantly reduces running time compared with using the standard element (in this case S4), whilst being computationally more efficient. Following a convergence check elements based on a 10 mm mesh were used for all specimens. A simple example based on a 300 x 420 mm flat plate loaded dynamically was used to test different element sizes. The results showed that using 10 mm elements provided an acceptable level of accuracy when compared with finer meshes (5 mm and 1 mm) as shown in Figure 7.41, while the computational time was much lower.

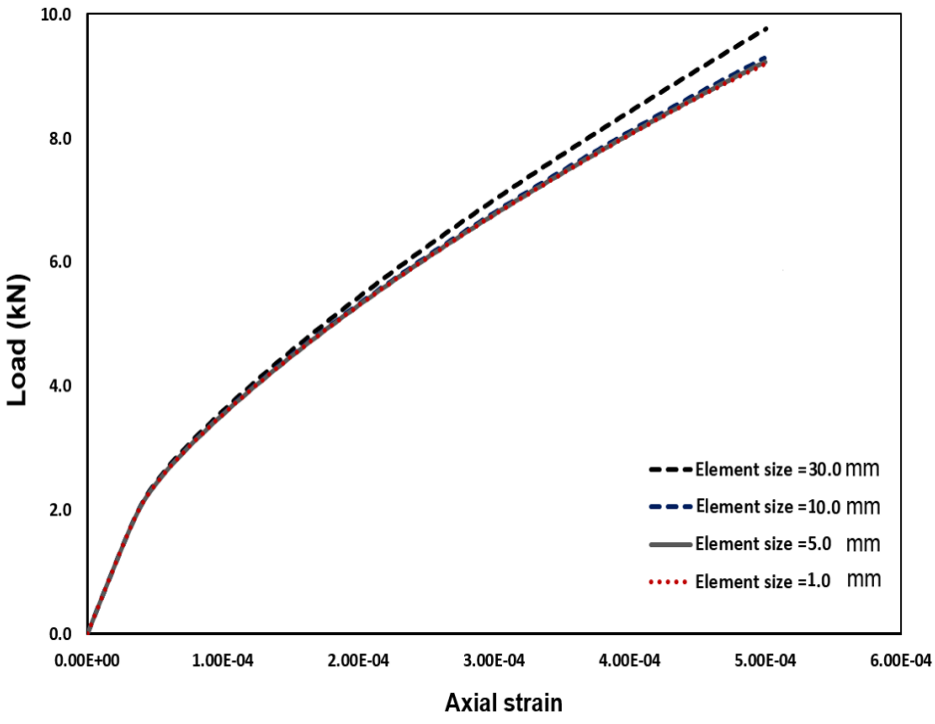

Figure 7.41: Model mesh sensitivity

7.7.3 Material properties

The mechanical properties used in the ABAQUS model (Table7.1) were taken from the material tests detailed in Section 7.2.2 and the material data sheet provided by the supplier. The test data was necessary to provide the plasticity properties for the analysis (Table 7.3).

Table 7.3: Plastic stress-strain data for aluminium material

Plastic strain %	Stress
0. 000	200
0. 310	230
0. 330	240
0. 350	250
0. 370	260
0. 420	270
0. 449	280
0. 579	290
0. 890	300
1.361	305
1.942	310
2.573	315
3.301	320
4.220	325
5.520	330

7.7.4 Geometric imperfections

7.7.4.1 Out of plane imperfections

Out-of-plane geometric imperfections were introduced to ensure the models used represented 'as-built' structures. In line with common practice, since their exact form was not known, they were modelled in the form of mode shapes obtained from an eigenmode analysis in ABAQUS/Standard with their amplitude scaled to give a representative level of imperfection.

To facilitate mode jumping, imperfections in the form of at least two eigenmodes were used. The imperfection values was measured using the DIC system results.

7.7.4.2 In-plane imperfections (Load eccentricity)

Further imperfections were generated during panel manufacturing due to some stiffeners being slightly longer than the skin, meaning that the these stiffeners were loaded before the rest of the panel. This produced a type of load eccentricity as shown in Figure 7.42a. The effect of these imperfections was to load the panels in two stages, with, the longer stiffeners (or in some cases parts of the skin) being loaded first and deforming (causing shortening) until they were level with the remainder of the panel (Figure 7.42b), at which point the load would be distributed across the whole edge as shown in Figure 7.42c. This effect was incorporated (as will be explained in the Section 7.7.7 later) in the explicit dynamic non-linear analysis of the models in order to accurately represent the behaviour of the real panels.

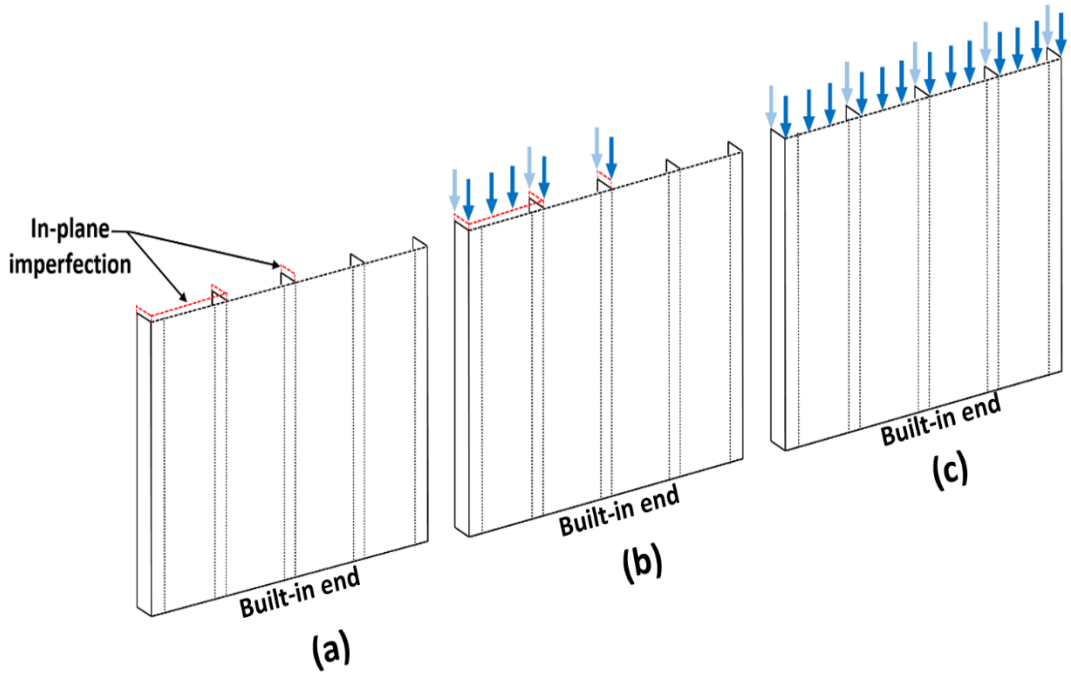

Figure 7.42: Effect of in-plane imperfections that generates a load eccentricity

7.7.5 Boundary conditions

The model's boundary conditions simulated the edges conditions in the rig test which included free longitudinal edges and a fully clamped (built-in) bottom edge and a top edge which was similar to the bottom except that in-plane axial displacements were enabled to allow the panel to be compressed. The stiffener web edges were also free to move. These boundary conditions are shown in Figure 7.43.

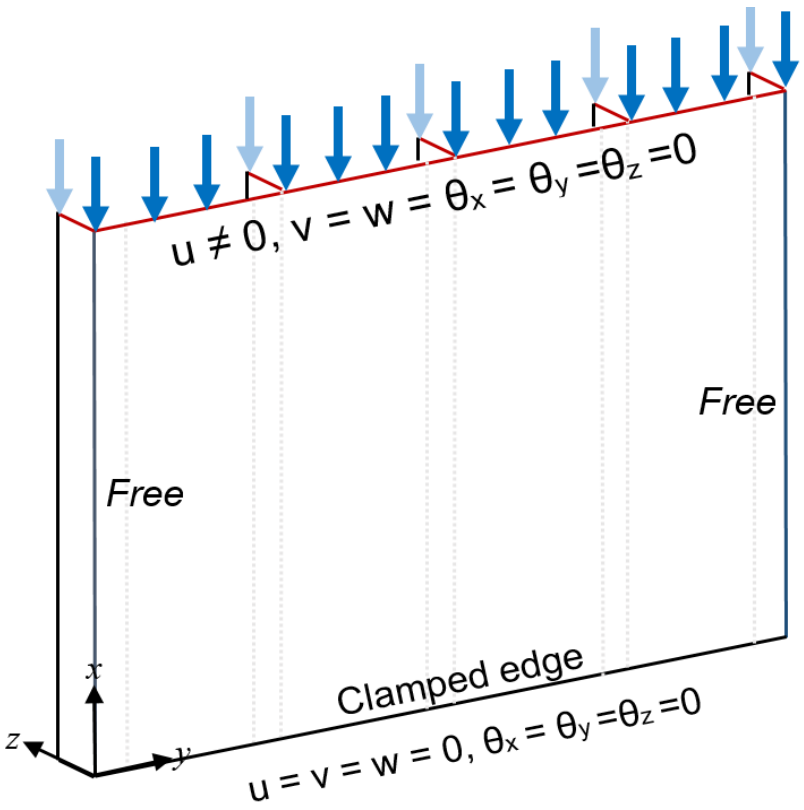

Figure 7.43: Model boundary conditions

7.7.6 Eigenvalue model

Linear eigenvalue analyses were conducted for each geometry to provide estimates of the buckling loads and to obtain the eigenmode shapes needed for modelling geometric imperfections. ABAQUS/Standard (version 6.14) was used for this.

An eigenvalue buckling problem finds the loads for which the model stiffness matrix becomes singular. The output eigenmodes are normalised so that the maximum displacement component is one unit. Scaled versions of these mode shapes, with amplitudes representative of the imperfections measured in the test specimens (using the DIC system) were used in the dynamic analyses since they provide a conservative approach when the exact form of the geometrical imperfections is unknown [156].

7.7.7 Explicit dynamic model

The simulated panel models, incorporating both material and geometric nonlinearities described in Sections 7.7.3 and 7.7.4 were analysed using the explicit dynamic solver step in ABAQUS/Explicit (version 6.14) [156]. As well as being ideal for analysing high-speed dynamic events, this solver has many advantages for the analysis of slower (quasi-static) processes, which are beneficial here. The use of a large number of small time increments in ABAQUS/Explicit is advantageous because each increment is relatively quick to compute (compared to the direct integration dynamic analysis procedure available in ABAQUS/Standard) as it does not require convergence iterations. The procedure uses diagonal ('lumped') element mass matrices whose inverses are simple to compute, significantly increasing computational efficiency. In addition, the vector multiplication of the inverse mass matrix by the inertial force requires only n operations, where n is the number of degrees of freedom in the model. Finally, the explicit procedure requires no global matrix operations and no tangent stiffness matrix calculation [156].

Models incorporating out of plane geometric imperfections based on the initial eigenvalue analysis underwent a two stage explicit dynamic analysis. In the first stage the effect of the initial in-plane geometrical imperfections generated during the panel manufacturing was simulated by applying displacements to

the panel components that were found to be longer when measured. In the second stage displacements were applied to the whole of the loaded edge to represent the loading after the longer sections had deformed to the same length as the rest of the panel. Both steps utilised a tabular load ramp to control the load applied on the panel (under displacement control).

7.8 Results and discussions

This section analyses the results from the finite element analyses for the three stiffened panel geometries and compares with those obtained experimentally in order to validate the models. FE results will be compared with the experimental results for the second panel in each geometry group because of the availability of complete details of the DIC system images for those panels, unlike the first panels for which DIC data is not available at the top and bottom of the images, Figure 7.44 shows the main specimen components.

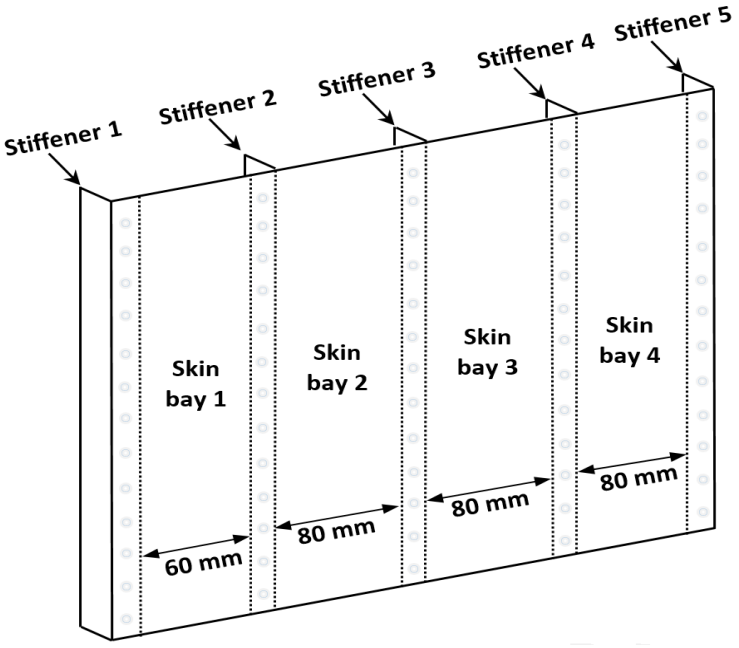

Figure 7.44: Stiffened panel components

7.8.1 Panel with R = 400 mm

Figure 7.45 compares the experimental results for the curved panel 400-2 described previously in section 7.6.1 with the finite element analysis results in terms of a load-shortening curve. Salient points are marked for discussion. As the experimental results have been discussed previously, the following discussion will be focused on the FE results and their comparison with the test data. The first part of the curve for the numerical results represents the first step which simulates the in-plane imperfections, which are applied to the third, fourth and fifth stiffeners of the panel. Initial buckling in the skin begins at point 1, with two buckles per bay as shown in Figure 7.46a, at a load level of 51.47 kN. The experimental out of plane displacement data shows relatively close correlation with the FE model, with some differences in the maximum negative deflection amplitude, which is higher in the experiments.

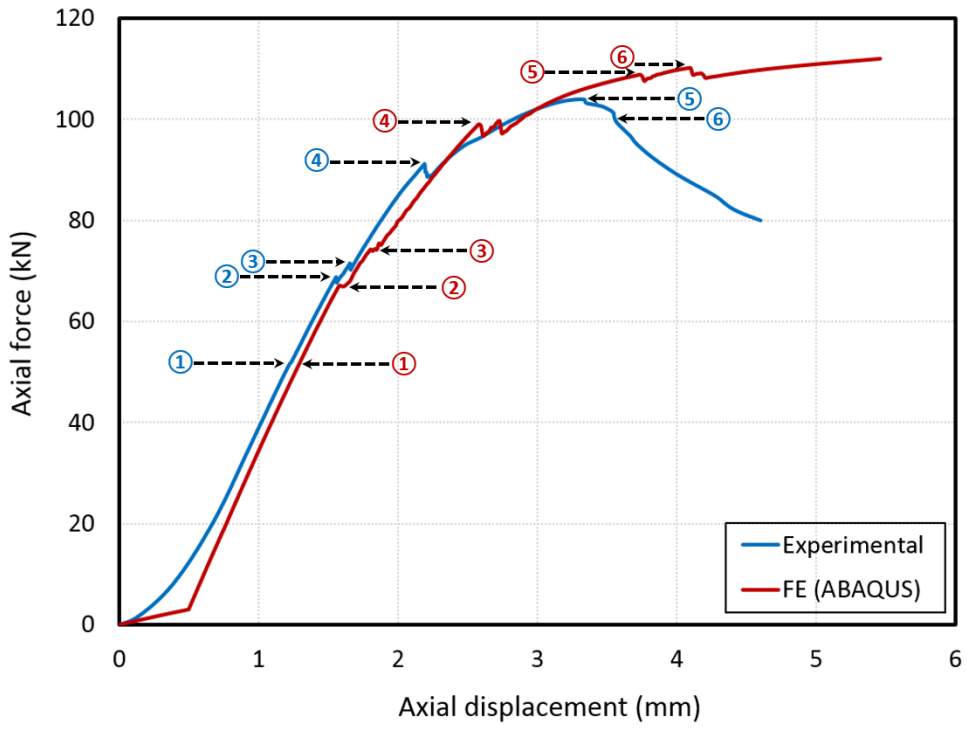

Figure 7.45: Panel 400-2 experiments vs FE model results comparison

This could be explained by the fact that the imperfection mode and amplitude applied in the model is estimated and may be conservative. At point 2 (Figure 7.45) a step is seen in both ABAQUS and experimental load-displacement curves as out of plane deformations increases. This increase in deformation can be seen clearly in both DIC and FE contour plots (Figure 7.46b) which show good agreement and continues to point 3 in Figure 7.46c with maximum out of plane displacement values (both negative and positive) continuing to increase. There is a full jump from *L/2* to *L/3* which can be seen in the out of plane displacement contours in Figure 7.46d at point 4. However there are some differences in how this occurs which can be seen by inspection of the full set of FE and DIC results. The main difference is that the jump in the ABAQUS mode shape occurs in all skin bays at the same time because the *L/3* shaped imperfection is introduced into the whole structure from the beginning. This is not the case for the specimens tested which will have different imperfections in each bay and in which therefore some bays will jump before others. The tested panel therefore jumps more gradually and this is reflected in the load versus end shortening plot where point 4 occurs later in the experimental plot than the FE one. In terms of the amplitudes of out of plane deformations there is close correlation between the two sets of results when the displacement is positive while it is slightly higher in the model when it is negative. A further jump is observed in the skin with the buckle pattern changing from *L/3* to *L/4* at point 5. The jump occurs in approximately the same sequence as the first jump with the experimental curves showing a partial jump in some skin bays initially while all bays jump at the same time in the FE model as illustrated in Figure 7.46e. The two modes are in better agreements later at point 6, Figure 7.46f, with the out of panel displacement amplitudes maintaining similar trends although the FE has a higher amplitude in the case of negative values.

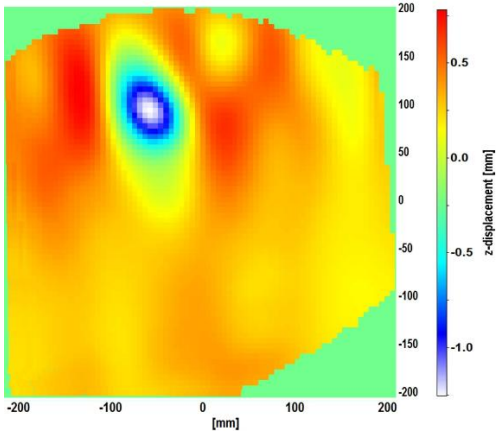

Point (1) DIC image

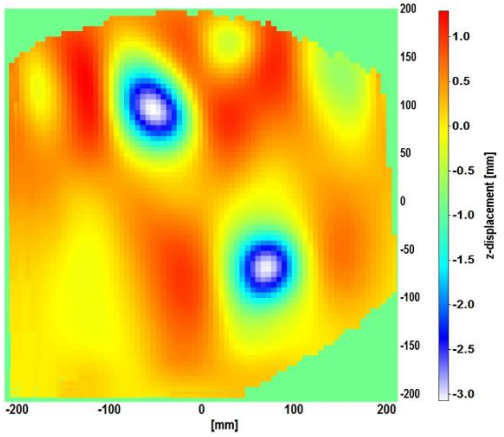

Point (2) DIC image

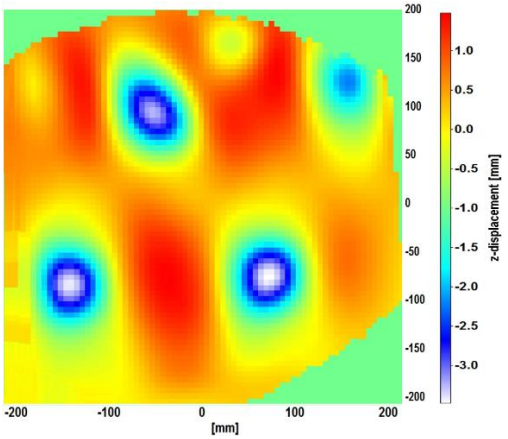

Point (3) DIC image

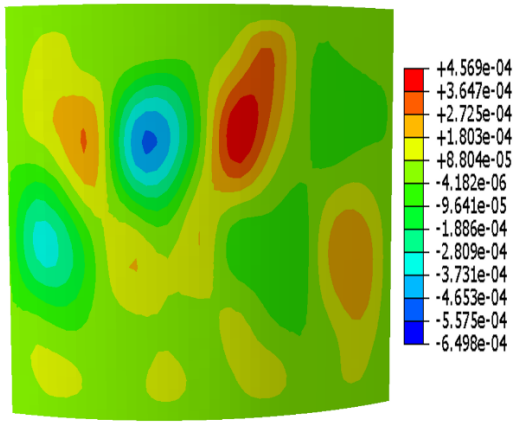

Point (1) FE contour z-displacement

(a)

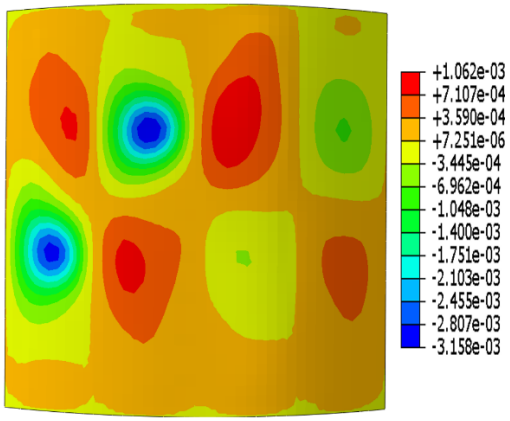

Point (2) FE contour z-displacement

(b)

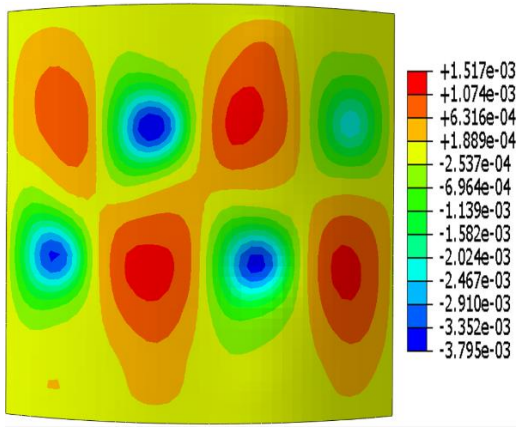

Point (3) FE contour z-displacement

(c)

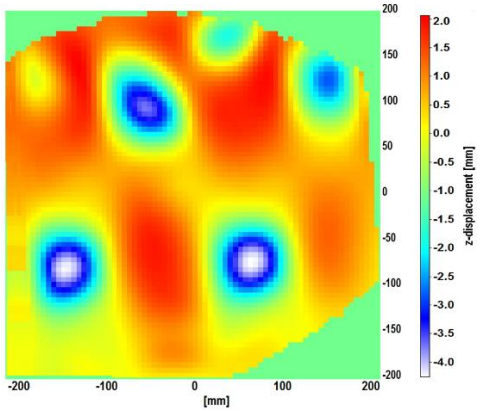

Point (4) DIC image

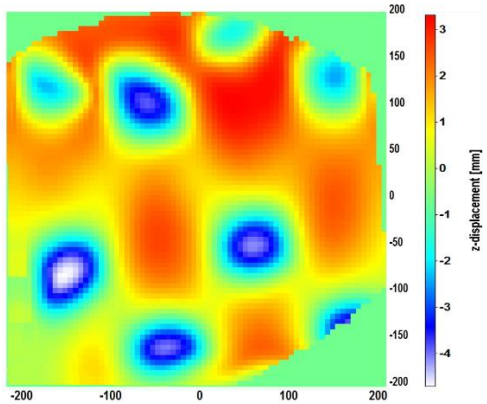

Point (5) DIC image

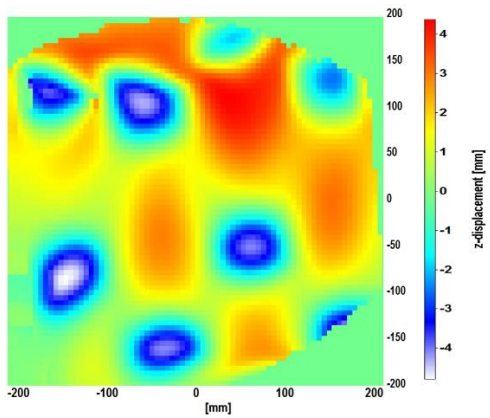

Point (6) DIC image

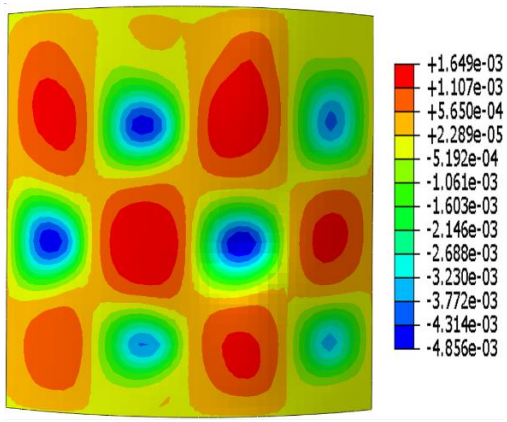

Point (4) FE contour z-displacement

(d)

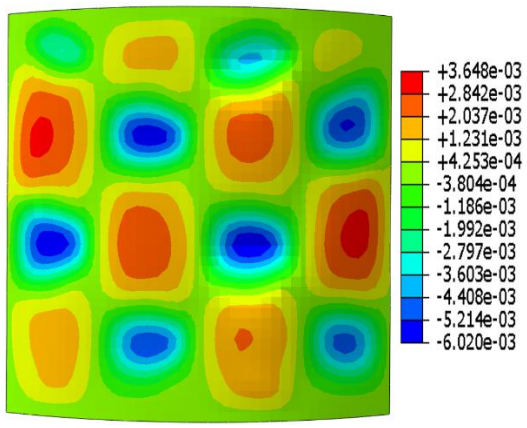

Point (5) FE contour z-displacement

(e)

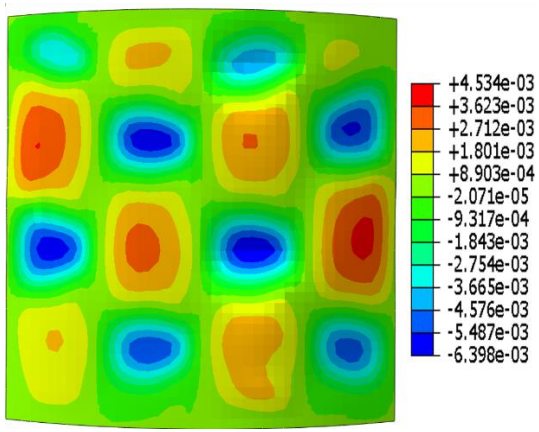

Point (6) FE contour z-displacement

(f)

Figure 7.46: Experiments vs FE out of plane displacement contours for panel 400-2

7.8.2 Panel with R = 800 mm

The numerical results of the FE model are again compared with experimental result for the second tested stiffened panel 800-2 as shown in Figure 7.47. The linear region at the beginning of the ABAQUS curve represents the first step of the analysis in which displacement was applied to specific stiffeners which were slightly longer than the rest of the panel. Five points on this load-shortening curves are of particular interest. Point 1 (49.5 kN) is the point at which the initial buckling configuration becomes apparent, with local buckling in the skin with half-wavelength *L/3*, Figure 7.48a. The mode shape for the FE model is similar to the experimental mode and appears at the same load level.

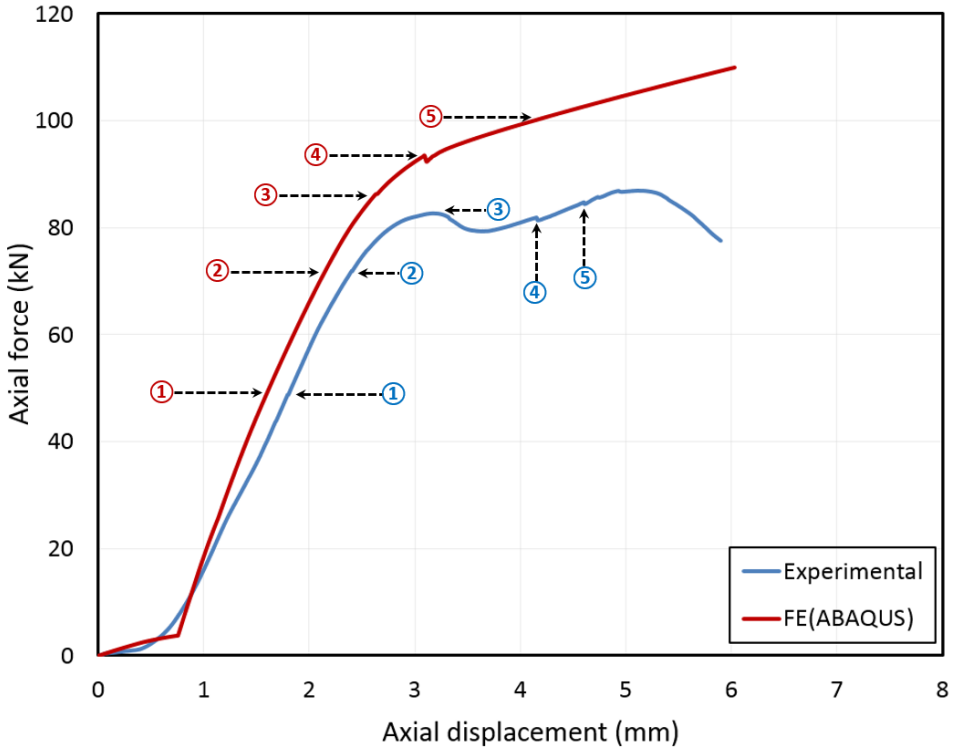

Figure 7.47: Panel 800-2 experiments vs FE model results comparison

Differences can be observed however, specifically in the maximum deflection amplitudes. The model agrees well with experimental results in terms of maximum negative out of plane displacement amplitudes, however, maximum values of positive displacement are seen to be greater in the experimental results. Mode shapes become more similar moving towards point 2 as shown in Figure 7.48b, although the maximum positive deflection seen in the test is double that predicted by the FE model. A mode jump from *L/3* to *L/4* is seen at point 3 in the experiment with a step in the load-displacement curve. In the FE model a small kink at a similar load potentially indicates the initiation of a jump which appears in the out of plane contour map in Figure 7.48c. The maximum positive experimental deflection increases rapidly at this point compared with the model data unlike the negative out of plane displacement for which the model has a slightly higher amplitude. A further jump occurs at point 4 as illustrated in Figure 7.48d, which can be observed clearly in both the DIC images and the contour maps from the model. Following this, the maximum positive out of plane displacement in the experiment increases significantly, particularly near the loaded edge, to more than 5 mm. This is not duplicated in the ABAQUS results which show a stable rise. This is potentially due to failure of the skin to stiffener bond reducing the stiffness of the panel in this area in the experiment. At point 5 and the stages after it (Figure 7.48e and 7.48f) deflection in the specimen continues to increase substantially, reaching more than 12 mm. The model predicts smaller values of deflection up to 3.6 mm at point 5, increasing to 10 mm by the end of the analysis.

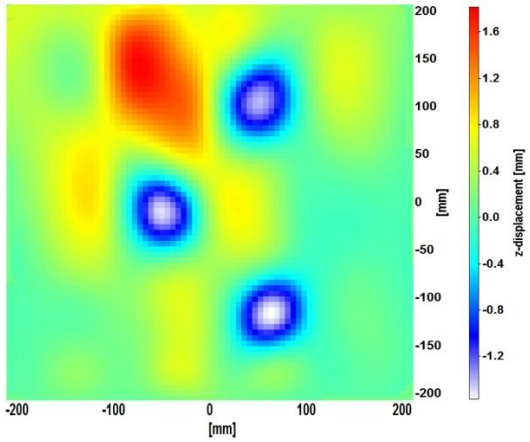

Point (1) DIC image

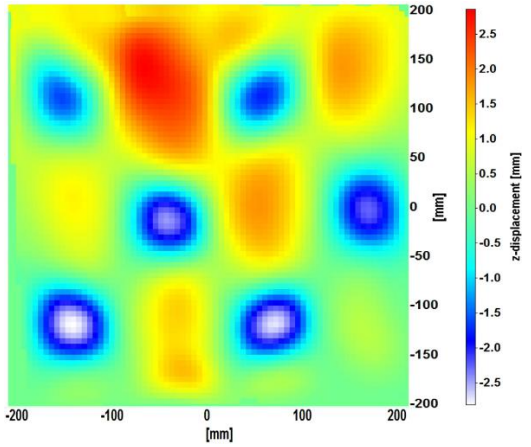

Point (2) DIC image

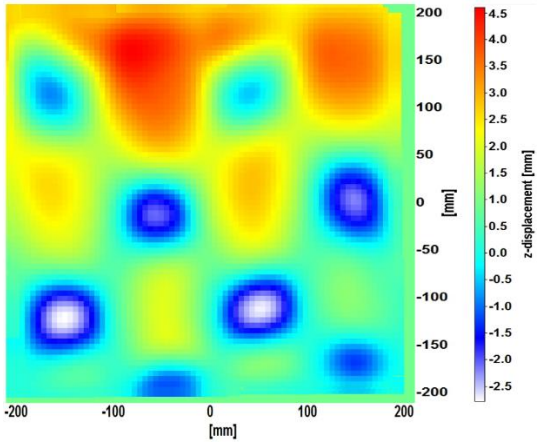

Point (3) DIC image

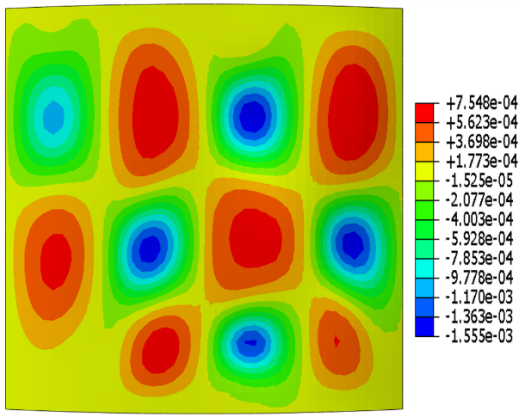

Point (1) FE contour z-displacement

(a)

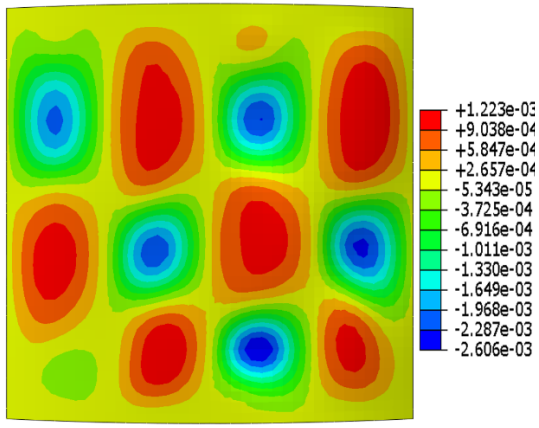

Point (2) FE contour z-displacement

(b)

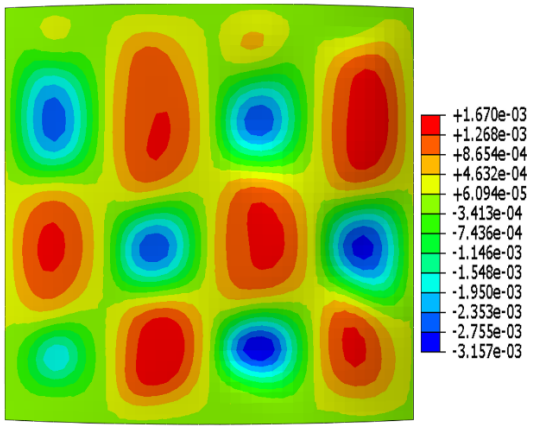

Point (3) FE contour z-displacement

(c)

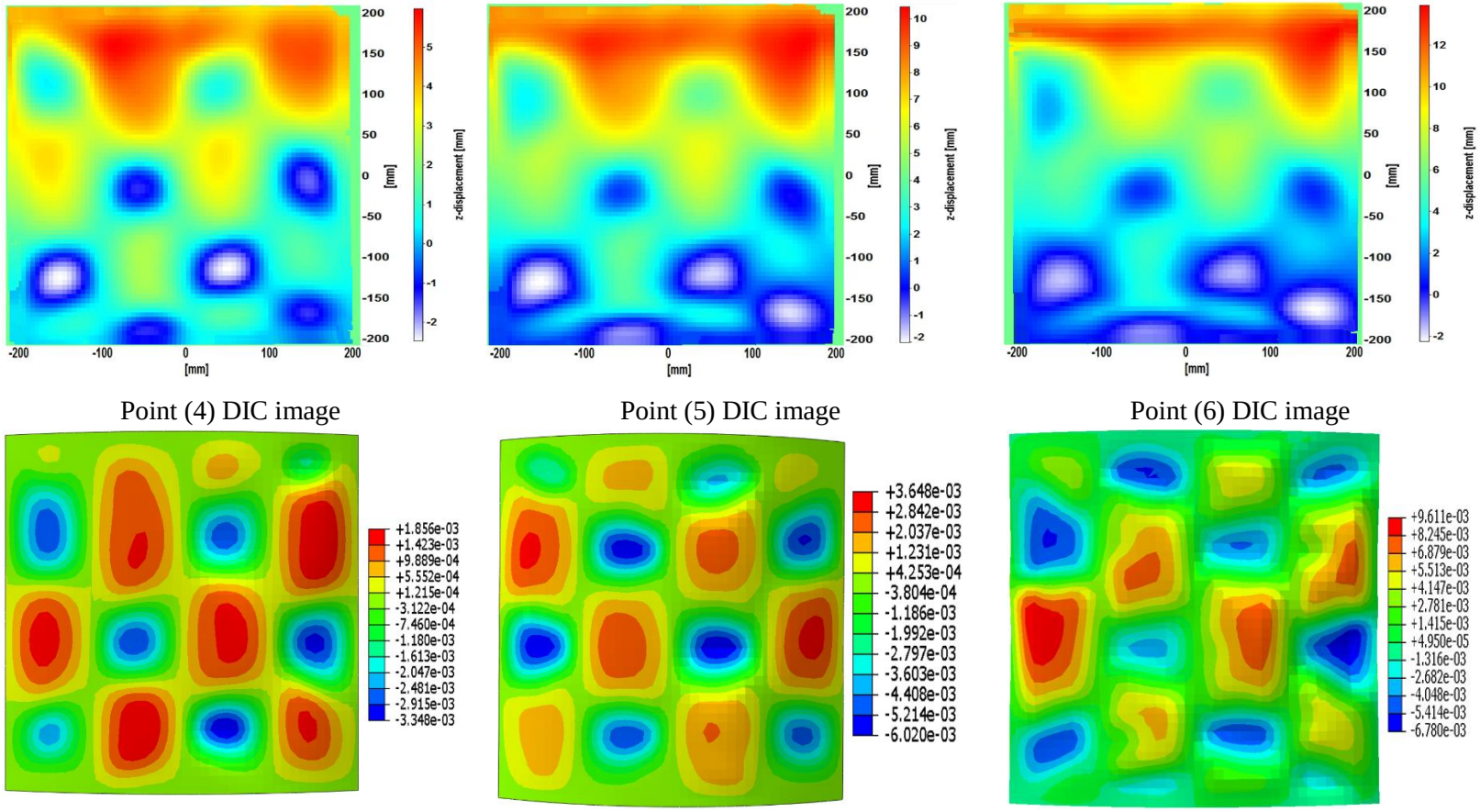

Point (4) DIC image | Point (5) DIC image | Point (6) DIC image

Point (4) FE contour z-displacement | Point (5) FE contour z-displacement | Point (6) FE contour z-displacement

(d) **(e)** **(f)**

Figure 7.48: Experiments vs FE out of plane displacement contours for panel 800-2

7.8.3 Flat panel

The results for the second flat panel will be discussed in this section. Figure 7.49 presents a comparison of the load versus displacement relationships between the experimental results and the numerical ones generated by the ABAQUS model. The curves are marked with six points, corresponding to changes in load versus displacement behaviour and mode shape. Initial buckling with half-wavelength L/3 occurs at point 1 corresponding to a load level 51.482 kN. Figure 7.50a shows slight differences in mode shape between the FE contours and the DIC images although the maximum out of plane displacements are in agreement. Point 2 which occurs at a load level 72.4 kN on both curves indicates the point at which the FE mode shape starts to change as new buckles start to initiate near the horizontal edges indicating a mode jump, see Figure 7.50b.

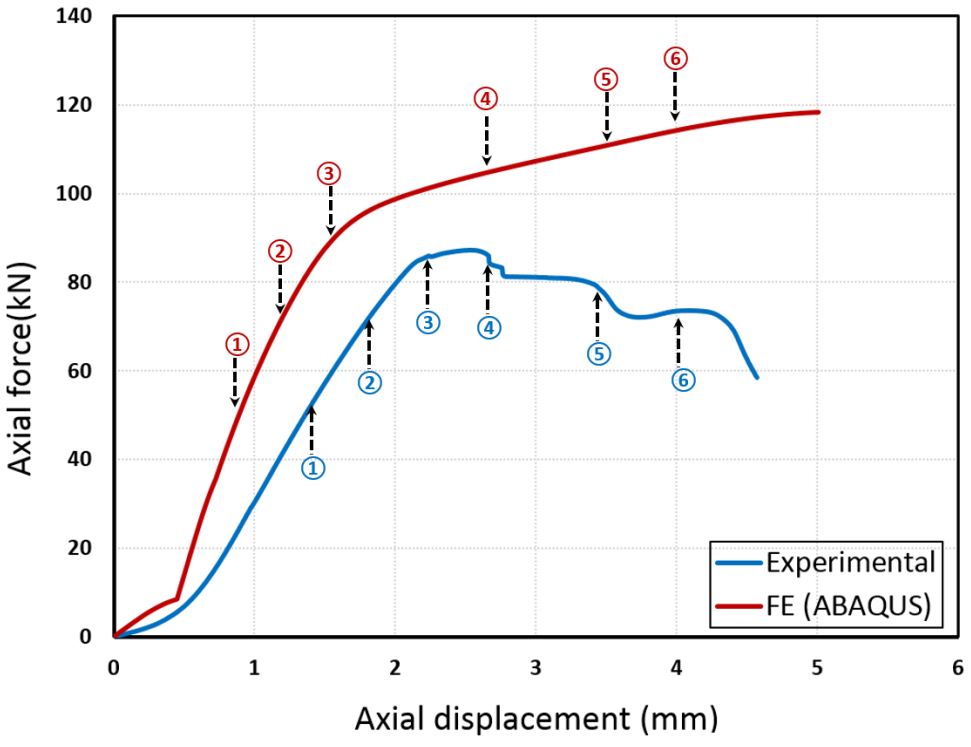

Figure 7.49: Flat panel experiments vs FE model results comparison

This change however occurs smoothly without a sudden change in the curve. The experimental mode shows slightly higher maximum deflections compared with the numerical result, and the mode is closer to *L/4*, differing from the FE mode which had *L/3* for boundary bays and L/5 for middle bays. At point 3, the ABAQUS mode shape changes from *L/3* to *L/5* without passing through *L/4* mode in all the skin bays (Figure 7.50c), while the experimental results show a change from *L/4* to *L/5* in the third skin bay. The experiments again demonstrate that each skin bay behaves differently in contrast to the FE results. Comparison of the maximum deflection amplitudes show they are higher in the test than the values predicted by ABAQUS which can be explained due to the effect of out of plane imperfections which will be different in the model from the experiment. The experimental curve shows a significant drop in the load at point 4 due to high levels of deformation in the panels with a number of buckles joining together causing the panel to begin to collapse (Figure 7.50d). The FE model shows slightly lower maximum deflection amplitudes than experiment. At points 5 and 6 the experimental panel continues to show high levels of deformation with substantial out of plane displacements near the loaded edge (Figure 7.50e and 7.50f).

This is very different from the ABAQUS results, possibly explaining the differences between the FE and experimental curves in Figure 7.49. The model results show a conservative trend and this is potentially explained due to two reasons. The main reason is because the skin comes away from the stiffeners in the experiment and this is not possible in the FE model due to fact that the bond is assumed to be perfect. In fact it is not perfect and it would be necessary to model the adhesive layer and allow it to fail using cohesive zone models in order to replicate the behaviour seen in the experiments. Moreover the out of plane displacement contour (buckling mode) was not exactly the same in the experiment.

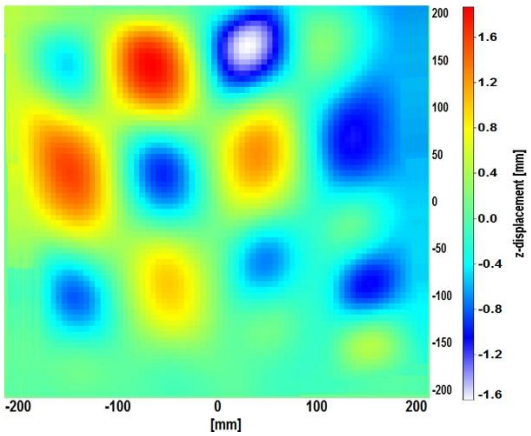

Point (1) DIC image

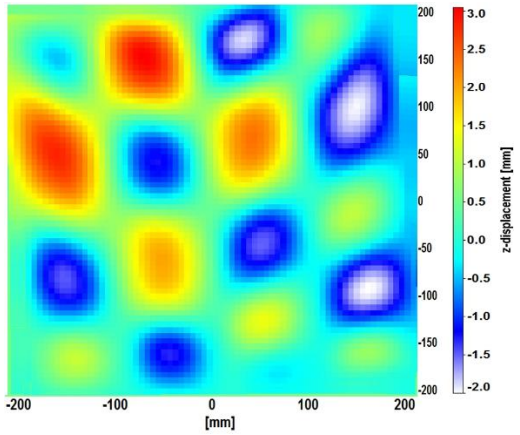

Point (2) DIC image

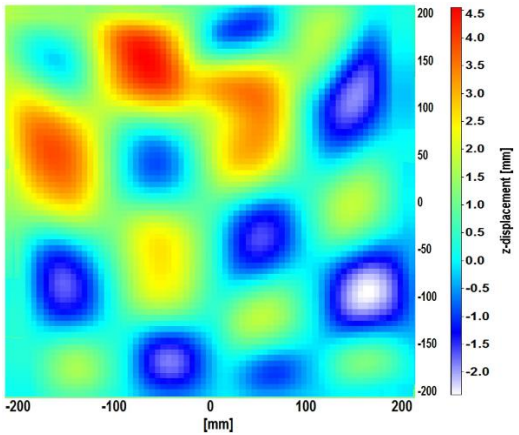

Point (3) DIC image

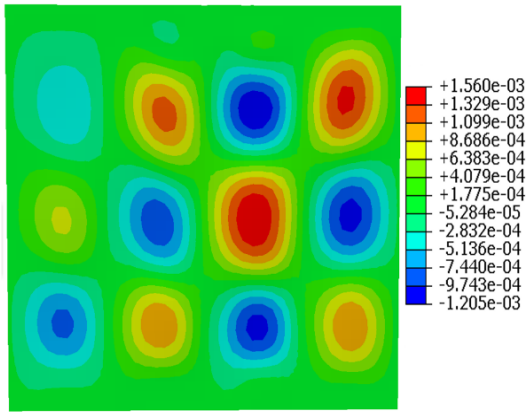

Point (1) FE contour z-displacement

(a)

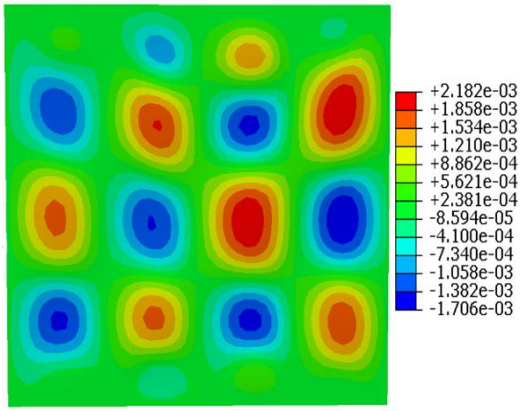

Point (2) FE contour z-displacement

(b)

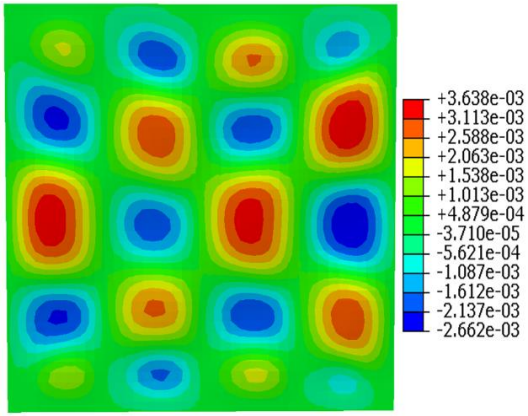

Point (3) FE contour z-displacement

(c)

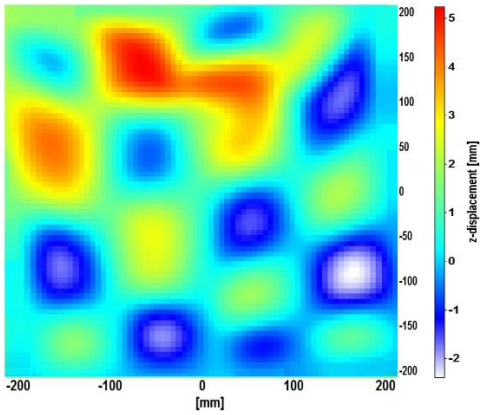

Point (4) DIC image

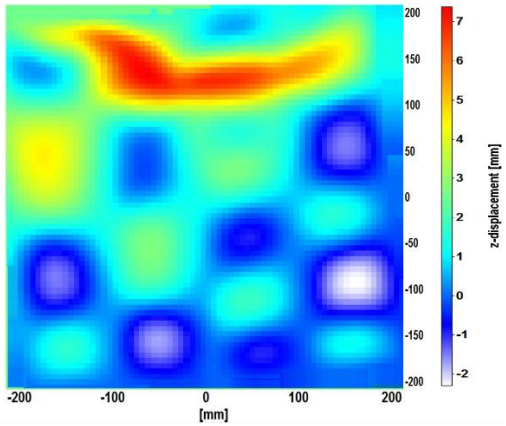

Point (5) DIC image

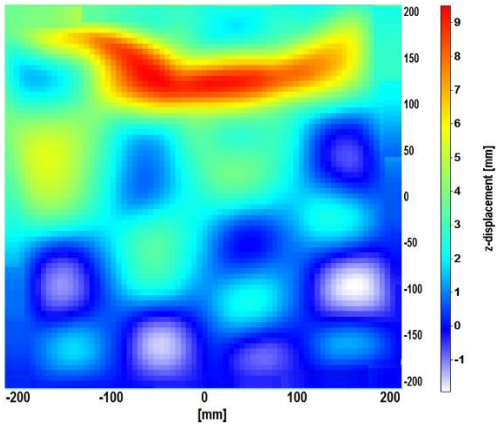

Point (6) DIC image

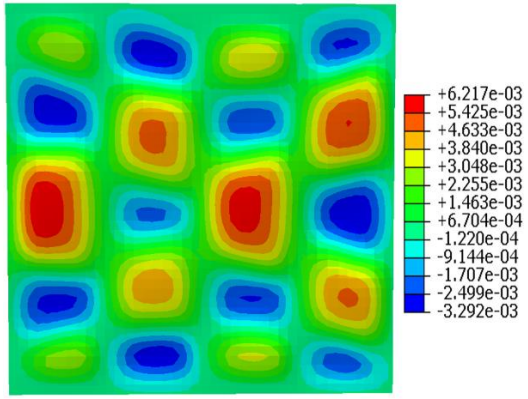

Point (4) FE contour z-displacement

(d)

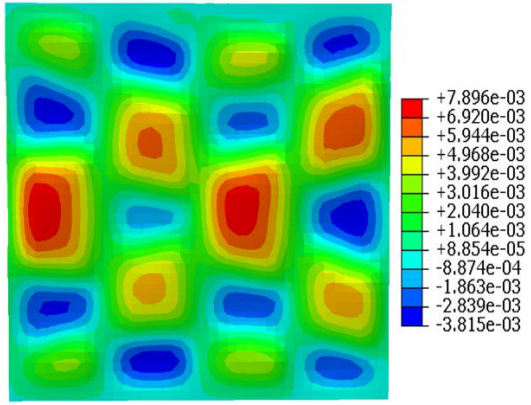

Point (5) FE contour z-displacement

(e)

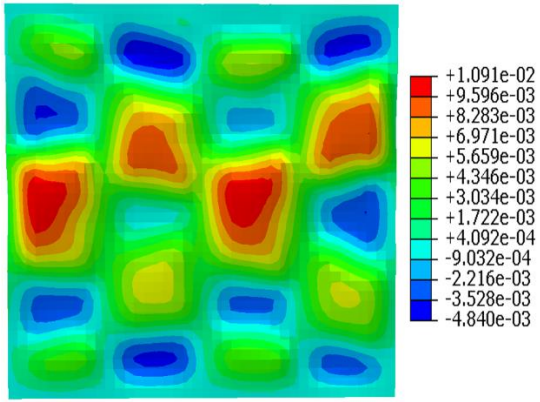

Point (6) FE contour z-displacement

(f)

Figure 7.50: Experiments vs FE out of plane displacement contours for flat panel

7.9 Chapter summary

This chapter focuses on the experimental work of six stiffened panels that have variable radii of curvature. The chapter started with a short description of the manufacture of the specimens including material properties obtained through testing to allow plasticity to be incorporated into the FE model and the machines used in this process. This was followed by details of the geometry and dimensions of the specimens. Monitoring techniques namely; Digital Image Correlation and strain gauging, were utilised to provide comprehensive data on the panel's responses and the deformation of constituent components (skin and stiffeners). The test set-up was then discussed followed by presentation of the experimental results. Finally the results of a series of numerical analyses performed using the finite element software ABAQUS to simulate the behaviour of the specimens tested to compare and validate the experimental results were presented. There are many facts that can be concluded from the experiments carried out in this chapter which are summarised as follows.

- Thin walled structures are generally sensitive to manufacturing imperfections (in or out of plane imperfection) which can produce completely different behaviour compared to the theoretical behaviour expected for a perfect structure.
- Despite the fact that advanced manufacturing in modern aerospace industry minimises the manufacturing imperfections, it is still difficult to manufacture a structural components with zero imperfections. Thus it is important for research purposes to explore its effect.
- Working with real structures under loading had many differences compared with theoretical approaches dealing with the same type of

components. Thus, improving the experimental conditions is essential for providing a close representation of the real behaviour of similar structural parts under loads.

- The connection parts between different structural components are still controversial topics in the research area which aims to optimise their performance (i.e. the skin-stiffener bond in this study).
- Comparing the experimental results with FE (ABAQUS) results showed the main differences between the practical and theoretical results. These differences clarify the difficulties in simulating exactly the test circumstances.
- The models used to compare the experimental results showed good agreement for curved panels with R=400mm, slightly less for R=800mm, while the flat panel result was relatively conservative.
- It is essential to improve the numerical and analytical models to simulate the real structural behaviour under different types of loading due to the expensive cost of high quality experimental research. Hence, this can lead to better understanding of its behaviour with a lower budget.

Chapter 8: Conclusions and future work

8.1 Conclusions

The research in this thesis has investigated buckling and post-buckling, including mode jumping, of thin-walled structures, namely plates and stiffened panels. The work focused on the use of numerical and experimental approaches to:

- Improve the buckling capacity of flat composite plates through a simple proposal to optimise stacking sequences, using anisotropy to increase the critical buckling load under different in-plane loading conditions such as compression, shear or a combination of both.
- Enhance the post-buckling analysis function in the exact strip software VICONOPT which provides a reduced order technique for optimising structures for buckling and post-buckling performance, by including buckling mode change (mode jumping). This contribution addresses a previously significant limitation of the software and has been validated using finite element analysis.
- Investigate experimentally the mode jumping phenomenon for a range of unsymmetrical panels with L-shape stiffeners and different radii of curvature to explore the actual behaviour under practical loading conditions of these components which form an important part of both wing and fuselage structures in the aerospace industry. By comparing the results obtained with numerical results generated using finite element analysis this has enabled the models used to validate the proposed mathematical approaches for predicting mode jumping to be verified.

More detailed conclusions relating to each of these contributions are presented below:

8.1.1 Improving the buckling capacity of composite plates

In Chapters 4 and 5, an optimisation approach utilising the anisotropic characteristics of composite plates to raise their buckling load was proposed. The main conclusions from this work can be summarised as:

- Under uniaxial in plane loading analysis showed that the buckling load factor dropped significantly as the value of lamination parameter ξ_3^D (which controls the anisotropic properties of the laminate) ranged between 0.0 and 0.75 (which is the maximum for a balanced laminate). This inverse relationship between the level of anisotropy and the buckling load factor under in plane compression indicates that designing laminates with ξ_3^D=0.0 for similar load cases will maximise their buckling load.
- For laminates under combined in-plane compression and shear loading, when the compression dominates, analysis showed that highest buckling loads were obtained when $\xi_3^D = \frac{N_{xy}}{N_x}$. This applied to plates with a variety of different aspect ratios.
- For laminates subject to combined in plane loading with shear loading dominant, results showed that higher buckling loads were obtained when $\xi_3^D = 0.75$. Consequently, for better buckling performance, it is recommended that laminates under these loading conditions should be designed with maximum anisotropy.
- When laminates are under pure in-plane shear the buckling load factor showed a significant increase when the skewing effect generated by the anisotropic properties had the reverse direction to the skewing

produced by the applied load. Conversely, a severe degradation in the buckling load capacity was seen when the anisotropy and shear act in the same directions. In this case therefore, laminates should be designed to maximise their level of anisotropy (to $\xi_3^D = 0.75$ in this study or $\xi_3^D = -0.75$ if shear is in the opposite direction) and to generate skewing acting against that generated by the shear load.

- The number of layers and the aspect ratios had only a minor effect on the general overall trends of the examined laminates.
- Results from both semi-analytical analyses using VICONOPT and numerical analyses using ABAQUS finite element software for a wide range of composite plates with different ply orientations under various in-plane loading conditions exhibited the same trends.
- Whilst manufacturing constraints are not considered in the current study, the results are expected to be similar when they are taken into account. Further work is currently being completed to incorporate these.

8.1.2 Enhancing post-buckling analysis through the introduction of mode jumping.

The work presented in Chapter 6 enhanced the post-buckling analysis in VICONOPT by including the effects of mode change in the geometrical nonlinear buckling zone. This was achieved using a number of different methods which enabled the values of strain at which a mode jump could occur to be predicted. The main conclusions from this investigation are:

- The effective width approach proposed provides a fast and simple mathematical method to calculate the strain at which a jump would occur. Despite providing accurate predictions in many cases, this

technique was overly conservative in others. This is due to the approximations such as the assumption that the middle strip (M.S.) carried zero load, which is in fact not completely true.

- A second approach utilising a strain energy comparison for different post-buckling equilibrium paths was more successful across the full range of geometries tested. A calculation method using different numerical approximations was proposed to calculate and compare the strain energy, namely: the third order polynomial method and the trapezoidal method. Despite the two mathematical methods depending on different calculation techniques, they produced very similar results and accurate predictions of the jumping strain values.
- The jumping mechanism was similar for both flat plates and stiffened panels: the skin buckled locally, and the occurrence of mode jumping depended significantly on the aspect ratio of the plate (panel) and the differences between the sequential post-buckling paths. The results also showed a small effect due to the material (isotropic or composite). In particular, mode jumping in composites was affected by stacking sequences since this affects both buckling and post-buckling behaviour.
- VICONOPT post-buckling analysis incorporating the techniques described above showed an acceptable level of agreement with finite element results using ABAQUS in terms of load-end shortening in the initial post-buckling stage. This agreement reduced however as results started to diverge in the advanced post-buckling zone due to the effect of mode jumps.
- The results of post-buckling analyses produced by VICONOPT for both flat plates and stiffened panels showed better agreement with

numerical analysis results after the effect of mode change had been considered.

- Finite element analyses predicted a smooth transformation between different mode shapes, whereas the exact strip method showed a sudden transition between the modes. This can be explained by the fact that the VICONOPT post-buckling results use a VIPASA analysis that assumes plates have a sinusoidal buckling mode with an integer number of half wavelengths. Thus, the jump occurs directly from mode m to mode m+1 without the transition stages seen in the ABAQUS results. This is particularly influenced by the imperfections introduced in the ABAQUS model, which facilitate jumping to the next mode shape.

8.1.3 Investigating mode jumping in stiffened panels experimentally

The experimental work carried out and discussed in Chapter 7 focused on investigating the post-buckling and mode jumping phenomenon for stiffened panels with differing geometries. The conclusions of this study are:

- Initial imperfections due to manufacturing defects had a substantial effect on the initial buckling loads and mode shapes. The effect of load eccentricity on the post-buckling behaviour and mode change phenomenon was particularly significant.
- The panels with the highest curvature of those tested (400 mm radius of curvature) showed similar trends with differences explained by their different imperfections positions and amplitudes. Both panels buckled locally with the unsupported plate sections jumping through a series of modes prior to the global failure of the panel. Numerical results predicted by ABAQUS finite element models showed good agreement with experimental results in terms of buckling mode shapes. However, the models predicted slightly higher mode jumping and collapse loads.

This behaviour could be explained due to the different out of plane positions and amplitudes of the imperfections in the model, which were based on eigenmode shapes scaled to represent measured defects rather than measured and modelled directly.

- Both panels with 800 mm radius of curvature showed lower initial buckling load values compared with the 400 mm panels as was expected since the level of curvature affects the initial stiffness of the panel. The two specimens showed similar experimental trends, appearing to buckle locally in the skin before failing globally due to severe deformation in the stiffener and skin-stiffener debonding. Underestimation of the effect of the imperfections led to the panels having lower buckling and failure loads in the experiment, than was predicted analytically. More significantly debonding of the stiffeners in the regions between the rivets, which was seen through visual inspection to be a major contributor to the final failure mode, was not included in the model, resulting in a non-conservative estimate of the stiffness of the panel during the latter stages of its loading and consequently higher buckling and failure loads.
- The final group tested, which consisted of two flat panels, varied significantly in their load versus end shortening behaviour. This was caused mainly by the effect of the load eccentricity due to initial in-plane manufacturing imperfections, which were considerably greater in one panel than the other. This resulted in stiffeners which were longer than the skin and hence carried all of the load initially and were therefore noticeably deformed before the panel itself was loaded. This reduced the level of support the stiffeners were able to provide to the panel. Both specimens had lower buckling loads than the panels discussed previously, again due to reductions in stiffness resulting from

the lack of curvature (as well as the increased level of imperfection).As well as non-uniformly distributed loads, the resulting stiffeners deformations caused early skin-stiffener disconnections, causing greater divergence between experimental and analytical results. Another possibility is that because the flat plate has lower stiffness than the curved one, the effect of the supports is more important. Therefore for the same level of deformation in the stiffeners its effect may be greater in the flat panel than it would be in the curved one.

- In all six specimens tested, it was observed that the skin bays often behaved independently, with individual bays exhibiting different mode shapes and jumping before or after neighbouring bays. This behaviour can be attributed to the panel's asymmetric geometry, load eccentricity and the differences between the imperfections found in each bay. This was not the case for the finite element model whose imperfections were based on the eigenmode, so would be similar (but not identical) for all bays. Consequently, mode jumping occurred in each bay at the same time due to the consistent imperfections introduced into each bay as discussed in Chapter 7.

8.2 Future work

- In terms of maximising the buckling capacity of composite plates under different load conditions, the optimisation guidelines proposed in the current work could be improved by using a modified branch and bound technique, incorporating manufacturing design constraints. Results could also be improved by using more orientation angles such as 0 and 90 to give greater design flexibility or investigates unbalanced and asymmetric laminates. In addition, it would be worth applying the

procedure developed to plates with different (in-plane or out of plane) boundary conditions, expanding its applicability. Finally it would be helpful to investigate the laminates studied experimentally to allow comparison to the theoretical results.

- The enhanced post-buckling technique proposed could be implemented in an improved VICONOPT post-buckling analysis currently under development which uses VICON analysis rather than the VIPASA analysis used in this work. This would provide greater more flexibility in evaluating mode jumps which are currently limited to jumps from mode m to m+1 due to VICON's ability to handle more complicated mode shapes. Consequently, it would be possible to investigate mode jumping under other loading conditions such as combined in-plane loading (compression and shear) and pure shear.
- The experimental work done in this study could be expanded in many ways, for example using a different shape of stiffeners or using composite stiffened panels. The use of symmetrical panels would lead to more uniform mode shapes. In terms of manufacturing and other imperfections, it would be of interest to examine the levels of uncertainty introduced by a variety of factors. A fuller understanding of buckling and post-buckling behaviour could be gained by using additional cameras in the DIC system thus allowing the stiffeners as well as the panels themselves to be monitored. This could also be achieved by increasing the number of strain gauges or using triaxial gauges to record strain. Experimental investigations could also be repeated for different types of loading such as shear or impact loading. It would also be useful to test damaged panels to explore the effect of the damage initiation and propagation on the mode jumping phenomenon.

- Finally, the finite element model used to simulate the experimental tests could be developed by using cohesive elements to allow skin stiffener separation to be modelled. Incorporating more precise representations of the initial out of plane imperfections in terms of amplitudes and locations would also lead to models which more accurately reproduce experimental behaviour.

References

[1] A. Chajes, Principles of Structural Stability Theory. Prentice Hall, 1974.

[2] (AGP) Aerospace Growth Partnership, “Means of Ascent The Aerospace Growth Partnership’s Industrial Strategy for UK Aerospace,” p. 44, 2016.

[3] Aerospace Technology Institute (ATI), “The Economic Impact of UK Aerospace Industrial Strategy,” 2017.

[4] S. Black, “Composite Rib Structure for Airbus A380 Vertical Tail,” 2004. [Online].Available: http://www.compositesworld.com/hpc/issues/2004/March/412.

[5] J. Hale, “Boeing 787 From Ground Up,” Boeing Comer. Aeromagazine, vol. 4, no. 6, p. 9, 2012.

[6] G. Kirchhoff, “Uber das gleichgewichi und die bewegung einer elasishem scheibe,” J. Pure Appl. Mathmatics, vol. 49, pp. 51–88, 1850.

[7] S. P. Timoshenko and S. Krieger, Theory of Plates and Shells. 1959.

[8] V. Novozhilov, Thin Shell Theory, 2nd edit. Springer Netherlands, 1959.

[9] C. Dym, Introduction to The Theory of Shells: structures and solid body mechanics, 1st edit. Elsevier, 1974.

[10] A. Ugural, Stresses in Plates and Shells, 2nd edit. McGraw Hill, 1981.

[11] E. Ventsel and T. Krauthammer, Thin Plates and Shells Theory: Analysis, and Applications. 2001.

[12] R. Szilard, Theories and Aplications of Plate Analysis. John Wiley & Sons, 2004.

[13] M. Sadd, Elasticity: Theory, Applications, and Numerics. Elsevier, 2010.

[14] J. N. Reddy, Theory and Analysis of Elastic Plates and Shells, 2nd editio. CRC Press, 2007.

[15] T. von Karman, “Festigkeitsprobleme im Maschinenbau, Encyclopädie der Mathematischen Wissenschaften IV.,” vol. 4, pp. 311–385, 1910.

[16] R. Jones, Buckling of Bars, Plates, and Shells, no. 4. Bull Ridge, 2006.

[17] L. Euler, “On the Strength of Columns,” Am. J. Phys., vol. 15, no. 4, pp. 315–318, 1947.

[18] W. F. Chen and E. Lui, Structural Stability: Theory and Implementation.

PTR Prentice Hall, 1987.

[19] S. P. Timoshenko and D. Young, “Theory of Structures,” 2nd edit., McGraw-Hill, 1965.

[20] Y. K. Cheung, Finite Strip Method in Structural Analysis. 1976.

[21] M. Cheung and Y.Cheung, “Natural Vibrations of Thin Flat-walled Structures with Different Boundary Conditions,” J. Sound Vib., vol. 18, no. 3, pp. 325–337, 1971.

[22] P. Babu and D.Reddy, “Frequency Analysis of Skew Orthotropic Plates by the Finite Strip Method,” J. Sound Vib., vol. 18, no. 4, pp. 465–474, 1971.

[23] G. Turvey and W. H. Wittrick, “The Influence of Orthotropy on the Stability of Some Multi-plate Structures in Compression,” Aeronaut. J., vol. 24, no. 1, pp. 1–8, 1973.

[24] D. Dawe, “Finite Strip Buckling Analysis of Curved Plate Assemblies under Biaxial Loading,” Int. J. Solids Struct., vol. 13, no. 11, pp. 1141–1155, 1977.

[25] T. Smith and S. Sridharan, “A Finite Strip Method for the Buckling of Plate Structures under Arbitrary Loading,” Int. J. Mech. Sci., vol. 20, no. 10, pp. 685–693, 1978.

[26] G. Bryan, “On the Buckling of Simply Supported Rectangular Plates Uniformly Compressed in One Direction,” Proc. London Math, vol. Soc 22, 1891.

[27] S. P. Timoshenko, “Bending and Buckling of Bimetallic Strips,” Opt. Soc, vol. 11, 1925.

[28] S. Levy, “Buckling of Rectangular Plates with Built-in Edges,” J. Appl. Mech., vol. 9.4, pp. 171–174, 1942.

[29] S. Batdorf and M. Stein, “Critical Combinations of Shear and Direct Stress for Simply Supported Rectangular Flat Plates.,” Natl. Advis. Comm. Aeronaut., vol. Technical, pp. 1–32, 1947.

[30] M. Stein and J. Neff, “Buckling Stresses of Simply Supported Rectangular Flat Plates In Shear,” Natl. Advis. Comm. Aeronaut., vol. No. 1222, no. AFL 2811, 1947.

[31] J. Rhodes, J. Harvey, and W. Fok, “The Load Carrying Capacity of Initially Imperfect Eccentrically Loaded Plates,” Int. J. Mech. Sci., vol. 17, no. 3, pp. 161–172, 1975.

[32] C. Bradfield, “Tests on Single Plates under In-plane Compression with

Controlled Residual Stress and Initial Out-of-flatness," Cambridge Univ. Eng. Dep., 1979.

[33] C. Bradfield, "Tests on Plates Loaded in In-plane Compression," J. Constr. Steel Res., vol. 1, no. 1, pp. 27–37, 1980.

[34] P. Stonor, "Unstiffened Steel Compression Panels with and without Coincident Shear," in Doctoral dissertation, University of Cambridge, PhD thesis, 1981.

[35] D. Mofflin, "Plate Buckling in Steel and Aluminium," PhD thesis, Univ. Cambridge, 1983.

[36] D. Mofflin, "Buckling of aluminum plates in compression," Behav. thin-walled Struct., pp. 399–427, 1984.

[37] W. H. Wittrick and F. W. Williams, "Buckling and Vibration of Anisotropic or Isotropic Plate Assemblies under Combined Loading," Int. J. Mech. Sci., vol. 16, no. 4, pp. 209–239, 1974.

[38] F. Williams and W. Wittrick, "Exact Buckling and Frequency Calculations Surveyed," J. Struct. Eng., vol. 109, no. 1, pp. 169–187, 1983.

[39] M. Anderson, F. Williams, and C. Wright, "Buckling and Vibration of Any Prismatic Assembly of Shear and Compression Loaded Anisotropic Plates with an Arbitrary Supporting Structure," Int. J. Mech. Sci., vol. 25, no. 8, pp. 585–596, 1983.

[40] D. Kennedy, F. Williams, and M. Anderson, "Buckling and Vibration Analysis of Laminated Panels Using VICONOPT," J. Aerosp. Eng., vol. 7, no. 3, pp. 245–262, 1994.

[41] D. Lam, F. Williams, and D. Kennedy, "Critical Buckling of Stiffened Panels with Discrete Point Connections," Int. J. Mech. Sci., vol. 39, no. 9, pp. 991–1009, 1997.

[42] M. P. Nemeth, "Buckling Behavior of Long Symmetrically Laminated Plates Subjected to Combined Loadings," vol. 3195, pp. 1–15, 1992.

[43] M. Nemeth, "Buckling Behavior of Long Anisotropic Plates Subjected To Restrained Thermal Expansion and Mechanical Loads," NASA Tech. Pap., vol. 23, no. 9, pp. 873–916, 1995.

[44] M. Nemeth, "Buckling Behavior of Long Symmetrically Laminated Plates Subjected to Shear and Linearly Varying Axial Edge Loads," NASA Tech. Pap. 3659, vol. 3659, pp. 1–46, 1997.

[45] M. Nemeth, "Buckling of Symmetrically Laminated Plates with

Compression, Shear, and In-plane Bending," AIAA Journal, vol. 30, no. 12. pp. 2959–2965, 1992.

[46] A. Watson, D. Kennedy, F. Williams, and C. Featherston, "Buckling and Vibration of Stiffened Panels or Single Plates with Clamped Ends," Adv. Struct. Eng., vol. 6, no. 2, pp. 135–144, 2003.

[47] C. Featherston and C. Ruiz, "Buckling of Flat Plates under Bending and Shear," Proc. Inst. Mech. Eng. Part C, J. Mech. Eng. Sci., vol. 212, no. 4, pp. 249–261, 1998.

[48] C. Featherston and A. Watson, "Buckling of Optimised Flat Composite Plates under Shear and In-plane Bending," Compos. Sci. Technol., vol. 65, no. 6, pp. 839–853, 2005.

[49] J. Loughlan, "The Influence of Bend–Twist Coupling on the Shear Buckling Response of Thin Laminated Composite Plates," Thin-Walled Struct., vol. 34, no. 2, pp. 97–114, 1999.

[50] J. Loughlan, "The Shear Buckling Behaviour of Thin Composite Plates with Particular Reference to the Effects of Bend-twist Coupling," Int. J. Mech. Sci., vol. 43, pp. 771–792, 2001.

[51] P. Weaver, "On Optimisation of Long Anisotropic Flat Plates subject to Shear Buckling Loads," in 45th AIAA/ASME/ASCE/AHS/ASC Structures, Structural Dynamics & Materials Conference, 2004.

[52] P. Weaver, "Approximate Analysis for Buckling of Compression Loaded Long Rectangular Plates with Flexural/twist Anisotropy," Proc. R. Soc. A Math. Phys. Eng. Sci., vol. 462, no. 2065, pp. 59–73, 2006.

[53] H. Abramovich, T. Weller, and C. Bisagni, "Buckling Behavior of Composite Laminated Stiffened Panels Under Combined Shear-Axial Compression," J. Aircr., vol. 45, no. 2, pp. 402–4013, 2008.

[54] R. Vescovini and C. Bisagni, "Buckling Analysis and Optimization of Stiffened Composite Flat and Curved Panels," AIAA J., vol. 50, no. 4, pp. 904–9015, 2012.

[55] Y. Liu and M. Pavlović, "A generalized Analytical Approach to the Buckling of Simply-Supported Rectangular Plates under Arbitrary Loads," Eng. Struct., vol. 30, no. 5, pp. 1346–1359, 2008.

[56] P. Jana and K. Bhaskar, "Analytical Solutions for Buckling of Rectangular Plates Under Non-uniform Biaxial Compression or Uniaxial Compression with In-plane Lateral Restraint," Int. J. Mech. Sci., vol. 49, no. 10, pp. 1104–1112, 2007.

[57] E. Byklum and J. Amdahl, “A simplified Method for Elastic Large Deflection Analysis of Plates and Stiffened Panels due to Local Buckling,” Thin-Walled Struct., vol. 40, no. 11, pp. 925–953, 2002.

[58] M. Eisenberger and I. Shufrin, “Buckling of Plates by the Multi Term Extended Kantorovich Method,” In Proceedings of the 7th EUROMECH Solid Mechanics Conference, Lisbon, Portugal, 2009, pp. 1–13.

[59] M. Khedmati, M. Zareei, and P. Rigo, “Sensitivity Analysis on The Elastic Buckling and Ultimate Strength of Continuous Stiffened Aluminium Plates Under Combined In-plane Compression and Lateral Pressure,” Thin-Walled Struct., vol. 47, no. 11, pp. 1232–1245, 2009.

[60] S. Zhang and I. Khan, “Buckling and Ultimate Capability of Plates and Stiffened Panels in Axial Compression,” Mar. Struct., vol. 22, no. 4, pp. 791–808, 2009.

[61] G. Grondin, A. Elwi, and J. Cheng, “Buckling of Stiffened Steel Plates—a parametric Study,” J. Constr. Steel Res., vol. 50, no. 2, pp. 151–175, 1999.

[62] M. Azhari, M. Abdollahian, and M. Bradford, “Local Buckling of Composite Laminated Plate Assemblies Using the Spline Finite Strip Method,” Adv. Struct. Eng., vol. 3, no. 2, pp. 173–178, 2000.

[63] H. Cox, “Buckling of Thin Plates in Compression,” Aeronaut. Res. Comm., vol. 1544, no. 2, 1933.

[64] H.Cox, “The Buckling of a Flat Rectangular Plate under Axial Compression and Its Behaviour After Buckling,” Aeronaut. Res. Comm., vol. 2041, no. 3, 1945.

[65] K. Friedrichs and J. Stoker, “The Non-Linear Boundary Value Problem of the Buckled Plate,” Am. J. Math., vol. 63, no. 4, pp. 839–888, 1941.

[66] K. Friedrichs and J. Stoker, “Buckling of the Circular Plate Beyond the Critical Thrust,” l. Appl, vol. 9, pp. 7–14, 1942.

[67] S. Bodner, “The Post Buckling Behaviour of a Clamped Circular Plate,” Q. Appl. Math., vol. 12, no. 4, pp. 397–401, 1955.

[68] S. Levy, “Bending of Rectangular Plates with Large Deflections,” NACA Technical Note 846. pp. 1–46, 1942.

[69] S. Levy, “Large Deflection Theory for Rectangular Plates,” Non-linear Probl. Mech. Contin., pp. 197–210, 1949.

[70] A. Neut, “Post-buckling Behaviour of Structures,” Advis. Gr. Aeronaut. Res. Dev., vol. 60, 1956.

[71] W. T. Koiter, “Introduction to The Post-buckling Behaviour of Flat Plates,” Mem. la Soc. R. des Sci. Liege, Ser. 5, No. 8, p. 17–40., 1963.

[72] W. T. Koiter, “Elastic Stability and Post buckling Behaviour,” Proc, Symp. Nonlinear Probl. ,Univ. Wisconsin Press. Madison, pp. 257–275, 1963.

[73] W. Koiter, “‘Over dc stabiliteit van het elastisch evenwicht’ (‘On the Stability of Elastic Equilibrium’),” Thesis, Delft, H. J. Paris, Amsterdam, vol. English tr, p. 833, 1967.

[74] J. Mayers and B. Budiansky, “Analysis of Behaviour of S.S. Flat Plates Compressed Beyond the Buckling Load into the Plastic Range,” Natl. Advis. Comm. AERONAUTICS, 1955.

[75] A. Walker, “The Post-buckling Behaviour of Simply-supported Square Plates,” Aeronaut. Q., vol. 20, no. 3, pp. 203–222, 1969.

[76] M. Stein, “Loads and Deformations of Buckled Rectangular Plates,” NASA 19980235521, vol. 40, 1959.

[77] J. Rhodes and J. Harvey, “The Post-buckling Behaviour of Thin Flat Plates in Compression with the Unloaded Edges Elastically Restrained Against Rotation,” J. Mech. Eng. Sci., vol. 13, no. 2, pp. 82–91, 1971.

[78] J. Reddy and W. Chao, “Large Deflection and Large-Amplitude Free Vibration of Laminated Composite-Material Plates,” Comput. Methods Nonlinear Struct. Solid Mech., pp. 341–347, 1981.

[79] M. Stein, “Postbuckling of Orthotropic Composite Plates Loaded in Compression,” AIAA J., vol. 21, no. 12, pp. 1729–1735, 1983.

[80] M. Stein, “Analytical Results for Post-buckling Behaviour of Plates in Compression and in Shear,” NASA Tech. Memo. 85766, vol. 84, 1984.

[81] M. Stein, “Postbuckling of Long Orthotropic Plates in Combined Shear and Compression,” AIAA J., vol. 23, no. 5, pp. 788–794, 1985.

[82] M. Stein, “Postbuckling of Long Orthotropic Plates under Combined Loading,” AIAA J., vol. 23, no. 8, pp. 1267–1272, 1985.

[83] G. Sun and F. Williams, “An Initial Post-buckling Analysis for Prismatic Plates Assemplies under Axial Compression,” Int. J. Solids Struct., vol. 34, no. 28, pp. 3705–3725, 1997.

[84] S. Wang and D. Dawe, “Spline FSM Postbuckling Analysis of Shear-deformable Rectangular Laminates,” Thin-Walled Struct., vol. 34, no. 2, pp. 163–178, 1999.

[85] M. Lillico, R. Butler, G. Hunt, A. Watson, and D. Kennedy, “Post-buckling

of Single and Multi-bay Panels Using Strut, Strip and FE methods," 19th AIAA Applied Aerodynamics Conference, 1329. 2001.

[86] R. Degenhardt, H. Klein, A. Kling, H. Temmen, and R. Zimmermann, "Buckling and Postbuckling Analysis of Shells under Quasi-Static and Dynamic Loads," DLR (German Aerosp. Center) Inst. Struct. Mech., 2002.

[87] E. Byklum, E. Steen, and J. Amdahl, "A Semi-analytical Model for Global Buckling and Postbuckling Analysis of Stiffened Panels," Thin-Walled Struct., vol. 42, no. 5, pp. 701–717, 2004.

[88] C. Lynch, A. Murphy, M. Price, and A. Gibson, "The Computational Post Buckling Analysis of Fuselage Stiffened Panels Loaded in Compression," Thin-Walled Struct., vol. 42, no. 10, pp. 1445–1464, 2004.

[89] R. Degenhardt and J. Delsemme, "Buckling and Postbuckling Analysis of a CFRP Stiffened Panel for a Better Material Exploitation," in the SAMTECH Users Conferences, Paris, France., 2005, pp. 1–7.

[90] R. Zimmermann, H. Klein, and A. Kling, "Buckling and Postbuckling of Stringer Stiffened Fibre Composite Curved panels - Tests and Computations," Compos. Struct., vol. 73, no. 2, pp. 150–161, 2006.

[91] A. Murphy, M. Price, C. Lynch, and A. Gibson, "The Computational Post-buckling Analysis of Fuselage Stiffened Panels Loaded in Shear," Thin-Walled Struct., vol. 43, no. 9, pp. 1455–1474, 2005.

[92] T. Möcker and H. G. Reimerdes, "Postbuckling Simulation of Curved Stiffened Composite Panels by The use of Strip Elements," Compos. Struct., vol. 73, no. 2, pp. 237–243, 2006.

[93] P. Buermann, R. Rolfes, J. Tessmer, and M. Schagerl, "A Semi-analytical Model for Local Post-buckling Analysis of Stringer- and Frame-stiffened Cylindrical Panels," Thin-Walled Struct., vol. 44, no. 1, pp. 102–114, 2006.

[94] F. Elaldi, "Buckling , Post-Buckling and Faulure Analysis," Proc. 8th Int. Fract. Conf., no. November, pp. 338–345, 2007.

[95] M. Bakker, M. Rosmanit, and H. Hofmeyer, "Elastic Post-buckling Analysis of Compressed Plates Using A two-Strip Model," Thin-Walled Struct., vol. 45, no. 5, pp. 502–516, 2007.

[96] I. Shufrin, O. Rabinovitch, and M. Eisenberger, "Elastic Nonlinear Stability Analysis of Thin Rectangular Plates Through A Semi-analytical Approach," Int. J. Solids Struct., vol. 46, no. 10, pp. 2075–2092, 2009.

[97] J. Rhodes, "Some Observations on The Post-buckling Behaviour of Thin Plates and Thin-walled Members," Thin-Walled Struct., vol. 41, no. 2–3,

pp. 207–226, 2003.

[98] S. Ghannadpour, H. Ovesy, and M. Nassirnia, “Nonlinear Post-buckling Analysis of Isotropic Plates Using Finite Strip Methods,” J. Aerosp. Sci. Technol., vol. 8, no. 1, pp. 11–19, 2011.

[99] C. Bisagni and R. Vescovini, “Analytical Formulation for Local Buckling and Post-buckling Analysis of Stiffened Laminated Panels,” Thin-Walled Struct., vol. 47, no. 3, pp. 318–334, 2009.

[100] R. Vescovini and C. Bisagni, “Single-mode Solution for Post-buckling Analysis of Composite Panels with Elastic Restraints Loaded in Compression,” Compos. Part B Eng., vol. B 43, no. 3, pp. 1258–1274, 2012.

[101] D. Stamatelos, G. Labeas, and K. Tserpes, “Analytical Calculation of Local Buckling and Post-buckling Behavior of Isotropic and Orthotropic Stiffened Panels,” Thin-Walled Struct., vol. 49, no. 3, pp. 422–430, 2011.

[102] L. Brubak and J. Hellesland, “Semi-analytical Postbuckling Analysis of Stiffened Imperfect Plates with a Free or Stiffened Edge,” Comput. Struct., vol. 89, no. 17–18, pp. 1574–1585, 2011.

[103] S. C. White, G. Raju, and P. Weaver, “Initial Post-buckling of Variable-Stiffness Curved Panels,” J. Mech. Phys. Solids, vol. 71, no. 1, pp. 132–155, 2014.

[104] N. Shanmugam, Z. Dongqi, Y. Choo, and M. Arockiaswamy, “Experimental Studies on Stiffened Plates Under In-plane Load and Lateral Pressure,” Thin-Walled Struct., vol. 80, pp. 22–31, 2014.

[105] J. Splichal, A. Pistek, and J. Hlinka, “Dynamic Tests of Composite Panels of An Aircraft wing,” Prog. Aerosp. Sci., vol. 78, pp. 50–61, 2015.

[106] H. Abramovich and C. Bisagni, “Behavior of Curved Laminated Composite Panels and Shells Under Axial Compression,” Prog. Aerosp. Sci., vol. 78, pp. 74–106, 2015.

[107] O. Oguaghamba, J. Ezeh, M. Ibearugbulem, and L. Ettu, “Buckling and Postbuckling Loads Characteristics of All Edges Clamped Thin Rectangular Plate,” Int. J. Eng. Sci., vol. 4, no. 11, pp. 55–61, 2015.

[108] J. Seo, C. Song, J. Park, and J. Paik, “Nonlinear Structural Behaviour and Design Formulae for Calculating the Ultimate Strength of Stiffened Curved Plates under Axial Compression,” Thin-Walled Struct., vol. 107, pp. 1–17, 2016.

[109] T. Lyman, L. Virgin, and R. Davis, “Application of Continuation Methods to Uniaxially Loaded Postbuckled Plates,” J. Appl. Mech., vol. 81, no. 3, p.

031010, 2013.

[110] L. Bauer and E. Reiss, “Nonlinear Buckling of Rectangular Plates,” J. Soc. Ind. Appl. Math., vol. 13, no. 3, pp. 603–626, 1965.

[111] W. Supple, “Hanges of Wave-form of Plates in the Post-buckling Range,” Int. J. Solids Struct., vol. 6, pp. 1243–1258, 1970.

[112] L. Cheo and E. Reiss, “Secondary Buckling of Circular Plates,” SIAM J. Appl. Math., vol. 26, no. 3, pp. 490–495, 1974.

[113] T. Nakamura and K. Uetani, “The Secondary Buckling and Post-buckling Behaviours of Rectangular Plates,” IInternational J. Mech. Sci., vol. 21, no. 5, pp. 265–286, 1979.

[114] D. Schaeffer and M. Golubitsky, “Boundary Conditions and Mode Jumping in the Buckling of a Rectangular Plate,” Commun. Math. Phys., vol. 69, no. 3, pp. 209–236, 1979.

[115] B. Matkowsky, L. Putnick, and E. Reiss, “Secondary States of Rectangular Plates,” Soc. Ind. Appl. Math., vol. 38, no. 1, pp. 38–51, 1980.

[116] E. Holder and D. Scshaeffer, “Boundary Conditions and Mode Jumping in the von Karman Equations,” Soc. Ind. Appl. Math., vol. 15, no. 3, pp. 446–458, 1984.

[117] H. Shen and J. Zhang, “Perturbation Analyses for the Postbuckling of Simply Supported Rectangular Plates under Uniaxial Compression,” Appl. Math. Mech., vol. 9, no. 8, pp. 793–804, 1988.

[118] R. Maaskant and J. Roorda, “MOde Jumping in Biaxially Compressed Plates,” Int. J. Solids Struct., vol. 29, no. 10, pp. 1209–1219, 1992.

[119] E. Riks, C. Rankin, and F. Brogan, “On the Solution of Mode Jumping Phenomena in Thin Walled Shell Structure,” Comput. Methods Appl. Mech. Eng., vol. 136, no. 1–2, pp. 59–92, 1994.

[120] E. Riks, C. Rankin, and F. Brogan, “On the Solution of Mode Jumping Phenomena in Thin-walled Shell Structures,” Comput. Methods Appl. Mech. Eng., vol. 136, no. 1–2, pp. 59–92, 1996.

[121] G. Salerno and R. Casciaro, “Mode Jumping and Attractive Paths in Multimode Elastic Buckling,” Int. J. Numer. Methods Eng., vol. 40, no. 5, pp. 833–861, 1997.

[122] C. Chang-jun and S. Xin-chun, “Mode Jumping of Simply Supported Rectangular Plates on Non-linear Elastic Foundation,” Int. J. Non. Linear. Mech., vol. 32, no. 1, pp. 161–172, 1997.

[123] D. Bushnell, C. Rankin, and E. Riks, “Optimization of Stiffened Panels in which Mode Jumping is Accounted for,” in 38th Structures, Structural Dynamics, and Materials Conference, 1997, p. 1141.

[124] P. Everall and G. Hunt, “Mode Jumping in The Buckling of Struts and Plates:A Comparative Study,” Int. J. Non. Linear. Mech., vol. 35, no. 6, pp. 1067–1079, 2000.

[125] G. Hunt and P. Everall, “Arnold Tongues and Mode-jumping in The Supercritical Post-buckling of An Archetypal Elastic Structure,” Proc. R. Soc. A Math. Phys. Eng. Sci., vol. 455, no. 1981, pp. 125–140, 1999.

[126] C. Chien, S. Gong, and Z. Mei, “Mode Jumping in The Von Kármán Equations,” SIAM J. Sci. Comput., vol. 22, no. 4, pp. 1354–1385, 2000.

[127] H. Chai, “Contact Buckling and Postbuckling of Thin Rectangular Plates,” J. Mech. Phys. Solids, vol. 49, no. 2, pp. 209–230, 2001.

[128] B. Falzon, “The Behaviour of Damage Tolerant Hat-stiffened Composite Panels Loaded in Uniaxial Compression,” Compos. - Part A Appl. Sci. Manuf., vol. 32, no. 9, pp. 1255–1262, 2001.

[129] B. Falzon and P. Steven, “Buckling Mode Transition in Hat-stiffened Composite Panels Loaded in Uniaxial Compression,” Compos. Struct., vol. 37, no. 2, pp. 253–267, 1997.

[130] B. Falzon and D. Hitchings, “Capturing Mode-switching in Postbuckling Composite Panels Using A Modified Explicit Procedure,” Compos. Struct., vol. 60, no. 4, pp. 447–453, 2003.

[131] H. Chen and L. Virgin, “Dynamic Analysis of Modal Shifting and Mode Jumping in Thermally Buckled Plates,” J. Sound Vib., vol. 278, no. 1–2, pp. 233–256, 2004.

[132] H. Chen and N. Virgin, “Finite Element Analysis of Post-Buckling Dynamics in Plates Part I: An asymptotic approach,” Int. J. Solids Struct., vol. 43, no. 13, pp. 3983–4007, 2006.

[133] H. Chen and W. Yu, “Postbuckling and Mode Jumping Analysis of Composite Laminates Using An Asymptotically Correct, Geometrically Non-linear Theory,” Int. J. Non. Linear. Mech., vol. 41, no. 10, pp. 1143–1160, 2006.

[134] H. Chen and N. Virgin, “Finite Element Analysis of Post-Buckling Dynamics in Plates. Part II: A non-stationary analysis,” Int. J. Solids Struct., vol. 43, no. 13, pp. 4008–4027, 2006.

[135] B. Falzon and M. Cerini, “An Automated Hybrid Procedure For

Capturing Mode-jumping in Postbuckling Composite Stiffened Structures," Compos. Struct., vol. 73, no. 2, pp. 186–195, 2006.

[136] A. Murphy, D. Quinn, and M. Price, "Initial Skin Buckling and Mode-jumping in Integrally Stiffened Metallic Panels," Exp. Anal. Nano Eng. Mater. Struct., pp. 785–786, 2007.

[137] H. Hofmeyer and J. Jaspart, "On the Modelling of Compressed Long Plates Related To Sheet-Section Behaviour," 5th Int. Conf. Thin-Walled Struct. ,Brisbane, Aust., pp. 2–9, 2008.

[138] B. Falzon, A. Faggiani, and D. Brunner, "Lay-up Optimisation of Composite Plates to Delay Mode-jump Instabilities," in 28th Congress of the International Council of the Aeronautical Sciences (ICAS), 2012, vol. 3.

[139] B. Falzon and A. Faggiani, "The Use of a Genetic Algorithm to Improve the Postbuckling Strength of Stiffened Composite Panels Susceptible to Secondary Instabilities," Compos. Struct., vol. 94, no. 3, pp. 883–895, 2012.

[140] H. Hofmeyer and J. Courage, "Analytical and Finite Element Modelling of Long Plate Mode Jumping Behaviour," Thin-Walled Struct., vol. 73, pp. 101–111, 2013.

[141] C. Wang, H. Tan, L. Lan, and L. Li, "Mode Jumping Analysis of Thin Film Secondary Wrinkling," Int. J. Mech. Sci., vol. 104, pp. 138–146, 2015.

[142] A. Watson and D. Kennedy, "Mode Jumping in Post buckled Stiffened Panels," in Fourth International Conference on Thin Walled Stractures (ICTWS 04), Loughborough, UK, 2004.

[143] W. Li, Y. Cheung, F. ASCE, and L. Tham, "Spline Finite Strip Analysis of General Plates," J. Eng. Mech., vol. 112, no. 1, pp. 43–54, 1986.

[144] M. Bradford and M. AzharI, "Buckling of Plates with Different End Conditions Using the Finite Strip Method," Comput. Struct., vol. 56, no. 1, pp. 75–83, 1995.

[145] D. Dawe and V. Peshkam, "A Note on Finite Strip Buckling Analysis of Composite Plate Structures," Compos. Struct., vol. 34, no. 2, pp. 163–168, 1996.

[146] H. Ovesy, J. Loughlan, and H. Assaee, "The Compressive Post-local Bucking Behaviour of Thin Plates Using A Semi-energy Finite Strip Approach," Thin-Walled Struct., vol. 42, no. 3, pp. 449–474, 2004.

[147] W. Wittrick, "General Sinusoidal Stiffness Matrices for Buckling and Vibration Analyses of Thin Flat-walled Structures," Int. J. Mech. Sci., vol.

10, no. 12, pp. 949–966, 1968.

[148] D. Kennedy, M. Fischer, and C. Featherston, “Recent Developments in Exact Strip Analysis and Optimum Design of Aerospace Structures,” Proc. Inst. Mech. Eng. Part C J. Mech. Eng. Sci., vol. 221, no. 4, pp. 399–413, 2007.

[149] W. Wittrick and F. Williams, “A General Algorithm for Computing Natural Frequencies of Elastic Structures,” Q. J. Mech. Appl. Math., vol. 24, no. 3, pp. 263–284, 1970.

[150] W. Wittrick and F. Williams, “An Algorithm for Computing Critical Buckling Loads of Elastic Structures,” J. Struct. Mech., vol. 1, no. 4, pp. 497–518, 1973.

[151] F. Williams and M. Anderson, “Incorporation of Lagrangian Multipliers into an Algorithm for Finding Exact Natural Frequencies or Critical Buckling Loads,” Int. J. Mech. Sci., vol. 25, no. 8, pp. 579–584, 1983.

[152] R. Butler and F. Williams, “Optimum Design using VICONOPT, a Buckling and Strength Constraint Program for Prismatic Assemblies of Anisotropic Plates,” Comput. Struct., vol. 43, no. 4, pp. 699–708, 1992.

[153] S. Powell, F. Williams, A. Askar, and D. Kennedy, “Local Postbuckling Analysis for Perfect and Imperfect Longitudinally Compressed Plates and Panels,” in the 39th AIAA/ASME/ASCE/AHS/ASC Structures, Structural Dy- namics and Materials Conference, Long Beach, CA, 1998.

[154] M. S. Anderson and D. Kennedy, “Postbuckling of Composite Stiffened Panels Using Exact Strip Analysis with Newton Iteration,” in 49th AIAA/ASME/ASCE/AHS/ASC Structures, Stractural Dynamics, and Materials Conference, 2008.

[155] B. Che, D. Kennedy, and C. Featherston, “Improved Exact Strip Postbuckling Analysis for Anisotropic Plates with Fixed, Free and Straight Edges,” in 28th Congress of the International Council of the Aeronautical Sciences (ICAS), 2012.

[156] “Dassault Systemes, Abaqus Analysis User’s Manual Version 6.14.” 2014.

[157]“https://archive.nytimes.com/www.nytimes.com/interactive/2013/07/29/business/The-Jump-to-a-Composite-Plane.html.” .

[158] F. Williams and D. Kennedy, “Analysis Features of VICONOPT, an Exact Buckling and Vibration Program for Prismatic Assemblies of Anisotropic Plates,” 31st Struct. Dyn. Mater. Conf. Struct. Struct. Dyn. Mater. Co-located Conf., vol. AIAA, no. Long Beach,CA,U.S.A., 1990.

[159] J. Loughlan, “The Shear Buckling Behaviour of Thin Composite Plates with Particular Reference to the Effects of Bend-twist Coupling,” Int. J. Mech. Sci., vol. 43, pp. 771–792, 2001.

[160] S. Selyugin, “Thin-Walled Structures Some Approaches to Buckling Analysis of Flexurally Anisotropic Composite Plates Subjected to Combined In-plane Loading,” Thin Walled Struct., vol. 98, pp. 375–383, 2016.

[161] R. Jones, Mechanics of Composite Materials. Taylor and Francis Ltd, 1999.

[162] C. Diaconu, C. Sato, and H. Sekine, “Layup Optimization of Symmetrically Laminated Thick Plates for Fundamental Frequencies using Lamination Parameters,” Struct. Multidiscip. Optim., vol. 24, no. 4, pp. 302–311, 2002.

[163] C. Diaconu and H. Sekine, “Layup Optimization for Buckling of Laminated Composite Shells with Restricted Layer Angles,” AIAA Journal, vol. 42, no. 10. pp. 2153–2163, 2004.

[164] J. Herencia, P. Weaver, and M. Friswell, “Local Optimisation of Anisotropic Composite Panels with T Shape Stiffeners,” in 48th AiAA/ASME/AHS/AHS structuractral Dynamics and Material Conference, Honolulu, Hawii, 2007.

[165] M. Miki, “Material Design of Composite Laminates with Required In-plane Elastic Properties,” in Progress in Science and Engineering of Composites, ICCM-IV, Tokyo, 1982, pp. 1725–1731.

[166] M. Miki and Y. Sugiyamat, “Optimum Design of Laminated Composite Plates Using Lamination Parameters,” AIAA J., vol. 31, no. 5, pp. 921–922, 1993.

[167] M. P. Nemeth, “Buckling Behavior of Long Symmetrically Laminated Plates Subjected to Shear,” 1997.

[168] C. Kassapoglou, Design and Analysis of Composite Structures: with Applications to Aerospace Structures. John Wiley & Sons, 2013.

[169] X. Liu, C. A. Featherston, and D. Kennedy, “Two-level Layup Optimization of Composite Laminate Using Lamination Parameters,” Compos. Struct., vol. 211, pp. 337–350, 2019.

[170] S. Soni, “Elastic Properties of T300/5208 Bidirectional Symmetric Laminates,” 1980.

[171] K. Marguerre, “The Apparent Width of the Plate in Compression,” NACA

TM-833, vol. 14, no. 3, pp. 1–32, 1937.

[172] G. Winter, “Strength of Thin Steel Compression Flanges,” Trans. ASCE, vol. 112, pp. 527–554, 1947.

[173] W. Koiter, “The effective Width of Flat Plates for Various Longitudinal Edge Conditions at Loads Far Beyond the Buckling Load,” Rep, 5287, pp. 365–374, 1943.

[174] H. Bengston, “Ship Plating under Compression and Hydrostatic Pressure,” pp. 80–116, 1937.

[175] “AALCO. 2017. Aluminium Alloy - Commercial Alloy - 6082 - T6-T651 Plate. Available at www.aalco.co.uk/datasheets/Aluminium-Alloy_6082-T6~T651_148.ashx [Accessed 10th October 2017],” Aalco Material Datasheet, 2017.

[176] BSI, “BSI Standards Publication Metallic Materials — Tensile testing Part 1 : Method of Test at Room Temperature,” BSI, 2016.

[177] A. Adhesives, “General-Purpose Foil Strain Gages KFG,” pp. 18–25.

Appendix

Appendix A: Derivation of the plate bending and buckling governing equations.

Starting with the out of plane displacement function assumptions:

$$w(x,y) = \frac{w_0}{2b^3}(3b^3y - y^3)\, sin\frac{m\pi}{a}x \tag{A1}$$

$$\frac{\partial^2 w}{\partial x^2} = -\frac{m^2\pi^2}{2a^2b^3}w_0(3b^3y - y^3)\sin\frac{m\pi}{a}x \tag{A2}$$

$$\frac{\partial^2 w}{\partial y^2} = -\frac{3y}{2b^3}w_0\sin\frac{m\pi}{a}x \tag{A3}$$

$$\frac{\partial^2 w}{\partial x\partial y} = \frac{m\pi}{2ab^3}(3b^3y - y^3)\cos\frac{m\pi}{a}x \tag{A4}$$

we shall use the following useful integrations:

$$\int_0^a sin^2\frac{m\pi}{a}x\, dx = \int_0^a \frac{1}{2}(1 - cos\frac{2m\pi}{a}x)\, dx = \frac{a}{2} \tag{A5}$$

$$\int_0^a cos^2\frac{m\pi}{a}x\, dx = \int_0^a \frac{1}{2}(1 + cos\frac{2m\pi}{a}x)\, dx = \frac{a}{2} \tag{A6}$$

From the elastic plate theory the bending and twisting moments are

$$M_x = -D(\frac{\partial^2 w}{\partial x^2} + \nu\frac{\partial^4 w}{\partial y^2}) \tag{A7}$$

$$M_x = -D(\frac{\partial^2 w}{\partial y^2} + \nu\frac{\partial^4 w}{\partial x^2}) \tag{A8}$$

$$M_{xy} = -D(1+\nu)\,\frac{\partial^2 w}{\partial x\partial y} \tag{A9}$$

where $D = (E\, h^3)/12(1-\nu^2)$

The equilibrium equation due to bending:

$$\frac{\partial^2 M_x}{\partial x^2} - 2\frac{\partial^2 M_{xy}}{\partial x \partial y} + \frac{\partial^2 w}{\partial y^2} + N_x \frac{\partial^2 w}{\partial x^2} + 2\frac{\partial^2 M_{xy}}{\partial x \partial y} + N_x \frac{\partial^2 w}{\partial x^2} = 0 \tag{A10}$$

Substituting equations (A7), (A8) and (A9) into equation (A10), the differential equation of plate buckling can be obtained as:

$$\frac{\partial^4 w}{\partial x^4} + 2\frac{\partial^4 w}{\partial x^2 \partial x^2} + \frac{\partial^4 w}{\partial x^4} = \frac{1}{D}\left(N_x \frac{\partial^2 w}{\partial x^2} 2\frac{\partial^2 M_{xy}}{\partial x \partial y} + N_x \frac{\partial^2 w}{\partial x^2}\right) \tag{A11}$$

To solve equation (A11) and calculate the buckling loads for a flat plate with SSSF edge conditions, apply the minimum principle of energy as follows. First the total strain energy of bending for the plate is:

$$U_b = \int_0^a \int_0^b \left[\left(\frac{\partial^2 w}{\partial x^2} + \frac{\partial^2 w}{\partial y^2}\right)^2 - 2(1-\nu)\left(\left(\frac{\partial^2 w}{\partial x^2}\frac{\partial^2 w}{\partial y^2} - \left(\frac{\partial^2 w}{\partial x \partial y}\right)^2\right)\right)\right] dydx \tag{A12}$$

The total work done equals the loss of the potential energy:

$$V = \frac{1}{2}\int_0^a \int_0^b \left[N_x \left(\frac{\partial w}{\partial x}\right)^2 + 2N_{xy}\left(\frac{\partial w}{\partial x}\frac{\partial w}{\partial y}\right) + N_y \left(\frac{\partial w}{\partial y}\right)^2\right] dydx \tag{A13}$$

The potential energy is minimised by solving the equation

$$\frac{\partial (U_b + V)}{\partial w_0} = 0 \tag{A14}$$

Substituting equations (A1), (A2), (A3) and (A4) into equation (A12) and performing the integrations will produce:

$$U_b = \frac{D}{2}\left[\frac{68}{35}\frac{m^4\pi^4 b}{8a^3} + \frac{6}{5}\frac{m^2\pi^2}{ab} + \frac{3}{2}\frac{a}{b^3}\right] w_0^2 \tag{A15}$$

while the work done due to external uniaxial compression load is:

$$V = -\frac{N_x}{2}\left[\frac{68}{35}\frac{m^2\pi^2 b}{8a}\right] w_0^2 \tag{A16}$$

Substituting equations (A15) and (A16) into equation (A14) and differentiating with respect to w_0:

$$\frac{D}{2}\left[\frac{68}{35}\frac{m^4\pi^4 b}{8a^3} + \frac{6}{5}\frac{m^2\pi^2}{ab} + \frac{3}{2}\frac{a}{b^3}\right] w_0 - \frac{N_x}{2}\left[\frac{68}{35}\frac{m^2\pi^2 b}{8a}\right] w_0 = 0 \tag{A17}$$

where w_0 is the out of plane displacement amplitude and cannot be equal to zero. So the buckling load for isotropic plate under uniaxial compression is:

$$N_x = D\left[\frac{m^2\pi^2}{a^2} + \frac{84}{17b^2} + \frac{105}{17}\frac{a^2}{m^2\pi^2 b^4}\right] \tag{A18}$$

Equation (A17) can be rewritten in terms of aspect ratio AR

$$N_x = \frac{D}{b^2}\left[\frac{m^2\pi^2}{(AR)^2} + \frac{105}{17}\frac{(AR)^2}{m^2\pi^2} + \frac{84}{17}\right] \tag{A19}$$

For laminates equations (A11) has the form

$$D_{11}\frac{\partial^4 w}{\partial x^4} + 2(D_{12} + 2D_{66})\frac{\partial^4 w}{\partial x^2 \partial x^2} + D_{22}\frac{\partial^4 w}{\partial x^4} = N_x\frac{\partial^2 w}{\partial x^2} \tag{A20}$$

and by applying the same procedure of minimum potential energy, the buckling load for the laminate under compressive load is:

$$N_x = \frac{1}{b^2}\left[\frac{m^2\pi^2 b^2}{a^2}D_{11} + \frac{84}{17}D_{12} + \frac{168}{17}D_{66} + \frac{105}{17}\frac{a^2}{m^2\pi^2 b^2}\right] \tag{A21}$$

In terms of aspect ratio equation (A21) can be written as

$$N_x = \frac{1}{b^2}\left[\frac{m^2\pi^2}{(AR)^2}D_{11} + \frac{84}{17}D_{12} + \frac{168}{17}D_{66} + \frac{105}{17}\frac{(AR)^2}{m^2\pi^2}\right] \tag{A21}$$

Appendix B: Comparison between different mathematical approaches of mode jumping strain detections with different layup:

Mode jumping strain vs aspect ratio for laminate [45 -45 0 90 -45 45 90 0]s aspect ratio:

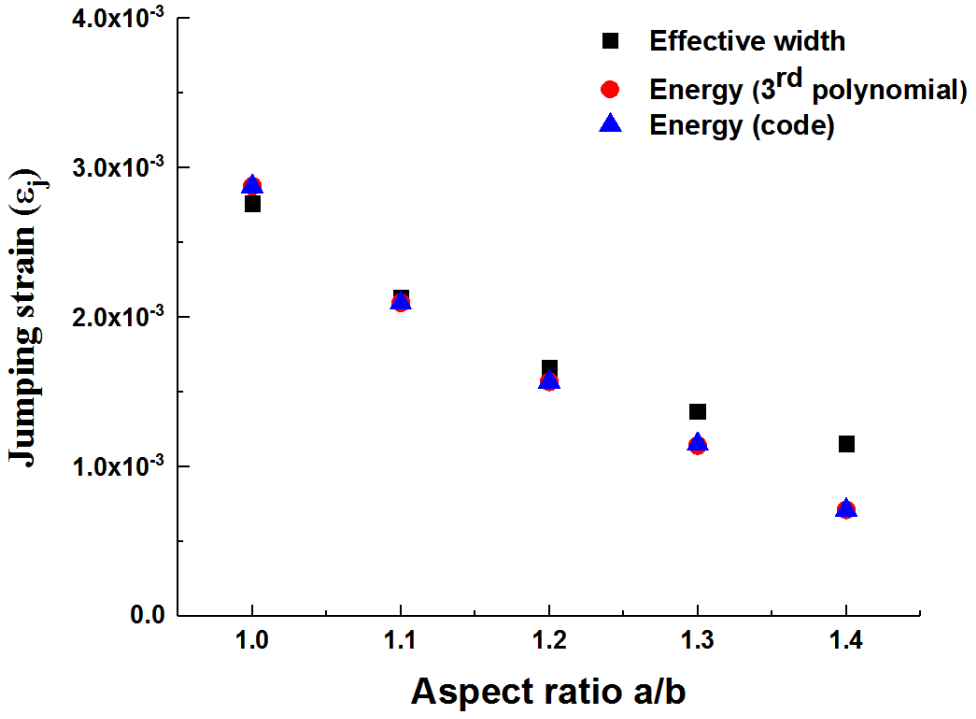

Figure B1: Mode jumps from *m*=1 to *m*=2

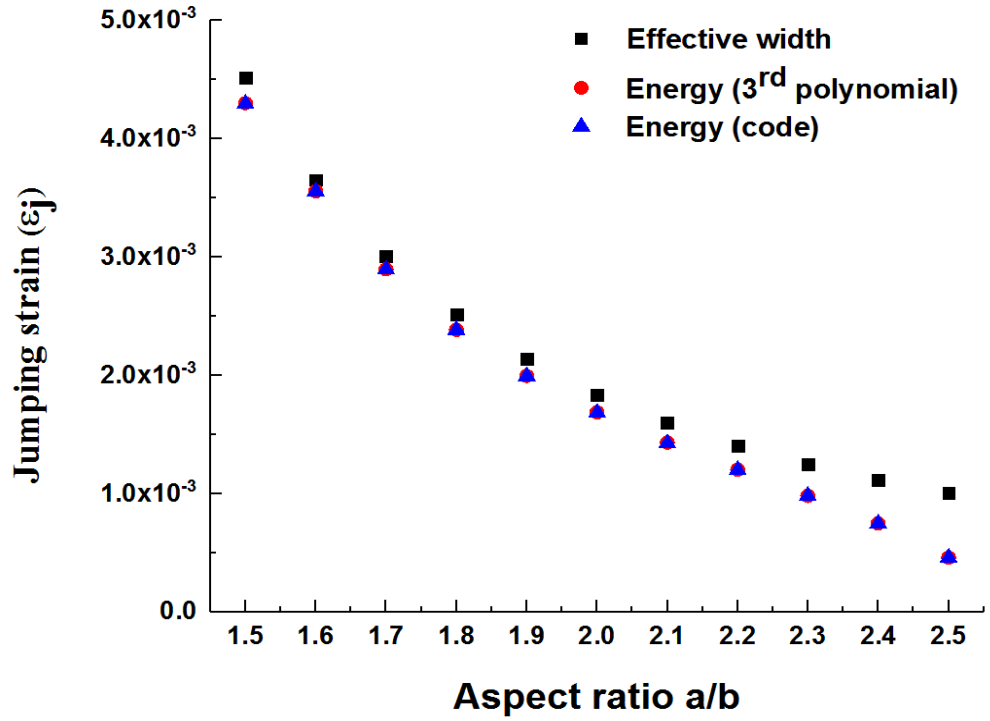

Figure B2: Mode jumps from *m*=2 to *m*=3

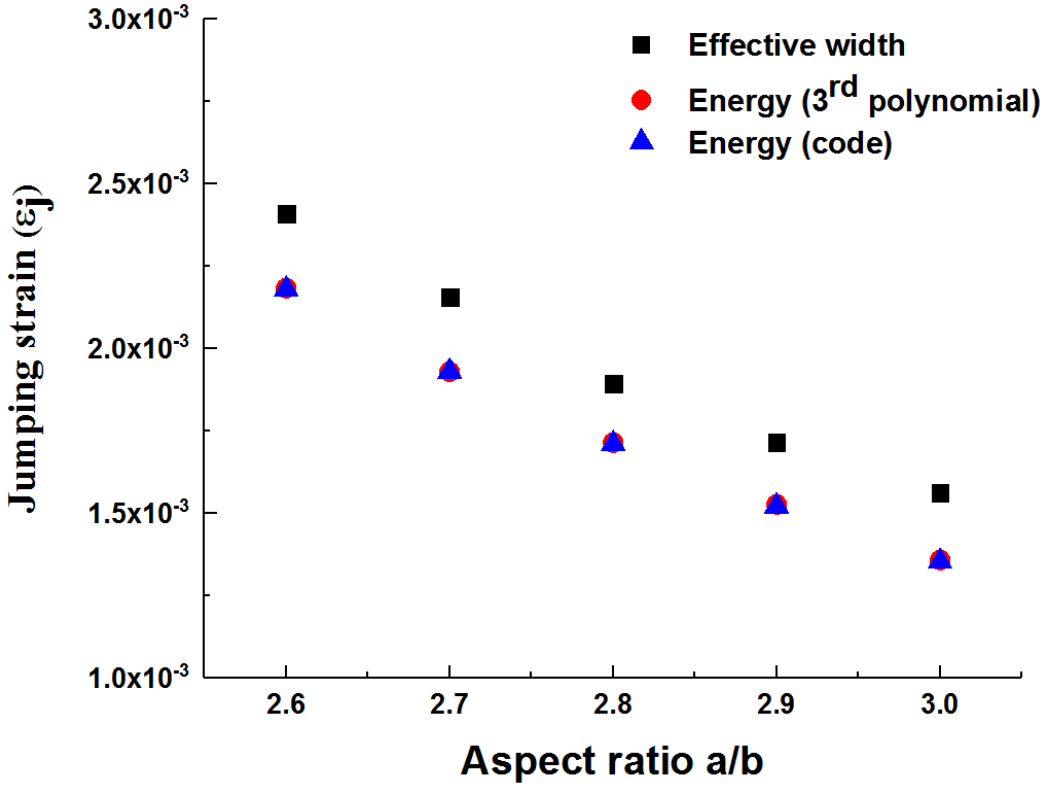

Figure B3: Mode jumps from *m*=3 to *m*=4

Appendix C

Example 3: plate jumps from m=3 to m=4

Results for isotropic and composite plate with layup sequence [45 -45 -45 45 -45 45 45 -45]s:

The mode jumping phenomenon for a plate that initially buckled with three half wavelengths will be discussed here for isotropic composites with aspect ratio between 2.4 and 3.0 by utilising both solutions approaches suggested to predict the jumping strain. An explanation for metal as well as composite plates with aspect ratio 3.0 will be described as an example of mode transformation from mode m=3 to m=4.

The isotropic plate with a/b =3.0 initially buckled with m=3 at load level 6.548 kN (strain 9.038E-5) while the buckling load for mode m=4 was equal to 7.105 kN (strain 9.817E-5). The jumping strain was 7.370E-4 using effective width approaches which was marginally lower than the jumping strain using the methods based on energy comparisons 7.748E-4 (7.723E-4) where the load is dropping from 20.3332 to 19.739 kN (20.290 to 19.701 kN) as presented in Figure C1.

The finite element analysis showed that the plates initially buckled with mode m=3 and at strain 1.081E-4. A tiny buckle started to form to make the buckling pattern move gradually and then a fourth buckle expanded to switch the buckling mode to four half wavelengths instead of three (Figure C2).

The laminates with aspect ratio 3.0 show almost the same behaviour as metal plates with some different features that will be discussed here. For instance, the jumping points estimated by effective width were, unlike the isotropic plate case with the same dimensions, higher than those predicted by methods based on the energy evaluations as shown in Figure C3. The ABAQUS model post-buckling results showed that the laminates have three buckles at strain value

5.599E-4. After that, a fourth half wavelength started to grow at strain 1.1434E-4 and continue to expand as the load increased to form a new mode configuration consisting of four sinusoidal buckles instead of three (Figure C4). The finite element analysis showed that the mechanism of mode switching is almost the same for all plates with different materials and dimensions, i.e. the mode jumping occurred gradually. Moreover, for all cases examined, the VICONOPT results showed a better agreement with ABAQUS post buckling analysis after including the mode jumping in the post-buckling region.

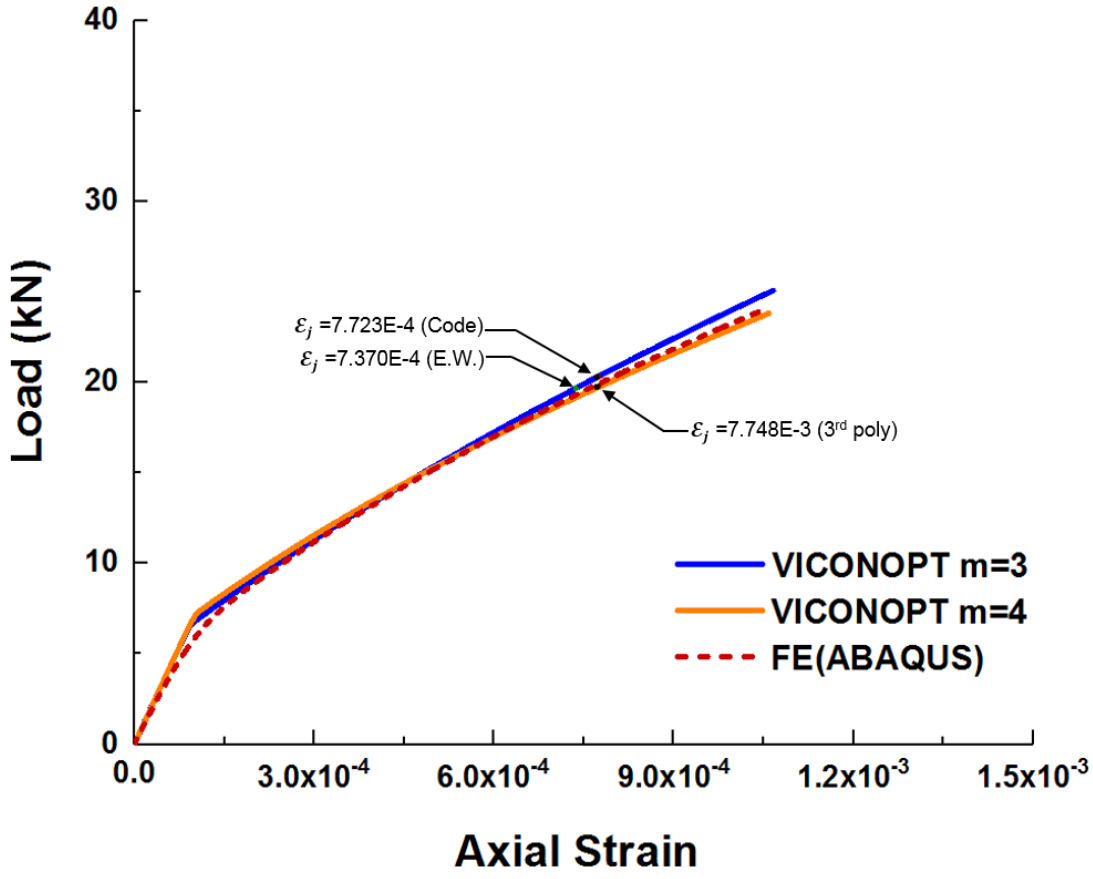

Figure C1: Load vs strain for isotropic flat plate, *a/b*=3.0

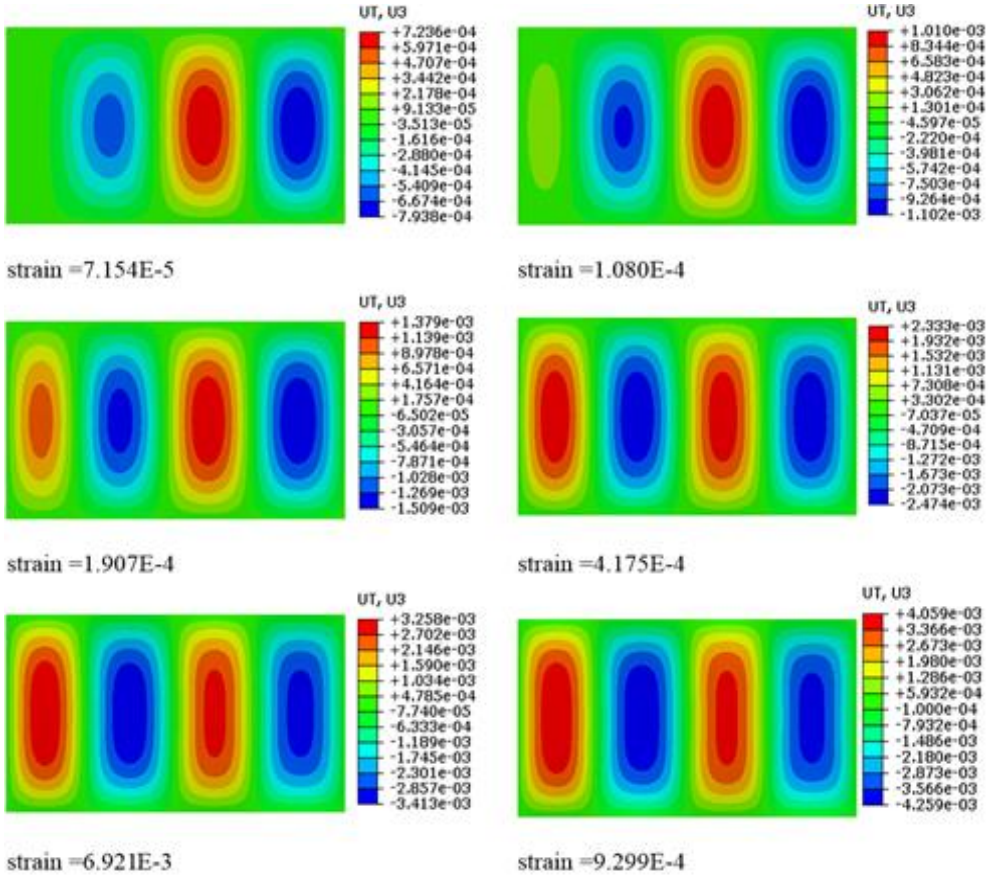

Figure C2: ABAQUS buckling mode for isotropic plate, *a/b* =3.0

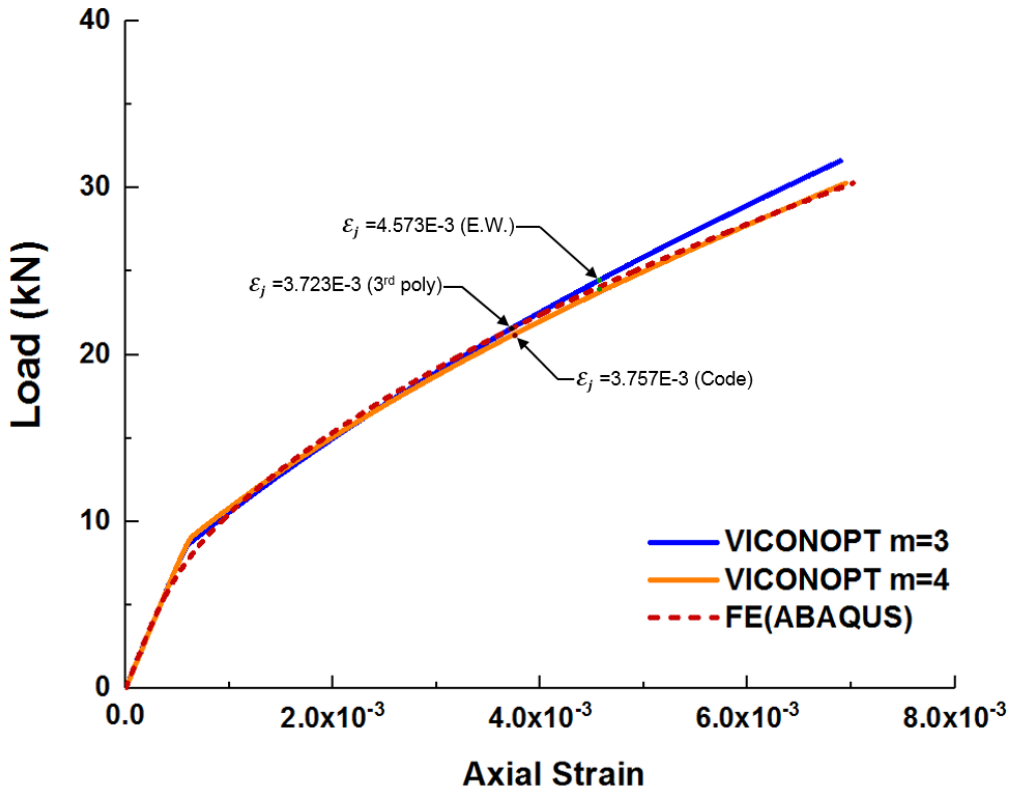

Figure C3: Load vs strain for laminate [45 -45 -45 45 -45 45 45 -45]s, *a/b*=3.0

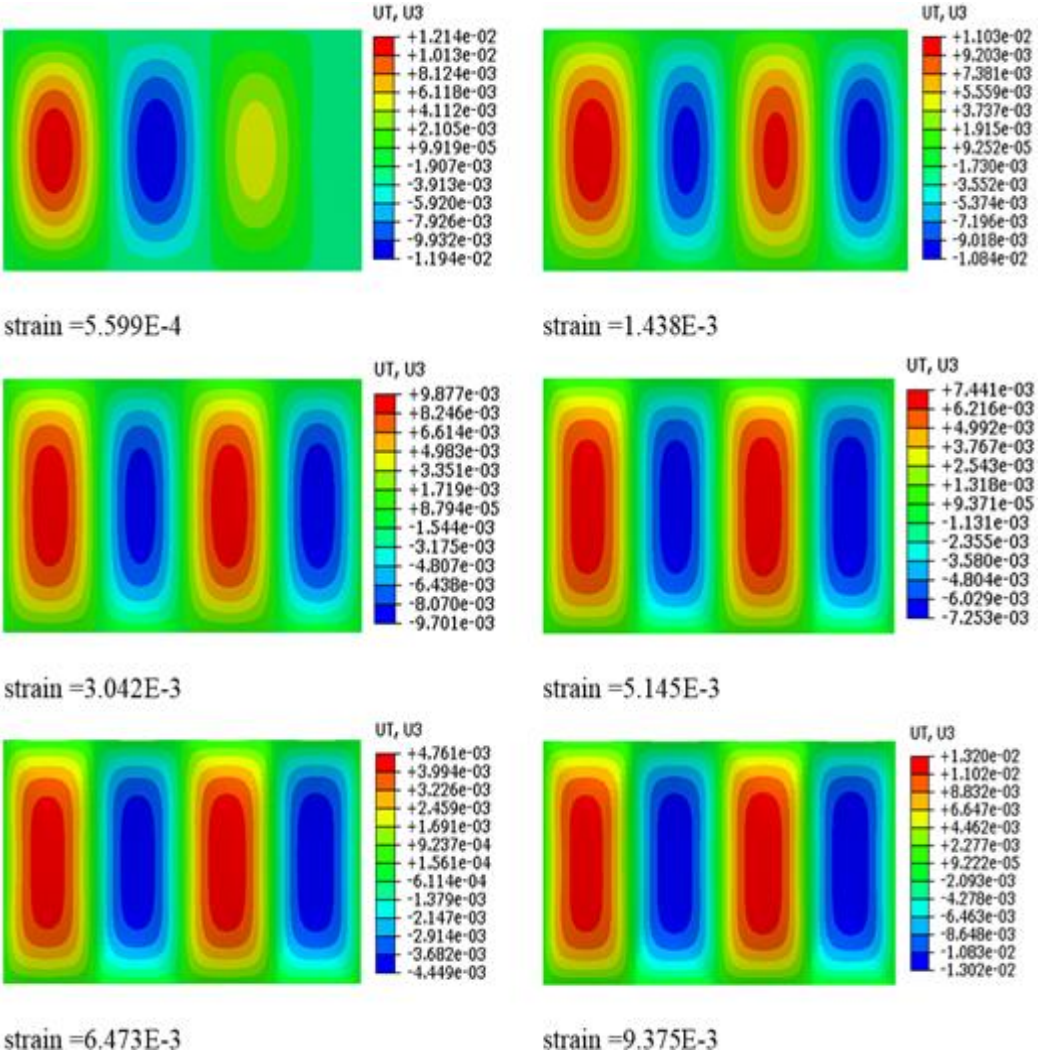

Figure C4: ABAQUS buckling mode for laminate [45 -45 -45 45 -45 45 45 -45]s, a/b =3.0

A comparison between the effective width and energy approaches to detect the mode jumping strain for plates or laminates initially buckling with mode m=3 and the jumping to m=4 is shown in Figures C5 and C6. The main noticeable feature of those results was that the effective width approach generally showed lower values of jumping strain for the isotropic plate and this trend was completely inverted for the composite plates.

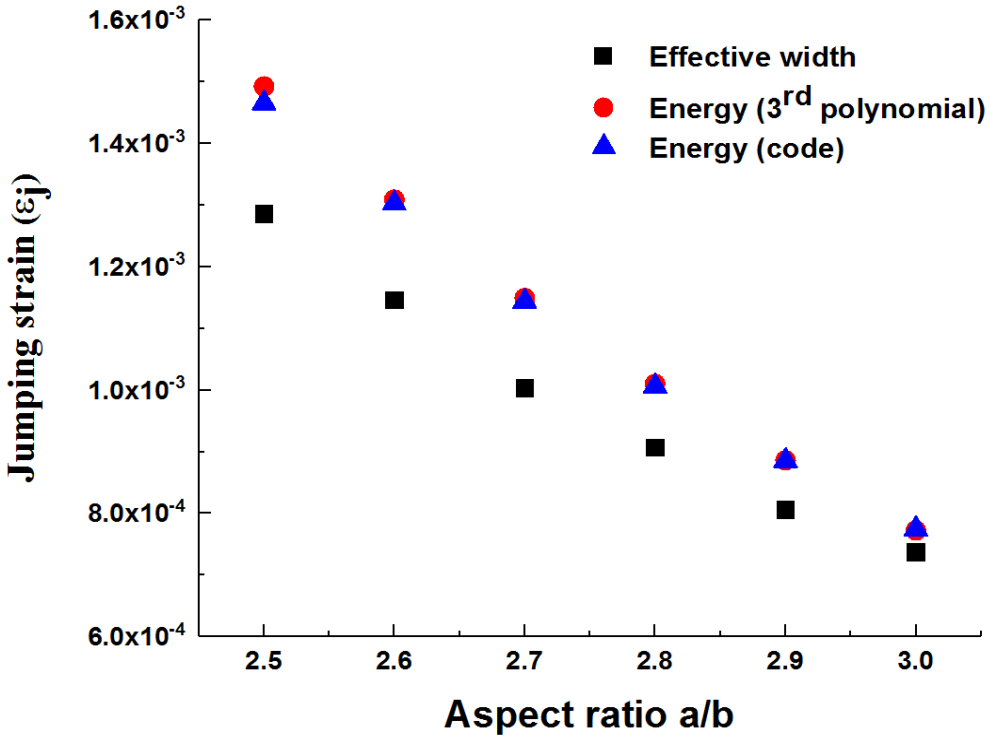

Figure C5: Mode jumping strain for a range of isotropic plates (jump from m=3 to m=4)

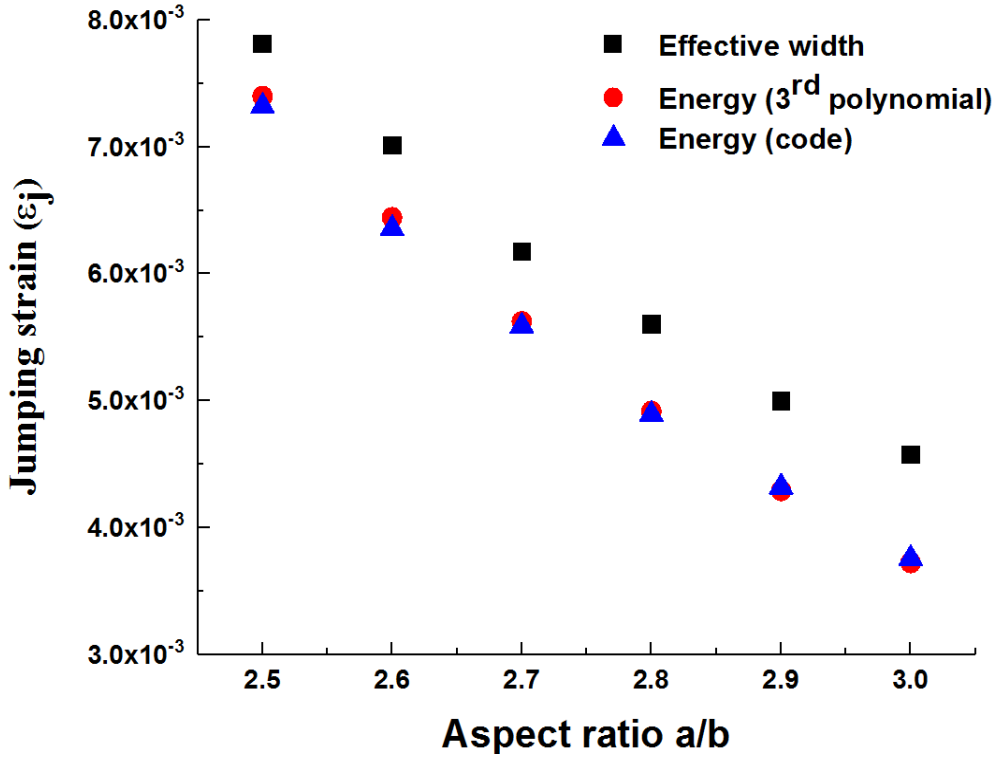

Figure C6: Mode jumping strain for a range of laminates [45 -45 -45 45 -45 45 45 -45]s (jump from m=3 to m=4)